

**Efficient Cardio-Vascular 4D-Flow MRI
enabled CFD to Improve In-Silico Predictions of
Post-Surgical Haemodynamics in Individual
Patients**

Molly Alice Cherry

Submitted in accordance with the requirements for the degree of
Doctor of Philosophy

The University of Leeds

Centre for Doctoral Training in Fluid Dynamics

School of Computing

September 2022

Intellectual Property and Publication Statements

The candidate confirms that the work submitted is her own, except where work which has formed part of jointly authored publications has been included. The contribution of the candidate and the other authors to this work has been explicitly indicated below. The candidate confirms that appropriate credit has been given within the thesis where reference has been made to the work of others.

Chapter 6 is based on work from a jointly authored publication:

Cherry, M., Khatir, Z., Khan, A., and Bissell, M. The Impact of 4D-Flow MRI Spatial Resolution on Patient-Specific CFD Simulations of the Thoracic Aorta. *Scientific Reports*. **12**, 15128 (2022).

The candidate was responsible for the research work undertaken within the publication including all data processing and numerical simulations, as well as being the main author of the manuscript. Malenka Bissell provided the 4D-Flow MRI data of the patient participating in the research. Zinedine Khatir, Amirul Khan, and Malenka Bissell are thesis supervisors and contributed equally to the editing of the manuscript.

This copy has been supplied on the understanding that it is copyright material and that no quotation from the thesis may be published without proper acknowledgement.

©2022 The University of Leeds and Molly Alice Cherry

The right of Molly Alice Cherry to be identified as Author of this work has been asserted by her in accordance with the Copyright, Designs and Patents Act 1988.

Acknowledgements

I would like to thank my academic supervisors Dr Amirul Khan, Dr Malenka Bissell, and Dr Zinedine Khatir who guided me and provided me with support throughout my PhD journey. Without their guidance, expertise and enthusiasm this project would not have been possible.

Thanks to Julio Sotelo Parraguez and Serigo Uribe for allowing me use of the *4D-Flow MRI APP*, and to Pablo Lamata and Harminder Gill for use of their 4D-Flow MRI data set from the flow phantom. I would also like to thank the management board of the EPSRC Centre for Doctoral Training in Fluid Dynamics (Grant Number EP/L01615X/1) for giving me this opportunity and allowing me to complete this thesis.

Finally, I would like to thank my family, without whom this thesis would never have been completed. To my Mum, who's support and belief in me never wavered, and my Dad, who read through every Chapter when I wasn't sure anything made sense. To Soraya and Flora, for encouraging me and always providing moral support, and to Sam, thank you. I wouldn't have got this far without the support you provided.

Abstract

This thesis focuses on creating a workflow that combines four dimensional flow magnetic resonance imaging with computational fluid dynamics techniques, and identifying the main difficulties that are associated with patient-specific modelling. With further development, the proposed workflow will allow post-surgical haemodynamics to be predicted prior to surgical intervention taking place, ensuring the best possible outcome is achieved for the individual patient.

The use of patient-specific computational fluid dynamic modelling in diagnostics and risk stratification, treatment planning, and surgical intervention is quickly becoming an invaluable tool and has proven key in multiple medical advances and breakthroughs. However, existing methods to combine medical imaging and computational fluid dynamics techniques often require invasive procedures to collect appropriate patient-specific data, require expensive software licenses, or have significant limitations within the methodologies, such as inlet conditions or spatial resolutions.

The research within this thesis provides a workflow to combine four dimensional flow magnetic resonance imaging and computational fluid dynamics, using open source software when possible, and a non-invasive and non-ionising imaging technique. The major challenges of patient-specific modelling are investigated. By increasing the complexity of the workflow incrementally, the impacts of physiologically accurate inlet boundary conditions are assessed, as is the human error that is introduced into patient-specific modelling through the geometry reconstruction process. The workflow created is tested on a wide age range of patients and bicuspid aortic valve phenotypes.

To validate the workflow created, the methods used were applied to an anatomical flow phantom, therefore the *in-vivo* challenges of the thoracic aorta moving radially and vertically, and the systemic circulatory system distal to the outlets were removed. This research has shown that the workflow proposed produces good agreement with four dimensional flow magnetic resonance imaging data, notably in the ascending aorta during the systolic phase of the cardiac cycle.

A significant challenge of patient-specific modelling that is often acknowledged yet not fully quantified is the spatial resolution of the four dimensional flow magnetic resonance imaging. Research therefore focused on determining how the spatial resolution at which the four dimensional flow magnetic resonance imaging data is acquired at impacts the subsequent patient-specific computational fluid dynamics simulations. The results presented show that coarse spatial resolutions have a significant impact on the results of numerical simulations. From the results presented, a recommendation of a minimum spatial resolution that should be used when conducting patient-specific simulations was made to avoid errors being introduced into the numerical simulations.

Contents

List of Figures	x
List of Tables	xviii
Glossary	xx
Acronyms	xxii
1 Introduction	1
1.1 Project Outline	1
1.2 Significance of Research	2
1.2.1 Motivation	3
1.3 Research Methods	3
1.3.1 Ethical Approval	3
1.4 Aims and Objectives	3
2 Review of Patient-Specific Cardiac Modelling	5
2.1 Introduction	6
2.2 Overview of the Aorta	6
2.2.1 The Cardiac Cycle	6
2.2.2 Anatomy and Physiology of the Aorta	7
2.2.3 Bicuspid Aortic Valve	8
2.2.4 Aortic Valve Replacement	10
2.2.5 Blood as a Fluid	11
2.2.6 The Importance of Wall Shear Stress	12
2.2.7 Helical Flow In Blood Vessels	13
2.3 4D-Flow Magnetic Resonance Imaging	14
2.3.1 Uses of 4D-Flow MRI	16
2.4 Theoretical Foundations	17
2.4.1 Computational Fluid Dynamics Models	17
2.4.1.1 RANS	17
2.4.1.2 DES	17
2.4.1.3 LES	18
2.4.1.4 DNS	18
2.4.1.5 LBM	18
2.4.2 Reynolds number	18

2.4.3	Non-Newtonian Fluids	19
2.4.3.1	Viscosity Models	19
2.4.3.2	Non-Newtonian Importance Factor	21
2.5	Computational Fluid Dynamics in Cardiac Medicine	22
2.5.1	Inlet Boundary Conditions	25
2.5.2	Outlet Boundary Conditions	26
2.5.2.1	0-Pressure	27
2.5.2.2	Outflow	27
2.5.2.3	Windkessel Models	27
2.5.3	Turbulence Modelling	31
2.5.4	4D-Flow MRI based CFD	33
2.5.5	Predicting Post-Surgical Outcomes with CFD	36
2.6	Fluid-Structure Interactions	38
2.6.1	Fluid-Structure Interaction of the Vessel Wall	39
2.6.2	Fluid-Structure Interaction of the Aortic Valve	43
2.7	Existing Software	44
2.7.1	SimVascular	44
2.7.2	HeartFlow	46
2.7.3	CRIMSON	46
2.7.4	FEops	46
2.8	Summary	47
3	Methodology	49
3.1	Introduction	50
3.2	Data Acquisition	51
3.3	Geometry Reconstruction	53
3.3.1	Human Error in Geometry Reconstruction	58
3.4	Meshing	59
3.4.1	Netgen	60
3.4.2	cfMesh	60
3.4.3	snappyHexMesh	61
3.4.4	Mesh Independence	62
3.4.4.1	Steady State Mesh Independence	62
3.4.4.2	Neonatal Transient Mesh Independence	63
3.4.4.3	Adult Transient Mesh Convergence	64
3.5	Boundary Conditions	65
3.5.1	Steady-state Plug Flow	65
3.5.2	Pulsatile Flow	66
3.5.3	Spatio-Temporal Variations	66
3.5.3.1	Interpolation of 4D-Flow MRI data	67
3.5.3.2	Curve Fitting	68
3.5.3.3	Implementation of Spatio-Temporal Boundary Conditions	73
3.6	Properties of Blood	74
3.6.1	Viscosity	74

3.6.2	Turbulence	74
3.6.3	Homogeneity	76
3.7	Quantification of Haemodynamic Indices	76
3.7.1	Flow Asymmetry	77
3.7.2	Flow Dispersion	78
3.7.3	Circulation	79
3.8	Limitations	79
3.9	Conclusions	80
4	Patient-Specific Results from Methodology Development	82
4.1	Introduction	82
4.2	Steady State Plug Flow	83
4.2.1	Peak Systole	84
4.2.2	Late Diastole	86
4.3	Pulsatile Plug Flow	87
4.3.1	Peak Systole	88
4.3.2	Late Diastole	89
4.4	Spatio-Temporal Patient Specific Flow	91
4.4.1	Systole	91
4.4.2	Diastole	95
4.5	Supra-Aortic Vessels Within the Neonatal Cohort	98
4.5.1	Systole	99
4.5.2	Diastole	101
4.6	Supra-Aortic Vessels Within the Adult Cohort	104
4.6.1	OXBAV012	104
4.6.1.1	Systole	104
4.6.1.2	Diastole	108
4.6.2	OXBAV071	111
4.6.2.1	Systole	112
4.6.2.2	Diastole	114
4.7	Limitations	116
4.8	Conclusions	117
5	Validation of the Methodology Using a Flow Phantom	120
5.1	Introduction	120
5.2	Methodology	121
5.2.1	Experimental Set-up	121
5.2.2	Geometry Reconstruction	122
5.2.3	Boundary Conditions	123
5.2.3.1	Inlet	124
5.2.3.2	Outlets	127
5.2.4	Numerical simulations	128
5.3	Results	128
5.3.1	Systole	128
5.3.2	Diastole	130

5.4	Limitations	132
5.5	Conclusions	133
6	The Impacts of 4D-Flow MRI spatial resolution on patient-specific CFD simulations	134
6.1	Introduction	134
6.2	Methodology	136
6.2.1	Data Acquisition	136
6.2.2	Geometry Reconstruction	137
6.2.3	Meshing	140
6.2.4	Boundary Conditions	140
6.2.5	Numerical Simulations	144
6.3	Results	144
6.3.1	Velocity	144
6.3.2	Wall Shear Stress	149
6.3.3	Flow Asymmetry	152
6.3.4	Flow Dispersion	152
6.3.5	Circulation	154
6.4	Limitations	154
6.5	Conclusions	156
7	Summary	158
7.1	Conclusions	158
7.1.1	Chapter 4: Patient-Specific Results from Methodology Development	158
7.1.2	Chapter 5: Validation of Methodology Using a Flow Phantom	159
7.1.3	Chapter 6: The Impacts of 4D-Flow MRI Spatial Resolution on Patient-Specific CFD Simulations	160
7.2	Implications of the Results	161
7.3	Further Work	161
	References	164

List of Figures

2.1	Schematic of the anatomy of the heart muscle during systole (where the aortic and pulmonary valves are open), demonstrating the location of the four chambers and the valves. Blue arrows indicate de-oxygenated blood, red arrows indicate oxygenated blood.	7
2.2	Schematic of anatomy of the thoracic aorta and supra-aortic branches.	8
2.3	Schematic of a cross section of the thoracic aorta and a close up of the aortic wall demonstrating the location of the inner intima, middle media, and outer adventitia.	9
2.4	Schematic of asymmetric BAV phenotypes with complete raphes from the parasternal short axis view with a TAV for comparison. R =right cusp, L =left cusp, N =non-coronary cusp.	9
2.5	4D-Flow MRI velocity acquisition method	15
2.6	Pulsatile velocity flow profiles applied to the inlet by Madhavan & Kemmerling [79]. Only the flow profile at the inlet was varied, all other parameters of the CFD simulations remained constant.	25
2.7	Inflow velocity profiles implemented by Youssefi <i>et al.</i> [74]; patient-specific (a), parabolic (b), and plug (c), at peak systole for a patient with BAV.	26
2.8	Schematic demonstrating the Windkessel effect in compliant arteries. Solid lines represent the vessel walls at that stage of the cardiac cycle, dashed lines represent the vessel wall location at the previous stage. Red arrows represent the movement of blood.	28
2.9	A two-element Windkessel model (a) and a three-element Windkessel model (b). C =compliance, R =peripheral resistance, R_c =characteristic resistance.	28
2.10	Lumped parameter networks that are coupled to 3D models to replicate the circulatory system, allowing for a multi-scale, closed loop modelling approach.	37
2.11	The <i>SimVascular</i> geometry workflow. Figure (a) demonstrates the path lines through the vessels of interest. Figure (b) demonstrates the 2D segmentations along the path lines. Figure (c) shows the lofted 3D model, and Figure (d) demonstrates the joining of vessels, taken from Updegrave <i>et al.</i> [158]	45
3.1	Workflow used in constructing patient-specific 4D-Flow MRI based CFD simulations.	50
3.2	Phase contrast images through velocity encoding in the V_x , V_y , and V_z directions, and a magnitude image viewed from the sagittal plane.	51

3.3	4D-Flow MRI image of the thoracic aorta of patient CoRaL071 shown in the sagittal plane before (a) and after (b) contrast adjustment has taken place and unwanted noise and vessels have been removed.	54
3.4	4D-Flow MRI images of the thoracic aorta of patient CoRaL071 shown in the sagittal plane, before (a) and after (b) threshold adjustment has taken place. . . .	55
3.5	4D-Flow MRI images of the thoracic aorta of patient CoRaL071 shown in the sagittal plane before (a) and after (b) segmentation has taken place to extract the thoracic aorta only.	56
3.6	Geometry reconstruction results before (a) and after (b) OpenSCAD is used to create planes for the inlet and outlet.	57
3.7	4D-Flow MRI scan data of the thoracic aorta and proximal supra-aortic vessels ((a) and (b)), and the reconstructed <i>in-silico</i> model of the thoracic aorta, overlaid on 4D-Flow MRI data ((c) and (d)) of the neonatal patient, CoRaL071.	57
3.8	4D-Flow MRI scan data of the thoracic aorta and proximal supra-aortic vessels ((a) and (b)), and the reconstructed <i>in-silico</i> model of the thoracic aorta, overlaid on 4D-Flow MRI data ((c) and (d)) of the adult patient, OXBAV012.	58
3.9	Spatially averaged volumetric flow rate (m^3s^{-1}) across the inlet for each of the five geometry reconstruction attempts of patient CoRaL071 at diastole, calculated from 4D-Flow MRI data.	60
3.10	Velocity magnitude (ms^{-1}) contours, determined from 4D-Flow MRI data, over the inlet plane at systole from each geometry reconstruction attempt of patient CoRaL071.	60
3.11	Velocity magnitude (ms^{-1}) contours, determined from 4D-Flow MRI data, over the inlet plane at diastole from each geometry reconstruction attempt of patient CoRaL071.	61
3.12	Potential meshing options explored; (a) shows the unstructured tetrahedral mesh created using Netgen, (b) shows the structured mesh created using cfMesh, (c) shows the structured mesh produced through the snappyHexMesh.	62
3.13	Mesh independence study in the ascending aorta conducting for steady-state simulations with a plug profile on adult patient OXBAV012.	63
3.14	Mesh independence study monitoring velocity magnitude across the x -axis and z -axis over a plane in the mid-ascending aorta for neonatal patient CoRaL071. . . .	63
3.15	Neonatal transient mesh independence study showing velocity magnitude contours over a slice in the mid-ascending aorta. Dashed lines represent x and z axis' used to plot velocity data.	64
3.16	Mesh independence study monitoring velocity magnitude across the x - and z axis over a plane in the mid-ascending aorta for adult patient OXBAV012.	64
3.17	Adult transient mesh independence study showing velocity magnitude contours over a slice in the mid-ascending aorta. Dashed lines represent x and z axis' used to plot velocity data.	65
3.18	Velocity magnitude (ms^{-1}) contours of the inlet boundary condition for neonatal patients with a TAV (CoRaL071 and CoRaL072) at systole, (a) and (c) demonstrate the boundary conditions applied to CFD simulations, whilst (b) and (d) demonstrate the boundary conditions found from 4D-Flow MRI data.	65

3.19	Velocity magnitude (ms^{-1}) contours of the inlet boundary conditions for neonatal patients with BAV (CoRaL072, CoRaL074, and CoRaL076) at systole, (a), (c), and (e) demonstrate the boundary conditions applied to CFD simulations, whilst (b), (d), and (f) demonstrate the boundary conditions found from 4D-Flow MRI data.	66
3.20	The revised location of the inlet plane.	67
3.21	4D-Flow MRI data points from the inlet coloured by volumetric flow rate (m^3s^{-1}) at all time-steps of the cardiac cycle for patient CoRaL071, $t =$ time-step, where $t = 0$ corresponds to $T = 0s$ and $t = 19$ corresponds to $T = 0.5263s$, Each time-step corresponds to $\Delta T = 0.0277s$, $t = 3$ is peak systole; $t = 20$ is late diastole.	68
3.22	The cubic interpolation of the 4D-Flow MRI volumetric flow rate (m^3s^{-1}) data, mapped onto the cell centres of the CFD mesh at each time-step of the cardiac cycle for patient CoRaL071, $t =$ time-step, where $t = 0$ corresponds to $T = 0s$ and $t = 19$ corresponds to $T = 0.5263s$, each time-step corresponds to $\Delta T = 0.0277s$, $t = 3$ is peak systole; $t = 20$ is late diastole.	69
3.23	Continuous temporal variation of the average volumetric flow rate (m^3s^{-1}) at the inlet over one cardiac cycle for patient CoRaL071 calculated from 4D-Flow MRI data.	70
3.24	Volumetric flow rate data (m^3s^{-1}) from 4D-Flow MRI (blue markers) and the surface fit approximating the flow profile (surface) at peak systole ($t = 3$) for patient CoRaL071. Polynomials of 2nd, 3rd, 4th, and 5th order are all presented.	70
3.25	Volumetric flow rate (m^3s^{-1}) data from 4D-Flow MRI (blue markers) and the function approximating the flow profile (surface) at late diastole ($t = 20$) for patient CoRaL071. Polynomials of 2nd, 3rd, 4th, and 5th order are all presented.	71
3.26	Volumetric flow rate (m^3s^{-1}) at each 4D-Flow MRI data point calculated through fitting a 5th order polynomial to the 4D-Flow MRI data for every time-step, $t =$ time-step, where $t = 0$ corresponds to $T = 0s$ and $t = 19$ corresponds to $T = 0.5263s$, each time-step corresponds to $\Delta T = 0.0277s$, $t = 3$ is peak systole; $t = 20$ is late diastole.	73
3.27	Velocity magnitude (ms^{-1}) contours of patient-specific spatio-temporal inlet boundary conditions for neonatal patients with TAV at systole ($t = 3$), (a) and (c) show CFD inlet conditions, (b) and (d) show 4D-Flow MRI data.	74
3.28	Velocity magnitude (ms^{-1}) contours of patient-specific spatio-temporal inlet boundary conditions for neonatal patients with BAV at systole ($t = 3$), (a), (c), and (e) show CFD inlet conditions, (b), (d), and (f) show 4D-Flow MRI data.	74
3.29	Variation in the Stokes number over the course of the cardiac cycle for neonatal patient CoRaL071.	77
3.30	Location of planes used for the quantification of haemodynamic indices. $A=inlet$, $B=mid\text{-}ascending\ aorta$, $C=transverse\ aortic\ arch$, $D=mid\text{-}descending\ aorta$, $E=outlet$	77

3.31	4D-Flow MRI velocity magnitude contours across a plane in the ascending aorta at systole of patient CoRaL071, the area with velocities in the top 15% (red markers), and the area with velocities in the bottom 85% (green markers) are highlighted, as well as the geometric centroid (X_a) and the centroid of the top 15% of velocities (X_b).	78
4.1	Maximum volumetric flow rate (m^3s^{-1}) at the inlet plane over one cardiac cycle for patient OXBAV012. Peak systole and late diastole are indicated as the time-steps chosen for steady-state plug profile simulations.	83
4.2	Contours of velocity magnitude (ms^{-1}) calculated through steady-state CFD simulations with a plug profile and 4D-Flow MRI data at peak systole ($t = 0.1071s$) at three planes of interest for patient OXBAV012. ($B=mid\text{-}ascending\ aorta$, $C=aortic\ arch$, $D=mid\text{-}descending\ aorta$).	84
4.3	Flow asymmetry (%), flow dispersion (%), and through plane circulation (mm^2s^{-1}) calculated at systole from 4D-Flow MRI data and steady-state plug profile CFD data at three planes of interest. ($B=mid\text{-}ascending\ aorta$, $C=aortic\ arch$, $D=mid\text{-}descending\ aorta$.)	85
4.4	Contours of velocity magnitude (ms^{-1}) calculated through steady-state CFD simulations with a plug profile and 4D-Flow MRI data at late diastole ($t = 0.8571s$) at three planes of interest for patient OXBAV012. ($B=mid\text{-}ascending\ aorta$, $C=aortic\ arch$, $D=mid\text{-}descending\ aorta$).	86
4.5	Flow asymmetry (%), flow dispersion (%), and through plane circulation (mm^2s^{-1}) calculated at diastole from 4D-Flow MRI data and steady-state plug profile CFD data at three planes of interest. ($B=mid\text{-}ascending\ aorta$, $C=aortic\ arch$, $D=mid\text{-}descending\ aorta$.)	87
4.6	Contours of velocity magnitude (ms^{-1}) calculated through pulsatile CFD simulations with a plug profile and 4D-Flow MRI data at peak systole ($t = 0.1071s$) at three planes of interest for patient OXBAV012. ($B=mid\text{-}ascending\ aorta$, $C=aortic\ arch$, $D=mid\text{-}descending\ aorta$.)	88
4.7	Flow asymmetry (%), flow dispersion (%), and through plane circulation (mm^2s^{-1}) calculated at systole from 4D-Flow MRI data and pulsatile plug profile CFD data at three planes of interest. ($B=mid\text{-}ascending\ aorta$, $C=aortic\ arch$, $D=mid\text{-}descending\ aorta$.)	89
4.8	Contours of velocity magnitude (ms^{-1}) calculated through pulsatile CFD simulations with a plug profile and 4D-Flow MRI data at diastole ($t = 0.8571s$) at three planes of interest for patient OXBAV012. ($B=mid\text{-}ascending\ aorta$, $C=aortic\ arch$, $D=mid\text{-}descending\ aorta$.)	90
4.9	Flow asymmetry (%), flow dispersion (%), and through plane circulation (mm^2s^{-1}) calculated at diastole from 4D-Flow MRI data and pulsatile plug profile CFD data at three planes of interest. ($B=mid\text{-}ascending\ aorta$, $C=aortic\ arch$, $D=mid\text{-}descending\ aorta$.)	90
4.10	Contours of velocity magnitude (ms^{-1}) at three planes of interest for all patients at systole. Velocity contours calculated through the CFD methodology are given in (a),(c) and (e). Velocity contours calculated by 4D-Flow MRI are given in (b), (d), and (f). ($B=mid\text{-}ascending\ aorta$, $C=aortic\ arch$, $D=mid\text{-}descending\ aorta$.)	92

4.11	Flow asymmetry (%) calculated at systole for the five neonatal patients with spatio-temporal patient-specific inlet conditions at the three planes of interest. CFD values are compared to 4D-Flow MRI data. (<i>B=mid-ascending aorta, C=aortic arch, D=mid-descending aorta</i>).	93
4.12	Flow dispersion (%) calculated at systole for the five neonatal patients with spatio-temporal patient-specific inlet conditions at the three planes of interest. CFD values are compared to 4D-Flow MRI data. (<i>B=mid-ascending aorta, C=aortic arch, D=mid-descending aorta</i>).	94
4.13	Through-plane circulation (mm^2s^{-1}) calculated at systole for the five neonatal patients with spatio-temporal patient-specific inlet conditions at the three planes of interest. CFD values are compared to 4D-Flow MRI data. (<i>B=mid-ascending aorta, C=aortic arch, D=mid-descending aorta</i>).	94
4.14	Contours of velocity magnitude (ms^{-1}) at three planes of interest for all patients at diastole. Velocity contours calculated through the CFD methodology are given in (a),(c) and (e). Velocity contours calculated by 4D-Flow MRI are given in (b), (d), and (f).	96
4.15	Flow asymmetry (%) calculated at diastole for the five neonatal patients with spatio-temporal patient-specific inlet conditions at the three planes of interest. CFD values are compared to 4D-Flow MRI data. (<i>B=mid-ascending aorta, C=aortic arch, D=mid-descending aorta</i>).	97
4.16	Flow dispersion (%) calculated at diastole for the five neonatal patients with spatio-temporal patient-specific inlet conditions at the three planes of interest. CFD values are compared to 4D-Flow MRI data. (<i>B=mid-ascending aorta, C=aortic arch, D=mid-descending aorta</i>).	97
4.17	Through-plane circulation (mm^2s^{-1}) calculated at diastole for the five neonatal patients with spatio-temporal patient-specific inlet conditions at the three planes of interest. CFD values are compared to 4D-Flow MRI data. (<i>B=mid-ascending aorta, C=aortic arch, D=mid-descending aorta</i>).	98
4.18	Geometry reconstruction of neonatal patient CoRaL072 showing the location of the additional three outlets when the supra-aortic vessels are included.	99
4.19	Contours of velocity magnitude (ms^{-1}) calculated through spatio-temporal patient-specific CFD simulations with the supra-aortic vessels included and 4D-Flow MRI data at systole at three planes of interest for the neonatal patient CoRaL072. (<i>B=mid-ascending aorta, C=aortic arch, D=mid-descending aorta</i>).	100
4.20	Velocity contours using cell data at the aortic arch during the systolic period for neonatal patient CoRaL072.	101
4.21	Flow asymmetry (%), flow dispersion (%), and through plane circulation (mm^2s^{-1}) at systole for neonatal patient CoRaL072 at three planes of interest with the supra-aortic vessels included, compared to the corresponding values when the supra-aortic vessels are neglected. (<i>B=mid-ascending aorta, C=aortic arch, D=mid-descending aorta</i>).	101

4.22	Contours of velocity magnitude (ms^{-1}) calculated through spatio-temporal patient-specific CFD simulations with the supra-aortic vessels included and 4D-Flow MRI data at diastole at three planes of interest for the neonatal patient CoRaL072. ($B=mid\text{-}ascending\ aorta, C=aortic\ arch, D=mid\text{-}descending\ aorta$).	102
4.23	Flow asymmetry (%), flow dispersion (%), and through plane circulation (mm^2s^{-1}) at diastole for neonatal patient CoRaL071 at three planes of interest with the supra-aortic vessels included, compared to the corresponding values when the supra-aortic vessels are neglected. ($B=mid\text{-}ascending\ aorta, C=aortic\ arch, D=mid\text{-}descending\ aorta$).	103
4.24	Geometry reconstruction of adult patients OXBAV012 and OXBAV071 showing the location of the additional three outlets of the supra-aortic vessels.	105
4.25	Contours of velocity magnitude (ms^{-1}) calculated through spatio-temporal patient-specific CFD simulations with the supra-aortic vessels included and 4D-Flow MRI data at systole at three planes of interest for the adult patient OXBAV012. ($B=mid\text{-}ascending\ aorta, C=aortic\ arch, D=mid\text{-}descending\ aorta$).	106
4.26	Flow asymmetry (%), flow dispersion (%), and through plane circulation (mm^2s^{-1}) at systole for patient OXBAV012 at three planes of interest. Results from steady state and transient simulations with a plug profile, and spatio-temporal patient-specific simulations with the supra-aortic vessels are compared alongside the corresponding 4D-Flow MRI data. ($B=mid\text{-}ascending\ aorta, C=aortic\ arch, D=mid\text{-}descending\ aorta$).	107
4.27	Velocity magnitude (ms^{-1}) data from the inlet plane at systole from 4D-Flow MRI data (a) and the calculated CFD inlet condition (b).	108
4.28	Contours of velocity magnitude (ms^{-1}) calculated through spatio-temporal patient-specific CFD simulations with the supra-aortic vessels included and 4D-Flow MRI data at diastole at three planes of interest for the adult patient OXBAV012. ($B=mid\text{-}ascending\ aorta, C=aortic\ arch, D=mid\text{-}descending\ aorta$).	109
4.29	Flow asymmetry (%), flow dispersion (%), and through plane circulation (mm^2s^{-1}) at diastole for patient OXBAV012 at three planes of interest. Results from steady state and transient simulations with a plug profile, and spatio-temporal patient-specific simulations with the supra-aortic vessels are compared alongside the corresponding 4D-Flow MRI data. ($B=mid\text{-}ascending\ aorta, C=aortic\ arch, D=mid\text{-}descending\ aorta$).	110
4.30	Velocity magnitude (ms^{-1}) data from the inlet plane at diastole from 4D-Flow MRI data (a) and the calculated CFD inlet condition (b).	110
4.31	Velocity magnitude data (ms^{-1}) over the inlet plane found from 4D-Flow MRI data at each time-step over the course of the cardiac cycle (a), and the calculated CFD inlet condition at the corresponding times (b) for patient OXBAV071.	111
4.32	Contours of velocity magnitude (ms^{-1}) calculated through the CFD methodology and 4D-Flow MRI at three planes of interest for patient OXBAV071 at systole. ($B=mid\text{-}ascending\ aorta, C=aortic\ arch, D=mid\text{-}descending\ aorta$).	112
4.33	Flow asymmetry (%), flow dispersion (%), and through plane circulation (mm^2s^{-1}) at systole for patient OXBAV071 at three planes of interest. ($B=mid\text{-}ascending\ aorta, C=aortic\ arch, D=mid\text{-}descending\ aorta$).	113

4.34	Contours of velocity magnitude (ms^{-1}) calculated through the CFD methodology and 4D-Flow MRI at three planes of interest for patient OXBAV071 at diastole. ($B=mid\text{-ascending aorta}$, $C=aortic arch$, $D=mid\text{-descending aorta}$).	114
4.35	Flow asymmetry (%), flow dispersion (%), and through plane circulation (mm^2s^{-1}) at diastole for patient OXBAV071 at three planes of interest. ($B=mid\text{-ascending aorta}$, $C=aortic arch$, $D=mid\text{-descending aorta}$).	115
5.1	Anatomical flow phantom used in the experimental set-up to validate CFD methodology. The silicone flow phantom is shown in the 4mm acrylic box. Image taken from Elastrat [187].	122
5.2	Flow circuit connected to the anatomical flow phantom.	122
5.3	4D-Flow MRI magnitude images taken in the coronal plane of the silicon flow phantom submerged in agar solution with BAV inserted. (a) demonstrates the open BAV, whilst (b) shows the aortic valve closed; one of the valve leaflets has restricted motion resulting in a reduced opening and an eccentric jet of blood being ejected.	123
5.4	4D-Flow MRI scan data of the flow phantom. (a) shows the 4D-Flow MRI data, (b) identifies the region where the two pipes with different diameters are joined (highlighted in red), as well as a region with a significant artefact in the data (highlighted in green), and (c) shows the reconstructed <i>in-silico</i> geometry using the method outlined in Section 3.3.	124
5.5	Velocity magnitude (ms^{-1}) contours across a slice in the z plane over the course of the cardiac cycle within the flow phantom. (a)=0s, (y)=0.7992s, with each timestep being 0.0333s is length.	125
5.6	Data points coloured by velocity magnitude (ms^{-1}) across the inlet plane over the cardiac cycle of the flow phantom, plotted using 4D-Flow MRI data (a), and the calculated inlet conditions applied in the CFD simulations (b).	126
5.7	Velocity magnitude vectors across the inlet plane of the flow phantom calculated through 4D-Flow MRI (a) and initial CFD simulations (b) at systole.	127
5.8	Streamlines coloured by velocity magnitude (ms^{-1}) within the flow phantom calculated through 4D-Flow MRI data (a) and initial CFD simulations (b) at systole.	127
5.9	Streamlines coloured by velocity magnitude (ms^{-1}) within the flow phantom calculated through 4D-Flow MRI data (a) and CFD simulations with the updated inlet boundary condition (b) at systole.	128
5.10	Contours of velocity magnitude (ms^{-1}) calculated through spatio-temporal patient-specific CFD simulations with the supra-aortic vessels included and 4D-Flow MRI data at systole at three planes of interest for the flow phantom. ($B=mid\text{-ascending aorta}$, $C=aortic arch$, $D=mid\text{-descending aorta}$).	129
5.11	Flow asymmetry (%), flow dispersion (%), and through plane circulation (mm^2s^{-1}) at systole for the flow phantom at three planes of interest. ($B=mid\text{-ascending aorta}$, $C=aortic arch$, $D=mid\text{-descending aorta}$).	130
5.12	Contours of velocity magnitude (ms^{-1}) at three planes of interest for the flow phantom at diastole. Velocity contours calculated through the CFD methodology are given in (a), (c), and (e). Velocity contours calculated by 4D-Flow MRI are given in (b), (d), and (f).	131

5.13	Flow asymmetry (%), flow dispersion (%), and through plane circulation (mm^2s^{-1}) values calculated using CFD and 4D-Flow MRI data at diastole for the flow phantom at three planes of interest.	132
6.1	4D-Flow MRI images in the same location in the sagittal plane of the thoracic aorta, taken at the four varying spatial resolutions for the patient CoRaL080. (a) = $4mm \times 4mm \times 4mm$, (b) = $3mm \times 3mm \times 3mm$, (c) = $2mm \times 2mm \times 2mm$, (d) = $1.5mm \times 1.5mm \times 1.5mm$	137
6.2	Location of inlet, outlet, and the plane of interest in the mid-ascending aorta for patient CoRaL080 (a), and the cross-section of the plane of interest in the mid-ascending aorta (b).	138
6.3	<i>in-silico</i> patient-specific geometries created from 4D-Flow MRI images from the four varying spatial resolutions for the patient identified as CoRaL080. (a) = $4mm \times 4mm \times 4mm$, (b) = $3mm \times 3mm \times 3mm$, (c) = $2mm \times 2mm \times 2mm$, and (d) = $1.5mm \times 1.5mm \times 1.5mm$	139
6.4	Volumetric flow rates (ml/s) at the inlet determined using 4D-Flow MRI data for all four spatial resolutions. The systolic and diastolic phases are shown enclosed by the dashed lines.	141
6.5	Velocity magnitude (ms^{-1}) contours over the inlet plane determined from 4D-Flow MRI data from the four 4D-Flow MRI spatial resolutions over the systolic (a) and diastolic (b) phases.	142
6.6	Maximum and mean velocity magnitude (ms^{-1}) data across the inlet plane calculated using 4D-Flow MRI data and CFD data at systole (a) and diastole (b).	143
6.7	Velocity magnitude (ms^{-1}) contours from the systolic (a) and diastolic (b) phases over a plane in the mid-ascending aorta, comparing 4D-Flow MRI and CFD for all spatial resolutions.	145
6.8	Velocity magnitude (ms^{-1}) along the x - and z -axis' across a plane at the mid-ascending aorta over the systolic and diastolic phases for the four CFD simulations based on the varying spatial resolutions.	148
6.9	Wall shear stress magnitude (Nm^{-2}) at eight locations on the mid-ascending aortic wall determined from 4D-Flow MRI data and CFD data during the systolic and diastolic phases of the cardiac cycle. <i>R=right, RP=right-posterior, P=posterior, LP=left-posterior, L=Left, LA=left-anterior, A=anterior, RA=right-anterior</i>	150
6.10	Average wall shear stress magnitude (Nm^{-2}) over the eight locations of the plane in the mid-ascending aorta, calculated with 4D-Flow MRI data and CFD data for all four spatial resolutions during the systolic and diastolic phases.	151
6.11	Flow asymmetry (%) calculated at the plane in the mid-ascending aorta from CFD and 4D-Flow MRI data at systole (a) and diastole (b) for all spatial resolutions.	153
6.12	Flow dispersion (%) calculated at the plane in the mid-ascending aorta from CFD and 4D-Flow MRI data at systole (a) and diastole (b) for all spatial resolutions.	153
6.13	Through plane circulation (mm^2s^{-1}) calculated at the plane in the mid-ascending aorta from CFD and 4D-Flow MRI data at systole (a) and diastole (b) for all spatial resolutions.	154

List of Tables

2.1	Boundary condition combinations for the inlet, supra-aortic branches, and outlet investigated by Pirola <i>et al.</i> [85]. <i>P-S=patient-specific, 3-E WM=3-Element Windkessel Model.</i>	31
3.1	Demographic of adult patients used within this research detailing BAV phenotype, direction of helical flow, age, Body Mass Index (BMI) and gender. (<i>RN=Right-Non-coronary, RL=Right-Left</i>).	52
3.2	Demographic of neonatal patients used within this research detailing the age (days) and weight (<i>kg</i>) of the patients.	52
3.3	Diameter, average velocity magnitude, and volumetric flow rate at systole and diastole across a slice in the ascending aorta for the five geometry reconstruction attempts on patient CoRaL071.	59
3.4	Number of divisions in the <i>x</i> , <i>y</i> , and <i>z</i> directions of the <i>blockMesh</i> used in the mesh independence studies.	62
3.5	Goodness of fit statistics comparing the 4 surface fits used to model the 4D-Flow MRI data at the inlet at peak systole (<i>t = 3</i>) and late diastole (<i>t = 20</i>). SSE=sum of squares due to error; RMSE=root mean square error.	72
3.6	Calculated Womersley and Reynolds numbers for the patients used within this research. Where Womersley and Reynolds numbers were unavailable, this was due to poor 4D-Flow MRI data quality that did not allow for appropriate or accurate segmentation to occur.	75
4.1	Maximum and mean velocity magnitude (ms^{-1}) data at the three planes of interest during systole calculated using 4D-Flow MRI data and CFD data, including a comparison between the two methods at each location. (<i>B=mid-ascending aorta, C=aortic arch, D=mid-descending aorta</i>).	106
4.2	Maximum and mean velocity magnitude (ms^{-1}) data at the three planes of interest during diastole calculated using 4D-Flow MRI data and CFD data, including a comparison between the two methods at each location. (<i>B=mid-ascending aorta, C=aortic arch, D=mid-descending aorta</i>).	108
4.3	Maximum and mean velocity magnitude (ms^{-1}) data for patient OXBAV071 at the three planes of interest during systole calculated using 4D-Flow MRI data and CFD data, including a comparison between the two methods at each location. (<i>B=mid-ascending aorta, C=aortic arch, D=mid-descending aorta</i>).	113

4.4	Maximum and mean velocity magnitude (ms^{-1}) data for patient OXBAV071 at the three planes of interest during diastole calculated using 4D-Flow MRI data and CFD data, including a comparison between the two methods at each location. ($B=mid$ - <i>ascending aorta</i> , $C=aortic arch$, $D=mid$ - <i>descending aorta</i>).	115
5.1	Maximum and mean velocity magnitude (ms^{-1}) data for the flow phantom at the three planes of interest during systole calculated from 4D-Flow MRI data and CFD data, including a comparison between the two methods at each location. ($B=mid$ - <i>ascending aorta</i> , $C=aortic arch$, $D=mid$ - <i>descending aorta</i>).	129
5.2	Maximum and mean velocity magnitude (ms^{-1}) data for the flow phantom at the three planes of interest during diastole calculated from 4D-Flow MRI data and CFD data, including a comparison between the two methods at each location. ($B=mid$ - <i>ascending aorta</i> , $C=aortic arch$, $D=mid$ - <i>descending aorta</i>).	131
6.1	Spatial ($x \times y \times zmm^3$) and temporal (ms) resolutions of 4D-Flow MRI scans used in recent studies (2010-2019) that have utilised 4D-Flow MRI to acquire haemodynamic data.	135
6.2	The number of voxels in the x and z directions for the four scan resolutions in a slice in the axial plane in the mid-ascending aorta	137
6.3	Inlet plane diameters (cm) for all 4D-Flow MRI scans calculated from 4D-Flow MRI data and CFD data.	138
6.4	Maximum and mean velocity magnitude (ms^{-1}) data at the inlet plane during systole calculated using 4D-Flow MRI data and CFD data, including a comparison between the two methods for each spatial resolution.	142
6.5	Maximum and mean velocity magnitude (ms^{-1}) data at the inlet plane during diastole calculated using 4D-Flow MRI data and CFD data, including a comparison between the two methods for each spatial resolution.	143
6.6	Maximum and mean velocity magnitude (ms^{-1}) data at the mid-ascending aortic plane during systole calculated using 4D-Flow MRI data and CFD data, including a comparison between the two methods for each spatial resolution.	146
6.7	Maximum and mean velocity magnitude (ms^{-1}) data at the mid-ascending aortic plane during diastole calculated using 4D-Flow MRI data and CFD data, including a comparison between the two methods for each spatial resolution.	147

Glossary

Abdominal Aorta The continuation of the thoracic aorta, running from the diaphragm to the iliac arteries.

Aortic Annulus The fibrous ring at the aortic orifice, it is considered the transition point between the left ventricle and the aortic root.

Aortic Bifurcation The point at which the abdominal aorta forks into the left and right iliac arteries.

Aortic Dissection Tearing in the inner layer of the aorta that causes the inner layer to separate from the middle layer.

Aortic Regurgitation or Aortic Insufficiency. Leaking of the aortic valve causing reversed flow back into the left ventricle.

Aortic Stenosis The narrowing of the aortic valve opening.

Aortic Valve The valve in the human heart between the left ventricle and the aorta, it controls the blood flow into the systemic circulatory system.

Aortic Valve Dysfunction The aortic valve ceases to function properly.

Arterioles The small diameter blood vessels that form part of the microvasculature that branch out from an artery and lead to capillaries.

Ascending Aorta The section of the aorta in the chest cavity that extends from the left ventricle to the aortic arch.

Atherosclerosis The build up of fats, cholesterol, and other substances that form deposits on arterial walls, leading to the narrowing of the vessels and the restriction of blood flow.

Bidirectional Cavopulmonary Anastomosis A surgical procedure in which the superior vena cava is disconnected from the right atrium and instead connected to the right pulmonary artery allowing de-oxygenated blood to bypass the heart and flow directly to the patients lungs.

Brachiocephalic Artery The first branch of the aortic arch, supplying oxygenated blood to the right arm, head and neck.

Carotid-Jugular Arteriovenous Fistula An abnormal connection or passageway between the carotid artery and the jugular vein.

Coaptation Area The region of the valve leaflets that overlaps during diastole.

Coarctation of the Aorta A congenital heart defect that is the narrowing of the aorta, resulting in abnormal blood flow.

Congenital Heart Defect A defect in the structure of the heart or great vessels that is present from birth. Symptoms vary greatly depending on the defect ranging from none to life threatening.

Descending Aorta The segment of the aorta beginning at the aortic arch and running down through the chest and abdomen.

Double Aortic Arch A rare congenital defect in which there are two aortic arches present, the two arches re-join to form the descending aorta. It is known to compress the trachea and/or oesophagus.

Endocarditis A potentially fatal bacterial infection inside the heart, most commonly found around the heart valves.

Endothelium A thin membrane of a single layer of cells (endothelial cells) that lines the inside of the heart and blood vessels.

Epigenetics The study of how behaviours and the environment can cause changes that impact how genes work. Epigenetic changes are reversible and do not change a DNA sequence, but change how the body reacts to the DNA sequence.

Great Vessels The large blood vessels bringing blood to and from the heart muscle (the aorta, the pulmonary artery, the pulmonary veins, the superior vena cava, and the inferior vena cava).

Iliac Arteries Arteries originating from the aortic bifurcation, supplying the pelvic region, hips, thighs and reproductive organs with oxygenated blood.

In-Silico Research or experiments conducted using computer modelling or simulation.

In-Vivo Research or experiments that take place in a living organism.

Infrarenal Aorta The segment of the abdominal aorta between the renal arteries and the iliac bifurcation.

Inner Intima The inner layer of the aortic wall.

Interatrial Septum The tissue that separates the right and left atria in the heart.

Interventricular Septum The tissue that separates the right and left ventricles in the heart.

Left Common Carotid Artery The second branch of the aortic arch, supplying the brain with oxygenated blood.

Left Subclavian Artery The third branch of the aortic arch, supplying the left arm with oxygenated blood.

Leukocytes Or white blood cells. Known to protect the body against foreign substances and disease.

Middle Media The middle layer of the aortic wall.

Neonatal Also known as newborn, the neonatal period refers to the first 28 days post birth.

Outer Adventitia The outer layer of the aortic wall containing the nerves.

Pulmonary Circulatory System The portion of the circulatory system which transports de-oxygenated blood from the right ventricle to the lungs, and carries the newly oxygenated blood back to the left atrium.

Pulmonary Hypertension High blood pressure within the pulmonary arteries, causing the pulmonary arteries become thickened and stiff, reducing the blood flow causing the right side of the heart to work harder, leading damage to the right side of the heart and eventually to heart failure.

Right Coronary Artery A major artery originating above the right cusp of the aortic valve that supplies the right ventricle of the heart with oxygenated blood.

Sinuses of Valsalva The widening of the aortic root just above the aortic valve.

Stroke Volume The volume of blood that is pumped from the left ventricle with every contraction of the heart muscle. Calculated as the difference between the end-systolic volume and the end-diastolic volume.

Supra-Aortic Vessels The vessels originating from the Aortic Arch; the Brachiocephalic artery, the Left Common Carotid artery, and the Left Subclavian artery.

Suprarenal Aorta The segment of the abdominal aorta between the diaphragm and renal arteries.

Systemic Circulatory System The portion of the circulatory system that transports oxygenated blood from the heart to the rest of the body, and carries the newly de-oxygenated blood back into the right atrium.

Thrombosis Local clotting of the blood in part of the circulatory system.

Total Cavopulmonary Connection A surgical procedure following on from a bidirectional cavopulmonary anastomosis. The inferior vena cava is also directly connected to the right pulmonary artery, allowing deoxygenated blood to bypass the heart and directly enter the lungs.

Transcatheter Aortic Valve Replacement A minimally invasive procedure to replace an aortic valve that fails to open fully due to aortic valve stenosis.

Acronyms

4D-Flow MRI 4-Dimensional-Flow Magnetic Resonance Imaging.

AAo Ascending Aorta.

AoA Aortic Arch.

ATAA Ascending Thoracic Aortic Aneurysm.

AVR Aortic Valve Replacement.

BAV Bicuspid Aortic Valve.

BMI Body Mass Index.

CFD Computational Fluid Dynamics.

CT Computed Tomography.

DAo Descending Aorta.

DES Detached Eddy Simulation.

DNS Direct Numerical Simulation.

EL Energy Loss.

FSI Fluid Structure Interaction.

LBM Lattice Boltzmann Methods.

LDA Laser Doppler Anemometry.

LDIR Low Dose Ionising Radiation.

LES Large Eddy Simulation.

MR Magnetic Resonance.

MRA Magnetic Resonance Angiography.

MRI Magnetic Resonance Imaging.

OSI Oscillatory Shear Index.

PC-MRI Phase-Contrast MRI.

PIV Particle Image Velocimetry.

POD Proper Orthogonal Decomposition.

RANS Reynolds Averaged Navier-Stokes.

RBF Radial Basis Functions.

RMSE Root Mean Square Error.

SSE Sum of Squares due to Error.

TAVR Transcatheter Aortic Valve Replacement.

TAWSS Time Averaged Wall Shear Stress.

TEE Transoesophageal Echocardiogram.

WSS Wall Shear Stress.

Chapter 1.

Introduction

Contents

1.1 Project Outline	1
1.2 Significance of Research	2
1.2.1 Motivation	3
1.3 Research Methods	3
1.3.1 Ethical Approval	3
1.4 Aims and Objectives	3

1.1 Project Outline

The aorta is the largest artery within the human body and circulates oxygenated blood through the body from the left ventricle. Separating the left ventricle from the aorta is the aortic valve. The aortic valve is key in regulating the flow that enters aorta, therefore a healthy valve is key in maintaining normal haemodynamics in the aorta. As the left ventricle contracts and relaxes through systole and diastole respectively, the changes in pressure within the left ventricle and the vortices that develop around the valve cause the aortic valve to open and close. When the aortic valve opens, it allows the oxygenated blood from the left ventricle to be ejected into the ascending aorta. As the valve closes it reduces the blood flow into the aorta.

Bicuspid Aortic Valve (BAV) is the fusion of two of the aortic valve cusps (or leaflets), meaning the aortic valve no longer has three cusps and no longer opens fully. This fusion results in an off-centre jet of blood being ejected into the ascending aorta with every heartbeat causing altered Wall Shear Stress (WSS) distributions on the aortic wall, and highly eccentric and helical flow patterns in the aorta. BAV has been shown to lead to numerous and serious complications that have high morbidity and mortality rates [1]. The BAV phenotype present is also known to influence the blood flow patterns that are seen in the ascending aorta [2]. It has been hypothesised that the resulting flow eccentricity and helicity from BAV could be used as a diagnostic tool and aid with risk stratification and treatment planning on an individual patient basis. The current treatment options for patients diagnosed with BAV is to undergo an Aortic Valve Replacement (AVR). The purpose of which is to restore a normal flow profile to the valve and normal haemodynamics to the thoracic aorta. A choice between a biological or mechanical AVR must be made, and is currently

guided by patient preference, with little to no consideration as to which would be more successful in restoring normal flow on a patient-specific basis.

4-Dimensional-Flow Magnetic Resonance Imaging (4D-Flow MRI) provides a means for diagnosis and monitoring of many cardiac pathologies, including BAV; this can be achieved by allowing the retrospective calculation of haemodynamic parameters of interest, such as WSS. The use of Computational Fluid Dynamics (CFD) based on 4D-Flow MRI data could produce a workflow that could be applied on a patient-specific basis concurrently with existing methods of treatment planning to improve individualised treatment plans, and provide a means to predict the post-surgical flow profile of an AVR prior to surgical intervention [3].

This project creates a methodology that combines 4D-Flow MRI and CFD successfully to create patient-specific simulations of the thoracic aorta. It demonstrates the potential the workflow has as a tool that could be used by clinicians for diagnosis, disease monitoring and treatment planning. It also highlights the difficulties of patient-specific in-silico modelling, and the challenges it presents. The limitations of using 4D-Flow MRI to construct the geometry and boundary conditions are investigated using the developed methodology, and recommendations are subsequently made for others attempting the same process. The haemodynamics and blood flow patterns predicted by the CFD simulations in the Ascending Aorta (AAo), Aortic Arch (AoA), and Descending Aorta (DAo) are investigated and compared to flow patterns found using 4D-Flow MRI. The impacts of the velocity profile at the aortic valve through the use of increasingly physiologically accurate inlet boundary conditions is also explored.

1.2 Significance of Research

Although research has previously been conducted into the effects BAV or an AVR have on the haemodynamics and blood flow patterns in the thoracic aorta, the results found have yet to be made into a tool that can be utilised by clinicians. This study makes a step in that direction and produces a methodology that can be followed to produce patient-specific simulations that predict the thoracic aorta haemodynamics in patients ranging in age from 1 day to 55 years. This research also makes recommendations as to the spatial resolution of the 4D-Flow MRI data that must be used when combining CFD and 4D-Flow MRI to model patient-specific haemodynamics. Despite being a known factor that influences the accuracy of CFD simulations it has yet to be quantified; this research quantifies the errors that can be attributed to the spatial resolution of the 4D-Flow MRI acquisition process and recommends a minimum requirement of spatial resolution if accurate CFD simulations are desired.

The outcomes of the research conducted in this project have the potential to aid clinicians in decision making. Treatment planning and risk stratification can be conducted on an individual patient basis based on the predicted post surgical haemodynamics with the potential to improve the quality of care received by the patient and the post surgical outcome. Finally, efforts have been made to use open access software whenever possible whilst developing the methodology as this will allow for clinicians across the globe to access the tool, resulting in more patients benefiting from the research conducted within this study.

1.2.1 Motivation

BAV is the most common congenital heart defect and is known to affect approximately 1.3% of all live births [4]. It has high morbidity and mortality rates and leads to a wide range of complications [1, 5]. By creating a tool that improves the accuracy of patient-specific CFD simulations, this will aid clinicians in diagnosis, disease monitoring, risk stratification and treatment planning. This will ensure the best outcome for the patient can be found in terms of which AVR is the correct choice to restore normal haemodynamics in the ascending aorta.

1.3 Research Methods

In order to create a workflow that combines CFD techniques with 4D-Flow MRI to produce patient-specific simulations, patient-specific geometries must be constructed from 4D-Flow MRI data before being implemented in numerical simulations. This is achieved by applying a threshold to all 4D-Flow MR images, and segmenting the thoracic aorta from each image. The threshold allows a degree of automation to be included as it will allow the majority of the vessel to be highlighted and extracted from the background tissue before manually segmenting the remaining areas of the vessel. From this, a 3D in-silico model will be produced.

A patient-specific inlet boundary condition must also be implemented for the methodology to be suitable, and is constructed from 4D-Flow MRI data. 4D-Flow MRI as an imaging technique can be used to measure the velocity field data in all three dimensions over time; this data is collected over a large number of cardiac cycles and averaged to provide the flow field within the thoracic aorta over a single cardiac cycle. The data for the inlet boundary condition is acquired by calculating the volumetric flow rate from 4D-Flow MRI data over a slice in the ascending aorta at the location of the aortic valve throughout the course of the cardiac cycle. The calculated data can then be applied to the inlet of the reconstructed geometry and patient-specific CFD simulations can then be run. A range of inlet conditions are tested including steady state plug profiles, plug profiles that vary temporally, and spatio-temporal patient-specific profiles. CFD simulations are conducted using the software OpenFOAM [6], and a cohort of both adult and neonatal patients are used, made up of healthy volunteers and patients with BAV. Alongside this, in collaboration with Kings' College London a flow phantom is used to validate the workflow created.

1.3.1 Ethical Approval

Ethics approval has been given to this study by the Leeds East Research Ethics Committee (18 / YH / 0439) and Berkshire Research Ethics Committee (10 / H0505 / 100). All data used in this study is anonymous and the identity of all subjects involved in this study is unknown to the author. All participants and/or parents/legal guardians have given written and informed consent to participate.

1.4 Aims and Objectives

Project Aims

1. To develop an in-silico methodology to combine CFD with 4D-Flow MRI that can aid clinicians in predicting the post surgical outcome for individual patients with BAV.

2. To identify and investigate the key areas that impact the accuracy and reliability of patient-specific 4D-Flow MRI based CFD simulations.

Objectives to meet aim 1:

1. Evaluate the state of current research in the field, and identify potential areas for novel work for combining 4D-Flow MRI and CFD using a literature review (Chapters 1 & 2).
2. Develop a workflow to construct patient-specific geometries for use in CFD simulations from 4D-Flow MRI data (Chapter 3).
3. Conduct patient-specific preliminary studies on both adult and neonatal patients, this will be accomplished through simulations at both peak systole and late diastole, as well as the full cardiac cycle (Chapter 4).
4. Devise and implement a method to incorporate inlet boundary conditions that are both spatially and temporally patient-specific, that would allow an AVR to be replicated (Chapter 3 & 4).
5. Validate the methodology created by using a flow phantom (in collaboration with Kings' College London) and compare 4D-Flow MRI and CFD results (Chapter 5).

Objectives to meet aim 2:

1. Highlight the challenges of patient-specific 4D-Flow MRI based CFD simulations (Chapter 2).
2. Compare and assess the difference between simulations with temporally patient-specific boundary conditions and those with spatio-temporally patient-specific boundary conditions (Chapter 4).
3. Conduct patient-specific simulations on patients with and without the supra-aortic vessels included to quantify the impacts the additional vessels have on the haemodynamics of the thoracic aorta (Chapter 4).
4. Investigate the impact 4D-Flow MRI spatial resolution has on subsequent patient-specific CFD simulations (Chapter 6).

Chapter 2.

Review of Patient-Specific Cardiac Modelling

Contents

2.1	Introduction	6
2.2	Overview of the Aorta	6
2.2.1	The Cardiac Cycle	6
2.2.2	Anatomy and Physiology of the Aorta	7
2.2.3	Bicuspid Aortic Valve	8
2.2.4	Aortic Valve Replacement	10
2.2.5	Blood as a Fluid	11
2.2.6	The Importance of Wall Shear Stress	12
2.2.7	Helical Flow In Blood Vessels	13
2.3	4D-Flow Magnetic Resonance Imaging	14
2.3.1	Uses of 4D-Flow MRI	16
2.4	Theoretical Foundations	17
2.4.1	Computational Fluid Dynamics Models	17
2.4.1.1	RANS	17
2.4.1.2	DES	17
2.4.1.3	LES	18
2.4.1.4	DNS	18
2.4.1.5	LBM	18
2.4.2	Reynolds number	18
2.4.3	Non-Newtonian Fluids	19
2.4.3.1	Viscosity Models	19
2.4.3.2	Non-Newtonian Importance Factor	21
2.5	Computational Fluid Dynamics in Cardiac Medicine	22
2.5.1	Inlet Boundary Conditions	25
2.5.2	Outlet Boundary Conditions	26
2.5.2.1	0-Pressure	27
2.5.2.2	Outflow	27

2.5.2.3	Windkessel Models	27
2.5.3	Turbulence Modelling	31
2.5.4	4D-Flow MRI based CFD	33
2.5.5	Predicting Post-Surgical Outcomes with CFD	36
2.6	Fluid-Structure Interactions	38
2.6.1	Fluid-Structure Interaction of the Vessel Wall	39
2.6.2	Fluid-Structure Interaction of the Aortic Valve	43
2.7	Existing Software	44
2.7.1	SimVascular	44
2.7.2	HeartFlow	46
2.7.3	CRIMSON	46
2.7.4	FEops	46
2.8	Summary	47

2.1 Introduction

The aim of this literature review is to provide a comprehensive assessment of the state of current research in haemodynamics in the human thoracic aorta. It will provide an overview of the relevant medical background needed for this research area; including the cardiac cycle, the anatomy of the aorta, and the congenital heart defect BAV, before discussing the current treatment options available to those with BAV. This will highlight the motivation behind this research topic. The use of 4D-Flow MRI to observe the haemodynamics of the thoracic aorta will be extensively discussed, as will the use of computational fluid dynamics in a medical setting. A discussion of turbulence models and rheology models that are appropriate for cardiovascular CFD will also be presented. The combination of the two techniques (4D-Flow MRI and CFD) will then be thoroughly reviewed and attention will be drawn to gaps in the literature. The use of fluid-structure interaction in a medical setting will also be examined, in particular focusing on the interaction between the aorta wall and the blood, as well as the aortic valve and the blood.

2.2 Overview of the Aorta

2.2.1 The Cardiac Cycle

The heart is a vital organ that supplies the entire human body with oxygenated blood and nutrients through the systemic and pulmonary circulatory systems. The heart muscle consists of two separate sides (left and right), and four individual chambers (atria and ventricles). The left and right sides are each made up of an atrium and a ventricle, and are separated from each other by the interatrial septum and the interventricular septum, which prevent any blood flow between the sides. The atria and ventricles are separated by valves, which allow the transfer of blood. The right atrium receives de-oxygenated blood from the body through the superior and inferior vena cava. Separating the right atrium and the right ventricle is the tricuspid valve. The right ventricle directs the de-oxygenated blood to the lungs via the pulmonary valve, through the pulmonary artery and the pulmonary circulatory system. The left atrium receives the newly oxygenated blood from the lungs through the left and right pulmonary veins. Separating the left atrium and left ventricle is

the mitral valve. The left ventricle then directs the oxygenated blood through the aorta and into the systemic circulatory system via the aortic valve (see Figure 2.1) [7].

As the ventricles are contracted by the heart muscle (ventricular systole) the aortic and pulmonary valves open; oxygenated blood is ejected into the aorta and the systemic circulatory system, and de-oxygenated blood is ejected into the pulmonary artery and the pulmonary circulatory system. Concurrently, the atria undergo diastole; the atria-ventricular valves (mitral and tricuspid) close and blood fills the atria, where pressure increases throughout ventricular systole. The atria fill up to an end-diastolic volume, at which point the atria-ventricular valves open, the aortic and pulmonary valves close, and the ventricles relax and are filled with blood (ventricular diastole) before entering into ventricular systole once again. Ventricular diastole occupies approximately two-thirds of the cardiac cycle in a resting state [8].

It is during ventricular systole that arterial blood pressure reaches a peak value (systolic blood pressure) - approximately 120mmHg in healthy subjects. The minimum arterial blood pressure is experienced during ventricular diastole (diastolic blood pressure) which is approximately 80mmHg in a healthy subject. The difference between the two arterial blood pressures is known as the pulse pressure.

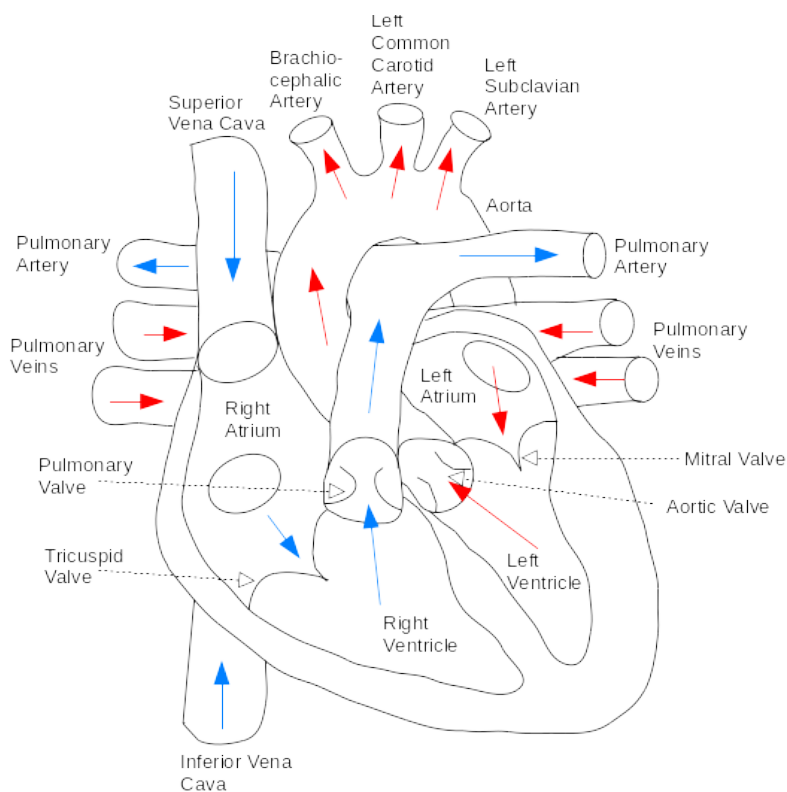


Figure 2.1. Schematic of the anatomy of the heart muscle during systole (where the aortic and pulmonary valves are open), demonstrating the location of the four chambers and the valves. Blue arrows indicate de-oxygenated blood, red arrows indicate oxygenated blood.

2.2.2 Anatomy and Physiology of the Aorta

The aorta is the largest artery in the human body, supplying the body with oxygenated blood from the left ventricle. It can be divided into two key sections; the thoracic aorta and the abdominal aorta. The thoracic aorta can be further subdivided into the ascending aorta, the aortic arch, and

the descending aorta, with the supra-aortic vessels (the brachiocephalic artery, the left common carotid artery, and the left subclavian artery) originating from the aortic arch (see Figure 2.2). The abdominal aorta can be subdivided into the suprarenal aorta and the infrarenal aorta, before ending at the aortic bifurcation where the iliac arteries originate [8].

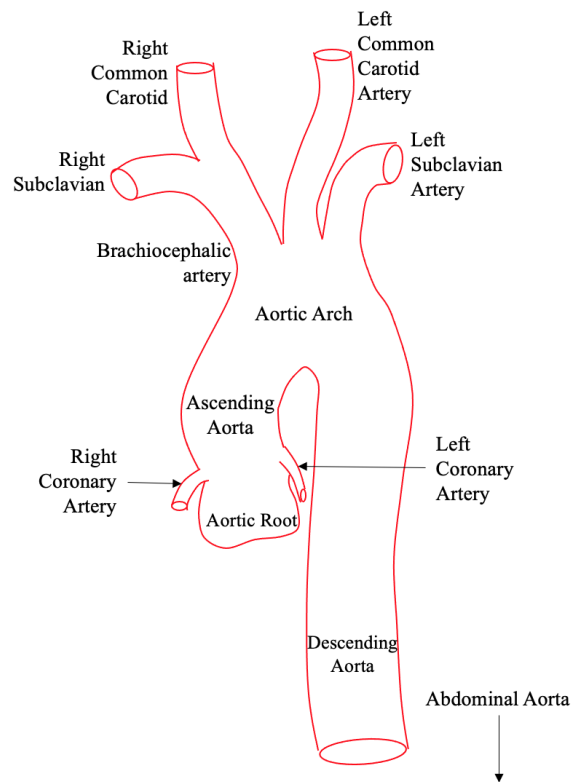


Figure 2.2. Schematic of anatomy of the thoracic aorta and supra-aortic branches.

The aortic wall is formed of three layers; the outer adventitia, middle media, and the inner intima as shown in Figure 2.3. The inner intima can be characterised by a membrane that is lined with endothelium, is in direct contact with the blood flow and is the layer most prone to injury or tears. The middle media is the thickest of the layers - composed of muscle fibres and elastic tissue making up approximately 80% of the aortic wall thickness. It is the middle media that gives the aortic wall its circumferential elasticity, allowing it to resist haemodynamic stresses. The thin outer adventitia contains the nerves. Its high collagen content confers the highest tensile strength of all three layers [9].

2.2.3 Bicuspid Aortic Valve

Congenital heart defects affect the normal function of the heart and are present from birth, and in most cases do not have an obvious cause as the underlying genetic and epigenetic causes are complex and to date are still poorly understood. Bicuspid Aortic Valve (BAV) is the most common congenital heart defect, known to affect approximately 1.3% of all live births [4]. In approximately 20 – 30% of all BAV cases, there are also cases within the immediate family, however a specific genetic cause has yet to be found [10]. It has a wide range of serious complications that lead to high morbidity and mortality rates; approximately 35% of BAV patients will suffer from severe complications [1]. These complications include but are not limited to aortic valve dysfunction, endocarditis, aortic stenosis, aortic regurgitation, aortic dilation and aortic dissection [5]. Approximately 50% of all patients undergoing surgery for aortic stenosis have an underlying diagnosis of

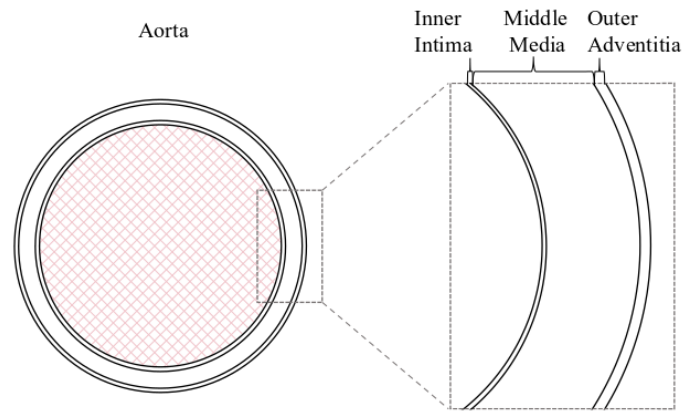


Figure 2.3. Schematic of a cross section of the thoracic aorta and a close up of the aortic wall demonstrating the location of the inner intima, middle media, and outer adventitia.

BAV [11], and in up to 80% of cases it has been associated with ascending aortic dilation [12].

The aortic valve separates the left ventricle from the aorta and is key in maintaining unidirectional flow, preventing the oxygenated blood from flowing back into the left ventricle (aortic regurgitation). In a healthy subject the aortic valve has three cusps (or leaflets) and is commonly called a Tricuspid Aortic Valve (TAV) (Figure 2.4a). A bicuspid aortic valve occurs when 2 cusps of the aortic valve fuse together during development in the womb, resulting in a bicuspid valve as opposed to the regular tricuspid valve. A fusion of the right and left cusps (RL BAV) has a prevalence of 70-80% (Figure 2.4b), a fusion of the right and non-coronary cusps (RN BAV) has a prevalence of 20-30% (Figure 2.4c), and a fusion of the non-coronary and left cusps (NL BAV) has a prevalence of approximately 1% (Figure 2.4d) [5]. Although Figure 2.4 demonstrates complete asymmetrical fusions (or raphe) between the two cusps, it is also possible for an incomplete raphe between the two fused cusps to form, as is also the case with a symmetrical fusion pattern.

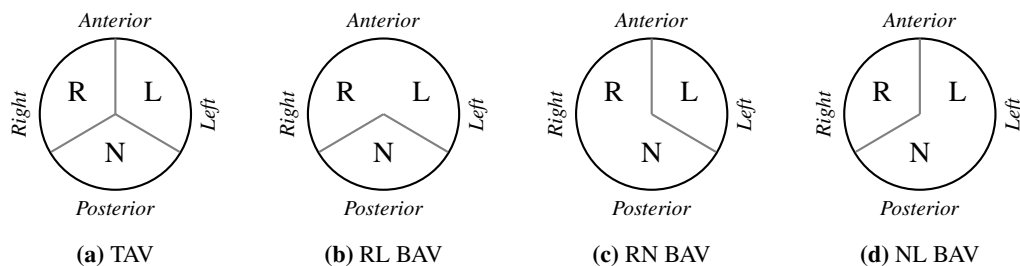


Figure 2.4. Schematic of asymmetric BAV phenotypes with complete raphes from the parasternal short axis view with a TAV for comparison. *R* =right cusp, *L*=left cusp, *N*=non-coronary cusp.

Bicuspid aortic valves do not allow the aortic valve to open fully at systole, meaning that the jet of blood ejected into the aorta at ventricular systole is not central - as it would be in a healthy subject with a TAV. The non-central jet impacts the ascending aortic wall, resulting in an area of elevated Wall Shear Stress (WSS) and an abnormal WSS distribution. Elevated and abnormal WSS distributions are considered to be major contributing factors for aortic dilation in BAV patients [2]. It was found by Nishimura *et al.* [10] that aortic dilation is more prevalent in those with a RN BAV fusion pattern, and that patients whose fusion patterns involve the non-coronary cusp are more likely to have dilation in the ascending aorta than in the sinuses of valsalva. An additional consequence of a non-central blood jet is a helical flow structure in the aorta. The abnormal rotational flow found with BAV is associated with increased ascending aortic dilation [13]. It was

observed in a study by Ha *et al.* [2] that the strength and rotational direction of the helical flow structure in the thoracic aorta was highly dependant on the aortic valve flow i.e. the patients' BAV phenotype will play a major role in influencing the strength and direction of the helical flow, the resulting WSS patterns, and therefore any aortic dilation present. It was recognised that aortic valve flow directed towards the posterior and right directions resulted in a right-handed helical structure, whereas an aortic valve flow in the left or anterior direction resulted in a left-handed helical structure. The 4D-Flow MRI results indicated that a RL BAV develops predominantly right-handed helical flow, whereas a RN BAV can also develop left-handed helical flow. The study by Ha *et al.* [2] concluded that an aortic flow that demonstrated right-handed helical flow experienced higher WSS values on the aortic wall as higher rotational velocities were experienced.

A review of the haemodynamics of BAV by Edlin *et al.* [3] agreed with the results presented by Ha *et al.* [2]; BAV is often associated with helical flow structures and flow eccentricity in the thoracic aorta. From this, it was suggested by Edlin *et al.* [3] that the blood flow patterns in the thoracic aorta may be a useful diagnostic tool, aiding disease progression predictions. Currently, risk stratification and treatment planning of individual BAV patients is based purely on geometric data of the aorta e.g. aorta diameter[11]. However, this is not an appropriate method as geometric parameters do not fully capture the complexity of BAV, with the consequence that morbidity and mortality often occur before the interventional threshold for surgical treatment is met [14]. The surgical intervention threshold is often an ascending aorta diameter greater than approximately 5cm, or 4.5cm if there is severe aortic stenosis or aortic regurgitation [10].

2.2.4 Aortic Valve Replacement

Worldwide, approximately 300,000 heart valve repair or replacement procedures are performed on an annual basis [15–17], with this number predicted to increase to 850,000 by 2050 [17]. A common treatment option for patients with a diagnosis of BAV is to undergo an Aortic Valve Replacement (AVR), and the majority of patients with a BAV will undergo this surgery during the course of their lifetime. An AVR involves either a biological or mechanical replacement being implanted, or a Ross Procedure being performed whereby the patients diseased aortic valve is replaced with their own pulmonary valve, and the pulmonary valve is replaced with that from a cadaver.

The most popular mechanical AVR is the bileaflet AVR. This is constructed from two rotating leaflets that are attached to the valve housing. The bileaflet mechanical AVR has a larger opening at systole than the other mechanical AVR alternatives and as such, is less likely to cause blood clots, but it is known to be prone to backflow. Mechanical AVR's have a much greater durability than biological AVR's, and can last up to 20-30 years. However, due to the increased risk of blood clotting associated with mechanical AVR's in general, the recipient must take anticoagulants for the remainder of their lifetime. A mechanical AVR does not produce a central jet of blood at systole, as a healthy TAV or biological AVR does, but instead produces multiple jets. A bileaflet mechanical AVR produces three separate jets [18].

Biological AVR's are a more popular treatment option than mechanical AVR's, with approximately 65% of patients receiving one in 2001, with that number rising to 82% in 2011 [19]. A biological AVR is commonly made of bovine or porcine tissue, and is less likely to cause blood clotting than the mechanical alternatives so the recipient is not required to take anticoagulants. However,

a biological AVR is considerably less durable than a mechanical AVR, lasting only 10-15 years [20] and as such the recipient is likely to require multiple AVR's and therefore multiple surgeries, which all carry risks, during their lifetime as a biological valve replacement is not an end-point treatment. The majority of biological AVR's fail as a result of structural deterioration of the valve leaflets, which often presents as tears in the leaflets themselves. Improving the durability of a biological AVR would have a significant clinical impact [21]. It has been hypothesised by Zakerzadeh *et al.* [21] that the use of *in-silico* modelling would allow for parametric studies of the AVR, allowing investigations into materials, placement location, angle etc. This has immeasurable advantages over *in-vivo* testing, and would allow for a highly accurate and personalised framework for treatment on an individual patient basis.

Work by De Gaetano *et al.* [22], Yoganathan *et al.* [23], and Xu *et al.* [24] investigated the use of *in-silico* parametric studies to optimise the aortic valve replacement. The optimal valve leaflet thickness was investigated by De Gaetano *et al.* [22] in order to determine the optimal design that leads to maximal coaptation area whilst simultaneously reducing the stresses on the valve leaflet. The best valve design that allows for optimal haemodynamics and the lowest possible risk of design related thrombosis was determined by Yoganathan *et al.* [23], whilst a framework for parametric design of aortic valve leaflets with a view to automate aortic valve reconstruction was produced by Xu *et al.* [24].

The main aim of an AVR is to restore healthy haemodynamics to the thoracic aorta, by restoring a normal blood flow profile at the valve. Nonetheless, this aim is not always achieved. It has been hypothesised that the AVR type is responsible for differing flow patterns post surgery [13]. It was found by Bissell *et al.* [13] that approximately 73% of patients who received a mechanical AVR experienced normal blood flow patterns in the ascending aorta post surgery, compared with all patients who received a bio-prosthetic AVR still exhibiting abnormal blood flow behaviour post surgery. This clearly indicates that the AVR type significantly affects the flow patterns.

2.2.5 Blood as a Fluid

Blood is a suspension that is composed of approximately 45% elements (red blood cells, white blood cells, and platelets) in a plasma [25]. Red blood cells are key in transporting oxygen around the body. They are the dominant element, therefore can be taken to have the largest influence on the mechanical properties of blood. Red blood cells are a flexible, biconcave structure approximately $8\mu\text{m}$ in diameter, $1\mu\text{m}$ thick in the centre, and $2 - 3\mu\text{m}$ at the edges [25]. White blood cells (or leukocytes) are vital in fighting infection within the human body, and although are marginally larger than red blood cells, they make up a significantly smaller proportion of the suspension (approximately 1%) so can be considered to be dynamically negligible. Platelets are biconvex structures that are approximately $2 - 3\mu\text{m}$ in diameter. Although they are more numerous than both white blood cells and red blood cells, they are smaller so account for a far smaller volume fraction of the suspension, thus can also be considered dynamically negligible. The plasma is a solution of large molecules. However, based on the scales of motion and the shear rates that are commonly found within human blood vessels, the plasma can be considered to be a Newtonian fluid with a viscosity of $\mu = \sim 0.0012 - 0.0016 \text{kgm}^{-1}\text{s}^{-1}$.

In blood vessels with a diameter larger than $100\mu\text{m}$, the suspension can be considered to be a homogeneous fluid as the scale of the elements within the suspension is significantly smaller than

that of the flow [25]. Within smaller blood vessels, such as the capillaries, it becomes inappropriate to assume that blood is a homogeneous fluid on the grounds that the diameter of red blood cells and the spacing between them becomes similar to the diameter of the vessels.

As discussed previously, both the white blood cells and the platelets can be considered dynamically negligible. The effect the red blood cells have on the fluid flow can be quantified by determining the Stokes number of the suspension; it is a dimensionless number that can be defined as a ratio of the momentum response time of the red blood cells to the time scale of the flow field [26]. A larger Stokes number indicates that the particles are larger or heavier, whilst a smaller Stokes number indicates that the particles will be smaller or lighter. If $St \ll 1$ then it can be assumed that the particles will likely follow the fluid motion, and act as a tracer would. If $St \gg 1$ then it can be taken that the particles are not influenced by the fluid motion. The Stokes number of the flow can be determined by Equation 2.1 [26], where ρ_p is the density of the particles in the suspension (red blood cells in this instance), D_p is the diameter of the particles, μ is the viscosity of the flow, D_0 is the diameter of the pipe through which the fluid is flowing (the aorta in this case), and U_0 is the velocity of the flow at the inlet of the pipe. As the thoracic aorta experiences pulsatile flow, it follows that the Stokes number of the suspension is not a constant value but instead varies with the velocity of the flow at the inlet.

$$St = \frac{\left(\frac{\rho_p D_p^2}{18\mu}\right)}{\left(\frac{D_0}{U_0}\right)} \quad (2.1)$$

For shear rates above $100s^{-1}$, it was found by Whitmore [27] that the viscosity of blood is independent of the shear rate. As the average shear rate in large arteries, such as the aorta, is greater than $100s^{-1}$, it follows that the suspension can be treated as not only homogeneous, but also a Newtonian fluid. However, there are limitations to the Newtonian assumption. The shear rate in large vessels is not consistently above $100s^{-1}$; it is much lower at the centre of the vessel and the pulsatile nature of blood flow also contributes to inconsistent shear rates. Therefore it is vital that the rheological model used to model blood is investigated further. Section 2.4.3.1 provides a more in depth discussion of rheological models that have been used to approximate blood.

2.2.6 The Importance of Wall Shear Stress

As discussed in Section 2.2.3, the WSS has been associated with non-central jets of blood being ejected as a result of a BAV. Wall Shear Stress is the tangential force that the movement of the blood through the vessel exerts on the vessel walls. It is caused by the friction of the blood against the vessel wall and is primarily felt by the endothelial cells, located at the interface between the blood flow and the vessel wall; the inner intima. It is known that changes in the WSS can produce alterations in the vessel wall that aim to accommodate the new flow conditions and restore the basal levels of WSS [28], with correlations between changes in WSS and the vessel diameter being present. This is possible as vascular cells are equipped with receptors that enable them to detect and react to changes in the forces that are generated by WSS and blood pressure. These changes that are seen in terms of vessel shape and composition as a result of acute changes in the forces experienced are known as vascular remodelling. An example of the flow-dependent vessel growth, or remodelling, can be seen in a carotid-jugular arteriovenous fistula. The velocity

in the vessel that is supplying the fistula (the carotid artery) increases significantly as the flow rate may be multiplied by a factor of 8, however the arterial calibre (or internal diameter) will experience growth until the WSS is normalised and reaches its basal level once again [29]. Under physiological conditions it has been shown that the mean WSS remains incredibly constant at a value within the range of $1 - 1.5 Nm^{-2}$, regardless of the section of the arterial network being considered and the animal species being studied (with the exception of the rat and the mouse)[28].

Many studies show that an elevated level of WSS in the greater curvature of the ascending aorta correlates with a stenotic BAV [3]. It has also been shown that a BAV results in higher levels of WSS in the ascending aorta than a TAV, and the regions of elevated WSS often correlate to the regions where thinning of the aortic wall and aortic dilation are found [30–33]. Several studies have also found that WSS distributions vary with the degree of stenosis and the BAV fusion pattern present, although the WSS is consistently elevated and asymmetrical [30–32, 34, 35]. From these studies, it is apparent that the WSS can be utilised in monitoring disease progression for a range of pathologies, and may help clinicians in treatment planning, particularly in terms of surgical planning for congenital heart defects such as BAV.

However, multiple studies have also concluded that utilising WSS to measure disease progression and track aortic growth may not be appropriate due to the reliability of the numerical calculations. The distribution trends can be collected and compared between healthy volunteers and patients, but any numerical comparison may not be valuable. This is largely due to the resolution of 4D-Flow MRI scans used to determine the WSS values [11]. It is also evident that 4D-Flow MRI underestimates WSS values. This arises as a singular static image from a frame is used to create the model of the vascular system of interest, meaning any wall motion is neglected. The thoracic aorta moves considerably throughout the cardiac cycle, which results in the vessel wall location in the 4D-Flow MRI scan being inaccurate, therefore the WSS measurements can be assumed to be inaccurate also.

2.2.7 Helical Flow In Blood Vessels

Helicity is a measure of the extent to which the blood flow exhibits corkscrew-like behaviour. A study by De Nisco *et al.* [36] investigated the role that helical flow plays in the initiation and progression of atherosclerosis in the coronary arteries. It was found that a high helical flow intensity has a strong positive association with the WSS magnitude. The regions of the arterial wall that were exposed to high levels of helical flow exhibited smaller wall thickness growth when compared to regions exposed to mid to low helical flow. Using CFD simulations of porcine coronary arteries, the study concluded that helical flow plays a significant role in protecting the arteries against atherosclerotic wall thickness growth, and shows potential for use as a marker for predicting wall thickness growth. The physiological importance of helical flow in the human aorta has also been investigated in the last decade, and it has also been found to serve an atheroprotective role. Research has shown that helical flow has an important role in mitigating flow disturbances close to the aorta wall, protecting the vessel from atherosclerotic development [37–40]. This is achieved by suppressing the low amounts of WSS that are known to cause plaque development [41]. In a study by Bissell *et al.* [13], helical flow in the ascending aorta was quantified by using the rotational component of flow, calculated through the integral of the vorticity with respect to the cross-sectional area of the ascending aorta. The helical flow can be categorised as defined by

Bissell *et al.* [42], with normal helical flow between $-5\text{mm}^2/\text{s}$ and $11\text{mm}^2/\text{s}$, abnormal right-handed rotational flow $> 11\text{mm}^2/\text{s}$, and abnormal left-handed rotational flow $< -5\text{mm}^2/\text{s}$. Complex flow is defined as low with no discernible rotational flow pattern. The absolute value of the rotational component of flow can be used to compare between patients irrespective of flow direction.

2.3 4D-Flow Magnetic Resonance Imaging

The human body is made up primarily of water molecules, which in turn are made up of hydrogen and oxygen atoms. The hydrogen and oxygen atoms all have a randomly aligned angular spin momentum. Within the nuclei of these atoms are protons, which are known to be sensitive to magnetic fields. A Magnetic Resonance Imaging (MRI) machine exploits this sensitivity by applying a magnetic field causing the spin momentum of the atoms to align in the direction of the external magnetic field. Short bursts of radio waves are then sent out to the region of interest, exciting the protons and changing their alignment. As the radio waves are turned off the protons re-align to the external magnetic field, and in doing so, send out radio-waves which are picked up by receivers in the MRI machine. These returning signals provide information about the location of the protons and help to distinguish between tissue types as the protons in different tissues respond to the radio-waves in distinct ways, producing distinctive signals. The returning signals are then combined to produce a detailed image of the region of interest. By adjusting the imaging parameters, various tissue types can be identified.

Phase-Contrast MRI (PC-MRI) builds on a conventional MRI, but incorporates velocity encoding to provide details on the velocity of the blood flow. All protons have a phase that is dependent on the velocity of the atom. By acquiring two sets of data with opposing magnetic gradients the phase shift between the two sets of results can be calculated. This phase shift can be converted to provide a flow velocity through velocity encoding. Velocity encoding requires a parameter, v_{enc} , to be selected to define the range of velocities that will be visible on the final PC-MRI images. The v_{enc} should be the maximum velocity that can be acquired during the PC MRI scan. The choice of v_{enc} is highly sensitive; a high value of v_{enc} allows the full range of velocities to be observed, but will often cause the lower velocities to be obscured as a result of the larger range, as well as producing a signal-to-noise ratio that is impractical. A lower value of v_{enc} will not obscure the lower velocities, but will cause aliasing on any value of velocity that is larger than v_{enc} . This aliasing is known to present the higher velocities as velocities moving in the opposite direction. The velocity of the blood flow is determined in each of the voxels within the vessel geometry. This is demonstrated in Figure 2.5; the voxels that make up the vessel of interest have been extracted, from the image field (2.5b), before the velocity is determined, through velocity encoding as discussed above, in each voxel to give the velocity field across the entirety of the vessel (2.5d). This is done at each time step to provide the flow field throughout the course of the cardiac cycle.

MRI is considered the gold standard of medical imaging techniques, and as such is a key tool in diagnostics and monitoring disease progression in clinical settings [8, 43, 44]. 4D-Flow MRI has evolved from this 'gold standard' imaging technique, allowing for accurate delineation of the blood flow at the location of interest in the subject, specifically within the heart and the large vessels. It is a non-invasive and non-ionising imaging technique, best described as PC MRI with

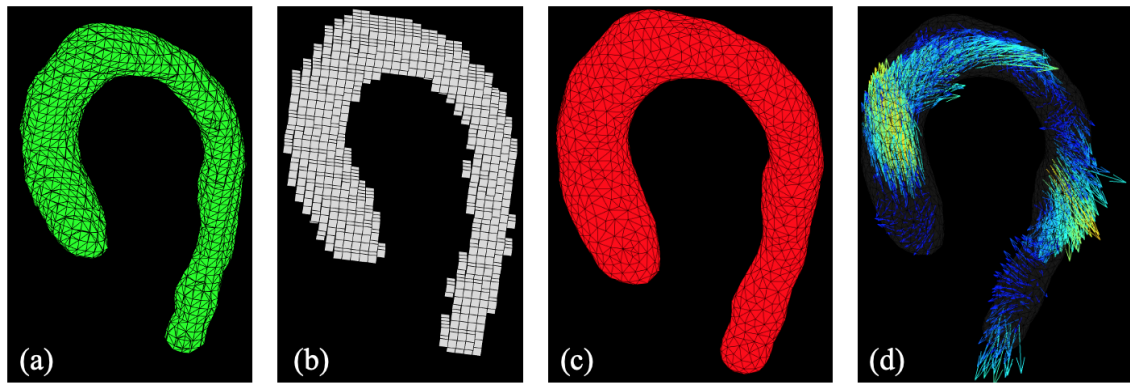


Figure 2.5. 4D-Flow MRI velocity acquisition method

flow encoding in all three dimensions, resolved with respect to these three dimensions as well as time (under free-breathing or diaphragm navigator-gated conditions) [44]. Data is acquired over hundreds of heartbeats, and averaged to provide a representative flow field for a single cardiac cycle. Approximately 70 – 80% of a patient's heartbeats during the 4D-Flow MRI scan are used to recreate the flow field for the average cardiac cycle. Therefore 4D-Flow MRI provides a reasonable representation of the average heartbeat. The heartbeats that are rejected for use are those in which the heart is in the wrong position within the chest. This occurs for a range of reasons, such as the patient moving, or breathing position in inspiration.

Although 4D-Flow MRI has been an available imaging technique for over a decade it has only recently become available in clinical settings due to recent reductions in scan times - only an additional 10-15 minutes are needed after a conventional MRI scan [43]. One of the main benefits of 4D-Flow MRI lies in the rich data sets that can be collected from the technique - multiple physiological parameters can be calculated retrospectively, including but not limited to WSS, Oscillatory Shear Index (OSI), and helicity, all of which have been hypothesised to be of importance in disease progression. From this, it is clear that the use of 4D-Flow MRI in clinical settings has the potential to increase understanding of abnormal blood flow and WSS distribution patterns, as well as help in monitoring disease progression, risk stratification and aid individualised treatment planning. The accuracy of 4D-Flow MRI is comparable to echocardiography, but is known to have better inter- and intra-observer reproducibility. This accuracy has led to 4D-Flow MRI also being used in non-cardiac settings [43].

In spite of the increasing popularity of 4D-Flow MRI, there are still many limitations to the technique. Primarily, the current coarse spatial and temporal resolutions available lead to underestimations of high blood flow velocities. There is also the potential for errors to be caused by motion artefacts. The cost of, and access to, the resources needed to conduct 4D-Flow MRI scans is also a key limitation, with prior knowledge of expected blood flow velocity required in order to correctly acquire the data.

The spatial and temporal resolutions of 4D-Flow MRI scans are a trade off with accuracy and time required for the scan acquisition, and the scan parameters must be decided when acquiring the 4D-Flow MRI data. The choice of spatial and temporal resolutions is driven by application, and is highly dependent on the blood vessels of interest. By reducing the temporal resolution of the 4D-Flow MRI scan, the time required to take the scan is reduced, however this is alongside reduced accuracy of the peak velocity and flow volume quantification as the flow features cannot

be fully resolved.

2.3.1 Uses of 4D-Flow MRI

There have been multiple studies using 4D-Flow MRI to observe BAV and AVR's, and how this altered inlet velocity profile affects the blood flow pattern in the aorta. A study conducted by Barker *et al.* [35] looked at how BAV affects WSS in the aorta when compared to control groups. This study concluded that the presence of BAV in a subject altered the haemodynamics in the ascending aorta - RL BAV was linked to the jet of blood ejected at systole impinging on the right anterior aortic wall, corresponding to a region of elevated WSS. This agreed well with the results presented by Barker *et al.* [45] and Hope *et al.* [46]. The cohort size in this study consisted of 15 BAV patients (12 RL BAV (of which 6 suffered from stenosis), and 3 RN BAV). The study used 3 control groups; group 1 consisted of 15 healthy TAV subjects with no history of heart, aortic or valve disease, group 2 consisted of 15 age-matched healthy TAV subjects, and group 3 consisted of 15 age and aortic size matched TAV subjects with an ascending aortic aneurysm. Despite the relatively large cohort size used in this study, no NL BAV patients were studied. This presents a large gap in the current knowledge regarding the haemodynamics of BAV that should be investigated.

A study by Rose *et al.* [47] used 4D-Flow MRI to track the progression of BAV in paediatric patients by assessing the flow pattern and changes in velocity in the aorta. A short time period between the baseline and follow-up scans was used, with the flow patterns and velocity showing no significant changes for any patient, but showing substantial differences between patients. This study demonstrated that 4D-Flow MRI is a robust method for observing aortic blood flow, and is capable of highly reproducible results. It can therefore be inferred that 4D-Flow MRI provides a reliable method of viewing patient specific haemodynamics within the thoracic aorta.

The feasibility of using 4D-Flow MRI to assess the flow in patients with aortic dissections was studied by de Beaufort *et al.* [48]. 4D-Flow MRI scans were conducted on 13 *ex-vivo* porcine aortas mounted to a flow loop as well as on 14 patients with aortic dissection. The intra- and inter-observer variability of 4D-Flow MRI was assessed on the porcine *ex-vivo* test subjects, as well as on the patients. Lins correlation coefficients of 0.98 and 0.96 were determined for the porcine subjects for intra and inter-observer variability respectively, and values of 0.98 and 0.97 respectively were determined for the human patients. Similar to the conclusions drawn by Rose *et al.* [47], it can be confidently concluded from the work by de Beaufort *et al.* [48] that 4D-Flow MRI allows for accurate and reliable assessment of the flow in the aorta, meaning it can be used in future work to determine aortic dissection haemodynamics.

The reliability of 4D-Flow MRI scans was investigated by van der Palen *et al.* [49] through the scan-rescan reproducibility. The variability in the WSS mean and WSS maximum were observed at five locations in the thoracic aorta. The study involved ten healthy adult patients who underwent two 4D-Flow MRI scans and the results between them compared. It was found that on average there was good scan-rescan reproducibility for the mean WSS values, however the variability in the maximum WSS values experienced was larger, reaching differences between the scan and rescan of up to 32% in the proximal ascending aorta.

2.4 Theoretical Foundations

2.4.1 Computational Fluid Dynamics Models

A wide range of CFD models exist that allow the turbulence in the flow to be determined, with a wide ranging cost associated with each approach. The computational cost of each approach is dependent on the scales that are modelled and those that are resolved. If more of the turbulence scales are resolved, the computational cost of the approach is higher, as is the accuracy. If the majority of the turbulence scales are modelled then the computational cost of the approach is lower, as is the accuracy. The Navier-Stokes equations are given in Equations 2.2 and 2.3

$$\rho \frac{\partial \mathbf{u}}{\partial t} + \rho(\mathbf{u} \cdot \nabla) \mathbf{u} = -\nabla P + \mathbf{F} + \mu \nabla^2 \mathbf{u} \quad (2.2)$$

$$\frac{D\rho}{Dt} + \rho \nabla \cdot \mathbf{u} = 0 \quad (2.3)$$

2.4.1.1 RANS

The Reynolds Averaged Navier-Stokes (RANS) equations provide a time-averaged approach to modelling a fluid flow, and they govern the transport of the averaged flow quantities. Additionally, the entire range of the turbulence scales are modelled, resulting in a modelling approach that requires reduced computational resources compared to the other approaches listed within Section 2.4.1. The RANS equations do not form a closed set, and as such additional information is required to achieve closure. This is achieved by incorporating a turbulence model into the simulation. A large range of turbulence models are available for use, and the choice is dependent on the geometry and flow being modelled. Despite the reduced resources required for RANS modelling, RANS provides less accurate and reliable results than the approaches that resolve more of the turbulence scales.

2.4.1.2 DES

The Detached Eddy Simulation (DES) hybrid technique is a modification of a RANS model whereby RANS is applied in the near wall and attached boundary layer regions, and Large Eddy Simulation (LES) subgrid models are applied for separated flows in the regions away from the wall. The LES region is commonly associated with the turbulence region where the larger turbulence scales play a more key role. DES is less computationally expensive than LES, and provides better time-averaged results than steady and unsteady RANS simulations. In addition, the accuracy of DES is typically superior to steady and unsteady RANS, whilst also circumventing the Reynolds number limitations that are present with LES. However, using a grid density that is both too fine for RANS and too coarse for LES can reduce the quality of results found from DES [50].

A significant limitation of the original DES model proposed by Spalart [51] is present when the mesh is refined locally in regions not intended to be scale-resolved, such as in areas of high geometric curvature or areas where multiple solid surfaces interact. As the criteria in DES for transitioning between RANS and LES compares the RANS length scale to the maximum grid sizing, the eddy viscosity may be reduced notably in the boundary layer with no mechanism to transfer

the modelled turbulence energy into resolved energy. Recent modifications to the DES model have attempted to rectify this limitation, which stop the transition from RANS to LES within the attached boundary layers based on the grid design.

2.4.1.3 LES

Large Eddy Simulation (LES) is a model used for turbulence. The concept behind the LES model is that the large eddies in a turbulent flow are solved explicitly, whilst the smaller eddies are accounted for via a subgrid scale model. The rationale behind LES can be summarised as momentum, mass and energy are transported by the larger eddies which are mostly problem dependent as they are influenced by the geometry and boundary conditions, the smaller eddies tend to be more isotropic and are less dependent on the geometry and are more universal, and that the probability of finding a universal turbulence model is much higher for smaller eddies. By resolving only the larger eddies, a much coarser mesh and larger time steps can be used than other methods such as DNS. However, LES still requires a finer grid resolution than RANS. As a consequence, LES has a higher computational cost in terms of memory and CPU time than RANS simulations.

The governing equations utilised in LES are found by filtering the time-dependent Navier-Stokes equations in either Fourier or configuration space. This filtering process filters out the eddies whose scales are smaller than the selected filter width or grid spacing used in simulations.

2.4.1.4 DNS

Direct Numerical Simulation (DNS) solves the Navier-Stokes equations without a turbulence model. This means that the entire range of length and time scale of the turbulence are resolved. As all scales of turbulence are solved in the computational mesh, the computational cost of DNS is high in terms of memory and time required. This limits its use for complex geometries and high Reynolds number flows.

2.4.1.5 LBM

The Lattice Boltzmann Methods (LBM) are a class of CFD methods that do not solve the macroscopic Navier-Stokes equations directly, but rather simulate a fluid density on a lattice with streaming and collision processes. LBM originates from the molecular description of a fluid. It is a versatile method that can model common fluid behaviours. The method is designed to run on parallel computing resources, and is an efficient method. LBM has the advantage over other CFD methods that it has the ability to deal with complex boundary, can incorporate microscopic interactions, and the parallelisation of the algorithm.

2.4.2 Reynolds number

The Reynolds number is the ratio of inertial forces to viscous forces. At low Reynolds numbers, the fluid flow is laminar as the viscous forces dominate the flow. A transition region is reached between $2300 < Re < 4000$ for pipe flow, above which the flow becomes fully turbulent where the inertial forces dominate. The Reynolds number (Re) can be calculated by using Equation 2.4, where ρ is the fluid density, u is the velocity, μ is the dynamic viscosity, ν is the kinematic viscosity and L is the characteristic length. Within this research project the thoracic aorta is the

vessel of interest, and as such L is taken to be the vessel diameter at the location of the aortic valve.

$$Re = \frac{\text{Inertial Forces}}{\text{Viscous Forces}} = \frac{\rho u L}{\mu} = \frac{u L}{\nu} \quad (2.4)$$

2.4.3 Non-Newtonian Fluids

Newton's law of viscosity states that the ratio of shear stress to shear rate is a constant (at a constant temperature and pressure) and is defined as the viscosity. If a fluid obeys this law, it is known as a Newtonian fluid. If the viscosity changes with the rate of deformation or shear strain i.e. a constant viscosity is not defined, then the fluid is classed as non-Newtonian. A fluid whose viscosity decreases as the shear strain rate increases is further classed as a shear thinning fluid. A shear thinning fluid responds immediately to a change in the shear strain rate. Blood is classed as a shear thinning fluid as its viscosity decreases with increases in the shear strain rate - highly favourable behaviour for a fluid moving through a blood vessel.

2.4.3.1 Viscosity Models

As there is no universally accepted viscosity model for blood, the use of various non-Newtonian blood models in CFD simulations was investigated by Johnston *et al.* [52]. The effects of five non-Newtonian models were studied (in addition to the Newtonian model as a reference); Generalised Power Law model [53], Walburn-Schneck model [54], Carreau model [55], Casson model [56], and the Power Law model [55]. Johnston *et al.* [52] concluded that the WSS distributions on the aortic wall were the same regardless of the model selected, however, the magnitude of the WSS varied between models. It was observed that at mid-range inlet velocities the models were virtually indistinguishable from each other. As expected, the Newtonian model had a tendency to underestimate the WSS when the inlet velocity was low, with the Power Law model and the Walburn-Schneck model presenting a significant difference at both high and low inlet velocities.

It was then cautiously advised, by Johnston *et al.* [52], that the best approach to modelling blood flow is with the Generalised Power Law model as it is better than the Newtonian model at the low velocities and low shear rates that are associated with diastole. This is key as diastole occupies approximately two thirds of the cardiac cycle. The Generalised Power Law incorporates the Casson model and agrees well with the Carreau model in regions of low to mid-shear, and for higher regions of shear it is similar to the Newtonian model. However, this study presents a large number of limitations; the study was conducted on the right coronary artery with a significantly smaller diameter (3 – 5mm in diameter) than the aorta, which will have an impact in the model chosen. The simulations conducted for this research were steady state, and as it was shown in the research that the non-Newtonian effects of blood are of importance at low velocities it must be considered that at times within the cardiac cycle the velocity of the blood will decrease. It should therefore be noted that transient simulations must also be conducted before appropriate advice on the viscosity model selection is given.

A study conducted by Caballero & Laín [57] looked into the effects of using the Newtonian model, the Carreau model [55], the Herschel-Bulkley model [58], and the Non-Newtonian Power Law model [59] as a way of modelling blood flow through a human thoracic aorta. This study found that

the WSS distribution was consistent across all models applied, with only the magnitude varying according to the model used. It was observed that at mid- to high- range velocities the models were virtually indistinguishable from each other. This is expected as at higher velocity rates the shear rates are higher, and as stated by Whitmore [27], shear rates above $100s^{-1}$ in blood can be treated as a Newtonian fluid. These results are all in agreement with those presented by Johnston *et al.* [52]. This study recommended the cautious use of the Non-Newtonian Power Law model as an approach to model blood flow under steady state conditions as the Carreau and the Herschel-Bulkley models slightly over-estimated the WSS magnitudes at high velocities, and at low flow velocities, the Newtonian model under-estimated the WSS.

The study by Caballero & Laín [57] undertook preliminary transient simulations in order to determine whether the same advice regarding viscosity models can be given to a pulsatile regime as for a steady state simulation. It must be considered whether or not the Non-Newtonian Power Law model is valid when the velocity inlet profile is pulsing, as the model was constructed using steady state conditions. Caballero & Laín [57] found no visual difference in WSS between Newtonian and Non-Newtonian simulations, concluding non-Newtonian effects are not of any importance when running transient simulations. It was suggested then that the Newtonian model would be a reasonable approximation for transient simulations of blood flow through a human thoracic aorta. However, as these are only preliminary results, a full study must be conducted into transient simulations before advice on the viscosity model choice can be confidently given.

These results agree with those found by Karimi *et al.* [60]. A selection of nine non-Newtonian viscosity models (Casson [56], K-L [61], Modified Casson [62], Carreau [55], Carreau-Yasuda [63], Cross [64], Power Law [61], Modified Power Law [65], and Generalised Power Law [66]), as well as Newtonian, were selected to model blood flow through the human thoracic aorta and three major branches off the aortic arch. It was found that all models presented the same WSS distribution patterns with the magnitudes varying according to the choice of model, with the exception of the Cross model which was significantly different. It was found that all models (excluding the Cross model) had a global non-Newtonian impact factor of $\bar{I}_G < 0.15$, suggesting Newtonian behaviour. This led to the conclusion that the Newtonian model is a suitable approximation to blood flow through a human thoracic aorta.

Similarly to the study by Caballero & Laín [57], it was suggested by Karimi *et al.* [60] that the use of the non-Newtonian models with a pulsatile flow may not be valid, as the models' parameters are calculated from steady-state viscosity experiments. The suggestion by Karimi *et al.* [60] implies that the models' parameters may need to be recalculated with data from transient viscosity experiments. The study by Karimi *et al.* [60] neglected the effects that aortic wall deformation would have on the blood flow, as did the studies by Johnston *et al.* [52] and Caballero & Laín [57], as the walls were assumed to be rigid. This may cause the WSS to be overestimated.

A study by Qiao *et al.* [67] utilised a two-phase non-Newtonian model to simulate blood within the human thoracic aorta coupled with FSI, as it was believed that the presence of blood cells and vessel compliance would significantly influence the haemodynamics. It is thought that the multi-element characteristics of blood are directly related to certain diseases, such as atherosclerosis and thrombosis. As a direct result of this, the study by Qiao *et al.* [67] opted not to neglect the shear thinning behaviour, or the red blood cells. It was determined that because of the low volume fraction of white blood cells and platelets they can be neglected. A modified Carreau-

Yasuda viscosity model was used and transient, patient-specific simulations were run. The results presented by Qiao *et al.* [67] suggested that better agreement was found when validated against experimental data with the two-phase non-Newtonian model, that with the one-phase Newtonian and one-phase non-Newtonian. Despite the novelty of this study, there are major limitations to it. Only one patient was studied, with the patient-specific geometry reconstructed from CT scan data. The vessel wall was assumed to be linearly elastic, isotropic and homogeneous, with a uniform thickness which is a non-physical assumption. The flow was also assumed to be laminar, despite a peak Reynolds number of $Re = 4892$ indicating the flow is within the turbulent regime for pipe flow. Qiao *et al.* [67] concluded that despite the additional computational time, the inclusion of the red blood cells was necessary and provided a significant increase in accuracy.

2.4.3.2 Non-Newtonian Importance Factor

The non-Newtonian importance factor, a concept introduced by Ballyk *et al.* [53], can be used to quantify the effects a non-Newtonian rheology model has on the WSS distribution in the domain. The non-Newtonian importance factor is defined as μ_{eff}/μ_{∞} , where μ_{eff} is the effective viscosity, and μ_{∞} is the undisturbed dynamic viscosity, or Newtonian viscosity of the fluid. For blood, $\mu_{\infty} = 0.0345P$. This initial value gives an indication of the overall significance of the non-Newtonian effects. This equation can be altered to give a local value of the importance factor, see Equation 2.5, where μ is the viscosity at any point within the flow [52]. For a Newtonian flow, $\bar{I}_L = 1$. Any value of \bar{I}_L that is notably different from 1 implies there are regions of non-Newtonian flow present.

$$\bar{I}_L = \frac{\mu}{\mu_{\infty}} \quad (2.5)$$

To determine a global value of the non-Newtonian importance factor, the relative difference between the viscosity and the Newtonian viscosity is determined at each point and presented as a percentage, see Equation 2.6, where N is the number of nodes, and μ is the viscosity at each of the nodes.

$$\bar{I}_G = \frac{1}{N} \frac{[\sum_N (\mu - \mu_{\infty})^2]^{1/2}}{\mu_{\infty}} \times 100 \quad (2.6)$$

A cut-off value of the global non-Newtonian importance factor that differentiates between Newtonian and non-Newtonian flow that is commonly used for blood flow in the thoracic aorta and the coronary arteries is 0.25, with any $I_G > 0.25$ being regarded as non-Newtonian flow [52, 57, 68]. In contrast to this, a lower value of 0.15 was used as the cut-off value for a study on the thoracic aorta by Karimi *et al.* [60]. This value was determined by evaluating I_G at five instances throughout the cardiac cycle across nine non-Newtonian viscosity models. It was found that at the times corresponding $I_G = 0.15$, all non-Newtonian viscosity models produced WSS values that were close to the Newtonian value. It was for this reason the lower value of $I_G = 0.15$ was selected as the cut-off value between Newtonian and non-Newtonian flow. The results presented by Karimi *et al.* [60] also indicated that I_G decreases as the cardiac cycle approaches peak systole, and increases during diastole as the blood flow begins to slow. This implies that the presence of pulsatile flow in the aorta has a significant impact on the viscosity model being used, therefore the

steady state results presented by Johnston *et al.* [52] and Caballero & Laín [57] must be viewed cautiously.

2.5 Computational Fluid Dynamics in Cardiac Medicine

CFD is a well known and common tool used in a multitude of engineering applications that has only recently been considered for use in medical settings, however it has rapidly become invaluable and has been central to multiple advances and breakthroughs. Through CFD modelling, the link between haemodynamics disturbances and atherogenesis has been well established, the deposition of atherosclerotic plaque at arterial bends and bifurcations has been explained [69], and the effects of WSS on endothelial homeostasis have begun to be understood [70]. By combining CFD modelling with cardiac imaging techniques, patient-specific models can be constructed that give detailed characterisation of the complex flow patterns that arise in the human body. A study by Morris *et al.* [70] reviewed the methods, benefits and challenges of using CFD within cardiac medicine. It was found that CFD models have the potential to reduce the cost, risk, and time often associated with clinical trials, and could allow for patient-specific modelling and virtual treatment planning [71]. CFD provides a minimally invasive method of observing blood flow within the subject. A series of assumptions that are regularly incorporated into CFD modelling were detailed by Morris *et al.* [70]. Many CFD models assume that the blood vessel walls are rigid, and are not affected by the fluid, nor do they impact upon the fluid. Although false, it is a common and an acceptable approximation as Fluid Structure Interaction (FSI) would need to be incorporated into the model to avoid this assumption. The integration of FSI into the models would dramatically increase the computational cost of each simulation, and although a useful tool for research purposes, it is not practical to wait for an extended period of time for simulation results that are needed for treatment planning or risk stratification. Section 2.6 provides a thorough discussion of the use of FSI in cardiovascular applications. It is also commonly assumed that the fluid-geometry boundaries are smooth. This is due to the poor resolution of the imaging techniques used in order to acquire patient-specific geometry. Finally, it is regularly assumed that blood is an incompressible, Newtonian fluid. Based on the findings by Karimi *et al.* [60] and Caballero & Laín [57], the assumption that blood can be treated as a Newtonian fluid when in the thoracic aorta is suitable for both steady state and transient simulations. This assumption is discussed in more detail in Section 2.4.3.1.

A study by De Jaegere *et al.* [72] used a CFD model of a transcatheter aortic valve replacement (TAVR) in an attempt to predict aortic regurgitation post-surgery. The model was validated by 60 patients. Computed Tomography (CT) was used to recreate patient-specific 3D models of the aorta, and the CFD results validated by post surgery echocardiography scans. It was found that the CFD tool accurately predicted the severity of aortic regurgitation experienced by patients post surgery when measured by either angiography or echocardiography. This study demonstrated that using CFD to predict surgical outcomes is feasible, and that there is scope for a CFD tool to help guide the surgeon to the best placement or size of the valve replacement. This was verified by comparing the CFD results to those from angiograms that were graded based on the severity of aortic regurgitation that could be seen. The clinicians were blind to the CFD results, and good agreement was found between them. However, the CFD simulations were steady state with an inlet velocity that is representative of diastole, so it is not known how the accuracy of the predictive tool

is affected by the variations of the cardiac cycle, including the higher velocities found at systole. Another limitation of this study is the imaging techniques that were selected to capture the aorta: angiography and echocardiography were selected to validate the CFD models, which are known to be techniques of inferior quality to MRI.

Another attempt to provide a non-invasive CFD method to analyse haemodynamics in the thoracic aorta was created by Zhu *et al.* [73]. Multi-Detector Computed Tomography Angiography (MDCTA) was conducted on 25 paediatric patients to collect patient-specific geometry; the peak systolic velocity and pressure data was collected via transthoracic echocardiography and cardiac catheterisation respectively. CFD simulations were then conducted using the patient-specific geometry and patient-specific boundary conditions applied using the transthoracic echocardiography data and a lumped parameter model. It was assumed that blood was incompressible, Newtonian, and the flow laminar. The CFD simulations were steady state, with the patient specific velocity from peak systole being applied to the inlet. Results suggested that the CFD methodology presented was an accurate way of obtaining flow velocity and pressure data. It was demonstrated that combining CFD and medical imaging has potential to be a useful tool in diagnostics. However, a limitation of this study is that the valve morphology was not considered to influence the inlet velocity profile, as it is known to [74]. The methodology used to collect the patient-specific data was invasive, and a multitude of techniques were needed. This presents a limitation to the clinical use of the tool. A significant amount of time and effort to collect the data to run a simulation is required; this invasive and lengthy procedure could be avoided by selecting a more appropriate cardiac imaging technique.

Bonfanti *et al.* [75] also investigated the potential of combining CFD with medical imaging. It was assumed again that blood was incompressible and laminar (a Newtonian viscosity of $4 \times 10^{-3} Pa.s$ was used, with mean Reynolds numbers of $665 < Re < 1506$, and peak Reynolds numbers of $1972 < Re < 2933$); it was taken that blood was a non-Newtonian fluid and the Carreau-Yasuda viscosity model was used with the parameters taken from Gijsen *et al.* [76]. The vessel walls were assumed to be rigid and a no-slip condition was applied. However, the compliance of the aorta wall was taken into account by using a lumped parameter model at the inlet. Although applying this boundary condition to the inlet allowed for accurate modelling of the haemodynamics in the descending aorta, it created a large limitation as the flow in the ascending aorta was no longer modelled accurately, making it an unsuitable boundary condition if the ascending aorta is of interest. The time-averaged WSS and the OSI, which indicates regions where the instantaneous WSS deviates from the flow direction giving a measure of the flow disturbance, were calculated for each patient and compared to commonly available medical imaging data. Although this study presented promising results that hinted at the combination of CFD and medical imaging producing a powerful and convenient tool that could enhance medical understanding, it was only validated on three subjects with the same pathology, so conclusions cannot be drawn with confidence.

CFD modelling of the human pulmonary artery was undertaken by Bordones *et al.* [77], and was validated experimentally through a pulmonary artery phantom using Particle Image Velocimetry (PIV), with a view to diagnosing and monitoring the mortality risk of patients with pulmonary hypertension. The patient-specific geometry was acquired from CT images, and used to construct both the phantom and the CFD geometry. During the CFD modelling, blood was assumed to be an incompressible, Newtonian fluid and the flow to be laminar. Results showed that the CFD mod-

elling agreed with the experimental measurements to within 1% when flow rates were compared, and to within approximately 5.9–13.1% when the velocity was compared. When the shear stresses were compared, good qualitative agreement was found, but discrepancies were evident in regions with high velocity gradients. The results presented suggest that CFD could be utilised as a useful tool in observing haemodynamics in individual patients. Despite the promising results, the study by Bordonas *et al.* [77] is limited as a constant inlet flow rate corresponding to the time-averaged flow rate determined from *in-vivo* measurements was used i.e. only steady state simulations were investigated. Another limitation of the study is in the validation as the phantom used was not fully rigid, as the CFD model was.

A study investigating a feasible methodology to evaluate patient-specific left atrium blood flow characteristics with a view to establishing a link between left atrium remodelling (the pathophysiological remodelling of the left atrium structure and function, commonly as a result of abnormal stresses such as those from obesity, hypertension, heart failure etc.) and intra-cardiac thrombosis was conducted by Otani *et al.* [78]. This was achieved through the use of CFD based on CT scan data to provide the patient-specific geometry, and a Transoesophageal Echocardiogram (TEE) to obtain blood velocity measurements and validate the CFD simulations. In order to simulate the blood flow, it was assumed to be incompressible, Newtonian and laminar (with mean Reynolds numbers in the range of $1100 < Re < 2400$). Transient simulations were conducted with five cardiac cycles being modelled for each simulation. The CFD results captured the characteristic features of left atrium blood flow typically observed through a TEE. The left atrium global flow characteristics captured through CFD were all in agreement with previous reports, and with the flow characteristics that are frequently observed with a transoesophageal echocardiogram.

The conclusion arrived at by Otani *et al.* [78] regarding the feasibility of utilising CFD as a clinical tool agrees with those presented by De Jaegere *et al.* [72], Zhu *et al.* [73], Bonfanti *et al.* [75], and Bordonas *et al.* [77]. It is clearly suggested by all studies that the use of CFD within a cardiac setting can aid in the understanding of haemodynamics and disease progression in a non-invasive manner. Although the methodology presented by Otani *et al.* [78] demonstrates the possibilities of CFD in cardiac medicine, there are still obstacles that need to be overcome. These are evident in the limitations of this study; FSI was neglected as there is a lack of knowledge about the material and mechanical properties of the aorta wall. Only two patients were considered, in order for CFD to be utilised practically within cardiac medicine larger numbers of patients, both healthy volunteers and those with pathologies must be included to validate the tool. The accuracy of the study is reliant on the resolution of the CT scan used to obtain the geometry (a slice thickness of 1mm was used). The validation of this study is also severely limited as quantitative comparison between the CFD data and the TEE data is difficult because of the differing physiological conditions e.g. heart rate at the time of the TEE and CT scan.

Although the studies discussed here have demonstrated the feasibility and potential of using CFD as a tool in cardiac medicine, all are preliminary studies and a tool has yet to be constructed that can be used in a clinical setting. All studies discussed are in need of extensive validation on a wider range and greater number of patients and healthy volunteers.

2.5.1 Inlet Boundary Conditions

The choice of inlet boundary condition when using CFD in cardiac medicine is of high importance and will greatly influence the haemodynamics of the vessel. Multiple studies have investigated the impacts of idealised and patient-specific inlet conditions. Research conducted into the effects the inlet velocity profile have on the flow solution by Madhavan & Kemmerling [79] found that the choice in velocity profile significantly impacts the flow in the immediate neighbourhood. The inlet flow profiles that were examined by Madhavan & Kemmerling [79] can be seen in Figure 2.6. All inlet conditions were pulsatile, with a waveform taken from Fuster *et al.* [80], and all outlets were set to an outflow condition. It was determined that downstream of 2 diameters distal to the inlet, the velocity profile at the inlet had little impact on the flow solution and results were qualitatively similar, regardless of the inlet boundary condition applied. This was echoed with WSS and pressure results. It was consequently recommended by Madhavan & Kemmerling [79] that if the flow close to the aortic valve was of interest, a patient-specific flow profile would be superior to the idealised ones investigated. It has also been highlighted by Madhavan & Kemmerling [79] that the usual practice of artificially extending the geometry proximal to the inlet, as is common practice when modelling the coronary arteries, is not a feasible or accurate solution to producing more physiological inlet boundary conditions. This is due to the complex nature of the *in-vivo* upstream conditions that are a present and a result of a beating heart and the subsequent movement of the aortic valve.

Although Madhavan & Kemmerling [79] investigated a range of inlet conditions (plug, parabolic, linear shear, and cubic shear), a patient specific velocity profile was not investigated. Simulations of the thoracic aorta and proximal supra-aortic vessels were undertaken, using the assumption that blood is a Newtonian, incompressible and homogeneous fluid, and the vessel walls are considered to be rigid.

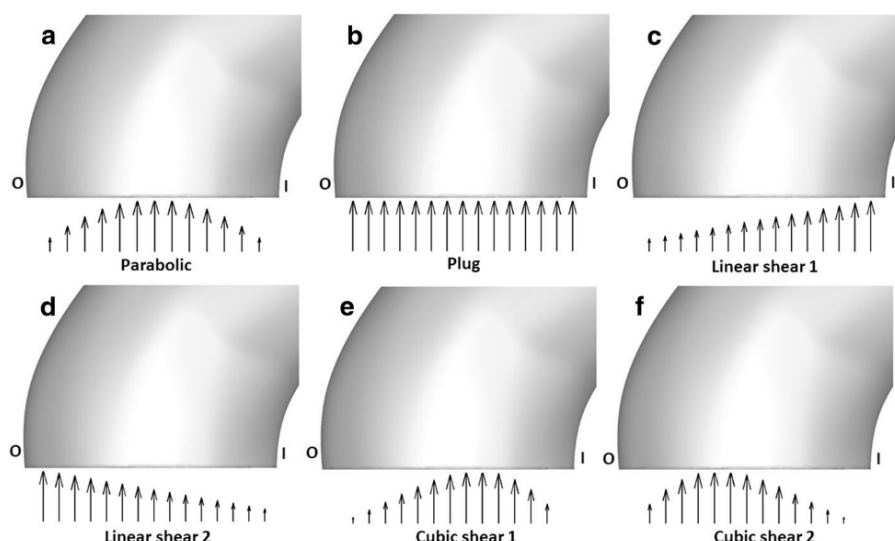


Figure 2.6. Pulsatile velocity flow profiles applied to the inlet by Madhavan & Kemmerling [79]. Only the flow profile at the inlet was varied, all other parameters of the CFD simulations remained constant.

Results found by Pirola *et al.* [81] agreed with those found by Madhavan & Kemmerling [79] in that the flow in the proximal ascending aorta, close to the inlet itself, is heavily influenced by the inlet condition. Pirola *et al.* [81] stated that the peak and mean velocities were underestimated by up to 41% when the boundary conditions are simplified. It was therefore concluded that a patient-

specific boundary condition derived from a 3-dimensional PC-MRI scan is essential to predicting the flow patterns and haemodynamics in the ascending aorta and aortic arch.

A study by Youssefi *et al.* [74] investigated the influence patient-specific inflow velocity profiles at the aortic valve have on the haemodynamics in the thoracic aorta. The patient-specific flow profiles were compared to idealised flow profiles that are based on the patients waveform, specifically parabolic and plug profiles, which are commonly used inlet profiles. For all inflow velocity profiles, pulsatile flow was implemented to replicate the full cardiac cycle. The thoracic aorta of two patients (1 healthy TAV, and 1 BAV) were reconstructed from Magnetic Resonance Angiography (MRA) data, and the patient-specific velocity profiles just above the aortic valve obtained through MRI scans. Similarly to the majority of cardiovascular CFD studies, blood was assumed to be incompressible, Newtonian, and the flow laminar. It was found that implementing idealised flow profiles significantly altered the velocity patterns and produced inaccurate haemodynamics in the thoracic aorta. In conjunction to the altered velocity patterns, it was found that idealised inflow velocity profiles underestimated the velocity magnitude, the radial component of velocity, the helicity, and the complex flow. Figure 2.7 demonstrates how a parabolic and plug velocity profile significantly simplify the inlet boundary condition.

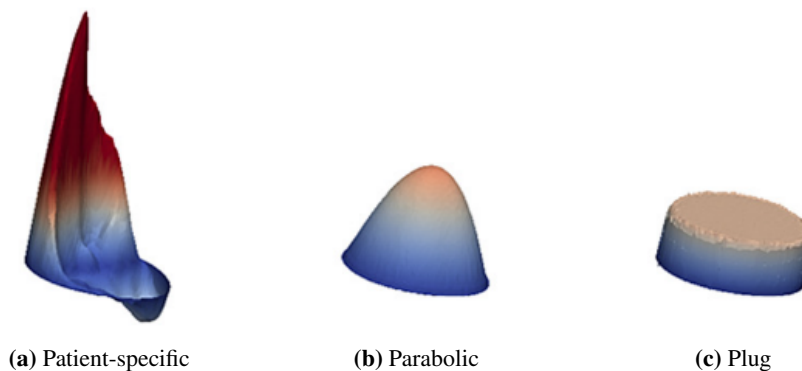


Figure 2.7. Inflow velocity profiles implemented by Youssefi *et al.* [74]; patient-specific (a), parabolic (b), and plug (c), at peak systole for a patient with BAV.

The complexity of the aortic valve, combined with its susceptibility to pathological changes implies that the inflow velocity profile is remarkably variable and subject to change. It therefore follows that any CFD analysis must take this variability into account and incorporate fully patient-specific boundary conditions to produce results that are accurate and can be used for diagnosis, risk stratification, and monitoring of disease progression. It is therefore inappropriate to implement idealised inflow velocity profiles that do not take into account the valve morphology when studying the haemodynamics in the thoracic aorta of both healthy and diseased subjects [74].

2.5.2 Outlet Boundary Conditions

The boundary conditions that are applied to the outlets when modelling the thoracic aorta have a significant impact on the haemodynamics within the vessel. Applying a boundary condition that can accurately replicate the physiological behaviour found at the distal ends of descending aorta and supra-aortic vessels is challenging, due to the complex nature of the cardiovascular system that extends beyond the limits of the vessel being modelled.

2.5.2.1 0-Pressure

A simplistic boundary condition that is frequently applied to the outlet at the inferior descending aorta is a 0-pressure boundary condition, which has been implemented in simulations for research conducted by Kimura *et al.* [82], Callaghan & Grieve [83], and Soudah *et al.* [84]. However, research by Pirola *et al.* [85] found that CFD simulations that utilise 0-pressure conditions at the inferior descending aorta did not capture the flow patterns in the descending thoracic aorta, proximal to the outlet, that are otherwise found using PC-MRI data, whilst also predicting lower flow velocities by up to 52%. A 0-pressure boundary condition is less frequently applied to the supra-aortic vessel outlets; it was also found by Pirola *et al.* [85] that the use of 0-pressure conditions at the supra-aortic branches significantly underestimated the flow volume that exited through the vessels. The use of a 0-pressure condition at the outlets resulted in pressure values that were nonphysical, and produced notable differences in Time Averaged Wall Shear Stress (TAWSS) and OSI measurements. It can therefore be assumed that for the outlets at the supra-aortic vessels a 0-pressure boundary condition is not suitable, and is not a suitable boundary condition for the descending aorta outlet if the descending aorta is the area of interest as it will produce non-physical haemodynamics. However, provided the ascending aorta is the region of interest, a 0-pressure outlet boundary condition at the distal end of the descending aorta may be suitable.

2.5.2.2 Outflow

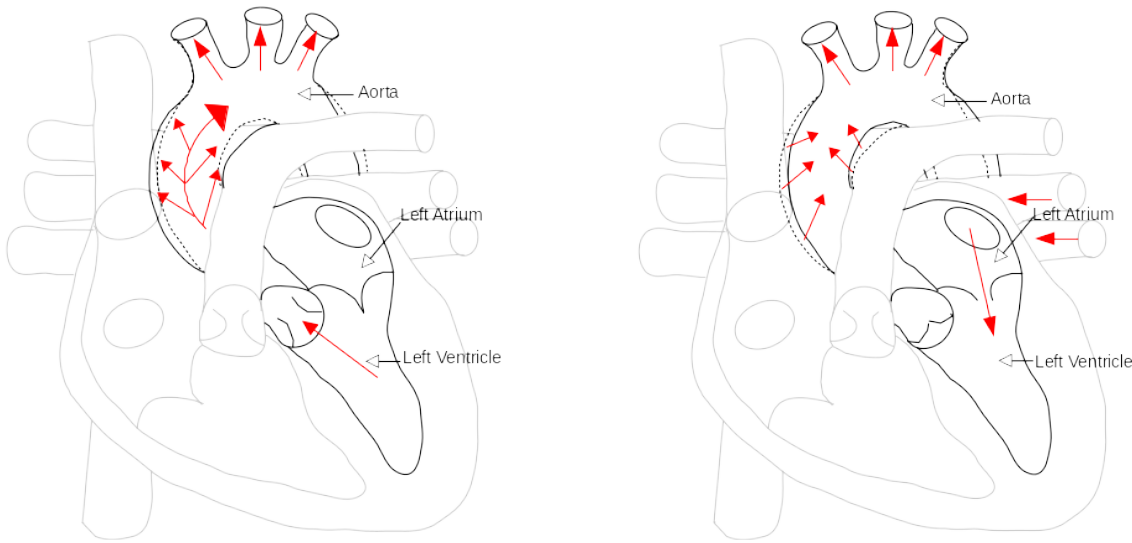
To rectify the issue of a 0-pressure boundary condition underestimating the flow volume leaving the domain through the supra-aortic vessels, an outflow boundary condition can instead be applied at the outlets. Outflow conditions allow for the appropriate flow volume to leave through each outlet based on the cross-sectional area of the vessel. It is a commonly applied boundary condition when there are branches present in the vessels of interest, such as at the supra-aortic vessels [57, 84], the iliac bifurcation [86], or the coronary arteries [36]. Although the volume of flow leaving the domain through each outlet can be corrected using this boundary condition, the impact of the systemic circulatory system distal to the outlets is not taken into account, despite being known to impact the flow within the vessel. As an outflow condition is still therefore a simplification of the flow, large discrepancies can still be found in the descending aorta, proximal to the outlet [79]. A significant limitation of the outflow condition is that prescribing a pressure for each outlet will cause the flow split to be entirely determined by the resistance to the flow of the branches being modelled in the domain of interest, entirely neglecting the dominant resistance of any vessels downstream of the domain of interest [87]. This limitation is also present to a more severe degree when a 0-pressure condition is applied.

The main deficiencies of the 0-pressure and outflow boundary conditions are their inability to take into account the systemic circulatory system that is present distal to the outlet planes and the compliance of the vessel itself; known as the Windkessel effect.

2.5.2.3 Windkessel Models

The aorta is known to be an elastic vessel [88], and as such, at the end of ventricular contraction (systole) the pressure within the aorta falls at a slower rate than within the left ventricle. This occurs as the elastic vessel acts as a reservoir over the course of systole, expanding to store a portion of the blood that is ejected from the valve in the periphery of the vessel [89], as shown in

Figure 2.8a. Over diastole, as the valve closes and the flow ejected from the valve falls to zero, the blood stored by the vessel wall flows through the vessel as it contracts, providing a continuous flow of blood through the circulatory system from the periodic flow exiting the left ventricle. This is demonstrated in Figure 2.8 and is known as the Windkessel effect.

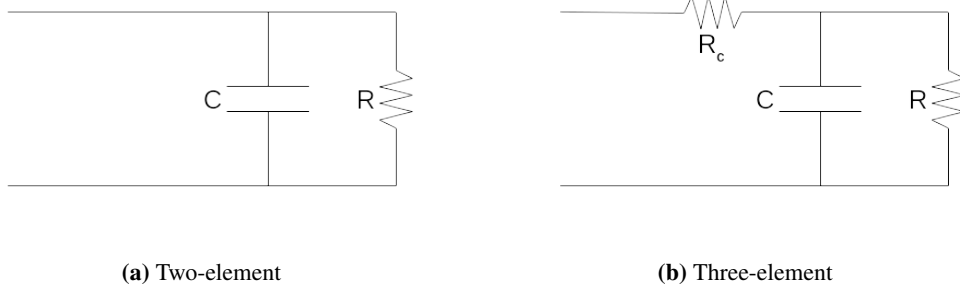


(a) Systole: the valve is open and blood flows through into the aorta, as the vessel is compliant the artery wall distends and 'stores' a fraction of the blood ejected.

(b) Diastole: the elastic rebound of the artery wall results in a force being applied to the blood in the arteries, continuing to drive blood through the vessels.

Figure 2.8. Schematic demonstrating the Windkessel effect in compliant arteries. Solid lines represent the vessel walls at that stage of the cardiac cycle, dashed lines represent the vessel wall location at the previous stage. Red arrows represent the movement of blood.

The Windkessel effect is analogous to an electric circuit, demonstrated by Figure 2.9. The blood flow can be thought of as the current, the arterial compliance as a capacitor, the peripheral resistance as a resistor arranged in parallel, and the blood pressure as the electrical potential. The resistance in the arterial system can be attributed mainly to the smaller vessels and arterioles whilst the compliance can be attributed to the elasticity of the vessel of interest. By combining the resistance of all the smaller vessels and arterioles, the peripheral resistance (R) of the systemic circulatory system can be found [90]. The compliance (C) can be determined through adding the compliance of all the vessels together [90].



(a) Two-element

(b) Three-element

Figure 2.9. A two-element Windkessel model (a) and a three-element Windkessel model (b). C =compliance, R =peripheral resistance, R_c =characteristic resistance.

Pulse pressure is a major indicator of mortality and morbidity [91, 92], and as arterial compliance will affect the pulse pressure it follows that the arterial compliance is of great importance and

should be accounted for in the boundary conditions of any cardiovascular modelling if clinical conclusions are to be drawn. The size and complexity of the systemic circulatory system prevents a three dimensional model of the arterial tree being integrated into the model of the thoracic aorta. However, the consequences of neglecting the downstream circulatory system are severe and causes inaccuracies in the predictions of the velocity and pressure within the aorta [87]. To take into account the resistance of the downstream vascular bed and the compliance of the vessel, a Windkessel model can be applied to the outlets within the domain of interest. This applies high fidelity modelling to the domain of interest, whilst concurrently applying a simpler model to the outlets to represent the arterial tree downstream and the compliance of the vessel.

The original two-element Windkessel model proposed by Frank [93] describes the arterial system using two parameters that have physiological meaning (R and C), whilst the more accurate three-element Windkessel model incorporates the characteristic resistance (R_c), placed in series to the pre-existing parallel network (Figure 2.9). This accounts for the combined compliance and inertance of the proximal ascending aorta at the valve location. Using the three-element Windkessel model, Equation 2.7 is produced which can be used to obtain the outlet pressure. The two-element Windkessel model is identical, not including the characteristic resistance (R_c) term.

$$\frac{\partial p}{\partial t} + \frac{p}{CR} = \frac{Q}{C} \left(1 + \frac{R_p}{R} \right) + R_c \frac{\partial Q}{\partial t} \quad (2.7)$$

The original two-element Windkessel is known to poorly predict the relationship between the pressure and the blood flow across the systolic period [94–97], however behaves similarly to the three-element during diastole [90]. The three-element Windkessel model overall predicts pressures that are close to the measured values, generally performing better than the two-element Windkessel. It can therefore be concluded that the three-element Windkessel model is a necessary improvement to the two-element Windkessel. A four-element Windkessel model has been proposed and used in some research studies [98], however the additional element that is incorporated, the inertance, that is placed in series with the characteristic resistance, is challenging to calculate. This severely limits the use of the four-element Windkessel model. It has been concluded by Westerhof *et al.* [90] that the four-element Windkessel model is not an improvement on the two-element Windkessel model.

The resistance (R) and the characteristic resistance (R_c) of each outlet must be determined in order to implement the three-element Windkessel model at each outlet. They are calculated from the following [14, 99]:

$$R_{total} = \frac{P}{Q} = \left(\sum_i \frac{1}{R_i} \right)^{-1} \quad (2.8)$$

Where R_{total} is the total resistance in the vascular system, P is the mean arterial pressure, Q is the mean flow, and R_i is the total resistance of each individual outlet comprised of the resistance and characteristic resistance for each outlet ($R_i = R_c + R$), and is calculated using Equation 2.9.

$$\frac{R_{total}}{R_i} = \frac{A_i}{A_{total}} \quad (2.9)$$

Where A_{total} is the total cross sectional area of all the outlets within the domain, and A_i is the cross sectional area of the individual outlet. A ratio between the characteristic resistance and the total resistance is assumed [100], allowing the resistance and characteristic resistance of each outlet to be determined.

$$\frac{R_c}{R_c + R} = 0.056 \quad (2.10)$$

The total arterial compliance (C) can be determined through multiple methods [90], with the most straightforward methods listed below. The arterial pressure must be a known parameter in each method.

The *decay time method* [93] assumes the decrease of the aortic pressure during diastole is equal to the decay time, RC , see Equation 2.11. This assumes that the pressure will decay to a negligible value. However this is not always appropriate, in which case a better fit for the aortic pressure decay time can be found in Equation 2.12.

$$P(t) = P_0 e^{-\frac{t}{RC}} \quad (2.11)$$

$$P(t) = P_0 e^{-\frac{t}{RC}} + P_1 \quad (2.12)$$

The *stroke volume over pulse pressure method* [101, 102] assumes that if the peripheral vascular system was blocked, then the stroke volume (ΔV) would increase the pressure by ΔP , the ratio of which gives the total arterial compliance, see Equation 2.13. Due to the simplistic nature of this method, it is thought to overestimate the vessel compliance by up to 60% [103, 104].

$$C = \frac{\Delta V}{\Delta P} \quad (2.13)$$

The *area method* [105] calculates the decay time during diastole as the area under the diastolic aortic pressure curve (P) divided by the pressure difference between the start time (P_1) and end time of diastole (P_2), demonstrated with Equation 2.14.

$$RC = \int_{t_1}^{t_2} \frac{P}{P_1 - P_2} dt \quad (2.14)$$

The three-element model is commonly used as an outlet boundary condition in 4D-Flow MRI based CFD simulations, and has been extensively validated and used [14, 81, 106–109]. Notably, in research conducted by Madhavan & Kemmerling [79], it was found that in terms of time-averaged WSS, both the two- and three-element Windkessel models differ from the outflow boundary condition (based on volumetric flow percentages like that used by Caballero & Laín [57]) by as much as 18%. However, it must be noted that despite this large variation, upstream of five diameters proximal to the outlet the variations between outlet boundary conditions was insignificant.

This agrees with results presented by Pirola *et al.* [85] where five combinations of boundary con-

ditions were investigated and it was found that a three-element Windkessel model should be the preferred outlet boundary condition choice for patient-specific CFD modelling of the aorta. The boundary condition combinations used can be seen in Table 2.1. Although it was found that there were significant differences in flow patterns between the varying boundary conditions, these were present in the descending aorta. The ascending aorta was not investigated. From qualitative images presented by Pirola *et al.* [85] it can be seen that the TAWSS and OSI appear similar in the ascending aorta and aortic arch, not including the supra-aortic vessels, regardless of the outlet boundary condition selected.

Case	Inlet	Supra-Aortic Branches	Outlet
1	3D P-S velocity profiles	3-E WM	3-E WM
2	3D P-S velocity profiles	3-E WM	P-S pressure waveform
3	3D P-S velocity profiles	Mass flow waveforms	P-S pressure waveform
4	3D P-S velocity profiles	Mass flow waveforms	0-pressure
5	3D P-S velocity profiles	0-pressure	0-pressure

Table 2.1. Boundary condition combinations for the inlet, supra-aortic branches, and outlet investigated by Pirola *et al.* [85]. *P-S=patient-specific, 3-E WM=3-Element Windkessel Model.*

2.5.3 Turbulence Modelling

It is commonly known that the normal condition for blood flow through most blood vessels in the human body is laminar, but it may become transitional or turbulent in pathological cases, such as distal to stenotic valve or stenotic vessel, or when there is an assistive device present [7, 110]. Turbulent flow is also found at the bifurcations of large vessels, and in the ascending aorta at high systolic ejection velocities. This turbulent flow can cause an increase in Energy Loss (EL) and an increased pressure drop [110]. It had also been suggested that a patient with BAV may experience higher levels of WSS and turbulence than a healthy TAV volunteer, these increased levels may play a significant role in amplifying the biological response of the ascending aorta and the aortic valve leaflets [111].

There is little consensus on how pulsatile flow, such as that within the cardiovascular system, impacts the transition to turbulence within pipe flow, such as a blood vessel. It is commonly reported that the transition threshold monotonically increases as the pulsation frequency increases (i.e. the Womersley number, α) [112–115], however other studies report a decreasing threshold for identical parameters and only observe an increasing threshold for low values of α [116, 117]. The Womersley number of a pulsatile flow in a pipe can be determined using Equation 2.15, where L is the length scale (vessel radius), ω is the angular frequency, ρ is the density of the fluid, and μ is the dynamic viscosity. It is a dimensionless number representing the relationship between the pulsatile flow frequency and the viscous effects. It can also be taken that a Womersley number of $\alpha \leq 1$ will produce a more parabolic, or sharp velocity profile, whilst a Womersley number of $\alpha \geq 10$ produces a much broader velocity profile, becoming closer to a plug profile.

$$\alpha = L \left(\frac{\omega \rho}{\mu} \right)^{\frac{1}{2}} \quad (2.15)$$

It was found by Xu *et al.* [118] that the transition to turbulence of pulsatile flow can be categorised by three regimes. The high frequency regime ($\alpha \geq 12$) is defined as the regime where the transition to turbulence is unaffected by the pulsation and turbulence is sustained as the Reynolds number is equal to or larger than the steady state threshold. The low frequency regime ($\alpha \leq 2.5$) can be defined as the regime in which the Reynolds number fluctuations are sufficiently slow such that the turbulent structures are able to react, the transitional thresholds within this regime are higher than in the high frequency regime, whilst transition to turbulence is delayed when compared to steady-state transition the turbulence. The third regime described by Xu *et al.* [118] states that when $2.5 \leq \alpha \leq 12$ the transition to turbulence threshold changes smoothly between the regimes.

Within a blood vessel network, it can be assumed that the angular frequency (ω), the density (ρ), and the dynamic viscosity (μ) remain somewhat constant. However, the radii of the vessels changes significantly, with up to three orders of magnitude difference between the large blood vessels and the capillaries. As the radius of the vessel reduces, the Womersley number reduces, tending towards $\alpha = 1$ in the small vessels. In these vessels, the flow is governed more by the viscous effects than the pulsatility of the flow. This is known as microcirculation [119].

A study by Miyazaki *et al.* [120] investigated the effects that three turbulence models had on the blood flow in the thoracic aortic in two patients; one healthy adult and one paediatric patient with a double aortic arch. The WSS and EL were validated and compared for both patients and all three turbulence models to 4D-Flow MRI data. The turbulence models that were investigated were laminar, Large Eddy Simulation (LES) using the Smagorinsky-Lilly model, and RNG k-epsilon ($k-\epsilon$). It was found that the RNG k- ϵ and LES simulations produced higher values of WSS and EL than the laminar simulation, as expected, due to eddy viscosity. It was also determined that the LES model did not agree with the data as well as the k- ϵ did as a result of the grid size that was being used. The grid size required to model the smallest of eddies is of the order of tens of micrometers (of the same scale as the leukocytes within the fluid). The grid size used in the LES simulations was the same as that used in the RANS simulations and therefore it was too large to compute the smallest eddies; LES saw a decreased correlation between the CFD results and the 4D-Flow MRI results. Miyazaki *et al.* [120] concluded that although the accuracy of the CFD simulation was improved by the inclusion of a turbulence model, the RNG k- ϵ turbulence model showed the highest correlation with the 4D-Flow MRI.

Ziegler *et al.* [121] conducted a study in which LES was used to capture the turbulent effects within the thoracic aorta. Simulations were run on two patients, and two inlet flow rates used for both patients. The blood flow was assumed to be Newtonian, non-pulsatile, and a blunt (plug) velocity profile was used. The resolution of the grid used was much higher than that used by Miyazaki *et al.* [120]; approximately three million cells were used compared to the one million used by Miyazaki *et al.* [120]. Due to the increased grid resolution, LES is an appropriate choice of turbulence modelling, as it resolves the larger eddies whilst computing the isotropic smaller eddies which are not dependent on the geometry using a subgrid-scale model, such as the Smagorinsky-Lilly [122], as in Miyazaki *et al.* [120] or WALE [123] as in Ziegler *et al.* [121]. As the larger eddies contain the majority of the turbulent energy, and are responsible for the majority of the momentum transfer

and turbulent mixing, LES is a more accurate turbulence method than most. Ziegler *et al.* [121] concluded that the LES method of modelling the turbulence produced results that agreed well with 4D-Flow MRI results.

Another study of the haemodynamics of the thoracic aorta was conducted by Hellmeier *et al.* [18]. In order to model the turbulence that is experienced in the thoracic aorta both pre- and post-valve replacement, the $k-\omega$ SST [124] turbulence model was used. The $k-\omega$ SST turbulence model was also implemented by Nordmeyer *et al.* [125], where haemodynamics of the thoracic aorta both pre- and post AVR were investigated, and steady-state simulations of peak systole run. The $k-\omega$ SST turbulence model is a two-equation RANS turbulence model, where k is the turbulent specific energy, and ω is the specific dissipation rate. The standard $k-\omega$ turbulence model predicts well in the near wall region, so is well suited to flows where the boundary layer is important, such as cardiovascular applications, where WSS is a key parameter. The $k-\omega$ SST model blends the accuracy of $k-\omega$ turbulence model in the near wall region with the free-stream independence of the $k-\varepsilon$ turbulence model. This ensures that the $k-\omega$ SST model is accurate for a wider range of flows than the standard $k-\omega$ model. A large benefit of using a RANS turbulence model over LES and DNS is the mesh resolution: a coarser mesh can be used, reducing the computational cost of the simulation. Shorter simulation times are beneficial if patient-specific CFD simulations are to be used in diagnosis and treatment planning.

2.5.4 4D-Flow MRI based CFD

A series of preliminary studies have been conducted combining CFD and 4D-Flow MRI. Biglino *et al.* [126] conducted a preliminary study intended to show the potential role CFD and 4D-Flow MRI can play in cardiac medicine by investigating the *in-vitro* haemodynamics of the thoracic aorta in a patient-specific flow phantom with the congenital heart defect, Transposition of the Great Arteries (TGA). In all CFD simulations, it was assumed that the flow was Newtonian and laminar, with rigid walls and no-slip conditions applied. A time-varying velocity function was applied to the inlet, to replicate the cardiac cycle. *In-vitro* experimental pressure data was recorded by a high-fidelity fibre-optic pressure sensor placed in the aortic arch. Mean pressure and flow data were then compared at intervals throughout the cardiac cycle (representing early systole, peak systole, late systole, and diastole). Good quantitative agreement was found between the two methods in terms of pressure and flow distribution data, and good qualitative agreement was found when streamlines throughout the cardiac cycle were plotted using both methods. Although it is clear the combination of CFD and 4D-Flow MRI can be used to improve the understanding of *in-vivo* haemodynamics, limitations of the study prevent any clinical conclusions being drawn: only two subjects were used and the fluid modelled in the CFD models was water, which is not representative of blood as a fluid as the physical properties of water vary from those of blood.

Research conducted by Hellmeier *et al.* [18] used both 4D-Flow MRI and CFD to observe how the haemodynamics in the aorta were affected by a virtual valve replacement. Simulations were conducted using the $k-\omega$ SST turbulence model, blood was assumed to be incompressible and the non-Newtonian generalised power law was used to model the viscosity. Only steady state simulations were run, which limits the study as the full cardiac cycle was not modelled. However, the inlet velocity selected replicated peak systole so modelled the highest velocities and forces experienced during the cardiac cycle. It was found that the haemodynamics and flow patterns,

and therefore the choice in valve replacement (either biological or mechanical), were affected by patient specific conditions. It was also determined that CFD based on 4D-Flow MRI may be a useful tool in surgical decision making, agreeing with the conclusions of Biglino *et al.* [126]. However, the study was validated on only 10 subjects so any conclusions of a clinical nature may be insufficiently robust. The predictive capabilities of the CFD simulations were not validated against post-AVR 4D-Flow MRI scans as they were not available, again limiting the robustness of any clinical conclusions. Another limitation of the study is that the fluid-structure interactions of the valves was neglected, and the AVR's were assumed to be open during the simulations.

Kimura *et al.* [82] conducted a study to observe the WSS distribution using 4D-Flow MRI based CFD in patients with BAV. During all CFD simulations, blood was treated as an incompressible, Newtonian fluid, with no turbulence model used. The aorta walls were treated as rigid with a no-slip condition applied, and with a zero pressure condition applied at the outlet. The simulation, run over 4 cardiac cycles, concluded that 4D-Flow MRI based CFD assessment of patient-specific haemodynamics is a feasible methodology. This study did not consider post surgical haemodynamics, or the various fusion patterns possible with BAV and as such it is only a preliminary study and cannot be used to draw clinical conclusions. Another severe limitation of this study is that the flow for all BAV patients was turbulent, but no turbulence model was used in the CFD simulations as selecting the correct model was deemed too challenging.

Another attempt to investigate the use of 4D-Flow MRI based CFD was conducted by Miyazaki *et al.* [120] on two subjects with a double aortic arch as discussed in Section 2.5.3. CFD simulations were conducted for a range of turbulence models, including laminar, RNG $k - \epsilon$, and LES. The WSS and energy loss were selected to be compared to 4D-Flow MRI results. It was found that the WSS was underestimated by the 4D-Flow MRI in the smaller vessels, and both the WSS and energy loss were less than half of that predicted by the CFD simulations. It was concluded that the spatial and temporal resolution of 4D-flow MRI was not fine enough to capture accurately the WSS and energy loss in the aorta, however it provides the only method of measuring blood flow *in-vivo*. The results presented by Miyazaki *et al.* [120] reveal that there is good correlation between CFD and 4D-Flow MRI in the distal portion of the aorta, but not in the proximal. This was suggested to be a result of insufficient boundary conditions, as flow in the distal aorta is governed primarily by the curvature of the aortic arch, whereas flow in the proximal section of the aorta is governed primarily by the inlet conditions. This study was therefore limited by the choice of inlet conditions. Although the boundary conditions were patient-specific, they did not accurately represent the cardiac cycle - only peak systole was simulated, and a flat profile was used. The lack of ventricular contraction in the inlet conditions was found to have a large impact on the helical flow patterns.

A study by Soudah *et al.* [84] evaluated the blood flow features in the thoracic aorta through a combination of CFD and 4D-Flow MRI. The WSS was selected to be compared as it can be used as a diagnostic marker in arterial disease and plays a significant role in the initiation and progression of many cardio-vascular diseases. In agreement with Miyazaki *et al.* [120], it was found that the 4D-Flow MRI did not accurately capture the WSS due to the limited resolution of the scans. As a consequence of the poor resolution, 4D-Flow MRI was instead used only to get the spatial domain and the boundary conditions for the CFD simulations. The CFD simulations used the familiar assumptions of an incompressible, Newtonian fluid with no turbulence modelling. The

peak systolic Reynolds numbers in the AAO, DAO and AAO were in the range of $3400 < Re < 4500$, which would categorise the flow as transitional to turbulent, meaning neglecting a turbulent model may not be appropriate. The blood vessel walls were assumed to be rigid with a no-slip condition applied, and a uniform inlet velocity applied that replicated the velocity present at peak systole. The main limitation to this research is that the haemodynamics of only one patient were investigated so conclusions of clinical significance cannot be drawn. Another significant drawback is that only steady-state simulations were run, so the effects of a pulsatile inlet condition were not investigated, nor was diastole.

A study conducted by Perinajova *et al.* [127] investigated the reliability of WSS measurements from 4D-Flow MRI based CFD simulations. The WSS depends on an accurate vessel wall location, however current commercial and research methodologies rely on manual segmentation to extract a patient-specific geometry. The study involved 10 patients, with the segmentation process occurring 4 times for each patient. The same boundary conditions were applied to each segmentation attempt of each patient and steady-state simulations at peak systole were run. It was concluded by the authors that the calculated WSS values were strongly influenced by any variations in segmentation. Through conducting a voxel-by-voxel analysis of the results, when compared with 4D-Flow MRI data, it was found there was only qualitative agreement. It was therefore concluded by the authors that it is best to be critical of WSS results from MRI-based CFD simulations to avoid misinterpreting the results.

Research by Jayendiran *et al.* [128] utilised 4D-Flow MRI based CFD to evaluate the influence eccentricity and aortic valve phenotype (BAV vs. TAV) had on the haemodynamics of a Ascending Thoracic Aortic Aneurysm (ATAA). The study involved five adult ATAA patients with BAV, five adult ATAA patients with TAV, and two healthy adult volunteers. Good qualitative agreement was found between the time-averaged CFD results and 4D-Flow MRI data in terms of velocity profiles across a plane in the axial direction. Good agreement was also found between the CFD results and the 4D-Flow MRI data in terms of the calculated flow eccentricity. Through the use of the 4D-Flow MRI based CFD simulations, it was concluded that flow eccentricity at the aortic root is a major contributing factor to the haemodynamics in ATAA's, regardless of whether or not the patient had BAV or TAV. This study clearly demonstrates that through combining CFD and 4D-Flow MRI techniques, medical advances and breakthroughs can be made.

As discussed by multiple studies, the spatial and temporal resolution of 4D-Flow MRI scan data are a large limitation to the accuracy of the data. The 4D-Flow MRI scan data is also affected by acquisition noise and flow artefacts. Research by Bakhshinejad *et al.* [129] proposed a methodology to run patient-specific CFD simulations based on 4D-Flow MRI images that addresses these three common limitations to merging the techniques, and that therefore reconstructs de-noised, divergence free, and high resolution flow fields. The proposed methodology uses Proper Orthogonal Decomposition (POD) to construct the orthonormal basis of the local sampling of the space of all possible solutions to the flow equations for both the lower resolution grid of the 4D-Flow MRI data and the higher resolution mesh of the CFD mesh. From this, a low-resolution, de-noised flow is obtained, before ridge regression is then used to create a high-resolution, de-noised, divergence free solution to the flow. When applied to a resolution similar to the 4D-Flow MRI, the POD method created maintained the smaller flow structures better than other CFD methods as well as eliminating the acquisition noise. Additionally, when applied to a higher resolution the POD

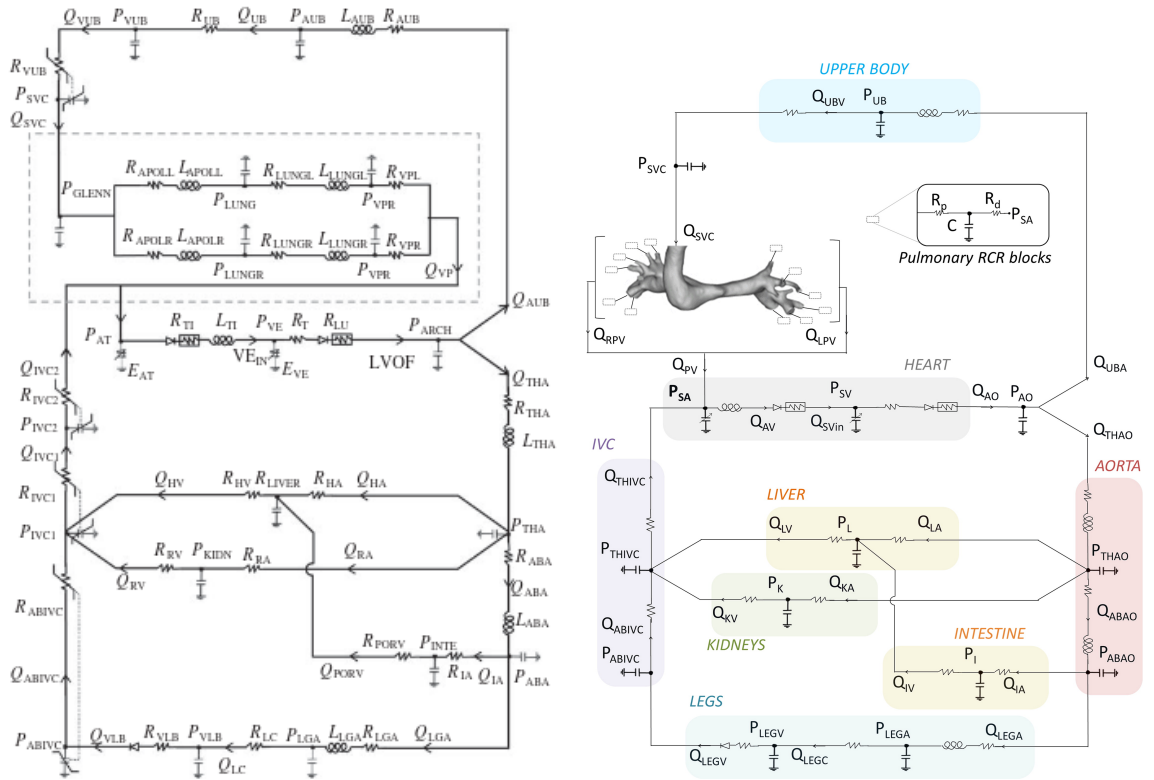
method was also shown to successfully recreate details that were previously not visible at lower resolutions. Bakhshinejad *et al.* [129] concluded that the POD method improves the accuracy of the flow-derived parameters that can be used to draw clinical observations.

2.5.5 Predicting Post-Surgical Outcomes with CFD

An effort to utilise fluid dynamics to help predict post-operative haemodynamics was made by Baretta *et al.* [130]. The objective of the study by Baretta *et al.* [130] was to perform virtual planning of surgical repairs (total cavopulmonary connection, TCPC) in a patient with a congenital heart defect resulting in a unidirectional heart, meaning the patient has a bidirectional cavopulmonary anastomosis. Using MR images the patients pre-operative state was reproduced, and a multi-scale closed loop approach to modelling was taken. The boundary conditions were calculated through a complex lumped parameter network of the entire circulatory system based on previous work [131, 132]. Implementing a lumped parameter model to calculate the boundary conditions removes the uncertainty that is often introduced into patient-specific simulations through the inlet and outlets. However, it must be noted that to replicate the entire circulatory system an extensive lumped parameter model was required (21 blocks), see Figure 2.10a, significantly increasing the complexity of the simulations. Alongside this, the complexity of the reproduced geometry must also be evaluated; the model included the superior vena cava, the right and left pulmonary arteries, and 22 pulmonary branches. Therefore the practicality of using this method to help clinicians predict post-operative outcomes is severely reduced because of the increased complexity.

Transient simulations were run, taking approximately 1.5 days per cardiac cycle. Blood was assumed to be a Newtonian, homogeneous fluid with a viscosity of $\mu = 0.004 \text{ kgms}^{-1}$ and a density of $\rho = 1060 \text{ kgm}^{-3}$. The vessel walls were assumed to be rigid. Three surgical approaches to a TCPC were simulated, whilst also investigating the impacts of exercise. The authors found that using pre-operative caval flows for post-operative boundary conditions was not appropriate, and that negligible differences in terms of global circulatory parameters were found between the three surgical approaches. It was noted that although the results are in line with recent literature studies, the improved clinical outcome of utilising a Y configuration TCPC was not yet demonstrated, therefore more research is needed to correlate the results from the multi-scale model to clinical outcomes. The methodology must also be applied to multiple patients to ascertain its usefulness as a clinical tool. Despite this, the study has successfully demonstrated how CFD can be utilised to predict post-surgical outcomes.

Similarly to research by Baretta *et al.* [130], Kung *et al.* [133] developed two multi-scale computational models of paediatric patients (5 months and 6 months old) with three dimensional models of the region of interest and closed loop systemic lumped parameter networks created with patient-specific data to model the boundary conditions. A 3D anatomical model was constructed using commercial software and contrast enhanced MRI data. The lumped parameter network used can be seen in Figure 2.10b, where only 5 main blocks were used to model the heart, upper and lower body vasculatures, and the left and right pulmonary vasculatures outside of the 3D models. Virtual surgery was performed on the two models before post-operative simulations were conducted by altering the geometry, and increasing the heart rate and decreasing the vascular resistance. It was found that virtually performing the same surgery in two patients can lead to difference haemody-



(a) Lumped parameter network coupled to the 3D anatomical region by Baretta *et al.* [130] to model the entire circulatory system beyond the surgical TCPC.

(b) Lumped parameter network coupled to the 3D anatomical region of the surgical junction by Kung *et al.* [133] to model the heart, upper and lower body vasculatures, and the right and left pulmonary vasculatures.

Figure 2.10. Lumped parameter networks that are coupled to 3D models to replicate the circulatory system, allowing for a multi-scale, closed loop modelling approach.

namics within the blood vessels, highlighting the importance of individualised treatment planning and surgery. Blood was assumed to be a Newtonian fluid with a density of $\rho = 1060 \text{kgm}^{-3}$ and a viscosity of $\mu = 0.004 \text{kgms}^{-1}$. The vessel walls were taken to be rigid, and 12 cardiac cycles run and results taken from the last one. The research agreed with that by Baretta *et al.* [130] in that the ability of multi-scale modelling to reproduce patient-specific flow and predict post-operative flow has been shown. It was concluded that patient-specific modelling can be used to show any physiological changes that may occur and are associated with different clinical conditions. However, more validation is required against clinical data and *in-vitro* data. There was also a lack of clinical data to allow for precise modelling of the changes in the physiological parameters from the pre- to post-operative state. The spatial resolution of the MRI acquisition must also be noted to be only $1 \text{mm} \times 1 \text{mm} \times 2 \text{mm}$; relatively coarse when considering the age and size of the patients participating in the research.

A review of utilising computational predictive modelling to help understand the biomechanical implications of a TAVR and to help pre-operatively predict the risks that are associated with the devices was conducted by Esmailie *et al.* [134]. In agreement with the conclusion with multiple studies [130, 133] it was highlighted that reduced order modelling can be used to significantly reduce the high costs and times that are currently required for computational predictions.

Dowling *et al.* [135] demonstrated the used of patient-specific computational modelling to predict the long term outcomes after a TAVR, with the goal of identifying which patients are at risk of

long term adverse outcomes. 203 patients were studied and post-operative CFD simulations run. It was found that the patients identified through CFD as at risk or long term adverse outcomes due to a significant level of para-valvular regurgitation had a higher rate of death than any other group of patients at 2 years post-surgery, suggesting patient-specific CFD simulations can help to identify at risk patients.

2.6 Fluid-Structure Interactions

The radius of the aorta varies by approximately 10% as a direct result of forces being exerted on the vessel walls by the blood flow during the cardiac cycle [136]. This substantial vessel compliance culminates in a complex FSI problem. Over the past two decades, FSI has become an important tool within cardiovascular engineering and its use in patient-specific surgical planning is now feasible. It is hypothesised that FSI is to become the 'gold standard' of numerical modelling in cardiac medicine [137]. However, patient-specific FSI simulations do not come without a spectrum of difficulties: primarily that biological tissue is anisotropic and decidedly non-linear. The material properties of the vessel wall are highly dependent on the patient, the region of the vessel being investigated, the type of vasculature, and any pathology present. The presence of the aortic valve must also be considered if the thoracic aorta haemodynamics are to be modelled thoroughly. An example of how FSI can be of use in clinical settings is through the monitoring of WSS. WSS is known to be a parameter of significance in a range of cardiovascular pathologies, in both diagnosis and monitoring progression, as discussed in Section 2.2.6. However, direct measurement of WSS *in-vivo* is infeasible. The use of FSI to measure WSS *in-silico* allows clinicians to make treatment decisions and monitor disease progression on a patient-specific basis in a non-invasive manner on a more physiologically accurate model than when using conventional CFD.

A common approach to incorporating FSI in cardiovascular applications, specifically the thoracic aorta, is the Arbitrary Lagrangian Eulerian (ALE) formulation - a partitioned, conforming mesh method. In a partitioned FSI approach the fluid and structural domains are treated independently, each with a separate set of governing equations and separate mesh. As the domains are independent of each other, an interface is necessary between the domains to allow the transfer of data at every time step; the inner intima is selected to be this interface in applications involving the vessel wall. By ensuring the mesh density of the domains are matched along the inner intima, interpolation errors can be minimised. Both domains must be re-meshed at each time step as the geometries change. This leads to a high computational cost. Therefore, a significant effort has been made to automate this process. An automated ALE formulation is known as a conforming mesh method. An advantage of partitioned FSI approaches is they facilitate the use of advanced CFD and Finite Element Analysis (FEA) techniques that have been developed separately [137].

Monolithic approaches contrast to partitioned approaches as they involve the fluid and structural domains being meshed together. A single set of governing equations is then applied to both domains concurrently. This means higher accuracy simulations at the cost of a more computationally expensive simulation when compared to loosely coupled (one-way coupled) partitioned approaches. For cardiovascular applications, a popular monolithic approach is the Immersed Boundary (IB) method [138]. This method is frequently used for studies that model the heart valves in detail. The IB method is often selected as the valve leaflets are thin and the deformation experienced is considerable [137, 139], see Section 2.6.2 for a more in-depth discussion. Within the

IB method, the fluid domain is considered using an Eulerian coordinate system, while the solid domain is considered using a Lagrangian coordinate system.

The method by which data is exchanged between the fluid and structural solvers must also be considered. This coupling at the interface of the domains is either one- or two-way. In a one-way coupled system, the fluid and structural domains are solved in series. The solution of one domain is used as either an initial or boundary condition for the other domain [140]. However, one-way coupled systems do not capture the full exchange between the fluid and structure. They do not allow transient problems to be solved, and as the body deforms the mesh does not adapt which leads to highly skewed elements. When there are large deformations (such as at the heart valves) the highly skewed elements lead to unstable solutions that present difficulties in converging, and are prone to errors [137]. As the flow through the cardiovascular system is inherently transient, it can be inferred that a one-way coupling is not a suitable method for haemodynamic applications. Despite the indisputable drawbacks to one-way coupled system, the numerical models produced are simpler and necessitate far fewer computational resources than two-way coupled systems. In a two-way coupled system the fluid and structural domains are solved in parallel. It requires the solutions of the fluid and structural domains be in agreement at each iteration and convergence must be reached together before moving forward to the next time step. A two-way coupled system allows transient problems to be modelled and solved, but requires more computational power than a one-way coupled system [140].

2.6.1 Fluid-Structure Interaction of the Vessel Wall

As the aorta is known to move throughout the cardiac cycle, a common limitation of patient-specific CFD simulations based on medical imaging is neglecting this movement of the vessel walls, and the resulting impact on the haemodynamics. A new strategy to incorporate this movement into CFD simulations of the thoracic aorta was implemented by Capellini *et al.* [141] and the feasibility tested. This new method modelled the patient-specific changes in the aortic geometry during the cardiac cycle in a way that overcomes the assumptions required for FSI and the complexity that comes with FSI simulations. The method suggested by Capellini *et al.* [141] was based on Radial Basis Functions (RBF) mesh morphing techniques and transient simulations, by reconstructing the aortic geometry at points throughout the cardiac cycle, a transient shape deformation was obtained, and a prescribed wall motion simulation can be run. The results were then compared to CFD simulations run with an aortic geometry based on the minimum and maximum aortic volume. Both the CFD and the RBF approaches took similar computational resources as the RBF does not require a FE solver for the description of the vessel structure. The segmentation process, meshing, and set-up of the models took a long period of time, making the additional time required to set up the RBF negligible. Conventional CFD simulations ran approximately three times faster than the RBF simulations however the additional time required is not comparable to that needed for full two-way FSI simulations. It was therefore concluded by Capellini *et al.* [141] that the technique is feasible and can be applied to study patient-specific haemodynamics.

Work by Crosetto *et al.* [142] investigated FSI between the blood flow and the aortic wall using the ALE formulation in an attempt to predict the haemodynamics of large blood vessels. FSI and rigid wall CFD simulations were run (using patient-specific geometry) in an effort to determine whether vessel compliance had a noteworthy effect on the haemodynamics. Crosetto *et al.* [142] found that

the rigid wall simulations were unsuccessful at predicting a range of blood flow patterns. A region of backwards flow around the inlet was predicted with the FSI model, presumed to aid in the closing of the aortic valve, and was not seen in rigid wall simulations. It was also noted that rigid wall CFD simulations continually overestimated the WSS magnitude, indicating FSI should not be neglected in cardiovascular applications.

Although more anatomically correct results were produced using the FSI model than those from the rigid wall simulations, considering the full FSI problem increased the computational cost of the simulation considerably. The rigid wall simulations required 64 processors, whereas the FSI simulations required 128 processors. The study conducted by Crosetto *et al.* [142] had several limitations despite showing the potential of FSI as a tool in cardiovascular medicine. The ratio of the aortic diameter to the vessel wall thickness was taken to be constant, as was the elastic modulus. Values were taken from *ex-vivo* samples of the human thoracic aorta from a study by Langewouters [143]. This assumption is physiologically incorrect as both parameters vary with location in the vessel, increasing in the distal direction. Blood was modelled as a Newtonian fluid and the arterial wall was taken to be a linear elastic structure. Only one healthy volunteer was used - in order to validate the study thoroughly, more volunteers must be used. It would also be of interest to utilise patients with existing pathologies such as BAV or aortic stenosis, to observe how the presence of disease affects the importance of FSI in the aorta.

Despite of the clear limitations of the study by Crosetto *et al.* [142], the novelty of the study was that the surrounding tissue in the chest cavity was included in the numerical model. It was determined that neglecting to include the surrounding tissue resulted in non-physical flow patterns, as the surrounding tissue is known to have a significant impact on the behaviour of the vessel [144]. The surrounding tissue was factored in to the numerical model by including a linear algebraic stress displacement constitutive relation on the outer adventitia (a Robin condition). As there is no agreed constitutive law for the heterogeneous tissue surrounding the aorta, this modelling technique produced only an approximation of the behaviour.

A two-way coupled system was applied by Nowak *et al.* [145] to predict the deformation, the pressure, and the WSS magnitude distribution of the human aorta. Nowak *et al.* [145] concluded that FSI should be included when modelling blood flow through arteries with a low stiffness. The work by Nowak *et al.* [145] focused on a paediatric patient with coarctation of the aorta; the focus on a paediatric patient increased the need to incorporate FSI into the model as paediatric blood vessels are more compliant than adult blood vessels as a result of increased levels of stenosis often found in adult vessels [146]. This increased compliance of paediatric vessels causes rigid wall models to overestimate the WSS magnitude by up to 50%. This presents a significant limitation to the rigid wall numerical model in terms of clinical use due to the importance of WSS. Another limitation to the study by Nowak *et al.* [145] is that the vessel wall was assumed to be approximately 10% of the local effective vessel radius, which although is not physiologically correct it simplifies the modelling process significantly as patient-specific data for material properties is not required.

Another assumption used by Nowak *et al.* [145] was that the aortic walls were modelled using a linear elastic model. This is a large simplification of the three layers that make up the aortic walls and it would be more appropriate for anisotropic constitutional laws to be used. These assumptions considerably limit the study by Nowak *et al.* [145] as they are all non-physical assumptions and so could prevent the study from having clinical significance.

Unlike multiple studies that model blood as Newtonian, Nowak *et al.* [145] modelled blood as a non-Newtonian fluid using the Carreau viscosity model [55]. Blood flow was assumed to be laminar, despite Reynolds numbers of $Re = 3396$ at peak systole. This is because the cardiac cycle is diastole dominant, with diastolic Reynolds numbers of $Re = 89$, implying that the flow was mostly laminar. Nowak *et al.* [145] noted that significant backflow was observed near the aortic root not otherwise observed with a rigid wall model, indicating that FSI must be considered when modelling blood flow in the aorta, in agreement with Crosetto *et al.* [142]. It is evident that the introduction of FSI influences the haemodynamics around the aortic valve which is of paramount importance when investigating the flow patterns and haemodynamics within the thoracic aorta.

The effects of a pulsatile inlet condition and the behaviour of the arterial wall using patient-specific models was evaluated by Alishahi *et al.* [147]. The human abdominal aorta was chosen to be modelled, and two subjects selected; one healthy volunteer and one patient with severe stenosis. A two-way coupled system and a partitioned approach was used. Alishahi *et al.* [147] found that despite wall deformation being slight, the consequences of it were noticeable and therefore vessel wall compliance plays a vital role in the haemodynamics in the thoracic aorta, agreeing with Crosetto *et al.* [142], Nowak *et al.* [145], Lantz *et al.* [148], and Reymond *et al.* [149]. Both rigid wall and FSI simulations were run, and the results compared to *in-vivo* results. The results for pressure displayed significant differences; it was found that the FSI model determined pressure to be up to 15% lower than the rigid wall simulations, and were more consistent with the values from the *in-vivo* results. When the WSS magnitudes were compared, it was evident that the rigid wall model predicted consistently higher values for both patients than the FSI model. The common assumptions of a constant wall thickness (1mm was selected), an isotropic, elastic material, and uniform material properties were all used, limiting the study by Alishahi *et al.* [147] as they are not physiologically accurate. Blood was assumed to be a non-Newtonian fluid with the power law viscosity model used, and the flow laminar.

The links between the aortic wall movement and the WSS magnitude and distribution were also explored by Lantz *et al.* [148]. Using a partitioned method with two-way coupling it was found that the time-averaged WSS was not affected by the vessel compliance, whereas the instantaneous value was noticeably affected by it. Lantz *et al.* [148] therefore concluded that if the instantaneous values were of interest FSI must be included in the numerical model. This is of importance when the maximum value of WSS is required, such as when investigating the link between WSS and disease progression. The flow was turbulent as the Reynolds numbers were found to be between $200 < Re < 7500$ at late diastole and early systole respectively, and the $k - \omega$ SST turbulence model was used. The study by Lantz *et al.* [148] is restricted as it applies the common assumptions that are often seen in cardiovascular FSI studies such as those used by Alishahi *et al.* [147], these assumptions are used because of the lack of known universal values and the difficulties in obtaining material properties that are patient-specific. The material properties used in all simulations were commonly used values taken from literature - the Poisson's ratio and density of the solid were taken from Bathe & Kamm [150], and a Young's modulus of 1MPa taken from Li & Kleinstreuer [151]. Finally, blood was taken to be a Newtonian fluid. Regardless of the clear limitations, the surrounding tissues in the chest cavity were included in the numerical model (as Crosetto *et al.* [142] did) by applying a linear elastic support boundary condition to the aortic wall. Although the inclusion of the surrounding tissue increases the accuracy of the FSI simulations as it better

represents the human aorta, a simplistic representation of the complex surrounding tissues was used. This is because the anatomically correct relationship between the surrounding tissue and the aortic wall is complex and difficult to determine.

Research conducted by Quarteroni *et al.* [152] suggested that vessel walls should be treated as an inelastic material in numerical models as the stress-strain curves when loaded and unloaded are different. Quarteroni *et al.* [152] also highlighted that the mechanical interaction between the fluid and structural domains is not the only interaction between the two domains that must be considered; there is a biochemical interaction that is generally overlooked by cardiovascular FSI studies due to its complexity. It was suggested that the biochemical interaction should be implemented by supplementing the Navier-Stokes equations with the linear advection diffusion equations. Quarteroni *et al.* [152] suggested that the ALE method should be used to solve the FSI problem as Crosetto *et al.* [142] did. Attention was then drawn to the difficulties of studying the fluid-structure interaction within large blood vessels. Determining a mathematical description of the mechanical behaviour of the vessel walls presents a significant challenge as found by the studies discussed within this Section. This challenge is in part due to the multiple layers that make up the arterial wall. The highly non-linear nature of the material properties [152] and vessel wall thickness also present significant challenges that must be overcome, as is obtaining patient-specific material properties.

Work by Reymond *et al.* [149] used an ALE formulation to investigate the effects vessel wall compliance had on the WSS magnitude and distribution, as did Lantz *et al.* [148]. Simulations using a rigid wall model as well as FSI were run, and the results compared. It was concluded that including the compliance of the aorta wall had a considerable effect of the WSS distribution. It was found that the rigid wall model systematically overestimated the WSS magnitude, as Alishahi *et al.* [147] found. The common assumptions of the vessel wall being linearly elastic and isotropic, and blood being a Newtonian fluid were applied, limiting the study as they are not anatomically correct assumptions. Only one patient was used; more volunteers are needed to fully validate the results to allow conclusions to be drawn with confidence. Despite the clear limitations, Reymond *et al.* [149] accounted for the heterogeneous tissue that surrounds the thoracic aorta with a method similar to Crosetto *et al.* [142] and Lantz *et al.* [148].

A two-way coupled ALE formulation was used to investigate the compliance of the aorta in the presence of aortic dissection by Bäumlér *et al.* [108]. It was found that the FSI results presented good agreement with those found by 4D-Flow MRI when pressure, WSS, and diameter of the vessel were compared. In addition to considering the effects of the surrounding tissue (through a Robin condition), Bäumlér *et al.* [108] also incorporated the tethering between the aorta and the spine through the intercostal and lumbar arteries. This was achieved by applying Dirichlet conditions to the locations on the outer adventitia where the vessels would be located. This tethering is normally overlooked in FSI studies due to the complexity it adds to the numerical model, making the research by Bäumlér *et al.* [108] novel. Despite this, the study was limited as it only investigated one patient, so needs extensive validation. The material properties used for the aortic wall were also not patient-specific, and blood was assumed to be Newtonian and incompressible.

The ascending aorta was modelled using a two-way coupled approach by Mendez *et al.* [153]. The results of the two-way coupled system were compared to rigid wall CFD simulations, and it was found that there was a good agreement between the models in terms of the WSS distribution, in

disagreement with the results presented by the majority of studies discussed [142, 145, 147, 149]. The agreement Mendez *et al.* [153] found between FSI and rigid wall simulations can be attributed to the presence of an ATAA, which is known to influence the stiffness of the aortic wall. The increased stiffness reduces the compliance of the aortic wall causing the FSI results to agree with the rigid wall simulation results. This demonstrates that for the specific pathology of ATAA, vessel compliance and therefore FSI can be neglected. It would be of interest to further this research and investigate the effects of a wider range of pathologies, such as BAV, on the importance of FSI. A limitation of this study is that it neglected to include the aortic valve, preventing the valve haemodynamics from being modelled correctly. The inclusion of FSI at the aortic valve would cause FSI to be a necessary addition to the simulations. This study is also limited in its applicability as it uses the common assumptions of blood being a Newtonian fluid, uniform material properties that are not patient-specific (and are instead based on population averaged values from *ex-vivo* mechanical test data), and uniform aortic wall thickness. This study also neglected the effects of the surrounding tissue, as did the studies by Nowak *et al.* [145], Alishahi *et al.* [147], and Hasan *et al.* [154]. Extensive validation of the work by Mendez *et al.* [153] is needed before any of the presented results can be of clinical use and any robust conclusions can be drawn.

2.6.2 Fluid-Structure Interaction of the Aortic Valve

Due to the complexity of the thoracic aorta, in addition to considering the interactions between the aortic wall and the blood flow, it is also necessary to consider the complex fluid-structure interactions around the aortic valve leaflets. As a result of the thin structures and the large deformations that are experienced, a method that is frequently used is the Immersed Boundary (IB) formulation.

An IB method to simulate the fluid-structure interaction of the aortic valve was implemented by Pasta *et al.* [155]. Patients with BAV and healthy volunteers were used. The study focused on the clinical significance of using an FSI model, as opposed to a comparison between an FSI and rigid wall model. A key aim of the study by Pasta *et al.* [155] was to find a new predictor that could be of use when there is a need to determine and quantify the risk of aortic dilation in a patient with BAV. Similarly to the studies discussed in Section 2.6.1, the common assumptions of a uniform wall thickness, and uniform material properties that are not patient-specific but instead taken from population averaged values were applied. The surrounding tissue was also not considered, despite it being known that it has a considerable effect on the results. Despite the limitations, this study did not assume the aortic wall was linearly elastic, but instead applied a fibre-reinforced constitutive model which took into account the collagen fibres that are present within the layers of the aortic wall [9].

In a similar approach to Pasta *et al.* [155], Sodhani *et al.* [139] used an IB method to evaluate the complex relationship between the valve leaflets and the blood flow at the aortic root. The FSI numerical model was validated against *in-vitro* measurements, and a good agreement between the results were found, indicating FSI should not be neglected when modelling aortic haemodynamics. The blood was assumed to be incompressible and Newtonian, and the $k - \varepsilon$ turbulence model was used. This study did not encounter issues regarding material properties as many studies have done, as a prosthetic heart valve was modelled, removing the need for patient-specific material properties. This study highlights the capabilities and the potential FSI models have in terms of surgical planning for valve replacement. However, the FSI between the aortic wall and the blood

flow was not included, limiting the study significantly.

A patient-specific FSI model of the aortic root and ascending aorta was constructed by Hasan *et al.* [154]. An IB method was used as the aortic valve was included in the model. The elasticity of the valve leaflets was based on a fibre-reinforced constitutive model that was fit to experimental data, similarly to the attempt by Sodhani *et al.* [139]. The work presented by Hasan *et al.* [154] demonstrated good agreement with clinical data when pressure and flow rates were compared - showing the potential FSI has as a surgical planning tool. The techniques used in this study have the potential to be extended to investigate a range of cardiovascular pathologies, such as BAV. However, there are significant limitations with the model that need resolving before the concept is taken further. The sinuses of valsalva and the ascending aorta were assumed to be rigid, which is not an anatomically correct assumption as the ascending aorta experiences considerable movement during the cardiac cycle [136]. Blood was also modelled as a Newtonian fluid. Flow was not fully resolved during systole at the valve leaflets because of the poor resolution of the FSI model. It also needs to undergo substantial validation before it can be of any clinical significance and conclusions can be drawn that will be robust. An additional limitation of the study is that the material properties that were used for the aortic valve leaflets were from porcine subjects, which gives rise to questions of whether it is applicable to human patients.

In contrast to the studies by Sodhani *et al.* [139], Hasan *et al.* [154], and Pasta *et al.* [156], the study by Tango *et al.* [157] attempted to use an ALE formulation to investigate the complex problem of the valve leaflets opening and closing. The results from the FSI model were validated against experimental PIV results using a flow phantom, as opposed to results taken from volunteers or patients. It was demonstrated by Tango *et al.* [157] that numerical models can play a vital role in predicting valvular pathologies as they do not face the same limitations as experimental set-ups do. It was also found that the ALE formulation was a suitable method to model a healthy heart valve. The valve leaflets were taken to be hyper-elastic and incompressible, however the fibres in the tissue were neglected, unlike the studies by Hasan *et al.* [154] and Pasta *et al.* [156]. The common assumptions of a linearly elastic vessel wall with a uniform thickness, and blood being a Newtonian fluid were applied, limiting the study considerably. However, the study was further limited as the aortic root was taken to be rigid, which is a nonphysical assumption, and the geometry used in both the FSI model and the experimental set-up was not patient-specific.

2.7 Existing Software

A range of softwares currently exist that attempt to combine medical images and CFD techniques to aid in predicting the blood flow within a range of vessels in the human body, and are listed and discussed within the following Section:

2.7.1 SimVascular

Developed at Stanford University, *SimVascular* is an open source software that provides a complete methodology to combine medical images and CFD, from segmenting medical images to running the resulting patient-specific CFD simulations [158]. It allows a patient-specific mesh, that can be used to run CFD simulations, to be constructed from medical images, taken from an MRI scan. This is achieved by identifying the blood vessel of interest and creating a pathline along it. A

pathline is constructed by creating a node within the vessel of interest every 5-25 images as you move inferiorly down the aorta from the axial viewpoint. By joining the nodes together a pathline is created. From this pathline, a model is created using a 2D lofted segmentation method. At each node previously created, the vessel is segmented, resulting in a series of 2-D segmentations along the aorta. The 2D segmentations are then lofted together with splines to create a 3D patient-specific model. At this point, it is possible to join together multiple vessels, if required. An unstructured tetrahedral mesh is then created, ready for any subsequent simulations. The *SimVascular* workflow discussed here can be seen in Figure 2.11. *SimVascular* allows for the fluid-structure interaction between the blood flow and the vessel wall to be considered through an ALE formation, however it does not consider the fluid-structure interaction at the aortic valve, instead relying on the boundary conditions at the inlet being altered to reflect patient-specific flow profiles throughout the cardiac cycle.

In Figure 2.11 it can be seen that increasing the number of 2D segmentations would increase the accuracy of the 3D model. This is a notable drawback to the *SimVascular* software, as the vessel of interest is not segmented in every image, so the geometry is an estimate, and key features may be overlooked. Although a good research tool, *SimVascular* has a number of drawbacks that prevent it from being a practical tool that is used by clinicians for patient-specific treatment planning, surgical planning, or device design. It is necessary to have prior knowledge in the software to be able to use it effectively, as well as the skills to interpret the medical images when creating the pipelines and segmentations. As such, it is not an intuitive software to use and would require training before use. The software also requires significant computational power and high quality graphics cards to render the 3D volume that is created through the segmentation and lofting process, which may not be accessible to all clinicians who have need of the tool.

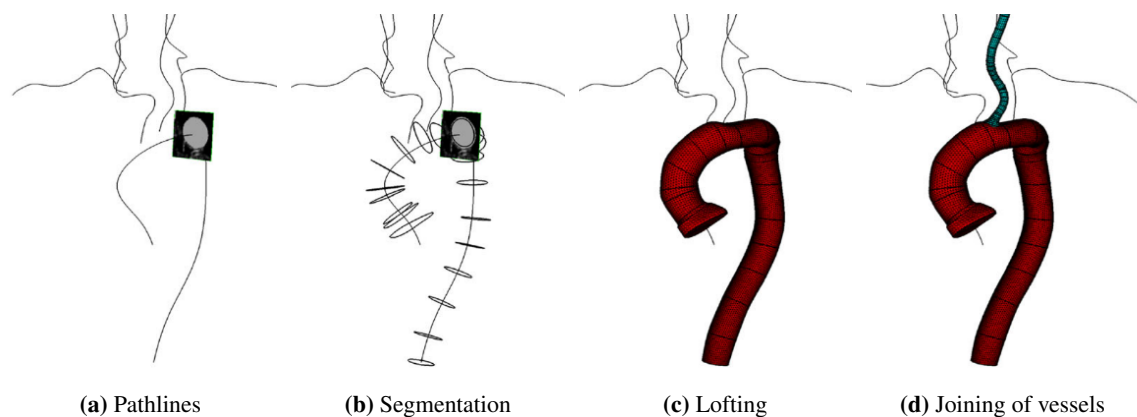


Figure 2.11. The *SimVascular* geometry workflow. Figure (a) demonstrates the path lines through the vessels of interest. Figure (b) demonstrates the 2D segmentations along the path lines. Figure (c) shows the lofted 3D model, and Figure (d) demonstrates the joining of vessels, taken from Updegrave *et al.* [158]

SimVascular has been excessively validated by a range of studies, observing the haemodynamics in an assortment of vessels with a large degree of variation in the pathologies present [159–162]. In particular, the study conducted by Bäumler *et al.* [108] used *SimVascular* to observe the haemodynamics in the thoracic aorta. Patient-specific meshes were created and the subsequent CFD and FSI simulations were performed with the *svFSI* solver used. Due to the complex geometry (an aortic dissection with the subsequent formation of a secondary flow channel) that was used in the study, the modelling software *meshMixer* [163] was used alongside *SimVascular*. It was also noted

by Bäumler *et al.* [108] that the geometry construction process within *SimVascular* was time consuming and would cause a bottleneck if multiple patients were used in a study. It was found that the methodology used in Bäumler *et al.* [108] produced results that showed an improved comparison to *in-vivo* medical images than previous studies have done, however there were still notable differences. Previous studies have reported deformations of the aortic dissections to be up to 1.3mm, whereas the study by Bäumler *et al.* [108] reported deformations of 13.4mm, within the range of expected values, and only a difference of 42.53% when compared to values found from 4D-Flow MRI data, which although is a large difference is a notable improvement on previous studies. Despite the improvement in results, it must be noted that this cannot be attributed to *SimVascular* solely. This is because the methods used, such as tethering the aorta through intercostal and lumbar arteries, pre-stress and external stress of the structural domain, and independently defining the elastic modulus for the dissection flap and outer vessel wall, are novel when compared other studies. The patient-specific geometry was obtained through CTA scans, with 4D-Flow MRI and blood pressure data used to determine the physiologically correct boundary conditions.

2.7.2 HeartFlow

A commercial software available in the United States, Europe, Canada, and Japan that is being used by clinicians to aid in diagnosis of heart disease, specifically any pathology within the coronary arteries, is *HeartFlow* [164]. Following on from a standard CT scan, *HeartFlow* uses the CT images to reconstruct a patient-specific model of the coronary arteries, before CFD simulations are run. Although the tool is used by clinicians, it has limited functions, as its primary purpose is to determine if there is sufficient blood flow reaching the heart through the coronary arteries. However, it is a non-invasive and interactive software that has been extensively validated, as such it has been granted FDA clearance and it successfully models the haemodynamics of the coronary arteries.

2.7.3 CRIMSON

CRIMSON is an open source software is based on *SimVascular* and allows for 3D haemodynamic simulations [165]. This tool uses reduced order modelling techniques, has FSI features and is able to post-process and visualise the results. It also enables the user to fine-tune the boundary conditions, allowing for the imposition of PC MRI flow data, as well as spatially varying vessel wall material properties. However the software has not yet been commercialised.

2.7.4 FEops

FEops allows the user to simulate the deployment of a TAVR device and the interactions it may have with the patients' aortic valve geometry [166]. The patient-specific geometry is reconstructed from pre-procedural electrocardiogram-gated multi-slice CT cardiac angiogram data, and parameters such as the device model, size, and the implantation depth can be altered and simulated. The workflow created was validated extensively [167]; allowing clinicians to make a surgical decision on 80 patients, before then making simulation data available to the clinicians for 42 of the patients. The primary outcome of the research was to determine whether the simulation data from *FEops* altered the initial decision made by the clinicians. It was found that in 39 patients, the initial decision was maintained, and no statistically significant difference was found in the clinical outcomes

between patients with and without the simulation data. Although no definitive conclusion can be made regarding the clinical impact of the workflow, the feasibility of using such a technology within a clinical environment has been demonstrated. The workflow also comes with a significant cost attached as large amounts of human resources are needed to segment the CT data and perform the analysis. It was hypothesised by Theriault-Lauzier *et al.* [166] that the workflow has potential to be of use in situations where the patient is high risk and comorbid, and will not tolerate a sub-optimal TAVR surgery. *FEops* as a predictive tool for surgical outcomes and risk identification has also been demonstrated through the work conducted by Dowling *et al.* [135].

2.8 Summary

This review of current literature gives a brief introduction to the congenital heart defect, BAV, highlighting the background to the motivation behind this research project. It also details the efforts made to create *in-silico* models of the thoracic aorta suitable for use in CFD, before evaluating the combination of CFD models and medical imaging, including combining CFD modelling and 4D-Flow MRI, and how it has been utilised so far as a clinical tool. Finally, the use of FSI in cardio-vascular applications was discussed in length. In summary:

- BAV is the most common congenital heart defect, occurring in approximately 1.3% of live births. It is the fusion of two of the aortic valve cusps, leading to an off centre jet of blood being ejected from the left ventricle every cardiac cycle. This is known to cause altered WSS distributions. It has been hypothesised that the resulting altered WSS distribution could be used in diagnosis and monitoring disease progression, as well as risk stratification and in the planning of patient-specific treatments.
- 4D-Flow MRI has only recently become a tool used in clinical settings due to recent improvements in spatial and temporal resolution, and scan time. It has been derived from conventional MRI, and captures the blood flow in the heart and large vessels. It is a non-invasive and non-ionising technique that is rich in data and allows for a multitude of useful haemodynamic parameters to be calculated retrospectively.
- To date, CFD models and medical imaging have been used in a number of investigations. Although the workflows detailed show promising results, no conclusions of clinical significance can be drawn as the number of subjects used in the studies has been too small, and the resolution of the medical imaging techniques too coarse. In CFD simulations it was frequently assumed that blood was incompressible, Newtonian, and laminar. However, the latter two assumptions are not always applied. As there are no agreed upon viscosity or turbulence models suitable for modelling blood flow, a wide range are still in use. Although recommendations have been made, they vary greatly and need further validation before being relied upon. It is also regularly assumed that the vessel walls are rigid and no-slip conditions applied. It has been shown that incorporating patient-specific inlet boundary conditions is key to accurately modelling the haemodynamics of the thoracic aorta, and the three-element Windkessel model is the most physiologically accurate outlet boundary condition available.
- The use of CFD and 4D-Flow MRI in a cardiac setting is a feasible method for modelling the haemodynamics in the thoracic aorta and multiple investigations have been conducted

to develop approaches of combining the two techniques. Despite results demonstrating the combination of methods shows potential as a clinical device, no study has yet to produce a tool that could be utilised in a clinical setting where conclusions drawn using it would be robust and reliable. This is due to the small number of subjects currently used in each study. Again, in the CFD simulations it was frequently assumed that blood was Newtonian, incompressible and laminar. Multiple studies acknowledge the spatial and temporal resolution of 4D-Flow MRI is insufficient, however its impacts on patient-specific CFD modelling have not been quantified.

- The incorporation of the fluid-structure interaction between the vessel walls and the blood flow has been investigated by multiple studies, and it has frequently been found that its inclusion significantly affects the WSS distribution and magnitude, with rigid wall simulations overestimating the WSS. The fluid-structure interaction between the blood flow and the aortic valve has also been investigated by multiple studies, and many conclude that the flow patterns are significantly altered through its inclusion in simulations. It is concluded by all FSI studies considered in this review of current literature that FSI is not to be neglected. However, FSI increases the computational cost considerably, so many not be appropriate if a predictive tool is to be utilised by clinicians for surgical planning. It was also noted that studies involving the fluid-structure interaction of the valve leaflets tend to neglect to compliance of the arterial wall. There is a gap in the literature therefore regarding studies involving the FSI between both the arterial wall and the valve leaflets, and the blood.
- Based on the literature reviewed in Section 2.6, it has been concluded that FSI will not be included in the numerical simulations for this research project. Although it has been made clear that the inclusion of FSI impacts the results of the simulation, it will prohibitively increase the complexity of the simulation significantly, and therefore will increase the computational cost of the simulations. This will cause the tool to become impractical for clinicians to utilise in patient-specific treatment planning, surgical planning, and risk stratification scenarios.
- Although there are open-source softwares that provide complete pipelines, from segmenting medical images to running patient-specific simulations, they are time consuming to use and have wide ranging limitations. The geometry construction processes are not user-friendly and require time and effort to use, and they provide only an estimate of the geometry as a significant portion of the geometry is lofted, and not segmented. In addition, many of the existing softwares can be applied only to certain vessels or certain pathologies or treatment options. The work within this research project will address this gap, and produce a robust methodology that produces accurate patient-specific geometries.

Chapter 3.

Methodology

Contents

3.1	Introduction	50
3.2	Data Acquisition	51
3.3	Geometry Reconstruction	53
3.3.1	Human Error in Geometry Reconstruction	58
3.4	Meshing	59
3.4.1	Netgen	60
3.4.2	cfMesh	60
3.4.3	snappyHexMesh	61
3.4.4	Mesh Independence	62
3.4.4.1	Steady State Mesh Independence	62
3.4.4.2	Neonatal Transient Mesh Independence	63
3.4.4.3	Adult Transient Mesh Convergence	64
3.5	Boundary Conditions	65
3.5.1	Steady-state Plug Flow	65
3.5.2	Pulsatile Flow	66
3.5.3	Spatio-Temporal Variations	66
3.5.3.1	Interpolation of 4D-Flow MRI data	67
3.5.3.2	Curve Fitting	68
3.5.3.3	Implementation of Spatio-Temporal Boundary Conditions	73
3.6	Properties of Blood	74
3.6.1	Viscosity	74
3.6.2	Turbulence	74
3.6.3	Homogeneity	76
3.7	Quantification of Haemodynamic Indices	76
3.7.1	Flow Asymmetry	77
3.7.2	Flow Dispersion	78
3.7.3	Circulation	79
3.8	Limitations	79
3.9	Conclusions	80

3.1 Introduction

Drawing on the review of research reported and discussed in Chapter 2, the methods outlined throughout Chapter 3 will focus on how an approach to combine CFD modelling with 4D-Flow MRI was created. This Chapter will describe how individual patient 4D-Flow MRI data is processed before undertaking patient-specific CFD simulations in OpenFOAM, version 6 [6]. The methods used to pre-process the Magnetic Resonance (MR) images will be outlined, as will the methods used to reconstruct the patient-specific *in-silico* thoracic aortic geometries. The process of meshing the geometry will be described, before the methods used to create spatio-temporal patient-specific boundary conditions are detailed. The methods used to run the numerical simulations are then described. All images presented in this Chapter relate to the neonatal patient identified as CoRaL071 (age = 5 days, weight = 4.4kg) with no suspected congenital heart defect, unless stated otherwise, however the methodology was repeated for all patients participating in this research. The workflow that was followed to create the methodology is summarised in Figure 3.1.

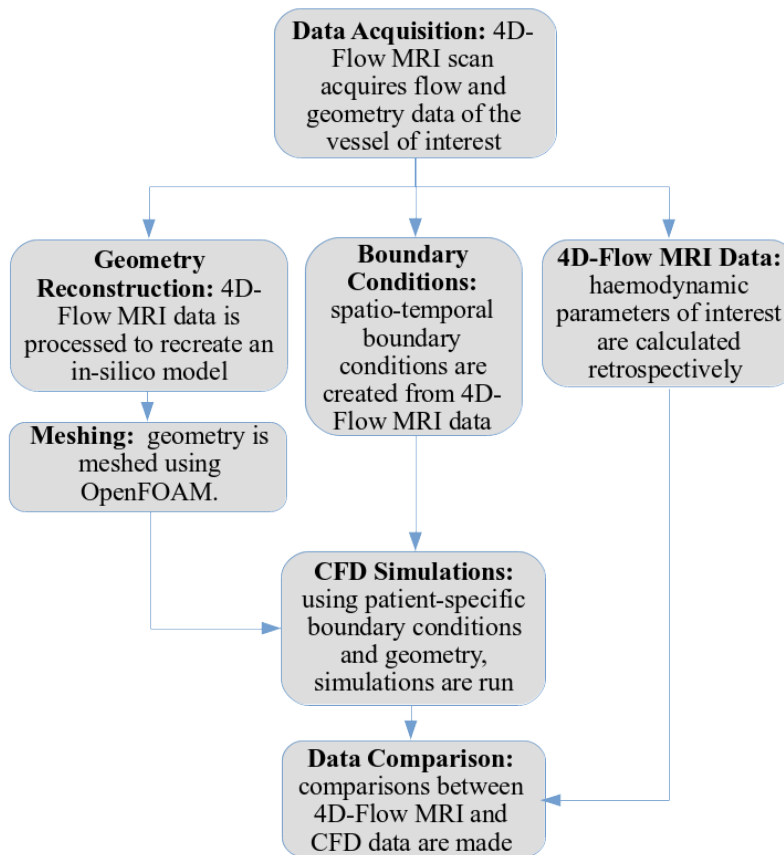


Figure 3.1. Workflow used in constructing patient-specific 4D-Flow MRI based CFD simulations.

Throughout the workflow, a conscious effort was made to use open source software where possible so that the methodology can be used at minimal cost and will be more accessible to clinicians across the globe. Although a licence is needed to use MATLAB [168], the in-house code used to process the 4D-Flow MRI images allows DICOM images from a range of MRI scanner makes and models to be read in, unlike many commercial codes, so may be of use in resource-limited situations.

Ethical approval has been given to this research by Leeds East Research Ethics Committee (18 /

YH / 0439) and Berkshire Research Ethics Committee (10 / H0505 / 100). All patient data within this thesis has been anonymised, and written and informed consent to participate has been given by all participants or parents/legal guardians where appropriate.

3.2 Data Acquisition

All patients participating in this research have undergone a 4D-Flow MRI scan to acquire phase contrast images of the thoracic aorta and the velocity flow field within it. Phase contrast images from a 4D-Flow MRI scan can be seen in Figure 3.2. A total of 12 patients were used in this research; 7 adult patients and 5 neonatal patients. Patients were eligible for inclusion in this study if they have BAV, and are suitable for a valve replacement. In the case of neonatal patients, patients with a suspected BAV were included in the study.

The adult cohort used in this research consisted of 3 RL BAV and 4 RN BAV, 5 of which experienced right handed helical flow, whilst 2 experienced left handed helical flow. All adult patients considered were yet to undergo AVR surgery. Table 3.1 shows the demographic for the 7 adult patients used within this study. Patients' data was used at difference stages of the methodology development, as a result of this and poor quality of 4D-Flow MRI data in some cases, not all patients' data was used for the full complexity workflow developed.

The neonatal patient demographic can be seen in Table 3.2. For all neonatal patients within this study, a prototype 4D-Flow MRI sequence was administered. This was a compressed sense flow-sensitive gradient-echo pulse sequence. 4D-Flow MRI data was gated retrospectively, and no respiratory motion suppression navigators were necessary due to the limited breathing motion in neonatal patients compared to the adult patients.

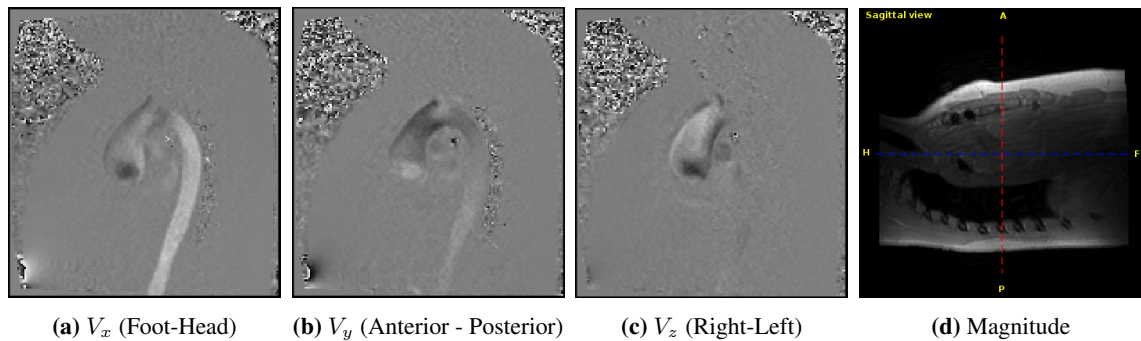


Figure 3.2. Phase contrast images through velocity encoding in the V_x , V_y , and V_z directions, and a magnitude image viewed from the sagittal plane.

The 4D-Flow MRI scans on all patients, excluding the neonatal cohort, were carried out on a 3T Magnetic Resonance system (Siemens 3.0T Trio TIM MRI). Scans were taken by medical teams of the entire thoracic aorta and the proximal supra-aortic vessels. A spatial resolution of $2mm \times 1.67mm \times 2.2mm$ and a temporal resolution of $40ms$ were used for all scans on adult patients, flip angle = 7 deg , bandwidth = $449Hz$. Three-dimensional velocity encoding was used with a sensitivity of $150 - 390cm/s$ in all directions, on a patient by patient basis, resulting in velocities higher than $150 - 390cm/s$ undergoing aliasing and presenting as a velocity going in the opposite direction.

All neonatal 4D-Flow MRI scans were acquired by medical staff on a 3T Magnetic Resonance

Patient Identifier	BAV Phenotype	Flow Direction	Age (years)	BMI	Gender
OXBAV003	RN	right	47	25.5	M
OXBAV012	RL	right	40	20.9	F
OXBAV017	RL	right	55	30.3	M
OXBAV021	RN	right	20	25	M
OXBAV022	RL	right	22	32.7	F
OXBAV071	RN	left	18	19.1	M
OXBAV102	RN	left	26	21.9	F

Table 3.1. Demographic of adult patients used within this research detailing BAV phenotype, direction of helical flow, age, Body Mass Index (BMI) and gender. (*RN=Right-Non-coronary, RL=Right-Left*).

Patient	Healthy/ BAV	Age (days)	Weight (kg)
CoRaL071	Healthy	5	4.4
CoRaL072	Healthy	3	3.0
CoRaL073	BAV	3	2.5
CoRaL074	BAV	1	2.7
CoRaL076	BAV	1	2.9

Table 3.2. Demographic of neonatal patients used within this research detailing the age (days) and weight (*kg*) of the patients.

system (Platform Software VE11c, Siemens 3.0 T PRISMA, Siemens Healthcare, Erlangen, Germany) using a spatial resolution of $1mm \times 1mm \times 1mm$ and a temporal resolution between $33.6 - 40ms$. The prototype sequence parameters used for neonatal patients were as follows: echo time = $2.68s$, repetition time = $5.1s$, flip angle = 7° , and bandwidth = $1578Hz/pz$. The images were acquired in approximately 1-2 minutes, which was dependent on the patients heart rate (average neonatal heart rate for the cohort = $120 - 150$ beats per minute).

When considering the spatial and temporal resolution of 4D-Flow MRI that is available, its use on neonatal patients must be questioned. As stated by Hofman *et al.* [169], no fewer than 6 voxels must be used to describe a vessel. When imaging neonatal patients, the number of voxels that describe the vessel is significantly closer to 6 than it is for adult patients, resulting in lower quality data being available to the researcher.

When imaging neonatal patients, it is common practice to use echocardiography as the first choice imaging technique because it is widely available to clinicians and non-invasive. For the purposes of this research echocardiography does not supply adequate flow quantification. Other imaging techniques available and commonly used include cardiac catheterisation which would provide an appropriate amount of detail about the flow. However, cardiac catheterisation carries substantially more risk as it requires ionising radiation, contrast agent, and general anaesthesia. Computed Tomography (CT) scans are also an available method of imaging neonatal patients, however it requires intravenous access, ionising radiation, and a contrast agent [43, 170–172]. With recent medical advances the life expectancy of patients with CHD is increasing, and as such the risks of exposure to Low Dose Ionising Radiation (LDIR) must be considered when studying and imaging neonatal patients. LDIR has been shown to increase the risk of cancer to the patient, in particular when the patient is young [173], whilst cumulative exposure over the patients lifetime has been shown to be associated with cancer in adults. Therefore the increasing life expectancy of those with

CHD provides more opportunity for carcinogenesis to occur [174]. Taking the risks of alternative imaging techniques into account, 4D-Flow MRI presents as the best imaging technique available.

3.3 Geometry Reconstruction

In order to combine 4D-Flow MRI data and CFD techniques to run patient-specific CFD simulations of the thoracic aorta, the aortic geometry of the patient in question must be extracted and reconstructed from 4D-Flow MRI data. A 3-Dimensional *in-silico* model for each individual patient must be created that is suitable for meshing. This can be achieved using the methodology detailed in the following paragraphs:

The 4D-Flow MRI scans produce a series of phase contrast images in the coronal, axial, and sagittal views in a DICOM format. The DICOM images are processed using in-house software written in MATLAB [168], also used by Nolte *et al.* [175] and written by Sotelo *et al.* [176, 177]. The in-house software will here-on be referred to as the *4D-Flow MRI APP*. Within the *4D-Flow MRI APP*, an angiographic image was created using the DICOM images files and the algorithm proposed by Bock *et al.* [178] that derives angiographic information from the data acquired in a 4D-Flow MRI scan without the need for additional Magnetic Resonance Angiography (MRA) scans.

With an angiographic image created, it becomes possible to extract the geometry of the blood vessel of interest by first adjusting the contrast of the images within the *4D-Flow MRI APP* to highlight the blood vessels of interest from the background tissue and vessels not of interest. Regions of the vessel with higher blood flow velocities appear brighter in the MRI images, therefore increasing the contrast causes the areas of lower velocity, such as the supra-aortic vessels and the periphery of the vessel, to be more visible. This makes the forthcoming segmentation process less complex, however also increases the need for a higher threshold in the next step. The contrast adjustment must be done on a patient-specific basis and is dependent on the flow velocities that are experienced within the vessel.

Within the *4D-Flow MRI APP*, all images have an initial contrast range of 0 – 250. In order to emphasise the thoracic aorta both limits of the contrast range can be adjusted. The impacts of adjusting the contrast range to 0 – 75 for patient CoRaL071 can be seen in Figure 3.3. It can be seen that altering the contrast range not only causes the ascending aorta to appear brighter in the image, but also makes the periphery of the vessel, and the descending aorta more clear. This is key in ensuring the vessel in its entirety is visible, and can be distinguished from the background tissue and surrounding vessels. However, the increase in contrast is applied to the entire image, meaning the vessels not of interest and background tissue also appear brighter.

A threshold is then applied universally to all 4D-Flow MRI images to remove any unwanted noise and smaller vessels from the images, leaving only the great vessels. The value of the threshold must be carefully selected; a high threshold will remove all the unwanted noise and smaller vessels, but will also remove areas of slow flow within the aorta, including a significant proportion of the descending aorta and the periphery of the vessel. This results in significant portions of the thoracic aorta having to be selected manually in the segmentation process in order to be included in the final geometry. A low threshold will keep the thoracic aorta intact but will also keep a significant proportion of the unwanted background noise and smaller vessels, which requires significant

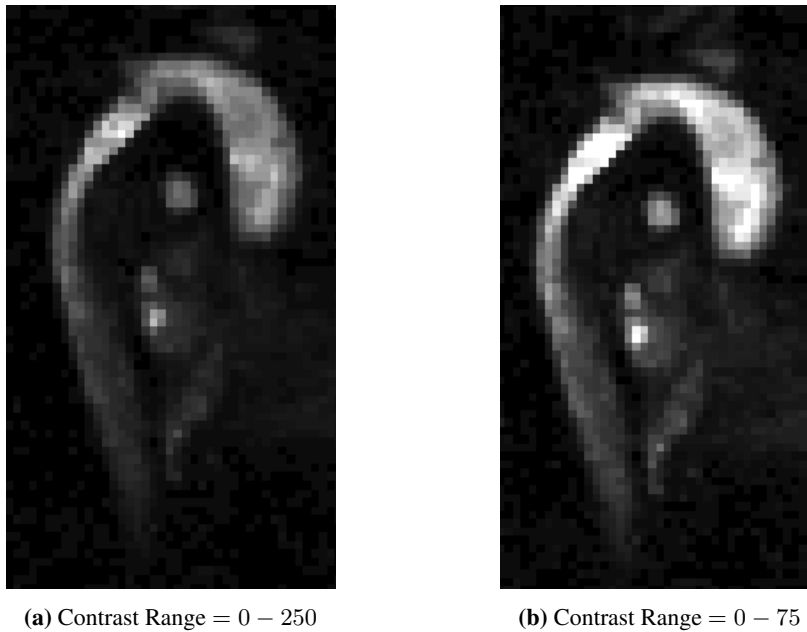


Figure 3.3. 4D-Flow MRI image of the thoracic aorta of patient CoRaL071 shown in the sagittal plane before (a) and after (b) contrast adjustment has taken place and unwanted noise and vessels have been removed.

portions of the geometry to be manually removed in the segmentation process. An inappropriate threshold will result in a large degree of manual segmentation being necessary, which may result in large levels human errors being introduced to the geometry.

Within the *4D-Flow MRI APP*, an initial threshold range of 0 – 250 is applied to all images. Both limits may be adjusted to select the option that requires the minimum amount of manual segmentation. Figure 3.4 demonstrates how applying an appropriate threshold to the images removes unwanted noise and smaller vessels, but can still result in significant manual segmentation being necessary. The sensitivity of the process is also demonstrated, indicating the level of care that must be taken with the process. As with the contrast adjustment process, the thresholding process is patient-specific and the values selected vary on a patient by patient basis.

With an appropriate threshold selected, the 4D-Flow MRI images can then be segmented in the sagittal, axial, and coronal planes using the *4D-Flow MRI APP* to highlight only the thoracic aorta. This is achieved by manually removing all traces of the vessels not of interest to this study. This results in only the thoracic aorta being present in the images (see Figure 3.5). During the segmentation process it is vital that the vessel wall is segmented correctly and accurately as the geometry and later calculations of haemodynamic parameters of interest, such as WSS, rely on this segmentation. Manual segmentation introduces a significant degree of error to the geometry reconstruction process due to uncertainties in the vessel wall location, primarily caused by low flow velocities at the periphery of the vessel.

Once the thoracic aorta has been highlighted in all 4D-Flow MRI images across all three planes, it is possible to create a 3-dimensional *in-silico* model of the vessel that can be used for patient-specific CFD simulations. This is achieved within the *4D-Flow MRI APP* by creating a tetrahedral mesh of the highlighted geometry using the iso2MATLAB toolbox within MATLAB [168]. The inlet and outlet locations are then selected so the velocity can be interpolated; the inlet location chosen is the approximate location of the aortic valve, and the outlet location selected is the fur-

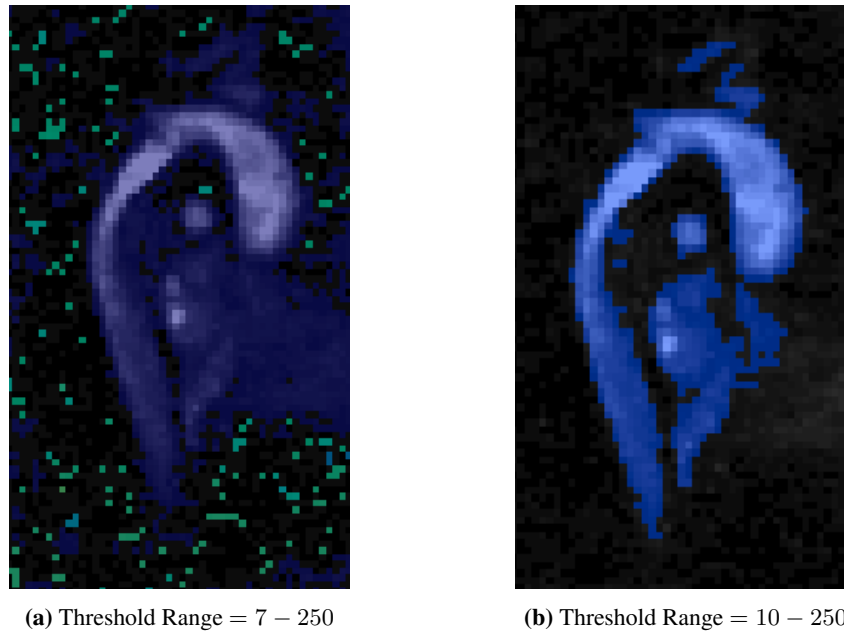


Figure 3.4. 4D-Flow MRI images of the thoracic aorta of patient CoRaL071 shown in the sagittal plane, before (a) and after (b) threshold adjustment has taken place.

these plane in the inferior descending thoracic aorta that is fully visible. This selection does not alter the geometry reconstruction nor create inlet and outlet patches, it merely provides the locations that are required for velocity interpolation to take place. The location of the inlet is an estimation as the location of the aortic valve is not indicated clearly in the 4D-Flow MRI scans. As such, the inlet location within all CFD simulations is subject to human error, which may effect the results recorded. Once the locations of the inlet and outlet are selected, cubic interpolation is used to calculate the velocity vector at each mesh node. From the interpolated velocity vector values, it is possible to retrospectively calculate a series of haemodynamic parameters such as WSS, OSI, vorticity, helicity, energy loss, and kinetic energy. The *4D-Flow MRI APP* produces files for each 4D-Flow MRI time-step in Visualisation Toolkit for unstructured grids format (.vtu), which allows the calculated haemodynamic parameters and the reconstructed geometry to be visualised throughout an average cardiac cycle of the patient. Although the haemodynamic parameters are calculated at each time-step recorded by the 4D-Flow MRI data, the reconstructed geometry is based only on 4D-Flow MRI images taken during peak systole, so are the maximum dimensions of the thoracic aorta.

The physical inlet and outlet patches of the *in-silico* geometry must be created before it is suitable for use in subsequent CFD simulations. This is achieved by first creating flat surfaces at the inlet and outlet locations previously determined before velocity interpolation occurs. The open-source software, OpenSCAD [179], allows flat surfaces to be created that are suitable for patches to be applied to at a later stage of the workflow. Figure 3.6a demonstrates the *in-silico* model that is produced from the *4D-Flow MRI APP* prior to the physical inlet and outlet surfaces being created, whilst Figure 3.6b shows the *in-silico* model once the inlet and outlet planes have been created using OpenSCAD. From OpenSCAD, a single stereolithography file (.stl) is produced that includes the correct geometric inlet, outlet, and aortic wall locations.

The locations created using OpenSCAD must be converted to patches to which boundary conditions can be applied within OpenFOAM. Using the open-source software NETGEN [180], this

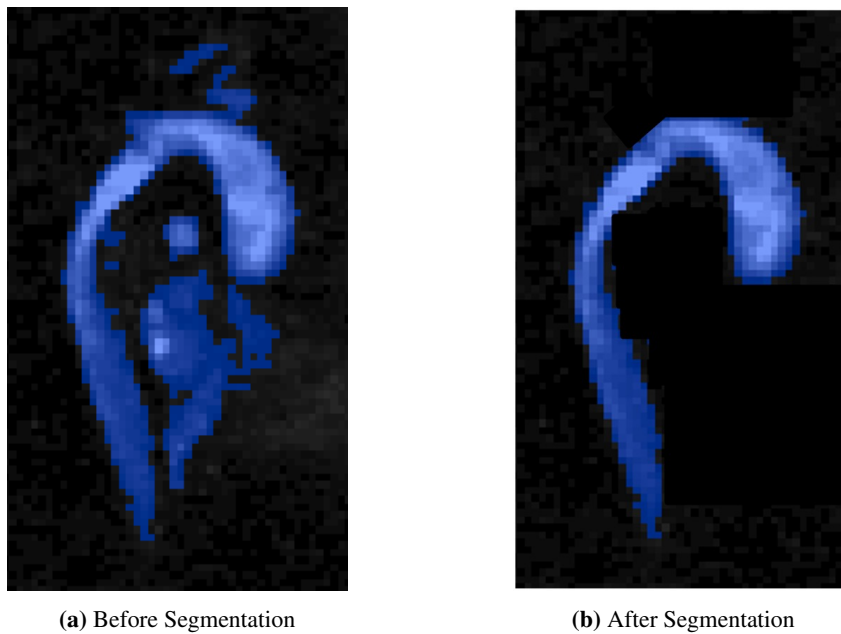


Figure 3.5. 4D-Flow MRI images of the thoracic aorta of patient CoRaL071 shown in the sagittal plane before (a) and after (b) segmentation has taken place to extract the thoracic aorta only.

is achieved using the builtin function whereby individual surfaces can be created based on the angle between the cells. Due to the significant angles between the inlet and outlet and the aorta wall, NETGEN creates three individual surfaces from the initial stereolithography file shown in Figure 3.6b which can be saved as separate stereolithography files corresponding to each patch. The individual stereolithography files can then be edited to include the desired patch names that correspond to the boundary condition names. The individual files are then collated into one, to create a stereolithography file of the patient-specific geometry that includes pre-allocated patches. The final reconstructed geometry can be seen in Figure 3.7 for the neonatal patient CoRaL071. It can be clearly seen that in a neonatal patient the vasculature that surrounds the thoracic aorta is intricate in nature and in areas it is challenging to distinguish the various blood vessels from each other. This can be compared to the reconstructed geometry of the adult patient OXBAY012, seen in Figure 3.8 where the edges of the vessels are significantly clearer, and vessels can be distinguished from each other.

In both Figure 3.7 and Figure 3.8, the thoracic and pulmonary arteries can be seen clearly, whilst the smaller vessels such as the supra-aortic vessels are not immediately apparent. The proximal supra-aortic vessels are more visible for an adult patient than for a neonatal patient, where they cannot be segmented to an appropriate accuracy level. It was recommended by Hofman *et al.* [169] that no fewer than 6 voxels be used to describe a vessel diameter. Based on the ascending aortic diameters of the neonatal cohort ($8.60\text{mm} \pm 0.83\text{mm}$) and the spatial resolution of $1\text{mm} \times 1\text{mm} \times 1\text{mm}$, it is clear that vessels that are significantly smaller than the ascending aorta will be described by too few voxels. Due to the number of voxels and the low flow velocities experienced within them, the supra-aortic vessels of neonatal patients can not be segmented from the background noise of the 4D-Flow MRI scan accurately enough for analysis. The supra-aortic vessels were therefore neglected in all initial simulations of neonatal patients.

Although the brachiocephalic artery is detectable for an adult patient, the left common carotid and left subclavian arteries are more difficult to discern. Due to the lack of consistency regarding the

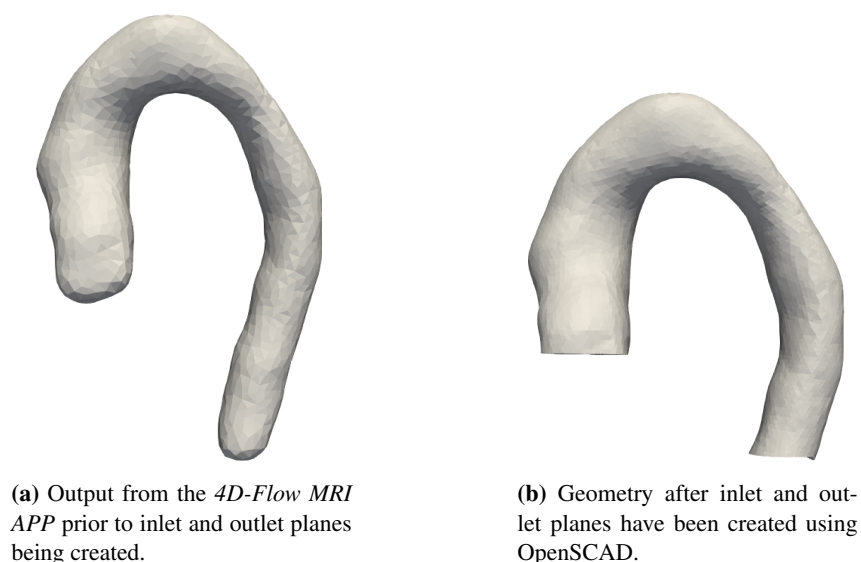


Figure 3.6. Geometry reconstruction results before (a) and after (b) OpenSCAD is used to create planes for the inlet and outlet.

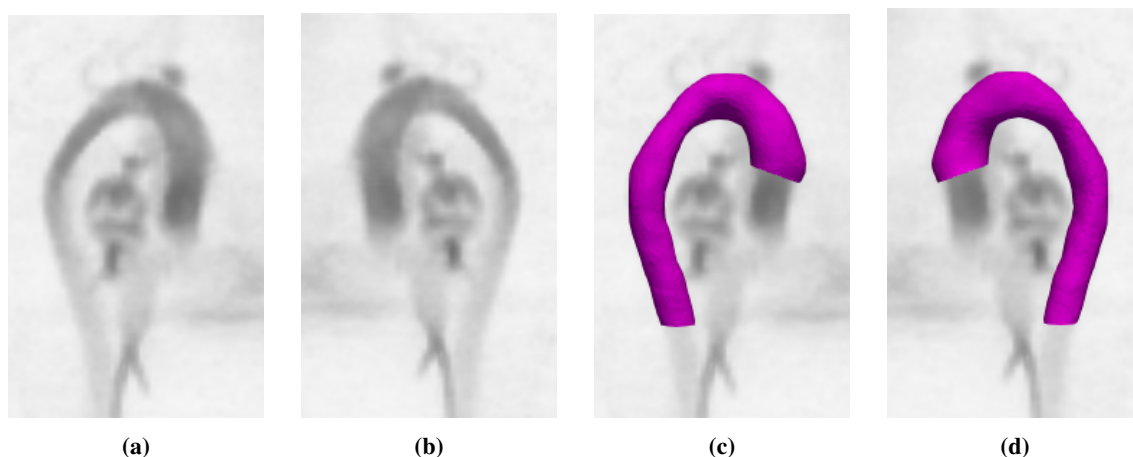


Figure 3.7. 4D-Flow MRI scan data of the thoracic aorta and proximal supra-aortic vessels ((a) and (b)), and the reconstructed *in-silico* model of the thoracic aorta, overlaid on 4D-Flow MRI data ((c) and (d)) of the neonatal patient, CoRaL071.

visibility of the supra-aortic vessels across the adult patient cohort, it was also decided to neglect the vessels for simplicity. However, the choice to not include the supra-aortic vessels limits the study as it excludes three outlets for the blood flow. This will alter the haemodynamics within the thoracic aorta, principally artificially increasing the velocities in the descending aortas due to the increased volumetric flow rate that will be experienced within them. The percentage of flow that leaves the thoracic aorta through the supra-aortic vessels is also unknown, as the cross sectional areas of the supra-aortic vessels is unable to be calculated as a result insufficient voxels and low flow velocities. A consequence of this is that it is not possible to correct the volumetric flow rate at the inlet to account for the flow that would otherwise leave the system through the supra-aortic vessels. It was suggested by Middleman [59] that approximately 5% of the inflow volume leaves through each of the supra-aortic vessels. However, these values are contradicted by Caballero & Laín [57], where it was suggested that 9.5% of the inflow volume leaves through the brachiocephalic artery, 5% through the left common carotid artery, and 6.5% through the left subclavian artery. The suggested volumetric flow rates apply only to adult patients, and are only

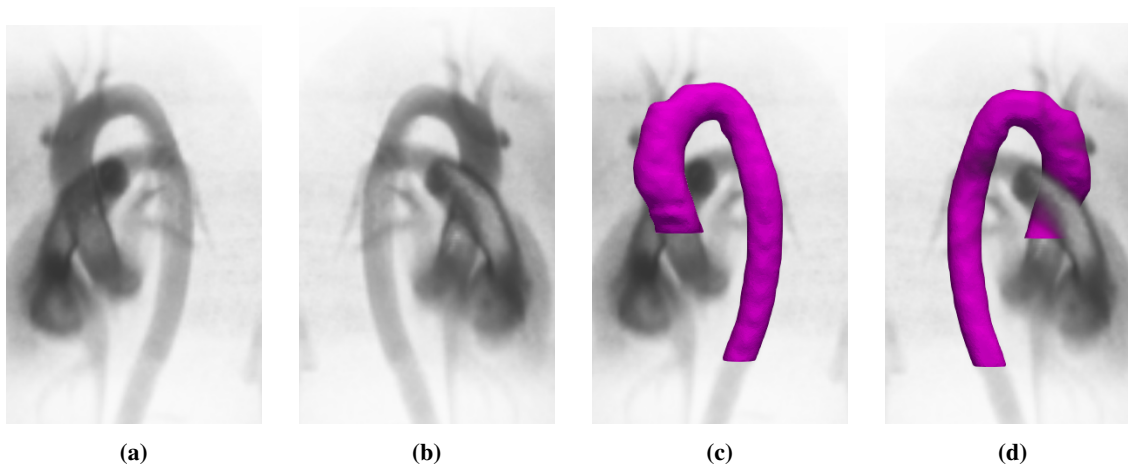


Figure 3.8. 4D-Flow MRI scan data of the thoracic aorta and proximal supra-aortic vessels ((a) and (b)), and the reconstructed *in-silico* model of the thoracic aorta, overlaid on 4D-Flow MRI data ((c) and (d)) of the adult patient, OXBAV012.

approximations. It has been suggested that for neonatal patients the percentage of the flow that leaves through the head and neck vessels is as high as 50% as a result of neonatal patients having proportionally larger heads than adults. As there are no commonly accepted percentages available for neonatal patients, adjusting the inlet volumetric flow rate to account for flow leaving through the supra-aortic vessels is not a feasible approach for a methodology that is intended to be suitable for patients of all ages.

Although adjusting the inlet volumetric flow rate would counter the artificially increased velocities within the descending aorta, it would also cause reduced velocities within the ascending aorta. It was decided that the ascending aorta is of more interest to clinicians than the descending aorta, therefore the inlet boundary condition was not adjusted to account for neglecting the supra-aortic vessels.

It is known that neglecting the supra-aortic vessels will cause incorrect haemodynamics to be predicted in the thoracic aorta by the patient-specific CFD simulations. Therefore, an attempt to include the supra-aortic vessels was made for both a neonatal patient and multiple adult patients to quantify the errors within the haemodynamics that can be attributed to neglecting the additional three outlets. In patients where the supra-aortic vessels are included, patient-specific outflow conditions are determined.

3.3.1 Human Error in Geometry Reconstruction

The geometry reconstruction process described in Section 3.3 is subject to significant human error caused by the large amount of approximation that is required when interpreting the 4D-Flow MRI images. The expertise of a medical professional when interpreting the images would decrease the human error involved in the process, however for scope of this research project this is not a feasible option. In an attempt to quantify human error in the geometry reconstruction process, the segmentation process was repeated five times on patient CoRaL071. From each geometry reconstruction attempt, a new *in-silico* geometry and corresponding patient-specific boundary conditions were created. The errors that were present in terms of geometry, velocity, and volumetric flow rate from the manual segmentation process were recorded. How these errors translated into the inlet conditions that were subsequently applied to patient-specific CFD simulations was also monitored.

The diameters of a plane in the ascending aorta for all five geometry reconstruction attempts can be seen in Table 3.3. Noticeable variation can be seen between geometry reconstruction attempts, with a mean and standard deviation of $10.77 \pm 0.3856 \text{ mm}$. In addition to the variation in the vessel diameter, the average velocity magnitude over the plane of interest in the ascending aorta varies also considerably at systole and diastole ($0.3497 \pm 0.01305 \text{ m.s}^{-1}$ and $0.02442 \pm 0.002154 \text{ m.s}^{-1}$ respectively). These errors accumulate in significant variation in the volumetric flow rate in the ascending aorta at both systole and diastole ($3.535E - 05 \pm 8.232\%$ and $2.987E - 07 \pm 49.42\%$ respectively). This clearly indicates that there are errors being introduced into the geometry used for the subsequent CFD simulations, and also shows that the 4D-Flow MRI velocity data to which CFD data will be compared is subject to human errors, and as such, the 4D-Flow MRI data should be treated with caution. It also raises questions as to how meaningful any clinical conclusions drawn from the 4D-Flow MRI data can be, when there are significant errors present in the data-set due to the geometry reconstruction.

Attempt	Diameter (<i>m</i>)	Systole		Diastole	
		Average Velocity Magnitude (<i>m.s</i> ⁻¹)	Volumetric Flow Rate (<i>m</i> ³ <i>s</i> ⁻¹)	Average Velocity Magnitude (<i>m.s</i> ⁻¹)	Volumetric Flow Rate (<i>m</i> ³ <i>s</i> ⁻¹)
1	0.01042	0.3416	2.987E-05	0.02857	1.808E-08
2	0.01072	0.3541	3.506E-05	0.02276	2.847E-07
3	0.01147	0.3285	3.805E-05	0.02287	3.727E-07
4	0.01085	0.3599	3.660E-05	0.02352	3.992E-07
5	0.01041	0.3643	3.719E-05	0.02436	4.188E-07

Table 3.3. Diameter, average velocity magnitude, and volumetric flow rate at systole and diastole across a slice in the ascending aorta for the five geometry reconstruction attempts on patient CoRaL071.

The variations in geometry and velocity result in the spatially averaged volumetric flow rate, determined from the 4D-Flow MRI data, at the inlet plane varying considerably with each geometry reconstruction attempt at both systole (Figure 3.9a) and diastole (Figure 3.9b). The variations present demonstrate the importance of ensuring the segmentation process is executed with care and precision. Any variations that are present in the volumetric flow rate at the inlet of the 4D-Flow MRI data will be translated directly into any subsequent patient-specific CFD simulations.

The differences in velocity flow patterns at diastole in the ascending aorta between the segmentation attempts of the thoracic aorta can be seen in Figures 3.10 and 3.11. It is also clear that the changes in vessel diameter and geometry are notable between geometry reconstruction attempts. From the differences in the vessel wall location, it is clear that using WSS as a haemodynamic marker is inappropriate, and will produce inaccurate results from both 4D-Flow MRI data and the subsequent CFD simulations.

3.4 Meshing

With the geometry constructed and the patches created, the domain must be meshed before use in CFD simulations. Multiple open-source meshing methods were tested to ensure the best approach was used: using Netgen [180] an unstructured tetrahedral mesh was created, a structured hexahedral mesh was created using the tool cfMesh [181], and a structured hexahedral mesh was created

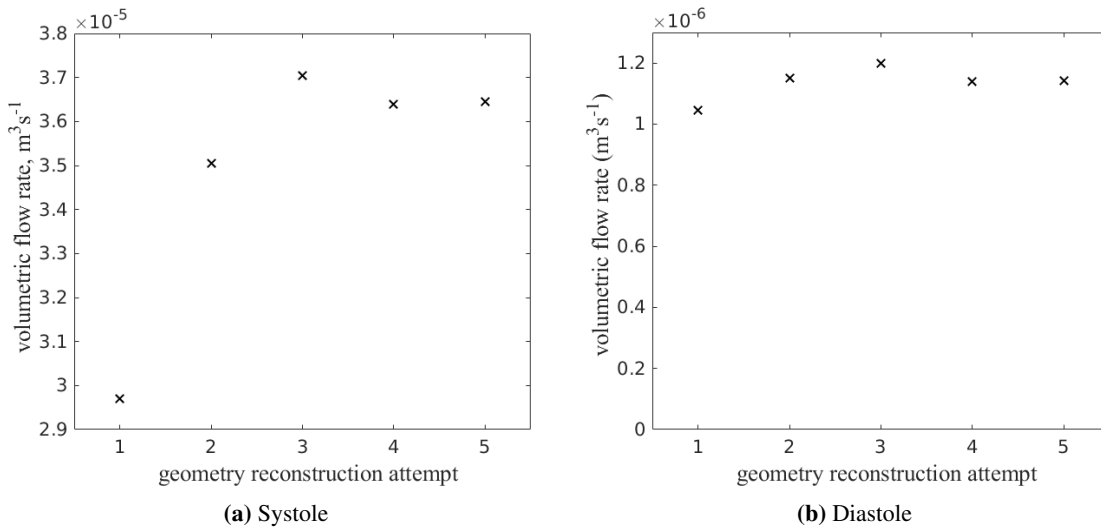


Figure 3.9. Spatially averaged volumetric flow rate ($\text{m}^3 \text{s}^{-1}$) across the inlet for each of the five geometry reconstruction attempts of patient CoRaL071 at diastole, calculated from 4D-Flow MRI data.

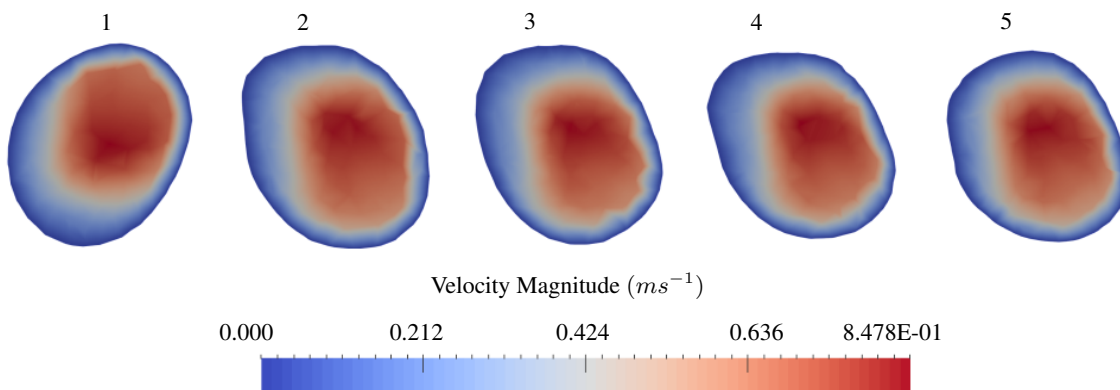


Figure 3.10. Velocity magnitude (ms^{-1}) contours, determined from 4D-Flow MRI data, over the inlet plane at systole from each geometry reconstruction attempt of patient CoRaL071.

using the OpenFOAM utility, *snappyHexMesh*. Before CFD simulations were run and results collected for analysing, a mesh sensitivity study was undertaken, see Section 3.4.4. The steps taken for each meshing method attempted are outlined below.

3.4.1 Netgen

As stated in Section 3.3, Netgen [180] was used to create and assign patches to the inlet, outlet, and aorta wall in the 3-dimensional *in-silico* model of the thoracic aorta. Once the patches were created and assigned to a surface, the domain was meshed and an unstructured tetrahedral mesh was created (see Figure 3.12a). The mesh created using Netgen had no areas of refinement or boundary layers, and was created by setting a maximum element size which was then applied over the entire domain. As no regions of refinement were created and the mesh was unstructured tetrahedral cells, this meshing method was deemed inappropriate.

3.4.2 cfMesh

Using the open source tool cfMesh [181], a structured hexahedral mesh that uses tetrahedral cells in the transition regions between different hexahedral element sizes was created (see Figure 3.12b).

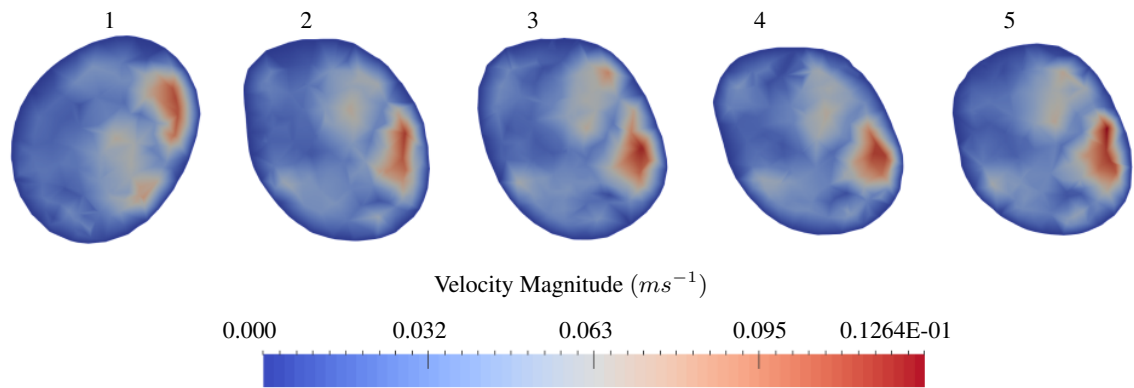
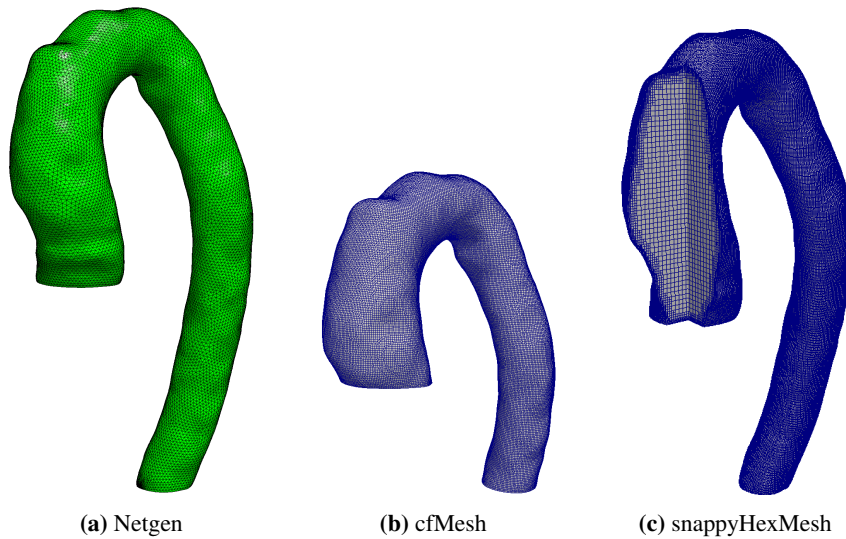


Figure 3.11. Velocity magnitude ($m s^{-1}$) contours, determined from 4D-Flow MRI data, over the inlet plane at diastole from each geometry reconstruction attempt of patient CoRaL071.

Although regions of refinement were created close to the vessel walls and the mesh was constructed with suitable cells, the introduction of additional software would increase the complexity of the methodology, limiting its potential use by clinicians as a predictive tool. The additional complexity was deemed unnecessary and the meshing method was not taken any further.

3.4.3 snappyHexMesh

The final meshing strategy created a background mesh using the *blockMesh* utility within OpenFOAM, consisting of hexahedral cells with an aspect ratio of approximately 1. Using the *snappyHexMesh* utility within OpenFOAM, surface features are then extracted from the stereolithography file of the reconstructed geometry with patches, seen in Figure 3.6b, and the cells of the initial background mesh are split and refined near the newly defined surface features. Two levels of refinement are used. Cells outside of the desired region are removed, leaving only the refined cells inside the vessel. The cells' vertex points are then snapped to the surface of the stereolithography file leaving a smooth surface. Finally, additional hexahedral cells are added near the surface to create a boundary layer. The resulting mesh is a structured mesh created with hexahedral cells with two layers of refinement, and a refinement region near the surfaces as seen in Figure 3.12c. For all CFD simulations in this study, the *blockMesh* and *snappyHexMesh* utilities with OpenFOAM have been used.



(a) Netgen

(b) cfMesh

(c) snappyHexMesh

Figure 3.12. Potential meshing options explored; (a) shows the unstructured tetrahedral mesh created using Netgen, (b) shows the structured mesh created using cfMesh, (c) shows the structured mesh produced through the snappyHexMesh.

3.4.4 Mesh Independence

3.4.4.1 Steady State Mesh Independence

A mesh independence study was conducted to ensure that all results from steady state patient-specific CFD simulations are independent of the mesh density being used. The meshes used for the mesh independence study were created using OpenFOAM's *blockMesh* and *snappyHexMesh* utilities as described in Section 3.4.3. Steady state, laminar simulations were run using the *simpleFoam* solver in OpenFOAM. A plug profile with a magnitude equal to the spatially averaged systolic velocity magnitude from 4D-Flow MRI data was applied to the inlet patch. Blood was assumed to be a Newtonian, incompressible, and homogeneous fluid. Five grids of varying density were tested, each increasing the number of elements within the initial *blockMesh* by 10% in the x , y and z directions with Mesh 1 being the coarsest mesh and Mesh 5 being the finest, see Table 3.4, the y -plus value of all meshes was approximately 1 or less. The velocity magnitude was plotted along the x -axis (Figure 3.13a) and z -axis (Figure 3.13b) across a plane in the mid-ascending aorta and was recorded for each mesh. It can be concluded from Figure 3.13 that Mesh 3, corresponding to 1,136,155 elements is a suitable mesh to use for all further steady state simulations as it accurately resolves the velocity and differs from Mesh 4 by an average of only 2.79% in the ascending aorta. This mesh was selected as it is the coarsest possible mesh that shows convergence, allowing computational resources and time to be kept to a minimum.

Mesh	<i>blockMesh</i> X divisions	<i>blockMesh</i> Y divisions	<i>blockMesh</i> Z divisions
1	68	116	189
2	75	129	210
3	83	142	231
4	90	155	252
5	98	168	273

Table 3.4. Number of divisions in the x , y , and z directions of the *blockMesh* used in the mesh independence studies.

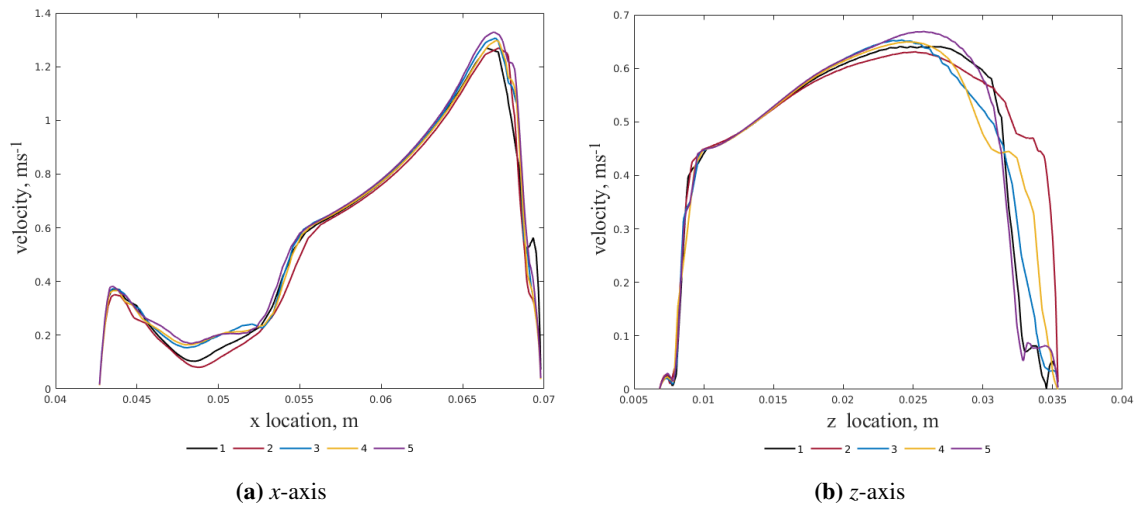


Figure 3.13. Mesh independence study in the ascending aorta conducting for steady-state simulations with a plug profile on adult patient OXBV012.

3.4.4.2 Neonatal Transient Mesh Independence

A mesh independence study was also conducted for transient simulations of a neonatal patient with patient-specific boundary conditions at the inlet, detailed in Section 3.5.3. Simulations of the full cardiac cycle were run, assuming blood was Newtonian, incompressible, and a homogeneous fluid (see Section 3.6 for the density and viscosity assumed), with the $k-\omega$ SST turbulence model incorporated. Five grids of varying density were used (see Table 3.4) the y -plus value of all meshes was approximately 1 or less, and the velocity magnitude recorded and plotted along the x -axis and z -axis for an axial plane in the mid-ascending aorta at peak systole when the highest velocities will be experienced within the domain. The velocity contours across the plane used for the mesh convergence study alongside the location of x -axis and z -axis. The results of the transient mesh convergence can be seen in Figure 3.14 for the neonatal patient CoRaL071.

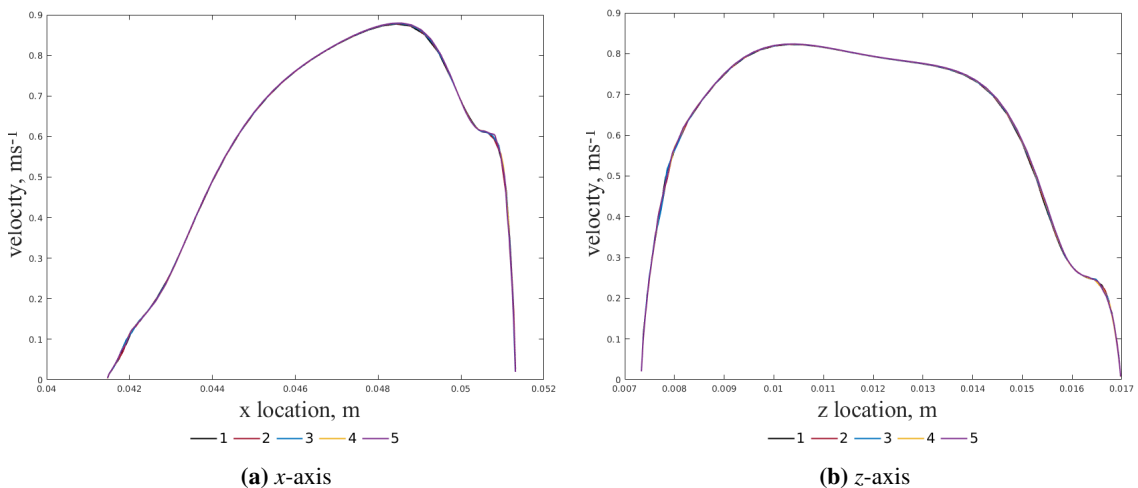


Figure 3.14. Mesh independence study monitoring velocity magnitude across the x -axis and z -axis over a plane in the mid-ascending aorta for neonatal patient CoRaL071.

It is clear that along both the x - and z -axis, the mesh densities used are not impacting the flow field and are in excellent agreement. From the results presented in Figures 3.14 and 3.15, it can be taken that the coarse meshing strategy (mesh 1), corresponding to 2,099,970 elements in

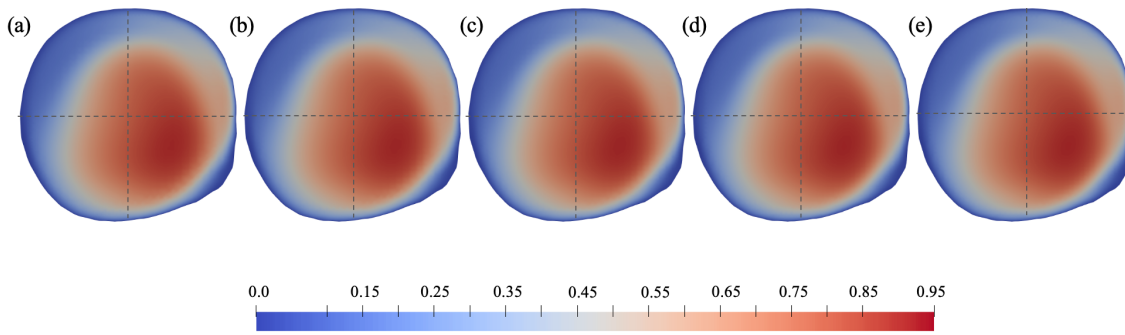


Figure 3.15. Neonatal transient mesh independence study showing velocity magnitude contours over a slice in the mid-ascending aorta. Dashed lines represent x and z axis' used to plot velocity data.

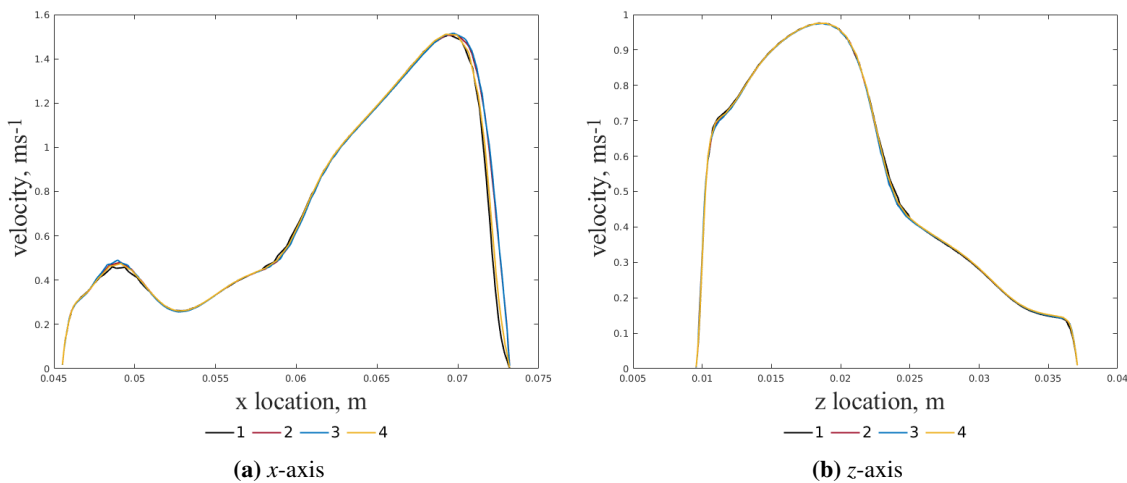


Figure 3.16. Mesh independence study monitoring velocity magnitude across the x - and z axis over a plane in the mid-ascending aorta for adult patient OXBVA012.

patient CoRaL071, is appropriate for the neonatal patients being considered within this research. However, as the neonatal patients' vessels are considerably smaller than those of the adult patients, the mesh density must also be investigated in adult vessels.

3.4.4.3 Adult Transient Mesh Convergence

A mesh convergence study was conducted on an adult patient (OXBVA012) with the supra-aortic vessels included and transient simulations were run with spatio-temporal patient-specific inlet conditions and outflow conditions applied to the outlets. Blood was assumed to be Newtonian, incompressible, and homogeneous (see Section 3.6 for density and viscosity of fluid). The $k - \omega$ SST turbulence model was incorporated into the model. Four grids of varying density (meshes 1-4 in Table 3.4) were used, the y -plus value of all meshes was approximately 1 or less, and the velocity magnitude along the x - and z -axis' across a plane in the mid-ascending aorta at peak systole were plotted, the location of which are shown in Figure 3.17. The results of the mesh convergence study can be seen in Figures 3.16 and 3.17. It is clear that the velocity magnitude is not being impacted by the mesh densities selected and the results are in excellent agreement. Based on the results from Figures 3.13 and 3.16, mesh 3 was selected for use for all simulations of adult patients as this mesh has been shown to produce results independent of mesh density for both steady state and transient results.

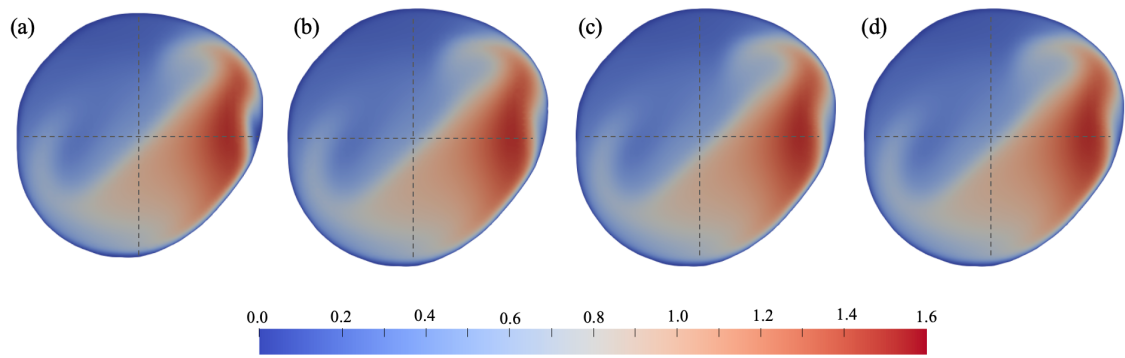


Figure 3.17. Adult transient mesh independence study showing velocity magnitude contours over a slice in the mid-ascending aorta. Dashed lines represent x and z axis' used to plot velocity data.

3.5 Boundary Conditions

3.5.1 Steady-state Plug Flow

To run patient-specific simulations, an appropriate boundary condition for the inlet must be created that accurately replicates the aortic valve. The inlet was initially assumed to be a constant volumetric flow rate in the positive y direction (a plug profile). This was determined from 4D-Flow MRI data using the spatially averaged velocity in the y direction at the inlet at each individual discrete time-step and the cross-sectional area of the inlet patch. The OpenFOAM boundary condition *flowRateInletVelocity* was utilised to implement the plug profile. Figures 3.18 and 3.19 demonstrate the steady-state plug flow boundary conditions applied to the inlet patch for the five neonatal patients at peak systole and the corresponding 4D-Flow MRI data from which the boundary conditions are calculated. The inlet boundary conditions shown in Figures 3.18 and 3.19 are a large simplification of the physical inlet condition; it can be seen that the use of a constant volumetric flow rate at the inlet produces a poor approximation of the 4D-Flow MRI data at the aortic valve at systole. It is also evident that the calculated inlet conditions provide a marginally better approximation to patients with TAV than BAV due to the highly eccentric flow profile that is present with BAV. Figures 3.18 and 3.19 show that to accurately model the haemodynamics in the thoracic aorta, spatio-temporal patient-specific boundary conditions must be incorporated at the inlet, as suggested by Youssefi *et al.* [74].

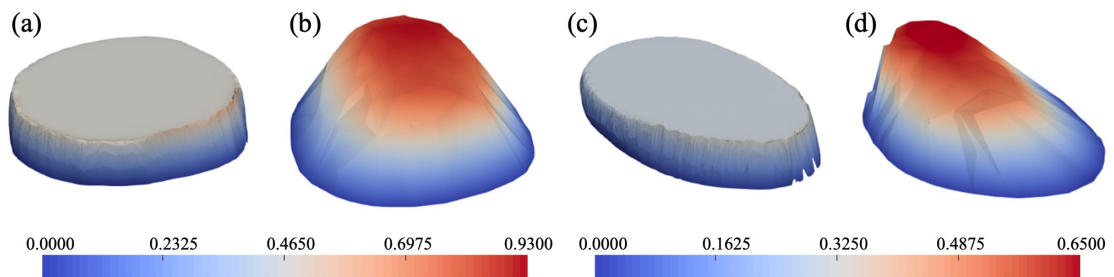


Figure 3.18. Velocity magnitude ($m.s^{-1}$) contours of the inlet boundary condition for neonatal patients with a TAV (CoRaL071 and CoRaL072) at systole, (a) and (c) demonstrate the boundary conditions applied to CFD simulations, whilst (b) and (d) demonstrate the boundary conditions found from 4D-Flow MRI data.

Initial simulations were run using the simplified steady-state plug profile inlet boundary condition, the outlet was set to a zero pressure boundary condition, the aortic walls are assumed to be rigid and a no-slip condition was applied.

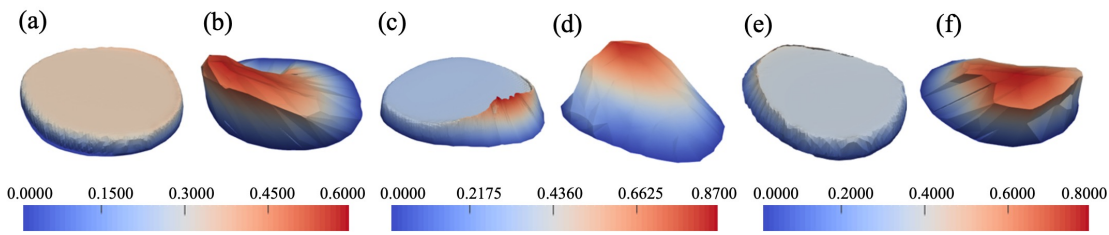


Figure 3.19. Velocity magnitude ($m.s^{-1}$) contours of the inlet boundary conditions for neonatal patients with BAV (CoRaL072, CoRaL074, and CoRaL076) at systole, (a), (c), and (e) demonstrate the boundary conditions applied to CFD simulations, whilst (b), (d), and (f) demonstrate the boundary conditions found from 4D-Flow MRI data.

3.5.2 Pulsatile Flow

Building on the steady state plug flow simulations, the inlet boundary conditions must be made more physiologically accurate, primarily ensuring that the cardiac cycle in its entirety is modelled. In order to replicate the full cardiac cycle and implement boundary conditions at the inlet that vary temporally, a pulsatile inlet condition must be incorporated in the numerical model. As the cardiac cycle is patient specific, the temporal variation of the inlet conditions must also be patient-specific. The temporal variation of the CFD model is dependent on the temporal variation of the 4D-Flow MRI scan, in which the cardiac cycle is detailed by approximately 20 discrete timesteps. Due to the coarse temporal resolution of the 4D-Flow MRI data, the flow data from which the inlet boundary condition for numerical simulations are calculated are only available at set increments of time throughout the cardiac cycle. A pulsatile inlet condition was incorporated into the numerical models and combined with the plug inlet condition. This was achieved by updating the magnitude of the plug profile at times that corresponded to the 4D-Flow MRI time-steps to match the 4D-Flow MRI data, and implemented in OpenFOAM using the *tableFile* boundary type.

Despite being an improvement to the steady state plug flow boundary conditions previously implemented, the temporal variation applied is discrete and not a continuous variation. A continuous variation would provide a more physiologically accurate inlet condition and better replicate the cardiac cycle. The spatial variation across the aortic valve is also not accounted for with this implementation as a plug profile is utilised. Using a plug profile does not replicate the flow profile from the aortic valve correctly and is not patient-specific, as discussed by Youssefi *et al.* [74] and shown by Figures 3.18 and 3.19. For all numerical simulations with a pulsatile plug profile incorporated, three cardiac cycles were run and results taken from the last cycle modelled.

The outlet was set to a zero pressure boundary condition, the aortic walls are assumed to be rigid and a no-slip condition was applied.

3.5.3 Spatio-Temporal Variations

In order to model a more physiologically accurate flow profile at the aortic valve, an inlet boundary condition that varies spatially as well as temporally must be incorporated into the numerical models. Implementing an inlet boundary condition that is spatially and temporally variable opens up the possibility of using the methodology detailed in this Chapter to predict haemodynamics in the thoracic aorta by modelling a range of BAV phenotypes and the various AVR treatment options. For the purposes of fully delineating the methodology used to create the spatio-temporal patient-specific inlet conditions implemented in the numerical model, only images of patient CoRaL071

from the neonatal cohort will be detailed when discussing the methods used.

Alongside increasing the complexity of the inlet boundary condition, the locations of the inlet patches were re-evaluated and new locations selected such that they were no longer parallel to the x -axis. Implementing an inlet that is parallel to the x -axis is nonphysical as the aortic valve sits at an angle within the ascending aorta. The angle of the inlet was altered so it was normal to the centre-line of the vessel, and was aligned with the angle at which the aortic valve sits within the thoracic aorta. The new location and angle of the inlet plane can be seen in Figure 3.20.

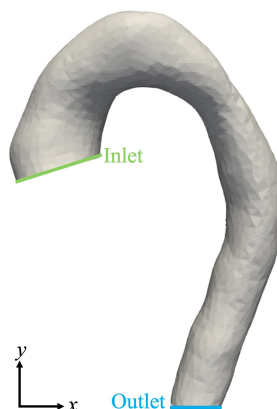


Figure 3.20. The revised location of the inlet plane.

To create inlet boundary conditions that are spatially and temporally patient-specific, the volumetric flow rate at each 4D-Flow MRI data-point across the inlet plane must be measured at each time-step. This can be seen in Figure 3.21 for patient CoRaL071. Figure 3.21 shows that the flow being ejected over the systolic phase of the cardiac cycle ($t = 2 - 4$) is approximately central, indicating a TAV. It is also clear that the plug profile used previously is an inadequate approximation of the flow profile present at all stages of the cardiac cycle as there is considerable non-uniformity in the flow rate across the inlet plane at and between each time-step, notably across the systolic phase of the cardiac cycle. There are high velocity gradients present across the inlet plane, both spatially and temporally. In order to replicate the flow profiles found in 4D-Flow MRI data at the aortic valve in CFD simulations, two approaches were tested to find the most suitable method that modelled the flow patterns correctly throughout the cardiac cycle.

3.5.3.1 Interpolation of 4D-Flow MRI data

The first method tested to implement spatio-temporal patient-specific inlet conditions was based on interpolation and mapping of the 4D-Flow MRI data. The mesh used in the CFD simulations was first created and the location of the cell centres across the inlet plane extracted. The 4D-Flow MRI inlet data shown in Figure 3.21 was then interpolated using cubic spline interpolation and mapped onto the cell centre locations of the CFD mesh at each individual time-step using in-house code written in MATLAB [168], making use of the *griddata* function. Figure 3.22 shows the volumetric flow rates mapped to the cell centres at the inlet of the CFD mesh through cubic spline interpolation of the 4D-Flow MRI data. The cell centre data at each time-step was then applied to the inlet plane of the numerical model in OpenFOAM using lookup tables to create a spatio-temporal patient-specific inlet condition that updates at times corresponding to 4D-Flow MRI time-steps.

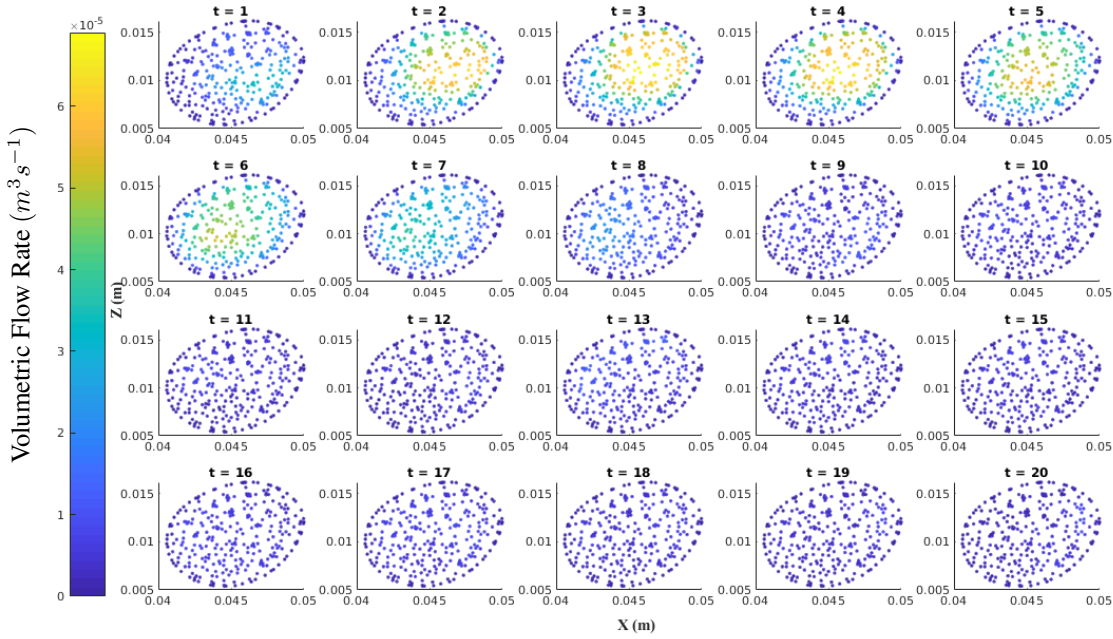


Figure 3.21. 4D-Flow MRI data points from the inlet coloured by volumetric flow rate (m^3s^{-1}) at all time-steps of the cardiac cycle for patient CoRaL071, t = time-step, where $t = 0$ corresponds to $T = 0s$ and $t = 19$ corresponds to $T = 0.5263s$, Each time-step corresponds to $\Delta T = 0.0277s$, $t = 3$ is peak systole; $t = 20$ is late diastole.

Although this method produces spatio-temporal patient-specific inlet boundary conditions, the temporal variation is discrete and matches the temporal resolution of the 4D-Flow MRI scan data. This method of creating patient-specific spatio-temporal boundary conditions for the inlet produces a text file for each time-step with the volumetric flow rate data for individual cell centres in the mesh, which can be called on during the course of the CFD simulation to reproduce a flow profile that is patient-specific at the inlet at each time-step. A significant limitation of this approach is the size of the text files produced from the interpolation. As the data was mapped onto the cell centres, the size of the files depended on the mesh density. Using the mesh density determined in Section 3.4.4 resulted in large data-sets at each time-step, slowing down the simulation and increasing the computational resources required. This method is also limited by the need to have created the mesh being used in the CFD simulations prior to creating the boundary conditions. Any change in the mesh therefore requires the boundary conditions to be updated as they would no longer be compatible. This results in a lengthier and more complex workflow which, when considering the potential application of the predictive tool, becomes less accessible to clinicians.

3.5.3.2 Curve Fitting

The second approach to recreating a spatio-temporal patient-specific inlet boundary condition created a surface fit of the 4D-Flow MRI data, which was then applied to the inlet patch of the *in-silico* model. The surface fit created is a function of x and z such that the volumetric flow rate will vary spatially with the coordinates of the cell centres of the CFD mesh. It must also be a function of the time, allowing the temporal variation of the cardiac cycle to be continuous rather than discrete. Using 4D-Flow MRI data, such as that in Figure 3.21, the spatio-temporal function was calculated from the volumetric flow rate data at the inlet plane.

A function that replicated the spatial variations of the volumetric flow rate at each 4D-Flow MRI

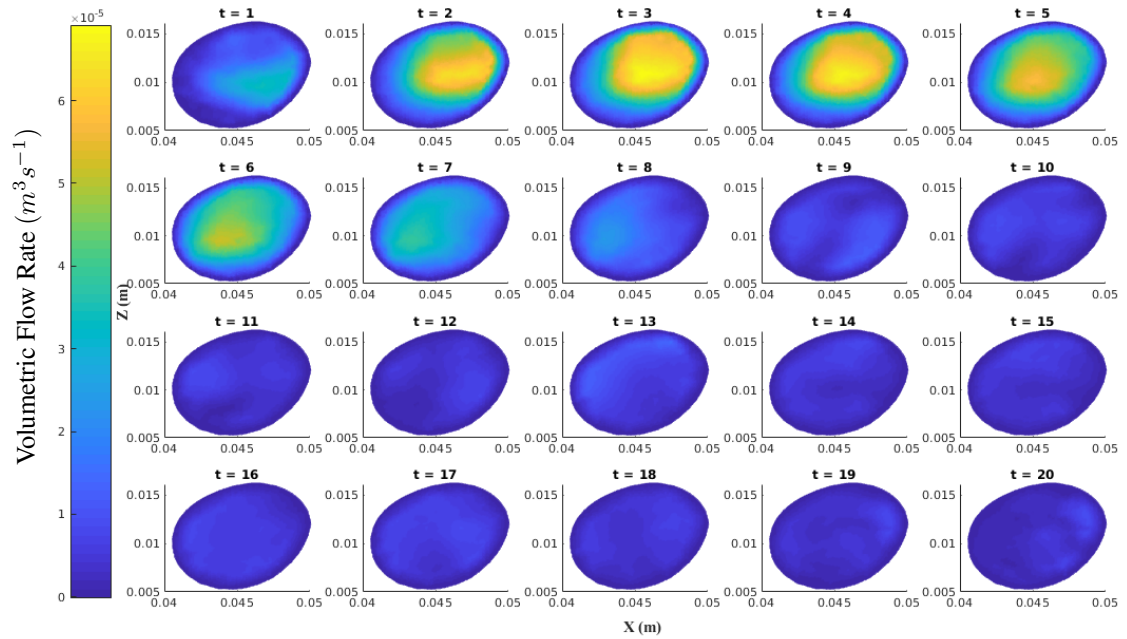


Figure 3.22. The cubic interpolation of the 4D-Flow MRI volumetric flow rate ($m^3 s^{-1}$) data, mapped onto the cell centres of the CFD mesh at each time-step of the cardiac cycle for patient CoRaL071, $t =$ time-step, where $t = 0$ corresponds to $T = 0s$ and $t = 19$ corresponds to $T = 0.5263s$, each time-step corresponds to $\Delta T = 0.0277s$, $t = 3$ is peak systole; $t = 20$ is late diastole.

time-step was created and a curve was fitted to the data across the timesteps to create a continuous temporal variation as opposed to a discrete variation. The flow profile at each time-step can therefore be replicated without the need for large data tables that slow the numerical simulation down, reducing the computational resources and time required. The impacts of creating a continuous temporal variation on the average volumetric flow rate can be seen in Figure 3.23. This method has the advantage over the interpolation method previously attempted in Section 3.5.3.1 as the CFD mesh can be changed after the boundary conditions have been created, as the data is not mapped onto a preallocated mesh. Making use of a function to describe the inlet condition allows idealised flow profiles, such as those resulting from AVR's to be implemented pre-operatively into patient-specific geometries. This expands the uses of the methodology created. Based on this, the implementation of spatio-temporal patient-specific inlet boundary conditions was achieved by fitting a function to the 4D-Flow MRI data; creating a tool that can accurately model the flow for a range of patients (neonatal, paediatric, and adult, as well as healthy, BAV, or AVR) is key in order for the tool to be of any use to clinicians.

To ensure the function with the best fit across the full cardiac cycle was selected, four functions of increasing order were applied to 4D-Flow MRI data at times corresponding to both peak systole ($t = 3$) and late diastole ($t = 19$), and the goodness of fit statistics were evaluated using the in-house code written in MATLAB [168]. Peak systole and late diastole were selected as the time-steps to test the functions as they present the largest differences in volumetric flow rate magnitude and flow profile present. It was determined that if the surface fit selected is appropriate at both peak systole and late diastole it will be suitable for the remainder of the cardiac cycle. Figure 3.24 demonstrates the qualitative performance of the four functions compared to the 4D-Flow MRI data at peak systole, whilst Figure 3.25 shows the qualitative performance of the four functions compared to 4D-Flow MRI data at late diastole. There is a large spike in the fit data

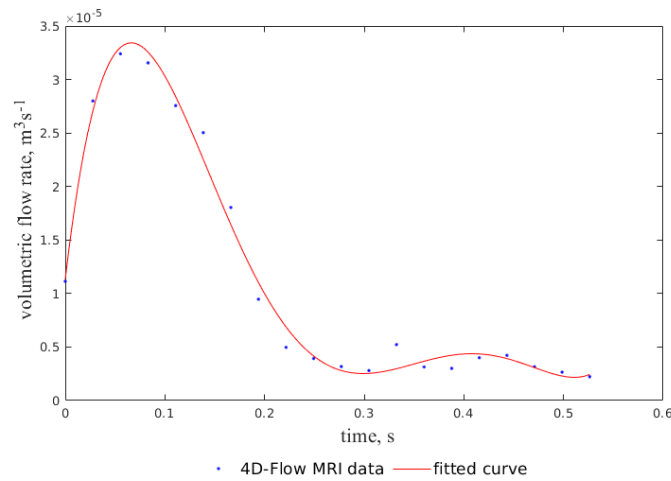


Figure 3.23. Continuous temporal variation of the average volumetric flow rate (m^3s^{-1}) at the inlet over one cardiac cycle for patient CoRaL071 calculated from 4D-Flow MRI data.

seen in the fifth order model at both peak systole and late diastole, and the third order model at late diastole. However these spikes lie outside of the $x - z$ range of the 4D-Flow MRI data of the inlet plane and as the quality of the surface fit outside of the 4D-Flow MRI data-points was not of relevance, the large spikes were not taken into consideration when selecting the best possible fit over the cardiac cycle. Lower order fits were included for consideration since if they provided a suitable approximation to the 4D-Flow MRI data, they would reduce the complexity of the numerical model greatly and reduce the time costs of the numerical simulations.

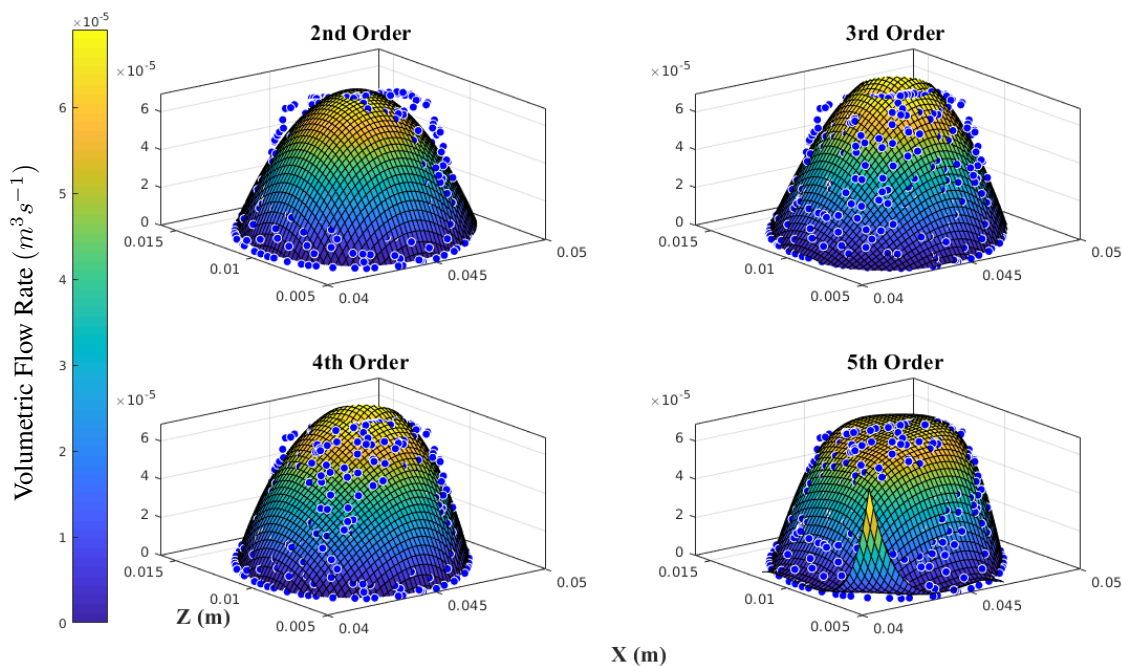


Figure 3.24. Volumetric flow rate data (m^3s^{-1}) from 4D-Flow MRI (blue markers) and the surface fit approximating the flow profile (surface) at peak systole ($t = 3$) for patient CoRaL071. Polynomials of 2nd, 3rd, 4th, and 5th order are all presented.

The performance of the four fits was evaluated quantitatively to ensure the best fit over all timesteps was selected to approximate the inlet condition in the CFD methodology. The Sum of Squares due to Error (SSE), Root Mean Square Error (RMSE), R-Square, and adjusted R-Square are calculated at peak systole ($t = 3$) and late diastole ($t = 20$) for the four surface fits and the results can be

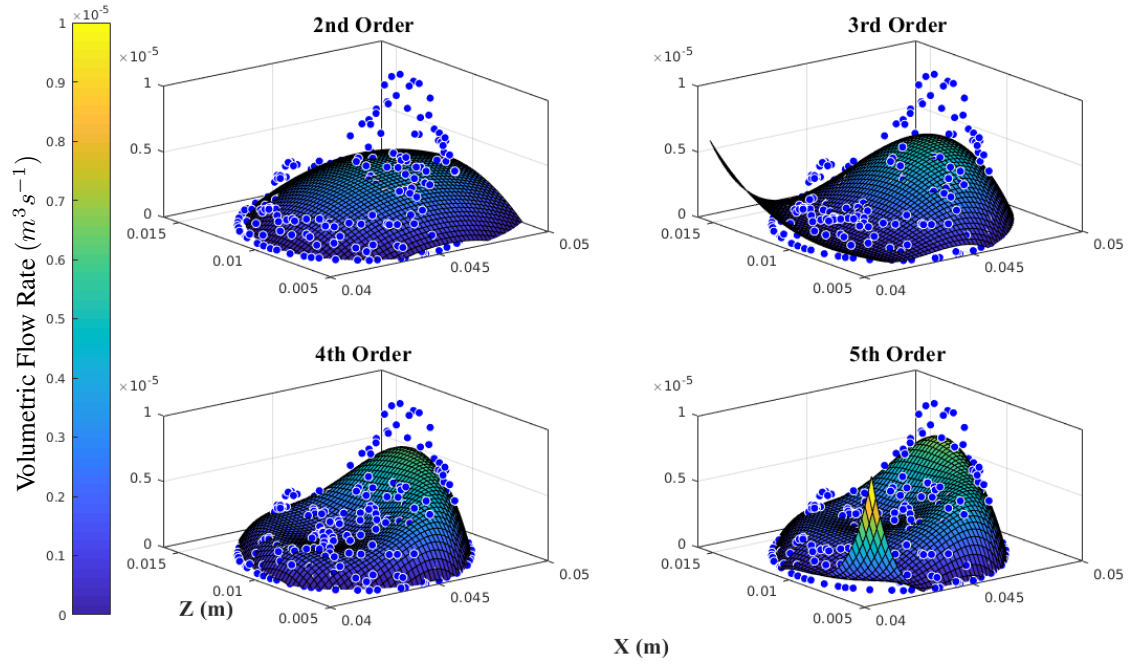


Figure 3.25. Volumetric flow rate (m^3s^{-1}) data from 4D-Flow MRI (blue markers) and the function approximating the flow profile (surface) at late diastole ($t = 20$) for patient CoRaL071. Polynomials of 2nd, 3rd, 4th, and 5th order are all presented.

seen in Table 3.5. The SSE measures the total deviation of the fit to the 4D-Flow MRI data with a SSE close to 0 indicating that there is a good fit of the model to the data and the random error component is small. It is calculated using Equation 3.1, where y_i is the observed value and \hat{y}_i is the value estimated by the fit.

$$SSE = \sum_{i=1}^n (y_i - \hat{y}_i)^2 \quad (3.1)$$

The R-square statistic provides a measure of how well the model predicts the 4D-Flow MRI data based on the amount of the variation that is explained by the model. It is the correlation between the 4D-Flow MRI values and the values predicted by the model. R-square is calculated using Equation 3.2 where SSE =sum of squares due to error and SST =total sum of squares. A R-square value close to 1 indicates that a large proportion of the variance in the 4D-Flow MRI data is accounted for.

$$R - square = 1 - \frac{SSE}{SST} = 1 - \frac{\sum_{i=1}^n (y_i - \hat{y}_i)^2}{\sum_{i=1}^n (y_i - \bar{y}_i)^2} \quad (3.2)$$

To ensure the R-square statistic is not increasing based on the number of fitted coefficients in the model, the adjusted R-square statistic is calculated for each fit. This adjusts the R-square statistic based on the residual degrees of freedom (v) (defined as the number of response values, n , minus the number of fitter coefficients, m), see Equation 3.3. As for the R-square statistic, an adjusted R-square value close to 1 suggests a good fit.

$$adjustedR - square = 1 - \frac{SSE(n-1)}{SST(v)} \quad (3.3)$$

The final statistic used to measure the goodness of fit of the models applied to the 4D-Flow MRI data is the RMSE. This statistic is a measure of the standard deviation of the random component in the data, and is defined by Equation 3.4, where $MSE = SSE/v$. As with SSE, a RMSE value close to 0 suggests the model is a suitable approximation of the 4D-Flow MRI data.

$$RMSE = \sqrt{MSE} \quad (3.4)$$

It can be seen in Table 3.5 that as the order of the surface fit increases, the R-Square and adjusted R-Square become closer to 1 for both systole and diastole, suggesting a greater proportion of the variance in the data is accounted for by the model. Concurrently, the SSE and RMSE tend towards 0 as the order of the fit increases, indicating the random error components of the model are small. As expected, this suggests that the models become more suitable for replicating the flow profile at the valve as the order of the fit increases at all time-steps. The data in Table 3.5 corresponds with the qualitative trends seen in Figures 3.24 and 3.25, with the higher order fits showing better agreement with the 4D-Flow MRI data, and a better approximation at peak systole than at late diastole. This can be demonstrated clearly by the second order model; only 42.39% of the variance is described by the fit at late diastole, increasing to 87.70% at peak systole for the same fit. This increases to 78.23% and 98.73% respectively for the fifth order fit. Although quantitatively, a second order model appears to produce a reasonable approximation of the 4D-Flow MRI data at systole, it can be seen in Figure 3.24 that this is not the case. For this reason, data from Figures 3.24 and 3.25 and Table 3.5 must all be taken into account when selecting an appropriate model of the 4D-Flow MRI data.

		2nd Order	3rd Order	4th Order	5th Order
Systole	SSE	2.2802e-08	1.0114e-08	7.266e-09	2.3492e-09
	R-Square	0.8770	0.8454	0.9608	0.9873
	Adjusted R-Square	0.8750	0.9438	0.9590	0.9865
	RMSE	8.5765e-06	5.7492e-06	4.9134e-06	2.8219e-06
Diastole	SSE	7.6260e-10	5.8783e-10	3.4501e-10	2.8814e-10
	R-Square	0.4239	0.5559	0.7393	0.7823
	Adjusted R-Square	0.4146	0.5428	0.7272	0.7676
	RMSE	1.5684e-06	1.3860e-06	1.0706e-06	9.8831e-07

Table 3.5. Goodness of fit statistics comparing the 4 surface fits used to model the 4D-Flow MRI data at the inlet at peak systole ($t = 3$) and late diastole ($t = 20$). SSE=sum of squares due to error; RMSE=root mean square error.

The disagreement between the models and the 4D-Flow MRI data at late diastole arises as there is no longer blood being ejected into the aorta at this stage in the cardiac cycle, meaning there is no longer a jet of blood creating a clear flow profile as there is at peak systole, this results in a significantly lower flow rate. All four fits tested struggle to model the lower flow rates with the same level of accuracy as they do the higher flow rates of systole. However, as this research aims to create a tool that can investigate the impacts of flow profile as a result of the valve phenotype or AVR present, it follows that the flow profile during systole is of greater importance than the flow profile during diastole. This is a result of the valve being closed during diastole, so the impacts of

valve phenotype or AVR type are less notable than at systole.

3.5.3.3 Implementation of Spatio-Temporal Boundary Conditions

Due to poor performance of the lower order fits at late diastole, the fifth order surface was selected to model the flow at the inlet plane of the domain over the course of the cardiac cycle. The equation used to model the flow profile at the valve is given by Equation 3.5, where x is the x -coordinate, z is the z -coordinate, and P_{00} through P_{05} are the coefficients that vary throughout the cardiac cycle and are described by 5th order equations which are themselves functions of time. The selected function was implemented into OpenFOAM at the inlet patch using the OpenFOAM boundary condition *codedFixedValue*.

$$\begin{aligned}
 F(x, z; t) = & P_{00} + P_{10}x + P_{01}z + P_{20}x^2 + P_{11}xz + P_{02}z^2 + P_{30}x^3 + P_{21}x^2z \\
 & + P_{12}xz^2 + P_{03}z^3 + P_{40}x^4 + P_{31}x^3z + P_{22}x^2z^2 + P_{13}xz^3 \\
 & + P_{04}z^4 + P_{50}x^5 + P_{41}x^4z + P_{32}x^3z^2 + P_{23}x^2z^3 + P_{14}xz^4 + P_{05}z^5 \quad (3.5)
 \end{aligned}$$

Figure 3.26 demonstrates the volumetric flow rates calculated using the spatio-temporal boundary condition created for patient CoRaL071, where the function was applied to the same data-points as the 4D-Flow MRI to allow for comparison. The calculated boundary conditions at systole for all 5 neonatal patients can be seen in Figures 3.27 and 3.28. The use of a fitted function produces inlet boundary conditions that are significantly more physiologically accurate and show much greater agreement to 4D-Flow MRI data than the plug profiles previously implemented, and shown in Figures 3.18 and 3.19.

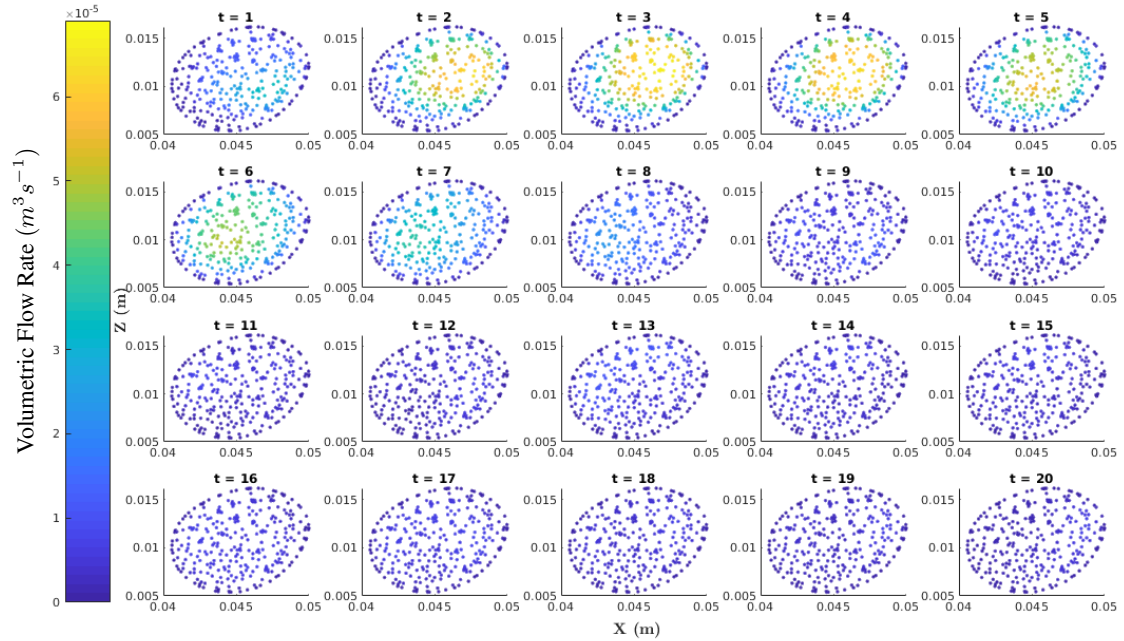


Figure 3.26. Volumetric flow rate (m^3s^{-1}) at each 4D-Flow MRI data point calculated through fitting a 5th order polynomial to the 4D-Flow MRI data for every time-step, $t = \text{time-step}$, where $t = 0$ corresponds to $T = 0s$ and $t = 19$ corresponds to $T = 0.5263s$, each time-step corresponds to $\Delta T = 0.0277s$, $t = 3$ is peak systole; $t = 20$ is late diastole.

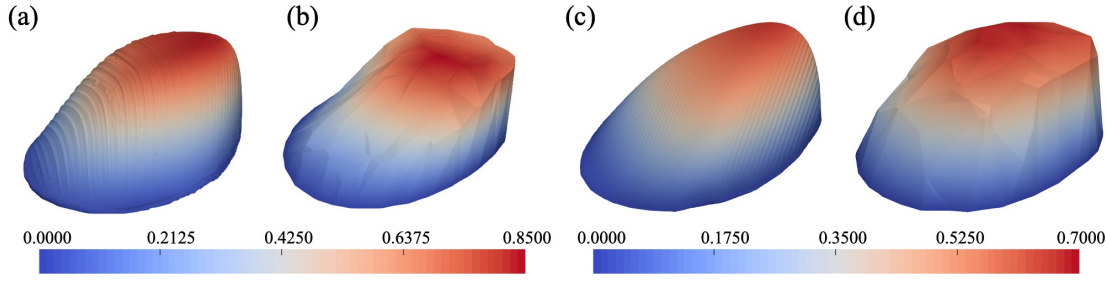


Figure 3.27. Velocity magnitude ($m s^{-1}$) contours of patient-specific spatio-temporal inlet boundary conditions for neonatal patients with TAV at systole ($t = 3$), (a) and (c) show CFD inlet conditions, (b) and (d) show 4D-Flow MRI data.

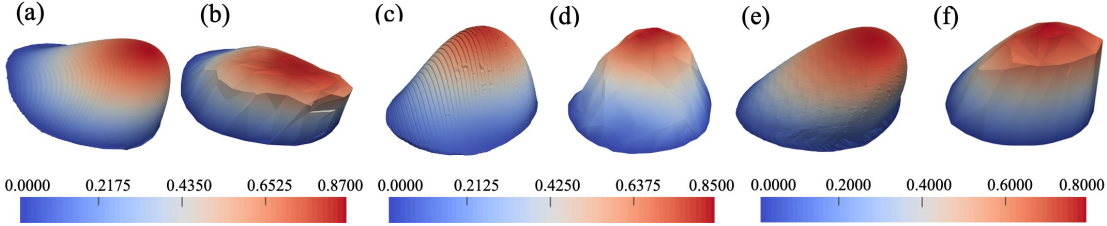


Figure 3.28. Velocity magnitude ($m s^{-1}$) contours of patient-specific spatio-temporal inlet boundary conditions for neonatal patients with BAV at systole ($t = 3$), (a), (c), and (e) show CFD inlet conditions, (b), (d), and (f) show 4D-Flow MRI data.

3.6 Properties of Blood

3.6.1 Viscosity

As discussed in Section 2.4.3.1 there is no universally accepted viscosity model for blood. It was established that in blood vessels with a small diameter, the non-Newtonian effects of blood become important [120]. However, as this study focuses on modelling blood flow through an artery with a large diameter, it can be assumed that blood behaves as a Newtonian fluid [120]. From the findings of Karimi *et al.* [60] and Caballero & Laín [57], this assumption can be taken to be appropriate.

Based on the literature reviewed in Chapter 2, the physical properties of blood that were used for all OpenFOAM simulations within this project unless otherwise stated are as follows:

- Dynamic viscosity: $\mu = 3.5 \times 10^{-3} Pa.s$
- Density: $\rho = 1060 \frac{kg}{m^3}$

Giving a kinematic viscosity of $\nu = 3.3 \times 10^{-6} \frac{m^2}{s}$ at $37^\circ C$, the average temperature of the human body.

3.6.2 Turbulence

Before a turbulence model is selected, it must first be determined if one is appropriate considering the pulsating boundary conditions. The effects that the pulsatile nature of the flow have on the transition to turbulence can be quantified by calculating the Womersley number, as discussed in Section 2.5.3. Using Equation 3.6, where $L =$ appropriate length scale, $\omega =$ angular frequency of oscillations, $\rho =$ density, $\mu =$ dynamic viscosity, $\alpha = 8.248$ for patient CoRaL071. This indicates that the flow for patient CoRaL071 can be categorised as mid-frequency flow, as $2.5 \leq \alpha \leq 12$, meaning the threshold for transition to turbulence is smooth and unaffected by the pulsatile nature

of the flow. It also indicates that the flow profile will be parabolic and will not resemble a plug profile.

$$\alpha = L \left(\frac{\omega \rho}{\mu} \right)^{\frac{1}{2}} = 0.004338 \times \left(\frac{11.94 \times 1060}{3.5 \times 10^{-3}} \right)^{\frac{1}{2}} = 8.248 \quad (3.6)$$

Womersley numbers are calculated for all patients involved in this research and can be seen in Table 3.6 for all 5 neonatal patients. It is clear that all neonatal patients experience a Womersley number within the $2.5 \leq \alpha \leq 12$ region, and all are below the threshold that would indicate a plug profile might be present. This further supports the use of spatio-temporal patient-specific inlet boundary conditions over plug profiles. The Womersley numbers for adult patients indicate that all patients experience high-frequency flow, and as such the transition to turbulence is unaffected by the pulsatile nature of the flow.

Patient	Womersley Number, α	Reynolds Number, Re, Range
CoRaL071	8.248	24.85 - 3102
CoRaL072	8.000	51.96 - 1946
CoRaL073	9.874	75.56 - 2681
CoRaL074	9.689	74.55 - 2709
CoRaL076	7.392	34.92 - 1891
OXBAV003	n/a	n/a
OXBAV012	19.83	149.3 - 6732
OXBAV017	n/a	n/a
OXBAV021	n/a	n/a
OXBAV022	27.68	713.4 - 22821
OXBAV071	27.53	366.5 - 5668
OXBAV102	33.87	772.6 - 2886

Table 3.6. Calculated Womersley and Reynolds numbers for the patients used within this research. Where Womersley and Reynolds numbers were unavailable, this was due to poor 4D-Flow MRI data quality that did not allow for appropriate or accurate segmentation to occur.

Using Equation 2.4 the Reynolds number of the blood flow in the aorta can be calculated to indicate whether a laminar or turbulent assumption is more appropriate. The Reynolds number must be calculated over the course of the cardiac cycle for all patients involved in this study (see Table 3.6 for the Reynolds number ranges for all patients used in this research). It can be seen that the Reynolds number experienced by all patients varies between the laminar, transitional, and turbulent regimes. The Reynolds number reaches a peak value during systole, with the lowest value occurring during diastole. The calculated values are also subject to a number of assumptions; the diameter of the vessel is not constant along the length of the thoracic aorta, and is also known to vary radially during the cardiac cycle. Therefore the values presented in Table 3.6 are estimates. Based on this it is clear that a turbulence model is required. The $k - \omega$ SST turbulence model was incorporated into all simulations of peak systole, and all simulations of the full cardiac cycle. Simulations of diastole were taken to be laminar. Individualised parameters for the $k - \omega$ SST turbulence model were determined for each patient participating within this research using Equations 3.7 and 3.8, where k is the turbulent kinetic energy, I is the intensity, U_{ref} is a reference velocity, ω is the turbulent specific dissipation rate, C_μ is a constant equal to 0.09, and L is a reference length scale.

$$k = \frac{3}{2}(I|U_{ref}|)^2 \quad (3.7)$$

$$\omega = \frac{k^{0.5}}{C_{\mu}^{0.25}L} \quad (3.8)$$

3.6.3 Homogeneity

As discussed in Section 2.2.5, the Stokes number of the flow can be determined over the course of the cardiac cycle to quantify the overall impact the red blood cells, white blood cells, and platelets have on the flow, and therefore whether the assumption that blood is a homogeneous fluid is appropriate. Using Equation 2.1 and the average velocity magnitudes at the inlet plane over the course of the cardiac cycle, it is possible to calculate the Stokes number variation, see Figure 3.29. The Stokes' numbers of only the red blood cells are determined for each patient, as the white blood cells are far less numerous than red blood cells and platelets are smaller. Therefore it can be assumed that provided the red blood cells do not impact the flow, the remaining particles in the suspension can be neglected. As expected, the Stokes number increases as the inlet velocity increases, however is still small enough such that the presence of the red blood cells in the fluid can be neglected and blood can therefore be treated as a homogeneous fluid as suggested in Chapter 2. For all patients participating in this research, the Stokes number was small enough such that blood could be treated as a homogeneous fluid.

The Stokes' numbers shown in Figure 3.29 can only be taken as an estimate. This is due to a significant number of assumptions that are used during the calculation. The density of the red blood cells is unknown and there is no universal value that can be utilised. For this reason, the particle density used when calculating the Stokes numbers in Figure 3.29 is calculated using values from literature; a value of $\rho_{rbc} = 1178 \text{kgm}^{-3}$ is used [67]. This value is arrived at by assuming the density of the plasma is $\rho_{plasma} = 1000 \text{kgm}^{-3}$ [182], the density of the overall mixture is $\rho_{mixture} = 1080 \text{kgm}^{-3}$ [76] and there is a red blood cell volume fraction of 0.45 at the inlet [183]. It is also assumed that the red blood cells are perfectly spherical, and not biconcave discs as they are known to be. The vessel diameter used is also an approximation as the aorta is not perfectly circular, but has imperfections, as well as being known to vary in size radially throughout the cardiac cycle. The viscosity is also not a constant value, as blood is known to be a non-Newtonian, shear-thinning fluid. Finally, the velocity used in the calculations is an average value of the velocity magnitude of the cross section of the inlet.

3.7 Quantification of Haemodynamic Indices

Alongside 2-dimensional and 3-dimensional visualisations of the flow throughout the thoracic aorta that will be used to validate the CFD workflow against the 4D-Flow MRI data, the flow asymmetry ($Flow_{asymmetry}$) and flow dispersion ($Flow_{dispersion}$) are also calculated at systole and diastole. $Flow_{asymmetry}$ and $Flow_{dispersion}$ are determined at three planes within the thoracic aorta: plane B (in the mid-ascending aorta), plane C (in the transverse aortic arch) and plane D (in the mid-descending aorta). Data from patient-specific CFD simulations is compared to the corresponding 4D-Flow MRI data to assess the accuracy of the workflow created. The approximate

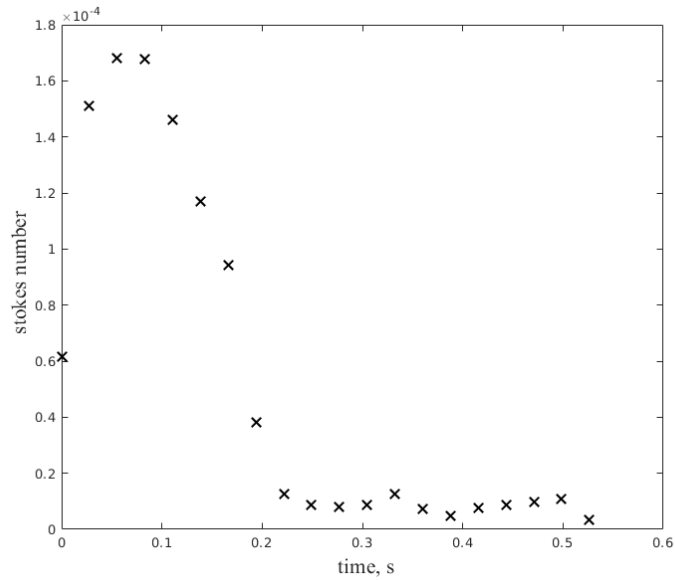


Figure 3.29. Variation in the Stokes number over the course of the cardiac cycle for neonatal patient CoRaL071.

location of the planes can be seen in Figure 3.30. The circulation of the flow is also calculated across the three planes of interest at systole and diastole in order to compare it to the values determined from the 4-Flow MRI data. It was decided that the WSS was not a parameter of interest within this research as it is known to rely heavily on an accurate vessel wall location, therefore accurate segmentation, and is known to be sensitive to the spatial resolution of the 4D-Flow MRI data.

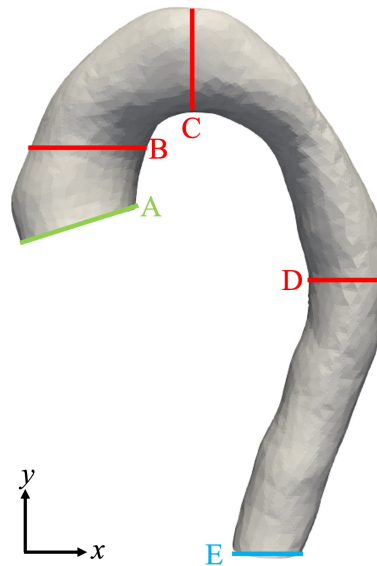


Figure 3.30. Location of planes used for the quantification of haemodynamic indices. *A=inlet, B=mid-ascending aorta, C=transverse aortic arch, D=mid-descending aorta, E=outlet.*

3.7.1 Flow Asymmetry

The flow asymmetry was determined to assess to what degree the flow was eccentric. Using the method outlined by Youssefi *et al.* [74], flow asymmetry was calculated by determining the distance between the centroid of the top 15% of velocities ($V_{max}^{15\%}$) within each plane ($\overline{X}_b =$

(x_b, y_b, z_b)) and the geometric centroid of the plane ($\overline{X}_a = (x_a, y_a, z_a)$), before dividing it by the equivalent radius of the plane (R_{eq}), see Equation 3.9 and Figure 3.31. Values calculated from CFD simulations are then compared to those from 4D-Flow MRI data.

$$Flow_{asymmetry} = 100 \times \frac{\sqrt{(x_b - x_a)^2 + (y_b - y_a)^2 + (z_b - z_a)^2}}{R_{eq}} \quad (3.9)$$

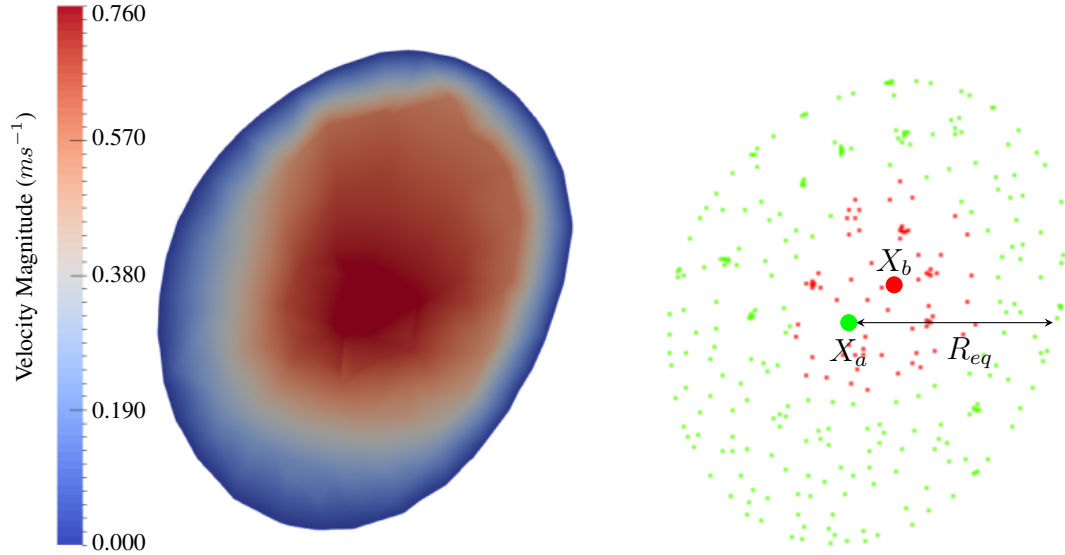


Figure 3.31. 4D-Flow MRI velocity magnitude contours across a plane in the ascending aorta at systole of patient CoRaL071, the area with velocities in the top 15% (red markers), and the area with velocities in the bottom 85% (green markers) are highlighted, as well as the geometric centroid (X_a) and the centroid of the top 15% of velocities (X_b).

A high flow asymmetry percentage indicates that the flow is highly eccentric and is likely biased towards the periphery of the vessel. A low flow asymmetry percentage indicates that the flow is likely central, and is biased towards the longitudinal axis of the vessel. A low flow asymmetry is desirable as it indicates the flow will not be impinging on the vessel wall. The flow asymmetry assumes that 'normal' flow is along the centre-line of the vessel.

As the data points for the 4D-Flow MRI are irregular, as shown in Figure 3.31, it is possible that the location of the data points themselves will skew the flow asymmetry metric and cause 4D-Flow MRI results to produce inaccurate data. As there is no gold-standard to compare the 4D-Flow MRI data to, the magnitude of any errors introduced via the 4D-Flow MRI data point locations is unknown.

3.7.2 Flow Dispersion

The flow dispersion was also determined using data from both patient-specific CFD simulations and the corresponding 4D-Flow MRI data to assess the velocity flow profile present and the agreement between the two methods. Using the methodology outlined by Youssefi *et al.* [74], the flow dispersion was calculated by dividing the area of the top 15% of velocities ($A_{V_{15\%}}$) by the geometric area of the plane of interest (A_{plane}), see Equation 3.10.

$$Flow_{dispersion} = 100 \times \frac{A_{V_{15\%}^{max}}}{A_{plane}} \quad (3.10)$$

A high flow dispersion percentage indicates that the flow profile is broad, and not a sharp profile. Whereas a low flow dispersion indicates the opposite is true of the velocity profile. If a low flow dispersion is present at the inlet, this further validates the decision to increase the complexity of the inlet boundary conditions, as a plug profile will be inadequate to model a high flow dispersion. It is expected that the flow dispersion will be greater in the mid-descending aorta (plane 3) as it is less affected by the inlet conditions than the ascending aorta (plane 1).

3.7.3 Circulation

The circulation of the flow in the thoracic aorta was determined as it provides a means to quantify the rotational components of the flow. The circumferential circulation is determined through the integral of the vorticity of the flow over a transverse plane in the thoracic aorta (ω). Using the method set out by Hess *et al.* [184], Equation 3.11 was used to calculate the circulation, where Γ is the 3D vector representing the circulation of the flow. The through plane component of the 3D circulation vector depicts the within plane rotation of the blood flow in the vessel, which is the component of interest to clinicians.

$$\Gamma = \iint_S \omega \cdot d\mathbf{S} \quad (3.11)$$

3.8 Limitations

A workflow combining 4D-Flow MRI data and CFD methods to create patient-specific simulations has been detailed within this Chapter. Although the method to create spatio-temporal patient-specific inlet boundary conditions has been discussed, there are notable limitations to the approach used. Primarily, the chosen method used produces only an estimation of the flow profile that is seen in the 4D-Flow MRI data, as only a 5th order surface fit is applied meaning there are significant levels of interpolation required between the data-points. Using an alternative method that directly mapped the 4D-Flow MRI data onto the CFD mesh constructed at the inlet would remove the interpolation errors, however would prohibitively slow the patient-specific simulations down. In addition to the interpolation errors, as the physical aortic valve structure is not included in the geometry, and instead the inlet condition is used to replicate the flow profile found after the valve leaflets, many secondary flow features caused by the movement of the valve leaflets will not be predicted by patient-specific CFD simulations. The opening and closing of the valve leaflets is known to impact the haemodynamics of the thoracic aorta and neglecting to include them therefore prevents the flow features from being modelled and produce inaccuracies in the CFD simulations, restricting the use of the workflow created, as discussed in Section 2.6.2.

Furthermore, FSI between the blood within the vessel and the vessel wall has been neglected and any surrounding tissue and tethering of the vessel is not included. It is commonly accepted that the movement of the thoracic aorta throughout the cardiac cycle will influence the haemodynamics within the vessel, as discussed in Section 2.6.1. The geometry of the vessel used for the entirety of the cardiac cycle is that of the peak systolic geometry, although this is accurate for the systolic

phase of the cardiac cycle, the volume of the thoracic aortic geometry will be too large for the diastolic phase of the cardiac cycle.

As detailed in Section 3.3.1, the geometry reconstruction process within the workflow presented in this research causes errors to be present in the geometry and the velocity data from the 4D-Flow MRI scan that will be introduced into any subsequent patient-specific CFD simulations. This limits the clinical conclusions that can be drawn from the patient-specific simulations, as agreement with the 4D-Flow MRI data does not necessarily indicate correct results. Another factor limiting the ability to draw clinical conclusions from the patient-specific simulations is the spatial and temporal resolution used to acquire the 4D-Flow MRI data. As an inappropriate resolution will affect the 4D-Flow MRI data in conjunction with the CFD data, agreement between the two data-sets cannot be said to be free from errors caused by insufficient resolutions.

Physiologically accurate outlet conditions such as the two- and three- element Windkessel models were not incorporated into the workflow, and as such the compliance of the vessel and the resistance of downstream systemic circulatory system distal to the outlet plane is not accounted for. This choice was made as *in-vivo* pressure data for the patients was not available for this research. In view of this, the most physiologically accurate outlet boundary conditions that could be implemented were 0-pressure if only one outlet was used and outflow conditions if multiple outlets were incorporated.

In addition to physiologically inaccurate outlet boundary conditions, the Newtonian and homogeneous assumptions made about blood are incorrect. Incorporating a viscosity model that accounts for the shear thinning properties of blood, as well as modelling the fluid as a suspension would ensure more physiologically accurate CFD simulations.

As discussed in Section 3.7.1, the method used to calculate the flow asymmetry metric may also contribute to discrepancies between the 4D-Flow MRI data and the subsequent CFD data.

3.9 Conclusions

The workflow proposed within this Chapter successfully integrates 4D-Flow MRI data and CFD techniques to produce patient-specific simulations for a range of patients and BAV phenotypes. 4D-Flow MRI data was used to reconstruct a patient-specific geometry through contrast adjustment, thresholding and segmentation. The inlet and outlet locations were then selected in physiologically accurate locations in the ascending and descending thoracic aorta, before spatio-temporal patient-specific inlet conditions were created. With a patient-specific geometry reconstructed and appropriate inlet conditions, patient-specific simulations can be run.

Patient-specific inlet conditions were created by iteratively increasing the complexity of the boundary condition, ensuring each iteration produced a more physiologically accurate flow profile. Spatio-temporal patient-specific inlet conditions were arrived at that allowed for a range of flow profiles to be replicated in the CFD simulations, meaning the workflow created is suitable for a range of aortic valve pathologies. As the spatio-temporal inlet conditions allow for various flow profiles to be incorporated into the numerical model, it can be assumed that the flow profiles that result from both biological and mechanical AVR's can also be applied to the inlet patch of the patient-specific reconstructed geometry to observe how the AVR procedure would impact the tho-

racic aortic haemodynamics. This would allow the workflow detailed within this Chapter to be used for treatment planning and predicting the outcomes of surgical intervention.

Alongside successfully integrating 4D-Flow MRI and CFD techniques, the workflow described within this Chapter highlights the challenges of patient-specific modelling, and suggests alternative approaches available, or quantifies the errors within the processes. The errors that can be attributed to the segmentation and geometry reconstruction process have been detailed and have been shown to cause variations in the vessel dimensions and volumetric flow rate at the inlet, whilst alternative approaches to creating patient-specific inlet conditions have been explored and the most suitable selected.

In order to assess the accuracy of the methodology created, results from each developmental stage must be compared to data from 4D-Flow MRI scans. A range of patients must be assessed, to evaluate the accuracy across all ages and BAV phenotypes. The results of the CFD methodology are compared to 4D-Flow MRI data within Chapter 4. The haemodynamic indices detailed in Section 3.7 are used to provide quantitative measures of agreement. An attempt to assess the accuracy of the methodology will be taken in Chapter 5, where the impacts the systemic circulatory system distal to the outlet has on the accuracy of the workflow created is assessed. This is achieved through a flow phantom where the the vessels downstream of the outlets are removed, and 4D-Flow MRI data is acquired in a controlled environment with pre-determined inlet conditions. This will remove the uncertainties regarding the outlet conditions and allow the accuracy of the workflow to be evaluated. The impact the spatial resolution the 4D-Flow MRI data is acquired at has on the 4D-Flow MRI data and the subsequent patient-specific CFD simulations must also be investigated and quantified, this research can be seen in Chapter 6.

With the exception of MATLAB, all software used when developing the workflow to integrate 4D-Flow MRI and CFD is open-source and requires no additional licenses or costs. This ensures the method created can be used by a range of clinicians at a minimal cost.

Chapter 4.

Patient-Specific Results from Methodology Development

Contents

4.1	Introduction	82
4.2	Steady State Plug Flow	83
4.2.1	Peak Systole	84
4.2.2	Late Diastole	86
4.3	Pulsatile Plug Flow	87
4.3.1	Peak Systole	88
4.3.2	Late Diastole	89
4.4	Spatio-Temporal Patient Specific Flow	91
4.4.1	Systole	91
4.4.2	Diastole	95
4.5	Supra-Aortic Vessels Within the Neonatal Cohort	98
4.5.1	Systole	99
4.5.2	Diastole	101
4.6	Supra-Aortic Vessels Within the Adult Cohort	104
4.6.1	OXBAV012	104
4.6.1.1	Systole	104
4.6.1.2	Diastole	108
4.6.2	OXBAV071	111
4.6.2.1	Systole	112
4.6.2.2	Diastole	114
4.7	Limitations	116
4.8	Conclusions	117

4.1 Introduction

The results shown throughout this chapter are collected during the development of the predictive tool and show the various stages of development. The results from increasing the complexity of the

inlet conditions are detailed, the inclusion of the supra-aortic vessels thereby increasing the number of outlets, and applying more physiologically accurate outlet conditions applied are detailed and discussed. How these stages of development influenced and contributed to the construction of the predictive tool is delineated. The limitations of the workflow and the areas that still require development are discussed.

The initial development of the workflow detailed in Chapter 3 was conducted on adult patients, shown in Table 3.1. However, as neonatal patient data became available to the authors, the development of the tool was conducted with neonatal patients in addition to adult patients to ensure it will capture the haemodynamics correctly for both adult and neonatal patients, as well as healthy patients and those who have a BAV diagnosis, and the various phenotypes that are possible.

4.2 Steady State Plug Flow

Initially, testing of the methodology was conducted on patient OXBAV012 (see Table 3.1 for patient data). Preliminary simulations were steady state and incorporated the simplistic inlet condition described in Section 3.5.1; a plug profile with a magnitude equal to the spatially averaged volumetric flow rate over the inlet plane, at timesteps representative of peak systole and late diastole. Steady-state simulations were run in order to verify that the methods used to acquire the data, construct the geometry, and extract the relevant velocity data to create patient-specific boundary conditions are correct and adequately replicate the geometry and haemodynamics of the thoracic aorta. Once this was verified, it was possible to progress onto more computationally expensive transient simulations that are more physiologically accurate. However, due to the simplicity of the steady state simulations and the assumptions made at the inlet, any comparison between the steady state numerical simulations with a plug profile and the inherently transient 4D-Flow MRI data can only be preliminary and must not be taken to have any clinical significance.

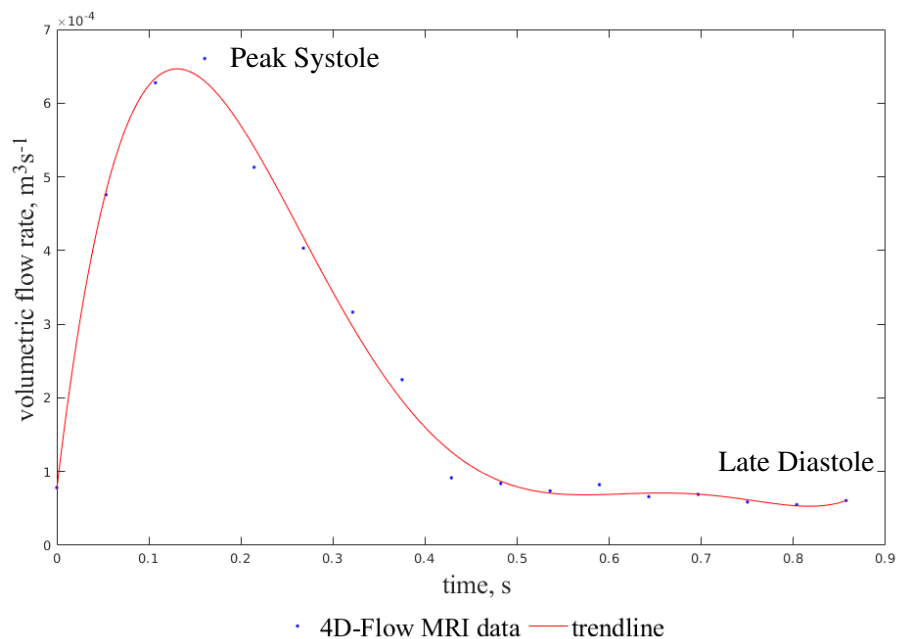


Figure 4.1. Maximum volumetric flow rate (m^3s^{-1}) at the inlet plane over one cardiac cycle for patient OXBAV012. Peak systole and late diastole are indicated as the time-steps chosen for steady-state plug profile simulations.

4.2.1 Peak Systole

An average volumetric flow rate of $Q = 4.644 \times 10^{-4} m^3 s^{-1}$ was used as the magnitude of the plug profile for simulations of peak systole ($t = 0.1071s$), and simulations were run using the steady state solver, *simpleFoam*, within OpenFOAM. This is a steady-state solver for incompressible, Newtonian, turbulent flow which uses the SIMPLE (Semi-Implicit Method for Pressure-Linked Equations) algorithm. A turbulence model was incorporated into the numerical model for simulations at peak systole as the Reynolds number was calculated to be $Re = 6732$, indicating the flow is transitional. The $k - \omega$ SST turbulence model was selected for reasons discussed in Section 2.5.3 and the turbulence intensity was set to 5% at the inlet, based on values from literature [18, 125, 148]. Patient-specific values of k and ω were calculated from 4D-Flow MRI data for each patient using Equations 3.7 and 3.8.

Velocity contours across three axial planes of interest in the mid-ascending aorta, aortic arch and mid-descending aorta from CFD and 4D-Flow MRI data at peak systole can be seen in Figure 4.2. It is clear that the velocity magnitude is grossly overestimated throughout the domain by the patient-specific CFD simulation when compared to 4D-Flow MRI data at the corresponding time in the cardiac cycle. Neither the magnitude or flow patterns are in agreement with those shown in 4D-Flow MRI data.

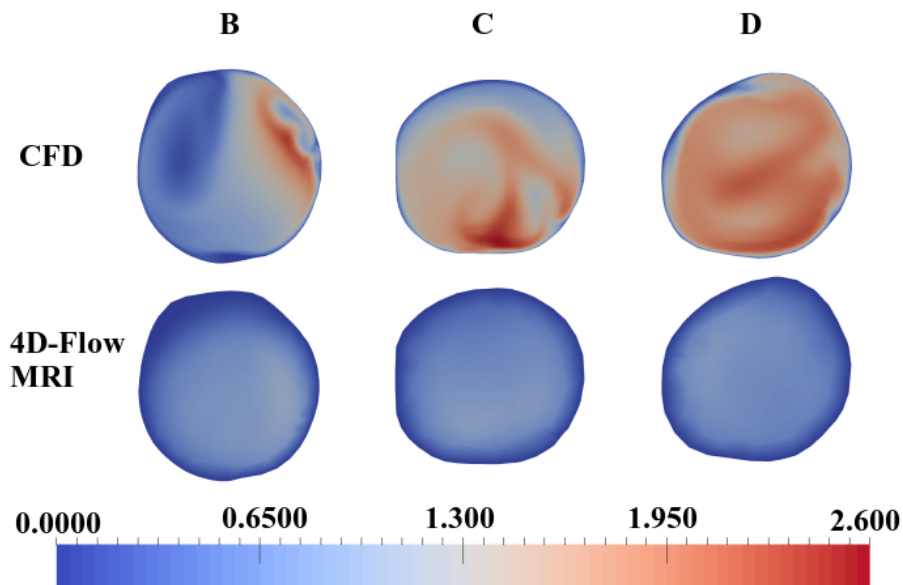


Figure 4.2. Contours of velocity magnitude (ms^{-1}) calculated through steady-state CFD simulations with a plug profile and 4D-Flow MRI data at peak systole ($t = 0.1071s$) at three planes of interest for patient OXBAV012. (*B*=mid-ascending aorta, *C*=aortic arch, *D*=mid-descending aorta).

Following the methods outlined in Section 3.7, the flow asymmetry, flow dispersion, and circulation of the flow were calculated at the three axial planes of interest in the mid-ascending aorta, aortic arch, and mid-descending aorta for both CFD and 4D-Flow MRI data. This can be seen in Figure 4.3. The flow asymmetry is over-estimated by CFD data in all three planes, significantly in the aortic arch and mid-descending aorta as the flow moves away from the inlet condition, increasing from a 15.90% difference in the mid-ascending aorta to 55.67% and 52.07% in the aortic arch and mid-descending aorta. As it is known that away from the inlet, the haemodynamics are primarily governed by the curvature and geometry of the aorta, it is likely these discrepancies are a result of neglecting the supra-aortic vessels. There is good agreement in the mid-ascending aorta and

mid-descending aorta in terms of flow dispersion, with differences of only 3.410% and 1.390% respectively when comparing CFD data to 4D-Flow MRI data. It can be seen that CFD data significantly overestimates the magnitude of the circulation in all locations (with differences of 24.51%, 179.0%, and 183.0% between CFD and 4D-Flow MRI data in planes B, C, and D respectively), and only predicts the correct direction of circulation in the aortic arch. In addition to incorrectly predicting the magnitude and direction, the CFD data predicts abnormal helical flow in all three planes of interest, whilst 4D-Flow MRI data suggests the levels of helical flow experienced by the patient are normal in all three locations.

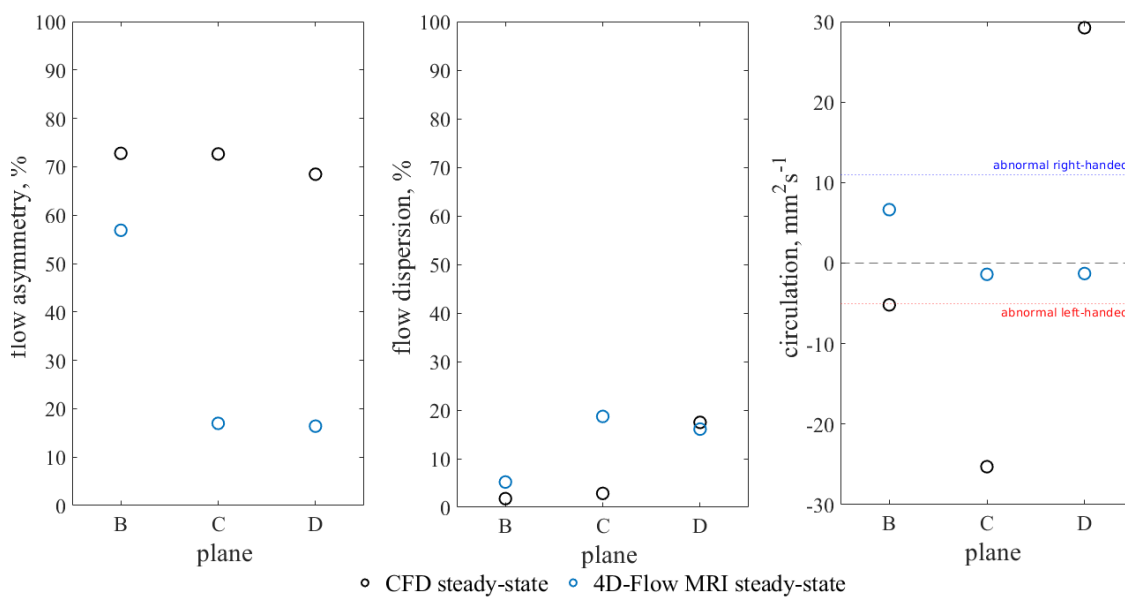


Figure 4.3. Flow asymmetry (%), flow dispersion (%), and through plane circulation (mm^2s^{-1}) calculated at systole from 4D-Flow MRI data and steady-state plug profile CFD data at three planes of interest. (*B*=mid-ascending aorta, *C*=aortic arch, *D*=mid-descending aorta.)

The discrepancies between the CFD and 4D-Flow MRI data can be attributed to multiple causes. Primarily, the plug profile that is applied at the inlet is insufficient and does not capture the haemodynamics of the aortic valve correctly. Many of the errors may also be a result of comparing steady state CFD results to the inherently transient 4D-Flow MRI data. Neglecting the supra-aortic vessels will be contributing to the elevated velocity magnitudes seen in the descending aorta, and the simplistic outlet boundary condition will also be influencing the haemodynamics present in the CFD data. The spatial and temporal resolution of the 4D-Flow MRI data must also be acknowledged as a potential source of error; it is likely that the resolution used to acquire the data is insufficient to accurately capture the complex haemodynamics within the vessel. The y location and angle of the inlet plane in the CFD simulations may also be contributing to the differences seen in the ascending aorta and aortic arch. As the aortic valve is not easily located in the MRI images, its location within the ascending aorta has been approximated for the simulations; it is likely that for the patient in question the inlet is further up the ascending aorta than initially assumed and inclined at an angle to the horizontal. Assuming the inlet plane is parallel to the horizontal is physiologically inaccurate.

4.2.2 Late Diastole

Simulations of late diastole ($t = 0.8571s$) for patient OXBAV012 were conducted using an average volumetric flow rate at the inlet of $1.698 \times 10^{-5} m^3 s^{-1}$. Simulations were run using the steady state solver, *simpleFoam*, within OpenFOAM. The flow was considered to be laminar as the mean Reynolds number was below the threshold for transitional or turbulent flow ($Re = 149.3$).

Contours of velocity magnitude at late diastole can be seen in Figure 4.4 comparing CFD data to 4D-Flow MRI data. It is evident that the flow patterns determined through CFD simulations vary significantly to those determined using 4D-Flow MRI data, however the magnitude appears to be more consistent between both sets of data, than what is seen in Figure 4.2. CFD data suggests much smoother flow throughout the entire thoracic aorta which is not present in the 4D-Flow MRI data.

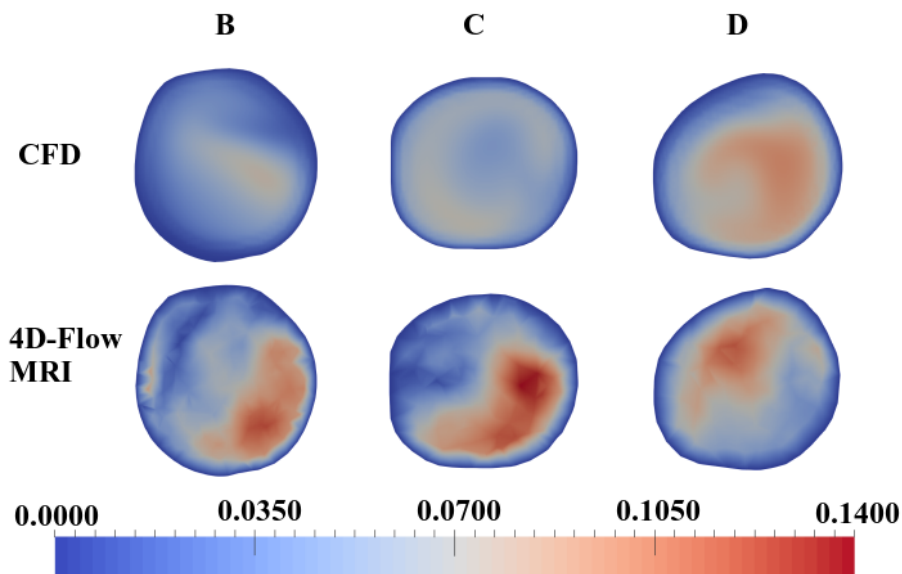


Figure 4.4. Contours of velocity magnitude (ms^{-1}) calculated through steady-state CFD simulations with a plug profile and 4D-Flow MRI data at late diastole ($t = 0.8571s$) at three planes of interest for patient OXBAV012. (B=mid-ascending aorta, C=aortic arch, D=mid-descending aorta).

The flow asymmetry, flow dispersion, and circulation for both CFD and 4D-Flow MRI data at late diastole can be seen in Figure 4.5. There are differences between the CFD data and 4D-Flow MRI data for both flow asymmetry and dispersion in all three planes. However, the flow asymmetry demonstrates improving agreement as the flow progresses through the thoracic aorta whilst flow dispersion suggests agreement decreases as the flow progresses through the thoracic aorta. Flow asymmetry increases from a 28.65% difference in the mid-ascending aorta to 1.360% in the mid-descending aorta. Flow dispersion agreement decreases from a 2.650% difference in the mid-ascending aorta to 13.77% in the mid-descending aorta. Despite the good levels of agreement seen in all three planes in terms of flow dispersion, it is overestimated by CFD simulations in all three locations likely due to the plug profile that is implemented. It can also be seen that the circulation values do not agree in terms of magnitude or direction at any location (with differences between the CFD and 4D-Flow MRI data of 169.0%, 132.4% and 197.0% in planes B, C, and D respectively). However, both CFD data and 4D-Flow MRI data indicate that the levels of helical flow found at all three planes are within normal limits.

The discrepancies between CFD and 4D-Flow MRI data indicate that the inlet boundary condition

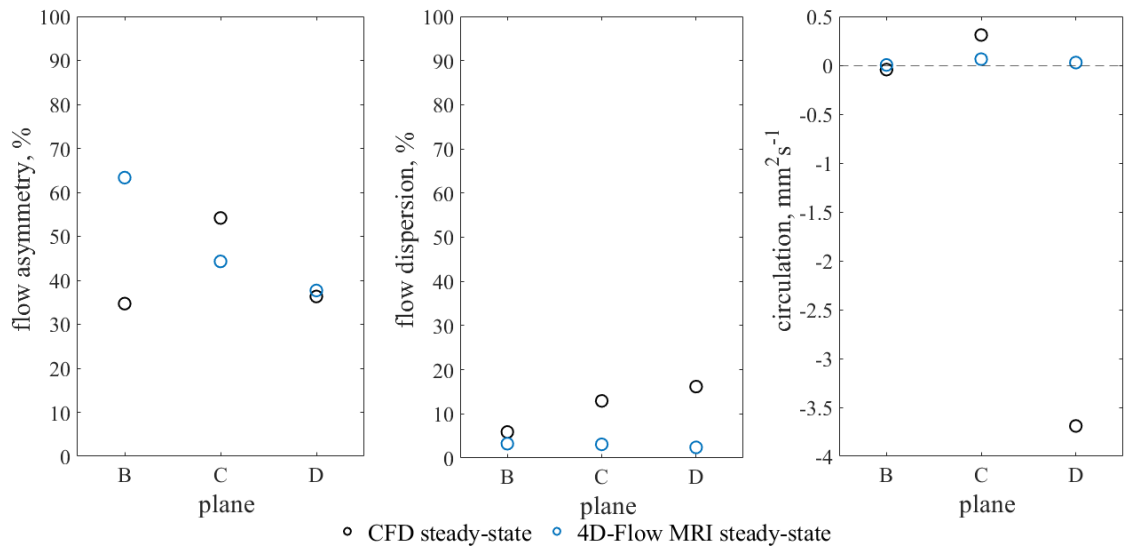


Figure 4.5. Flow asymmetry (%), flow dispersion (%), and through plane circulation ($\text{mm}^2 \text{s}^{-1}$) calculated at diastole from 4D-Flow MRI data and steady-state plug profile CFD data at three planes of interest. (B =mid-ascending aorta, C =aortic arch, D =mid-descending aorta.)

applied is inadequate and must be altered to better replicate the aortic valve and the flow profile that is present. It is also likely that the discrepancies in flow patterns are caused by comparing steady-state simulations with transient 4D-Flow MRI data. Further causes of these errors are discussed in Section 4.2.1.

Based on the accuracy of the steady-state plug profile results collected, boundary conditions at the inlet that model the full cardiac cycle were implemented as the next incremental change, working towards the aim of including physiologically accurate boundary conditions in the CFD workflow. This allows a more meaningful comparison between the CFD and 4D-Flow MRI data, as steady-state data will no longer be compared to inherently transient data.

4.3 Pulsatile Plug Flow

Following the method outlined in Section 3.5.2, the full cardiac cycle was modelled by incorporating a pulsatile inlet boundary condition. The magnitude of the plug profile applied at the inlet was varied according to the average volumetric flow rate across the inlet at each discrete time-step recorded by 4D-Flow MRI data during the cardiac cycle. Three cardiac cycles were modelled using the *pisoFoam* solver for turbulent, incompressible, transient flows within OpenFOAM, and the results taken from the last cycle to ensure periodicity was reached. Simulations were run using patient-specific data and geometry from the patient OXBAV012. Using the same patient as Section 4.2 allows transient results to be compared to steady state results, enabling the differences to be observed. Results from the CFD simulations were compared to 4D-Flow MRI data at peak systole and late diastole. As the flow varied between the laminar, transitional, and turbulent regimes throughout the cardiac cycle, the $k - \omega$ SST turbulence model was incorporated into the CFD model.

4.3.1 Peak Systole

Contours of velocity magnitude at peak systole can be seen in Figure 4.6. It is evident that there is limited agreement between CFD results and 4D-Flow MRI data in terms of the flow patterns seen and the velocity magnitude. As stated by Miyazaki *et al.* [120], flow in the ascending aorta is governed by the inlet conditions whilst flow in the aortic arch and descending aorta is governed by the geometry and curvature of the vessel, therefore the disagreement in the ascending aorta, where the flow is being governed by the inlet conditions, points to insufficient inlet conditions whilst the differences in the aortic arch and descending aorta suggest the lack of supra-aortic vessels and non-physical outlet conditions are the cause of the discrepancies in the flows. This indicates that the inlet conditions, despite replicating the inherently transient nature of the cardiac cycle, are still insufficient and do not accurately replicate the blood flow that is being ejected from the aortic valve at systole. Despite the velocity magnitude being grossly overestimated by the CFD methods, introducing a pulsatile inlet condition reduces the difference in maximum velocity magnitude between the CFD methods and the 4D-Flow MRI data when compared to the steady state simulations with a plug profile. A pulsatile inlet condition produces a 99.80% increase of maximum velocity magnitude when compared to 4D-Flow MRI data, reduced from a 141.08% increase when a steady state plug profile is applied to the inlet.

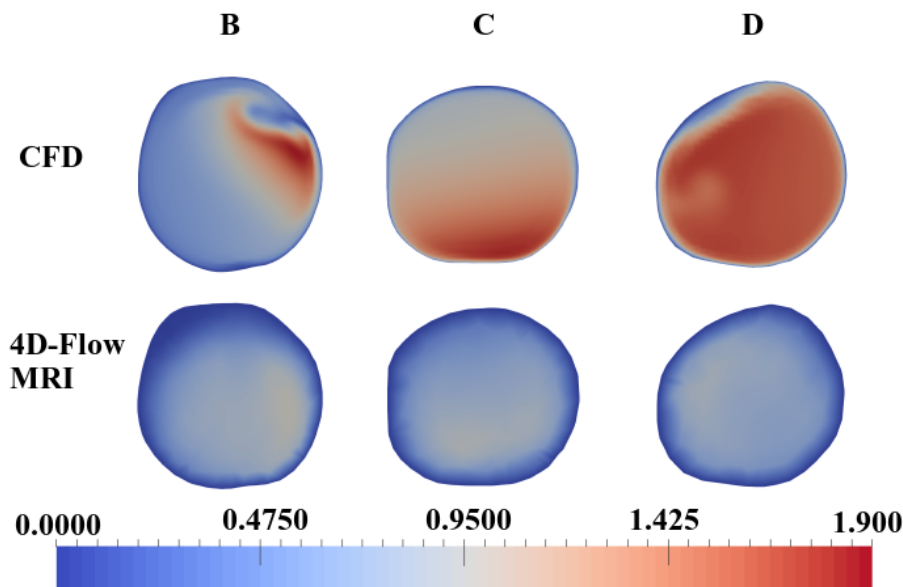


Figure 4.6. Contours of velocity magnitude (ms^{-1}) calculated through pulsatile CFD simulations with a plug profile and 4D-Flow MRI data at peak systole ($t = 0.1071s$) at three planes of interest for patient OXBAV012. (B=mid-ascending aorta, C=aortic arch, D=mid-descending aorta.)

The flow asymmetry, flow dispersion, and circulation values that were calculated at the three planes of interest at systole can be seen in Figure 4.7 compared to the corresponding 4D-Flow MRI values at the same time-step. It is clear that there are significant discrepancies between the CFD data and the 4D-Flow MRI results. However, there is on average improved agreement between the CFD results and the 4D-Flow MRI results in terms of flow asymmetry and flow dispersion when compared to results from the steady state CFD simulations; the average difference between CFD values and 4D-Flow MRI data across all locations reduces from 90.51% to 71.95% for flow asymmetry and the average difference across all locations between the CFD data and 4D-Flow MRI data reduces from 84.49% to 74.15% for flow dispersion when compared to the steady state

CFD simulations. Circulation data does not show improved agreement in terms of magnitude when compared to the steady state CFD simulations, as CFD data consistently under-estimates the magnitude at all three planes of interest by 199.8%, 198.2%, and 199.3% across planes B, C, and D respectively. However, the circulation direction suggested by both CFD and 4D-Flow MRI agrees at all three locations when a pulsatile inlet condition is used. Despite the increasing difference in circulation magnitude values between the CFD and 4D-Flow MRI data, at all three planes, both CFD and 4D-Flow MRI data indicate the helical flow levels are within a normal range ($-5\text{mm}^2\text{s}^{-1} \leq \Gamma \leq 11\text{mm}^2\text{s}^{-1}$). It can therefore be concluded that incorporating a pulsatile inlet condition improves the accuracy of the CFD methods at systole.

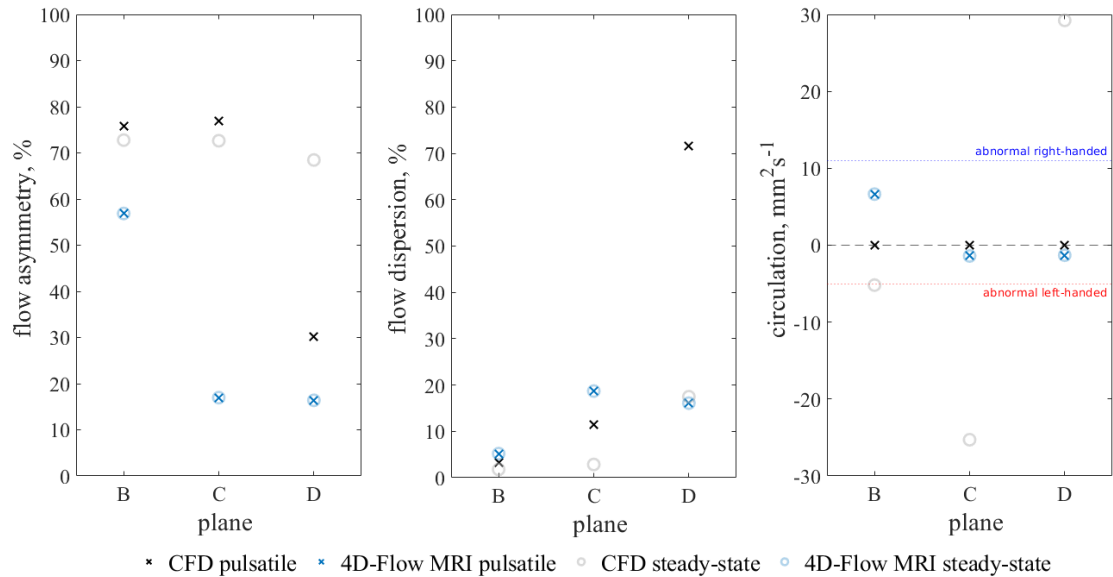


Figure 4.7. Flow asymmetry (%), flow dispersion (%), and through plane circulation (mm^2s^{-1}) calculated at systole from 4D-Flow MRI data and pulsatile plug profile CFD data at three planes of interest. (*B*=mid-ascending aorta, *C*=aortic arch, *D*=mid-descending aorta.)

4.3.2 Late Diastole

Results from a pulsatile simulation for patient OXBAV012 with a plug profile were also recorded at late diastole and compared to the corresponding 4D-Flow MRI time-step. Contours of velocity magnitude in the three axial planes of interest can be seen in Figure 4.8. There are clear discrepancies between the CFD results and the 4D-Flow MRI data in the ascending aorta with the CFD methodology over-estimating the magnitude of the velocity, likely a result of the inlet conditions being inadequate. The velocity magnitude in the aortic arch and mid-descending aorta appears to agree between the two methods to a better degree than the remainder of the domain.

The disagreement between the CFD results and the 4D-Flow MRI data can also be seen in the flow asymmetry, flow dispersion, and circulation results shown in Figure 4.9. There is excellent agreement in the mid-ascending aorta in terms of flow dispersion with the two methods predicted values only 0.1400% apart, however as the flow progresses through the aorta the disagreement increases, from 4.760% in the aortic arch to 35.20% in the mid-descending aorta. The flow asymmetry is overestimated at all three locations by the CFD simulations, with the differences in the mid-ascending aorta, aortic arch and mid-descending aorta of 18.56%, 35.61%, and 30.25% respectively. The circulation demonstrates discrepancies in both magnitude and direction when

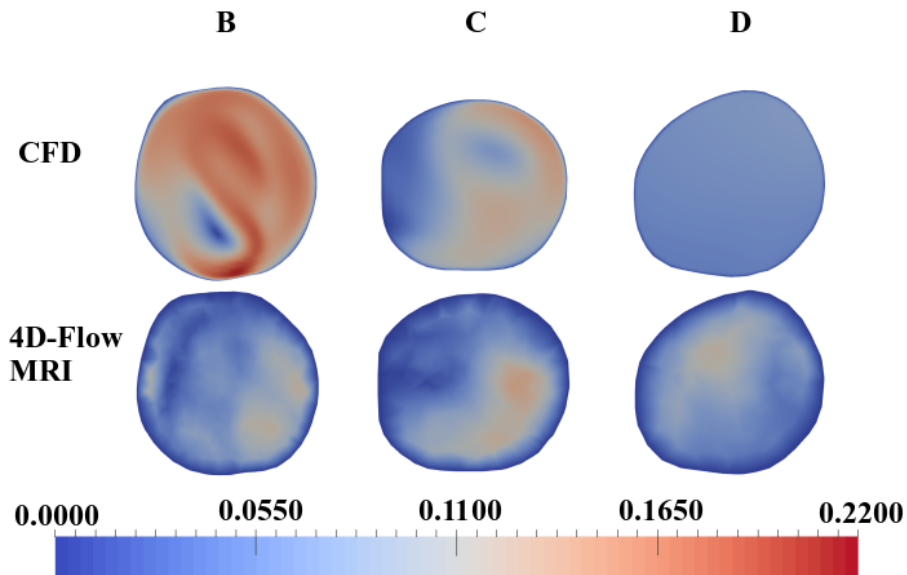


Figure 4.8. Contours of velocity magnitude ($m\cdot s^{-1}$) calculated through pulsatile CFD simulations with a plug profile and 4D-Flow MRI data at diastole ($t = 0.8571s$) at three planes of interest for patient OXBAV012. ($B=mid\text{-ascending aorta}$, $C=aortic arch$, $D=mid\text{-descending aorta}$.)

compared to 4D-Flow MRI data, however, similarly to the results at peak systole, both CFD and 4D-Flow MRI data indicate the helicity levels at all three planes of interest are within the normal range. These results further imply that the inlet conditions are inaccurate, and the decision to neglect the supra-aortic vessels impacts the flow considerably throughout the thoracic aorta.

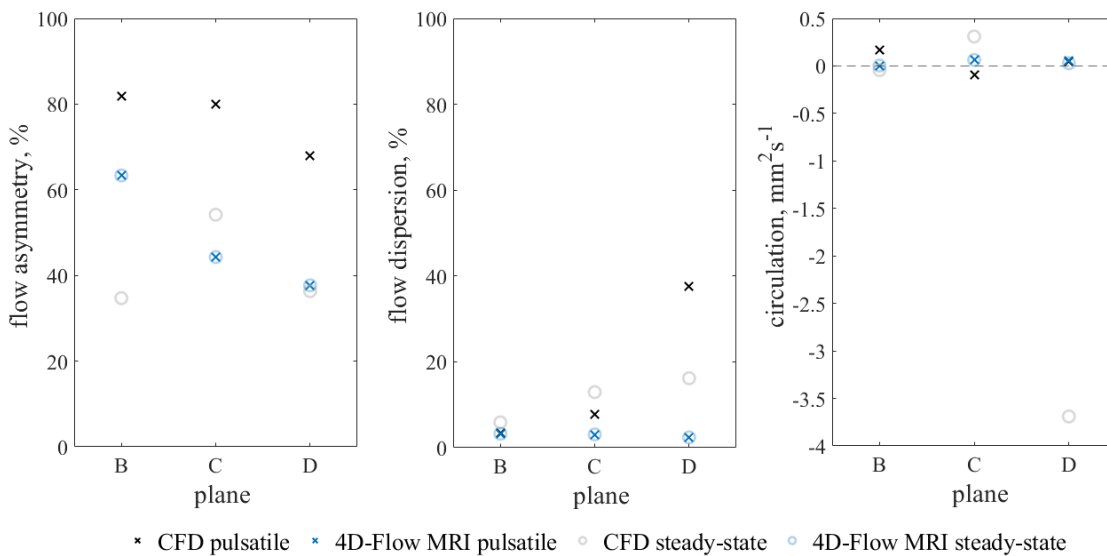


Figure 4.9. Flow asymmetry (%), flow dispersion (%), and through plane circulation ($mm^2 s^{-1}$) calculated at diastole from 4D-Flow MRI data and pulsatile plug profile CFD data at three planes of interest. ($B=mid\text{-ascending aorta}$, $C=aortic arch$, $D=mid\text{-descending aorta}$.)

Based on the results presented within this section, it is clear that the flow patterns at the inlet are contributing significantly to the discrepancies seen between the CFD and 4D-Flow MRI data. Therefore, the next incremental change to the methodology was to incorporate spatio-temporal patient-specific inlet conditions.

4.4 Spatio-Temporal Patient Specific Flow

The methodology was updated to include spatio-temporal patient-specific inlet boundary conditions, using the steps outlined in Section 3.5.3. Results from CFD simulations with a spatio-temporal patient-specific inlet condition at systole and diastole are presented for the five neonatal patients listed in Table 3.2. At this point in the research the patient cohort was altered to neonatal patients to observe how the methodology would function with a thoracic aorta of a significantly smaller size to the adult patients used in previous simulations. Neonatal patients were also selected as far as the authors are aware, studies combining CFD and 4D-Flow MRI methods have not been undertaken on neonatal patients. Three cardiac cycles were run using the large time-step solver, *pimpleFoam*, for transient, turbulent, incompressible flows within OpenFOAM, which uses the merged PISO-SIMPLE algorithm. A variable time-step was implemented using the *adjustTimeStep* functionality of *pimpleFoam* with the initial patient-specific Δt set using the Courant number, (see Equation 4.1 where C is the Courant number, u is the velocity magnitude, Δt is the time step size, and Δx is the length between the mesh elements). All results are taken from the last cardiac cycle simulated to ensure periodicity was reached. Throughout the course of the cardiac cycle, the flow progressed through the turbulent, transient, and laminar regimes. Therefore the $k - \omega$ SST turbulence model was incorporated into the numerical models for all patients with patient-specific parameters. Blood was again assumed to be an incompressible, Newtonian, and homogeneous fluid. In addition to the more physiologically accurate inlet condition, the angle of the inlet plane was adjusted to a more physiologically accurate angle.

$$C = u \frac{\Delta t}{\Delta x} \quad (4.1)$$

4.4.1 Systole

Contours of velocity magnitude were plotted in the three planes of interest for all neonatal patients and CFD results compared to 4D-Flow MRI, see Figure 4.10. In patients 1-4 there is good agreement in the mid-ascending aorta. The agreement between CFD results and 4D-Flow MRI data in the ascending aorta is likely a result of the improved inlet conditions as the velocity profile is at the inlet is now replicated correctly. However, as the flow progresses through the thoracic aorta there is significantly less agreement between CFD and 4D-Flow MRI data. There are notable differences in the velocity magnitude as well as the flow patterns in the descending aorta and aortic arch with the velocity magnitude being largely overestimated by the CFD results. It is likely these errors stem from the choice to not include the supra-aortic vessels at this stage, and therefore is a result of the geometry being incorrect, as opposed to the flow being incorrectly predicted by the numerical methods, and is supported by the findings of Miyazaki *et al.* [120] where it is found that flow in the descending aorta is governed by the geometry and curvature of the vessel. The oversimplified outlet condition in the descending aorta will also contribute to errors in the descending aorta.

The flow asymmetry, flow dispersion, and circulation were calculated at all three planes of interest for each of the five neonatal patients using the methods discussed in Section 3.7. Flow asymmetry can be seen in Figure 4.11, whilst flow dispersion is shown in Figure 4.12. Circulation results are shown in Figure 4.13. The differences in flow asymmetry increase in the aortic arch and

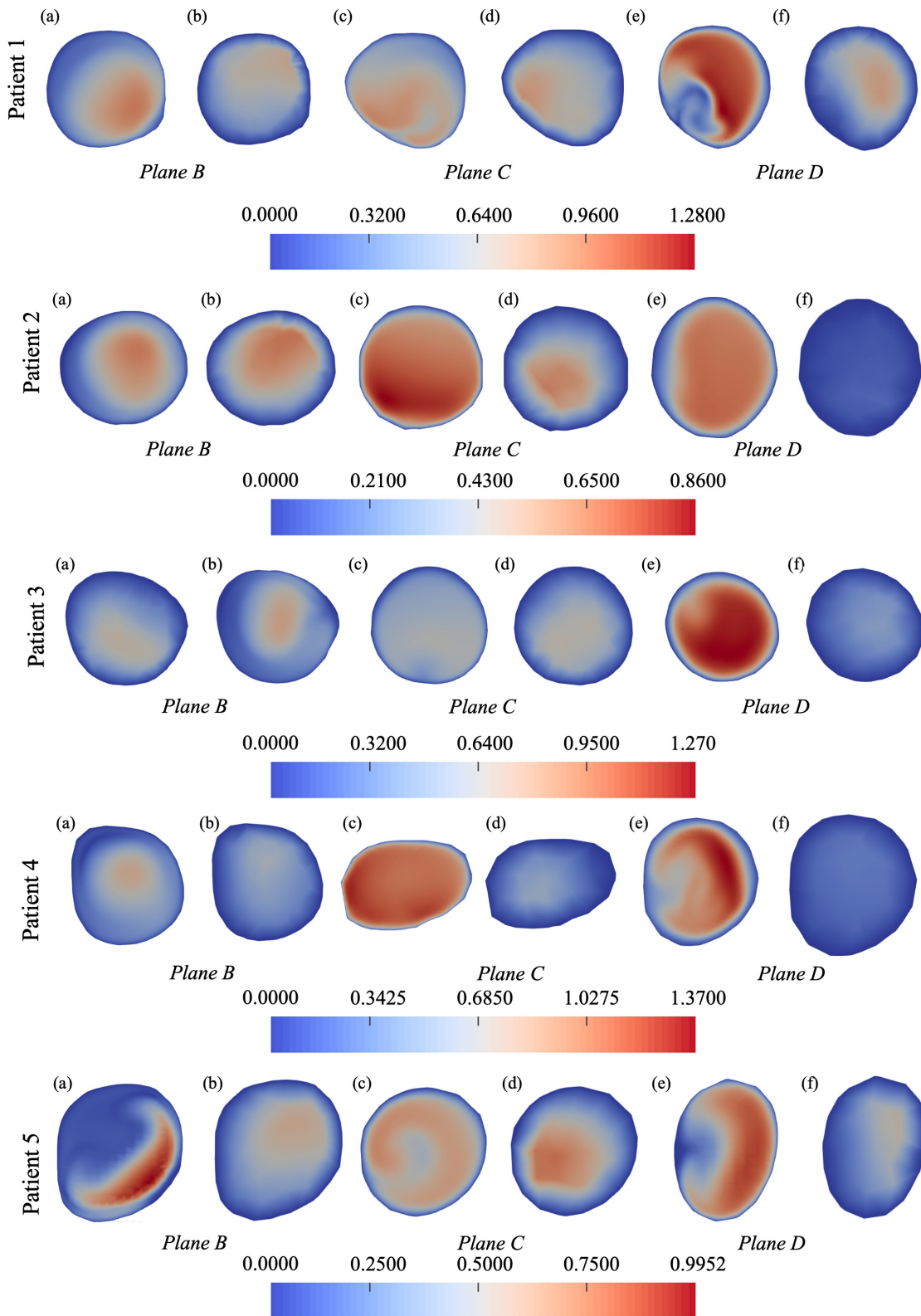


Figure 4.10. Contours of velocity magnitude ($m s^{-1}$) at three planes of interest for all patients at systole. Velocity contours calculated through the CFD methodology are given in (a),(c) and (e). Velocity contours calculated by 4D-Flow MRI are given in (b), (d), and (f). (*B*=mid-ascending aorta, *C*=aortic arch, *D*=mid-descending aorta).

descending aorta compared to the mid-ascending aorta. Flow in the mid-ascending aorta experiences an average difference between CFD results and 4D-Flow MRI data across all five patients of 10.72%, increasing to 21.91% and 20.23% in the aortic arch and descending aorta respectively.

The markedly higher agreement in the mid-ascending aorta suggests that the spatio-temporal inlet conditions produce more accurate flow than the steady state and pulsatile plug profiles, which produced flow asymmetry differences between CFD results and 4D-Flow MRI data of 15.90% and 18.97% respectively in the mid-ascending aorta. This highlights the improvement made by incorporating an inlet condition that has continuous spatio-temporal variations, notably at systole.

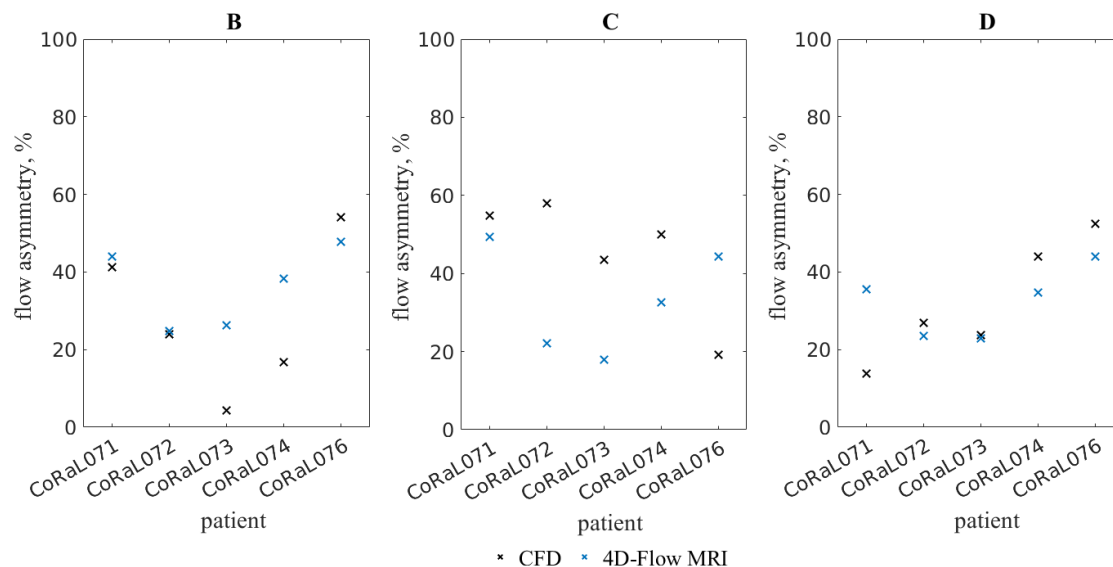


Figure 4.11. Flow asymmetry (%) calculated at systole for the five neonatal patients with spatio-temporal patient-specific inlet conditions at the three planes of interest. CFD values are compared to 4D-Flow MRI data. (B=mid-ascending aorta, C=aortic arch, D=mid-descending aorta).

The agreement between CFD results and 4D-Flow MRI data for flow dispersion decreases as the blood flow progresses through the thoracic aorta. There is excellent agreement in the mid-ascending aorta with an average difference between methods across all five patients of 3.14%, increasing to 8.70% in the aortic arch, and 22.28% in the descending aorta. Although there is no improvement in the agreement levels of flow dispersion between 4D-Flow MRI and CFD data when compared to steady-state and pulsatile plug profile CFD simulations, agreement in the mid-ascending aorta remains excellent, and is $\leq 5\%$. The increasing disagreement as the flow progresses through the thoracic aorta highlights that the geometry is clearly incorrect and the outlet boundary condition is insufficient.

The circulation was determined at all three planes of interest at systole and CFD results were compared to the 4D-Flow MRI results for all five patients, shown in Figure 4.13. The magnitude of the circulation is significantly overestimated by CFD methods in 80% of the neonatal patients in all three planes. There are significant discrepancies between the values and directions. Direction agrees in 60% of patients in the mid-ascending aorta, however this reduces to 20% in the aortic arch, before rising again to 60% in the descending aorta. It can be seen in the mid-ascending aorta, CFD and 4D-Flow MRI agree in only two patients that there is normal helical flow levels, reducing to only one patient in the aortic arch, and increasing to four patients in the descending aorta. It is likely the reduced agreement in terms of circulation direction and helicity abnormality seen in the aortic arch is a consequence of neglecting the supra-aortic vessels. As the supra-aortic vessels begin at the aortic arch it is clear they will influence the flow patterns in that region of the thoracic aorta heavily.

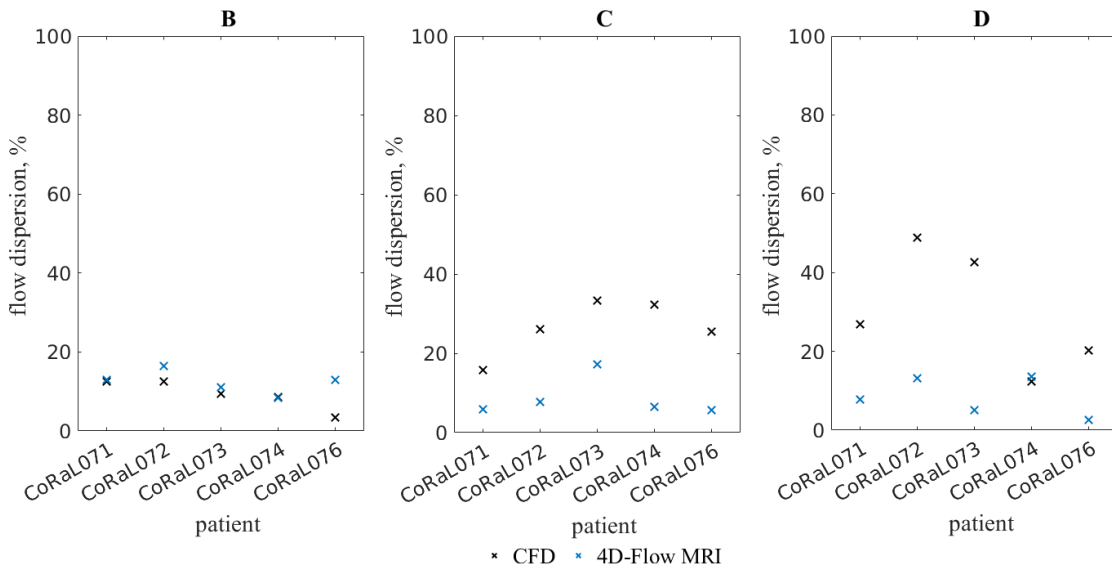


Figure 4.12. Flow dispersion (%) calculated at systole for the five neonatal patients with spatio-temporal patient-specific inlet conditions at the three planes of interest. CFD values are compared to 4D-Flow MRI data. (*B*=mid-ascending aorta, *C*=aortic arch, *D*=mid-descending aorta).

The age of the patients must also be considered when observing the circulation values; circulation decreases with age and as such, higher values are to be expected when a young population is being studied. The circulation values for the neonatal patients determined through 4D-Flow MRI appear to be consistent with the values found in the study by Hess *et al.* [184], where the mean age of participants is 36.7 years. This brings to light the possibility of 4D-Flow MRI underestimating the circulation in the thoracic aorta within the neonatal population, whilst also suggesting a potential explanation to the significantly higher circulation values calculated through CFD methods for some patients.

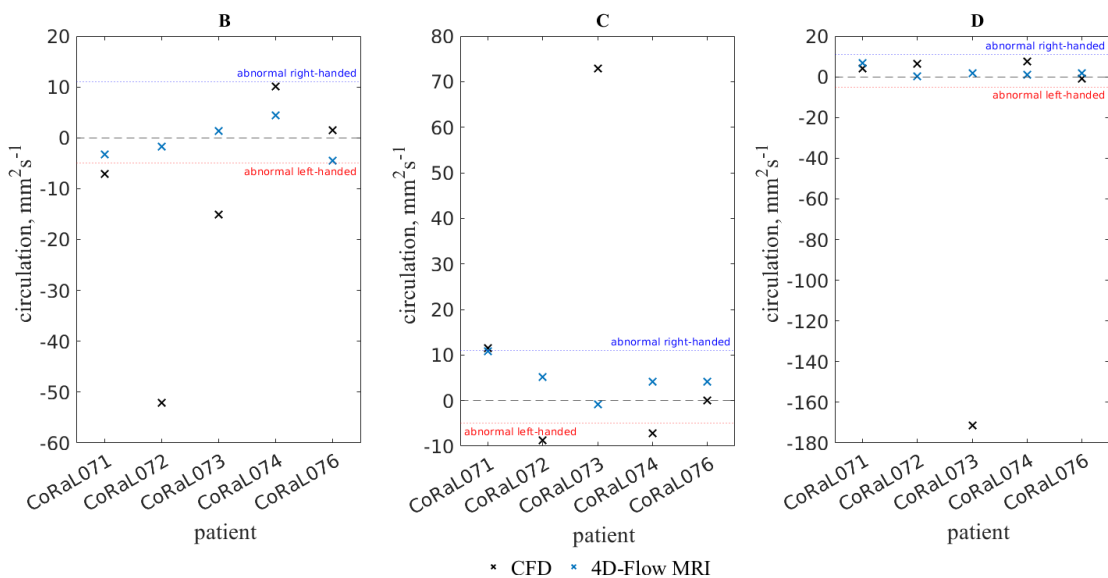


Figure 4.13. Through-plane circulation (mm^2s^{-1}) calculated at systole for the five neonatal patients with spatio-temporal patient-specific inlet conditions at the three planes of interest. CFD values are compared to 4D-Flow MRI data. (*B*=mid-ascending aorta, *C*=aortic arch, *D*=mid-descending aorta).

4.4.2 Diastole

Contours of velocity magnitude were plotted over the three planes of interest for all neonatal patients at diastole, and compared to data from 4D-Flow MRI scans. Figure 4.14 indicates that the agreement within the ascending aorta between CFD results and 4D-Flow MRI appears to be qualitatively reduced when compared to results from systole. This is possibly a consequence of the fluctuations within the velocity profile at the inlet being on a much smaller scale than those present at systole; when the surface fit is applied to the 4D-Flow MRI data to create the inlet boundary condition, the smaller scale fluctuations will be neglected when compared to the much larger variation seen over the systolic period. This can be seen clearly in patient CoRaL071; although the average magnitude is similar, the flow patterns vary significantly as the small variations are not modelled in the CFD results. It is also likely the discrepancies during diastole are a result of neglecting to incorporate the aortic valve leaflets in the numerical model. As the valve leaflets will be influencing the *in-vivo* 4D-Flow MRI data, this will produce differences in the flow around the aortic valve between the CFD and 4D-Flow MRI data.

The CFD methodology overestimates the velocity magnitude within the descending aorta for all patients, this is a result of the supra-aortic vessels not being included, causing a higher volume of flow to pass through the descending aorta, resulting in a higher velocity than the 4D-Flow MRI suggests. The velocity magnitude is also overestimated in the aortic arch of patients 2,3, and 4. Again, it is likely this is a consequence of neglecting the supra-aortic vessels. As the location of the supra-aortic vessels varies on a patient by patient basis, the location of the supra-aortic vessels relative to the slice of interest will be a factor in why the velocity magnitude is overestimated in the aortic arch of only some patients. From these results it is clear that if the aortic arch and descending aorta are of interest to the clinicians, then neglecting the supra-aortic vessels will artificially increase the velocity magnitude of the blood flow within the vessel which must be accounted for before any clinical conclusions are made.

The flow asymmetry and flow dispersion were calculated using the methods discussed in Section 3.7 at all three planes of interest for all neonatal patients included in the study, and results compared to 4D-Flow MRI data. Figures 4.15 and 4.16 show flow asymmetry and flow dispersion results for planes in the ascending aorta, aortic arch, and descending aorta. The flow asymmetry indicates significant differences between CFD and 4D-Flow MRI data. The average difference in the flow asymmetry between the methods across all five neonatal patients is 18.91%, 15.51%, and 13.34% in the mid-ascending aorta, the aortic arch, and the descending aorta respectively. The higher discrepancies in the ascending aorta may be a consequence of the flow in that location being guided more by the inlet condition than the geometry of the vessel. As discussed previously, the inlet conditions at diastole neglect the small fluctuations and the movement of the valve leaflets that are seen in the 4D-Flow MRI data, as a result the location of the top 15% of velocities may not be as accurate as the 4D-Flow MRI data.

It is clear that at all three locations, the CFD methodology overestimates the flow dispersion, predicting a much broader profile than suggested by 4D-Flow MRI data. The average differences between the CFD and 4D-Flow MRI data at the three locations are 30.11%, 43.63%, and 41.26% in planes B, C, and D respectively. It is likely this is another consequence of the smaller fluctuations in the flow being neglected by the CFD inlet boundary condition; the inlet condition

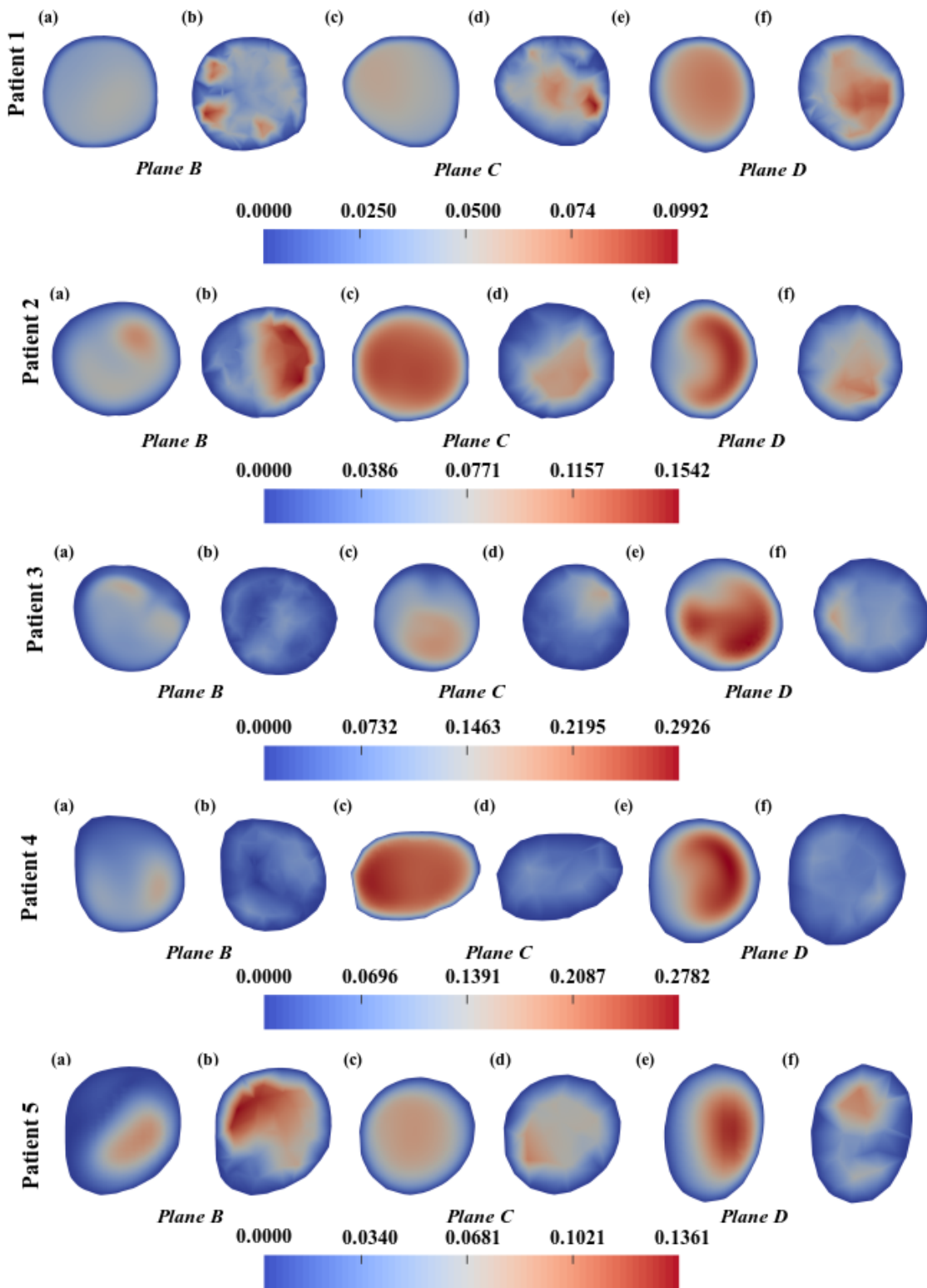


Figure 4.14. Contours of velocity magnitude ($m \cdot s^{-1}$) at three planes of interest for all patients at diastole. Velocity contours calculated through the CFD methodology are given in (a), (c) and (e). Velocity contours calculated by 4D-Flow MRI are given in (b), (d), and (f).

being applied produces a much smoother and uniform profile than 4D-Flow MRI data suggests is present. With a more uniform inlet condition it is likely the flow itself will progress through the thoracic aorta with a broader profile.

Similarly to circulation at systole, there are notable differences in the circulation values between

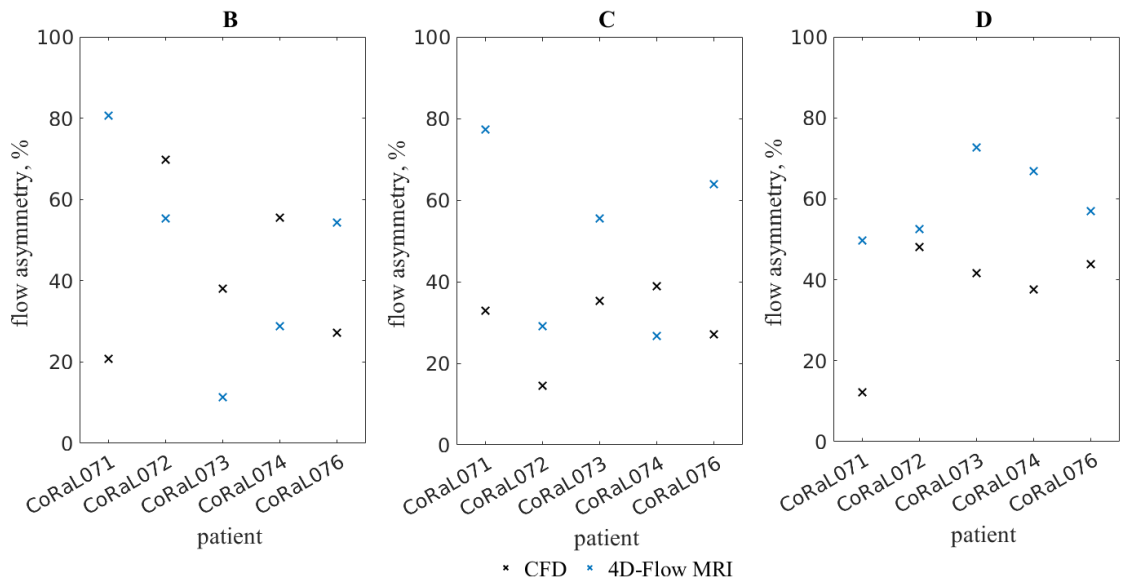


Figure 4.15. Flow asymmetry (%) calculated at diastole for the five neonatal patients with spatio-temporal patient-specific inlet conditions at the three planes of interest. CFD values are compared to 4D-Flow MRI data. (B=mid-ascending aorta, C=aortic arch, D=mid-descending aorta).

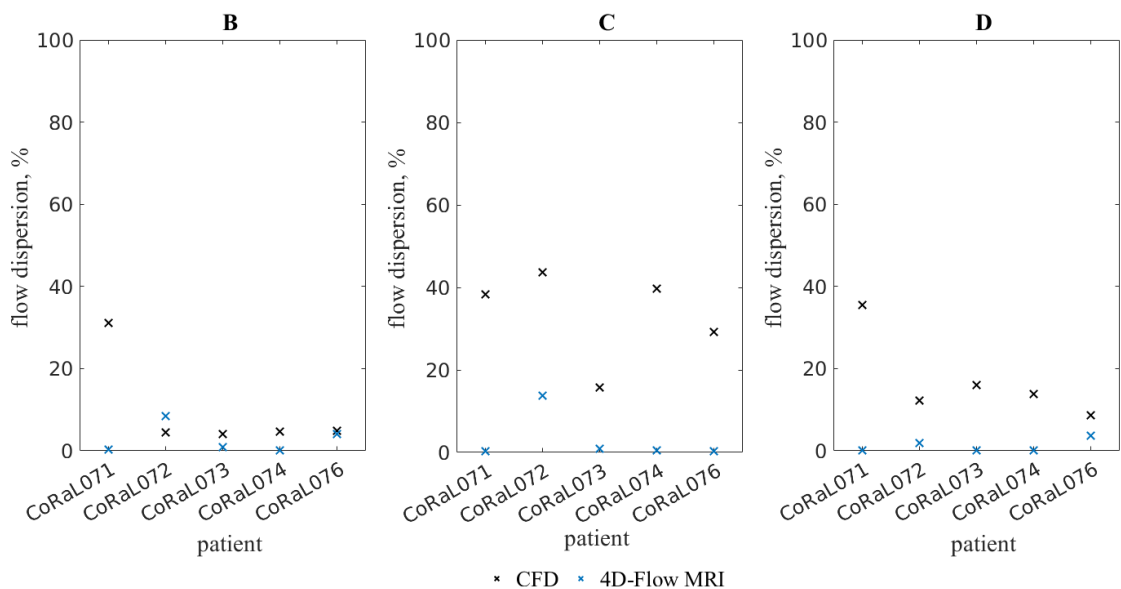


Figure 4.16. Flow dispersion (%) calculated at diastole for the five neonatal patients with spatio-temporal patient-specific inlet conditions at the three planes of interest. CFD values are compared to 4D-Flow MRI data. (B=mid-ascending aorta, C=aortic arch, D=mid-descending aorta).

methods at diastole (see Figure 4.17). The average differences between CFD and 4D-Flow MRI data across the planes in the mid-ascending aorta, aortic arch, and mid-descending aorta are 180.6%, 102.2%, and 151.3% respectively. CFD results overestimate the circulation magnitude in all five patients in the aortic arch, and in patient CoRaL073 in all three planes. In the ascending aorta the circulation direction agrees in only 1 patient, in the aortic arch 2 patients, and 3 in the descending aorta. It is possible to attribute this increasing agreement in circulation direction as the flow move through the thoracic aorta to the small errors in the inlet condition; the flow in the ascending aorta is primarily governed by the inlet condition, and not the inclusion of the supra-aortic vessels and the geometry of the domain. Therefore it can be assumed that neglecting the smaller fluctuations in the velocity profile alters the circulation in the ascending aorta significantly at di-

astole. The discrepancies in magnitude and direction in the aortic arch and mid-descending aorta can be attributed to inaccuracies in the vessel geometry, primarily neglecting the supra-aortic vessels. Despite the clear differences in the magnitude and direction, both CFD and 4D-Flow MRI data indicate normal levels of helical flow in 4 neonatal patients, and disagree only for patient CoRaL073, where the magnitude is considerably overestimated by CFD data.

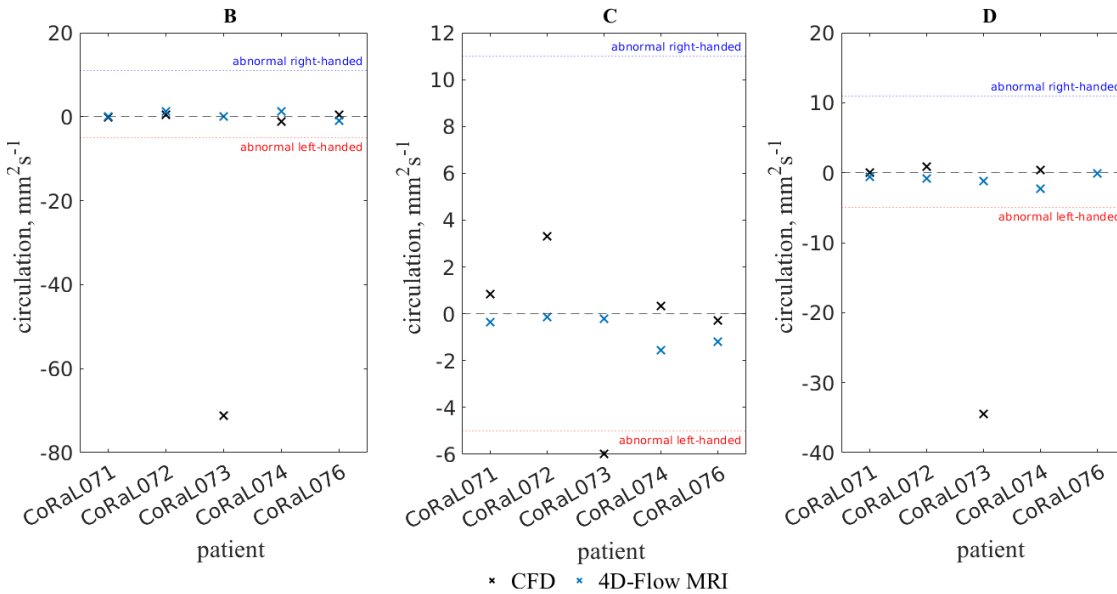


Figure 4.17. Through-plane circulation ($mm^2 s^{-1}$) calculated at diastole for the five neonatal patients with spatio-temporal patient-specific inlet conditions at the three planes of interest. CFD values are compared to 4D-Flow MRI data. (*B*=mid-ascending aorta, *C*=aortic arch, *D*=mid-descending aorta).

4.5 Supra-Aortic Vessels Within the Neonatal Cohort

As discussed in Section 4.4, it is evident that neglecting the supra-aortic vessels causes notable discrepancies between the CFD methodology and the 4D-Flow MRI results. To address the errors caused by neglecting the supra-aortic vessels, the thoracic aorta and supra-aortic vessels of neonatal patient CoRaL072 were reconstructed and the haemodynamics modelled and compared to the 4D-Flow MRI data. Patient CoRaL072 from the neonatal cohort was selected as they were the only neonatal patient whose supra-aortic vessels were visible enough on the 4D-Flow MRI scan data to attempt the geometry reconstruction process detailed in Section 3.3. In all other neonatal patients participating in this research, the supra-aortic vessels were not visible in the 4D-Flow MRI scan due to the low flow velocities present and the small size and intricate nature of the vessels; where sections of the vessels were visible they were described by too few voxels (< 6) to provide an accurate representation of the blood flow through the vessel [169]. The reconstructed geometry and locations of the additional outlets of neonatal patient CoRaL072 with the supra-aortic vessels included can be seen in Figure 4.18. Disregarding the changes in geometry and boundary conditions, the CFD simulations were set up and run in the same manor as discussed in Section 4.4.

As an additional three outlets were included in the numerical model, the outlet boundary conditions were updated from 0-pressure to a more physiologically accurate condition. Outflow percentages were prescribed at each outlet based on the cross sectional area of the vessel. It was determined that

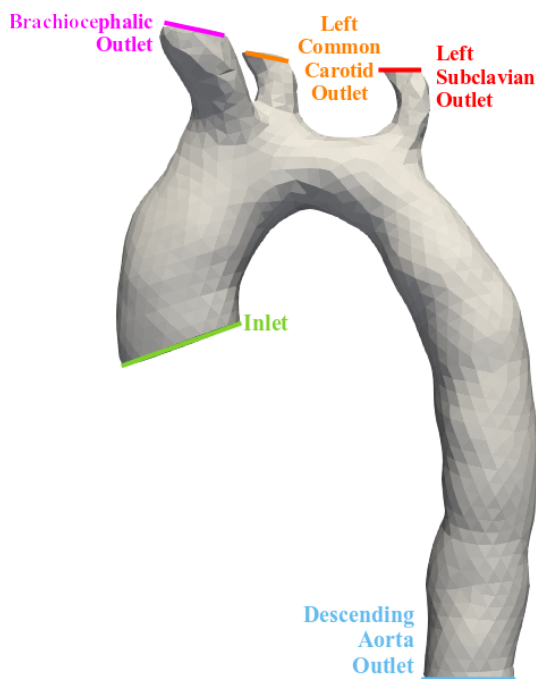


Figure 4.18. Geometry reconstruction of neonatal patient CoRaL072 showing the location of the additional three outlets when the supra-aortic vessels are included.

approximately 28% of the inflow volume leaves through the brachiocephalic artery, 9% through the left common carotid artery, 6% through the left subclavian artery, and 57% through the descending aorta. These values are higher than suggested by both Caballero & Laín [57], and Middleman [59] as expected, as the outflow percentages suggested in both studies were for an adult patient and it is known that neonatal patients have proportionally larger heads and therefore will have proportionally larger head and neck vessels. The inlet condition applied was spatio-temporally patient-specific, as used in Section 4.4, with a continuous temporal variation.

The cardiac cycle was simulated and results from the systolic and diastolic periods, were compared to 4D-Flow MRI results with the same geometry, as well as being compared to CFD and 4D-Flow MRI results without supra-aortic vessels to observe the differences that can be attributed to altering the geometry.

4.5.1 Systole

Results from the systolic period were compared to 4D-Flow MRI at the three planes of interest. Contours of velocity magnitude from the CFD methods and 4D-Flow MRI data can be seen in Figure 4.19. When compared to the corresponding 4D-Flow MRI data, there is a clear improvement in the CFD data in the aortic arch and the descending aorta when the supra-aortic vessels are included. The maximum velocity magnitudes predicted by CFD and 4D-Flow MRI are within 16.59% of each other at the aortic arch, compared to 29.45% when the supra-aortic vessels are neglected. This improvement is more notable in the descending aorta, where the difference between the maximum velocity magnitude predicted by CFD and 4D-Flow MRI are within 25.35% of each other, compared to 78.20% when the supra-aortic vessels are neglected. In the ascending aorta, the agreement between CFD and 4D-Flow MRI remains relatively constant, increasing from 4.50% when the supra-aortic vessels are neglected to 5.27% when the supra-aortic vessels are included,

with CFD under-predicting the velocity magnitude in both cases. This data supports the hypothesis that the inclusion of the supra-aortic vessels is key to accurately modelling the aortic arch and descending aorta, and does not largely impact the accuracy in the ascending aorta. It can also be seen in Figure 4.19 that the flow patterns are consistent between CFD and 4D-Flow MRI, notably in the ascending aorta. This demonstrates that the method used to construct patient-specific inlet conditions is successful in replicating the blood flow in the ascending aorta at systole.

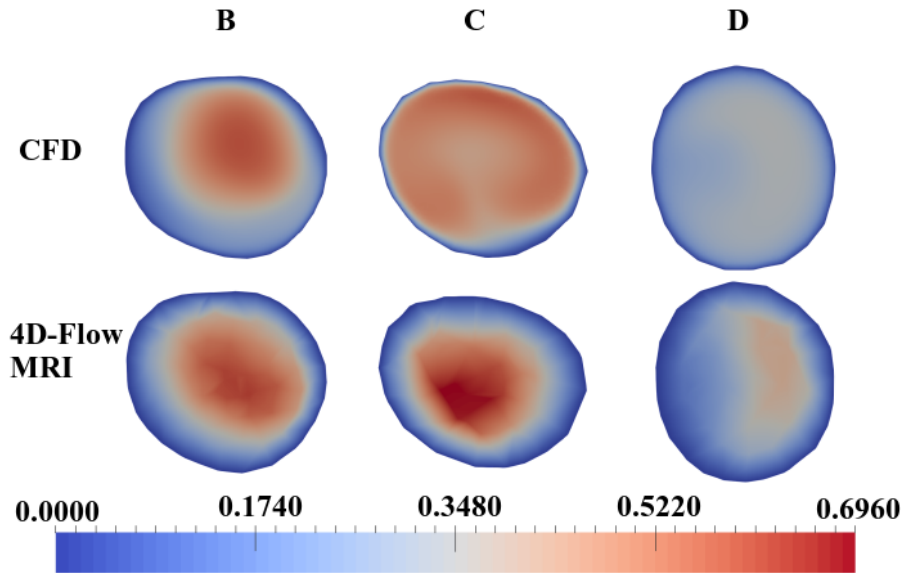


Figure 4.19. Contours of velocity magnitude (ms^{-1}) calculated through spatio-temporal patient-specific CFD simulations with the supra-aortic vessels included and 4D-Flow MRI data at systole at three planes of interest for the neonatal patient CoRaL072. (*B*=mid-ascending aorta, *C*=aortic arch, *D*=mid-descending aorta).

Despite the improved performance of the CFD methodology there are still discrepancies at the aortic arch and descending aorta. The outflow percentages prescribed at the three additional outlets are approximations, and are subject to significant human error as they are dependant on the cross sectional area of the individual supra-aortic vessels, which is in turn dependent on the geometry reconstruction. Due to the intricate nature, slower flow speeds, and smaller size of the vessels of neonatal patients, they are difficult to observe in the 4D-Flow MRI data, and as such the segmentation and geometry reconstruction process will not be as accurate compared to the thoracic aorta. This will lead to errors in the volumetric flow rates prescribed to the outlets. This will not cause such large issues when adult patients are used in the research as the supra-aortic vessels in an adult patient are fully visible and significantly larger than in the neonatal population. An additional consideration is that the supra-aortic outlets are less than 5 diameters downstream of the aortic arch, and as such flow in the aortic arch will be affected by insufficient boundary conditions as although outflow conditions provide an improvement to the 0-pressure conditions used previously, they are still physiologically inaccurate.

The discrepancies seen may also be a result of the *4D-Flow MRI APP* that is used to interpolate the velocity data from the 4D-Flow MRI data and allow it to be visualised. Figure 4.20 demonstrates the velocity magnitude cell data for both 4D-Flow MRI and CFD data in the aortic arch. It is clear that the cells are significantly larger and irregular in the 4D-Flow MRI data. It is therefore likely that this may be influencing the 4D-Flow MRI data, particularly the haemodynamic indices of interest such as the flow asymmetry and flow dispersion.

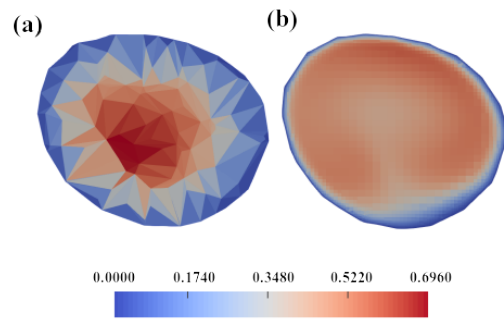


Figure 4.20. Velocity contours using cell data at the aortic arch during the systolic period for neonatal patient CoRaL072.

The flow asymmetry, flow dispersion, and circulation were determined at three planes of interest for neonatal patient CoRaL072, and compared to 4D-Flow MRI data, as well as to both CFD and 4D-Flow MRI data from simulations where the supra-aortic vessels are neglected. Figure 4.21 indicates that the circulation values calculated through the CFD methodology have improved significantly with the inclusion of the supra-aortic vessels and show better agreement with the circulation magnitude values predicted by 4D-Flow MRI, whilst the differences between CFD and 4D-Flow MRI for flow asymmetry and flow dispersion have remained approximately constant. It can also be seen that the levels of helical flow seen in all three planes of interest are well below the limits of abnormal flow from both CFD and 4D-Flow MRI data; this shows an improvement from CFD simulations without the supra-aortic vessels, where in both the ascending aorta and aortic arch, CFD data suggested the levels of helical flow were abnormal.

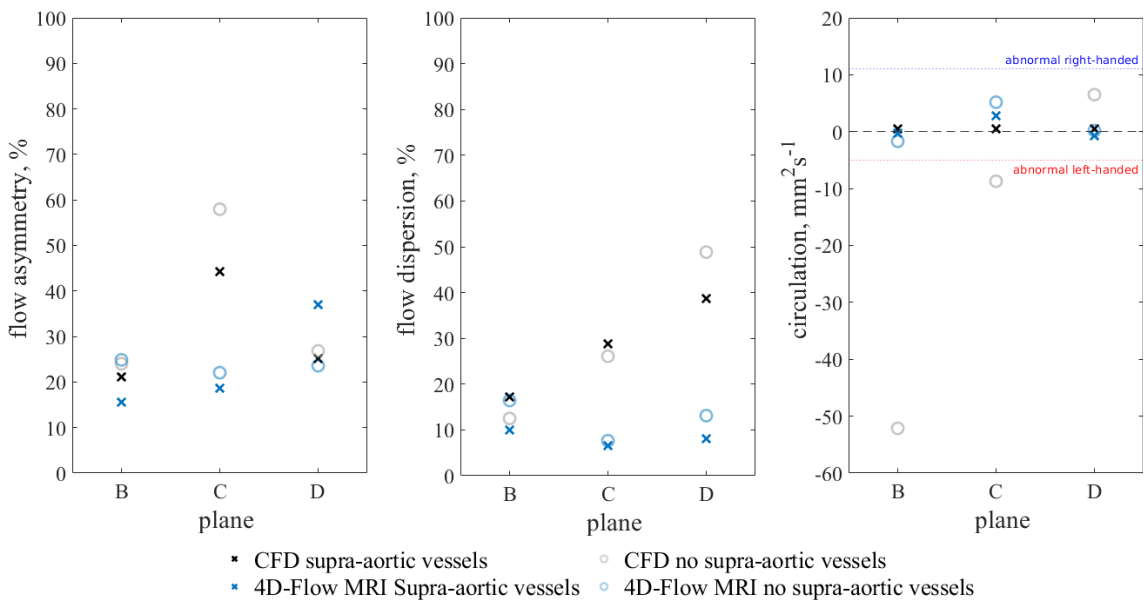


Figure 4.21. Flow asymmetry (%), flow dispersion (%), and through plane circulation (mm^2s^{-1}) at systole for neonatal patient CoRaL072 at three planes of interest with the supra-aortic vessels included, compared to the corresponding values when the supra-aortic vessels are neglected. (*B*=mid-ascending aorta, *C*=aortic arch, *D*=mid-descending aorta).

4.5.2 Diastole

Velocity contours at diastole determined through CFD show an improved agreement to the 4D-Flow MRI data when compared to CFD data from simulations that neglect the supra-aortic vessels.

The inclusion of the supra-aortic vessels causes the difference in maximum velocity magnitude between CFD and 4D-Flow MRI in the descending aorta to reduce from 21.44% when the supra-aortic vessels are neglected to only 7.74%, and from 36.59% to 17.52% in the ascending aorta. However, there are evidently significant differences in the aortic arch, with CFD grossly overestimating the velocity magnitude. It is possible this difference is due to insufficient outlet conditions not replicating the haemodynamics at diastole correctly. As discussed in Section 2.5.2, the vessel walls act as a reservoir during systole and the elastic rebound helps to drive the blood through the vessel at diastole. As this is not modelled by the outlet conditions it follows that they are not accurately replicating the diastolic haemodynamics. When observing the flow patterns present in the aorta, it is evident that the smaller fluctuations are yet again not picked up by the inlet conditions that are used, causing the CFD methodology to produce a flow profile that is broader and more central than 4D-Flow MRI suggests. In addition the haemodynamics of the movement of the aortic valve leaflets is neglected by the numerical model, whilst being included in the 4D-Flow MRI data.

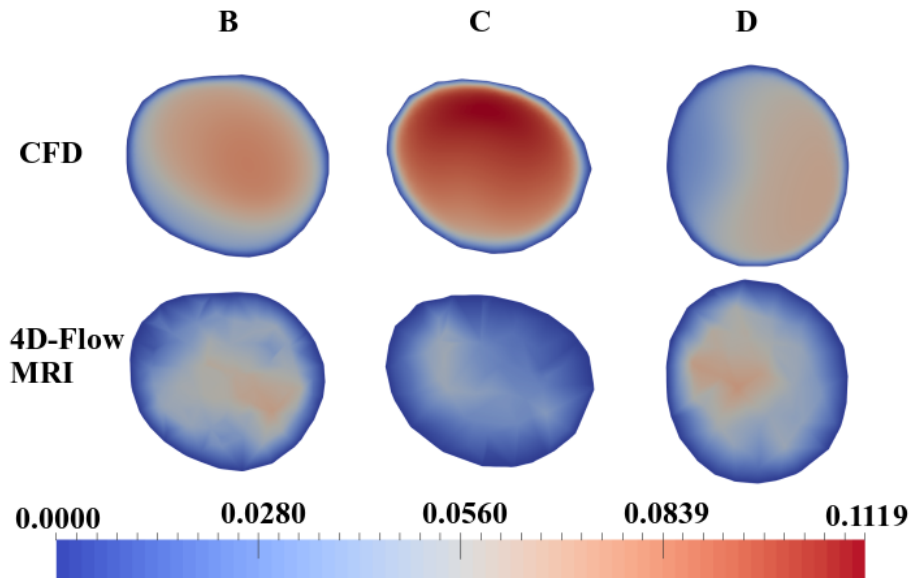


Figure 4.22. Contours of velocity magnitude (ms^{-1}) calculated through spatio-temporal patient-specific CFD simulations with the supra-aortic vessels included and 4D-Flow MRI data at diastole at three planes of interest for the neonatal patient CoRaL072. (*B*=mid-ascending aorta, *C*=aortic arch, *D*=mid-descending aorta).

Results from circulation also show improvements when compared to the geometry without supra-aortic vessels included in the ascending aorta and aortic arch, see Figure 4.23, with differences between CFD and 4D-Flow MRI data reducing to 96.93% and 113.5% in the mid-ascending aorta and aortic arch respectively from 196.7% and 182.1%. The circulation direction agrees in all three planes of interest, compared to none when the supra-aortic vessels are neglected. The magnitude of the circulation also shows better agreement when the supra-aortic vessels are included than when they are neglected. It can also be seen that CFD and 4D-Flow MRI data agree that the levels of helical flow in all three planes of interest are normal. The flow dispersion is overestimated in all three planes of interest by the CFD methodology and produces worse agreement than when the supra-aortic vessels are not included, however it is likely this is a result of the smaller fluctuations present at diastole being neglected due to the much larger variations present at systole, as discussed in Section 4.4. There are also large differences present in all three planes of interest

in the flow asymmetry results and agreement between CFD and 4D-Flow MRI data is marginally reduced compared to CFD simulations when the supra-aortic vessels are not included, with the average agreement over all three planes reducing from 11.14% to 17.22%, again this is a likely consequence of the inlet condition neglecting the smaller fluctuations present and the outlet conditions not accurately replicating the haemodynamics of diastole, and therefore affecting flow in the aortic arch and by extension descending aorta as the outlet boundary condition is within five diameters of the flow through the thoracic aorta. It is also likely that the spatial resolution of the 4D-Flow MRI scans is contributing significantly to the large discrepancies found between the CFD and 4D-Flow MRI data.

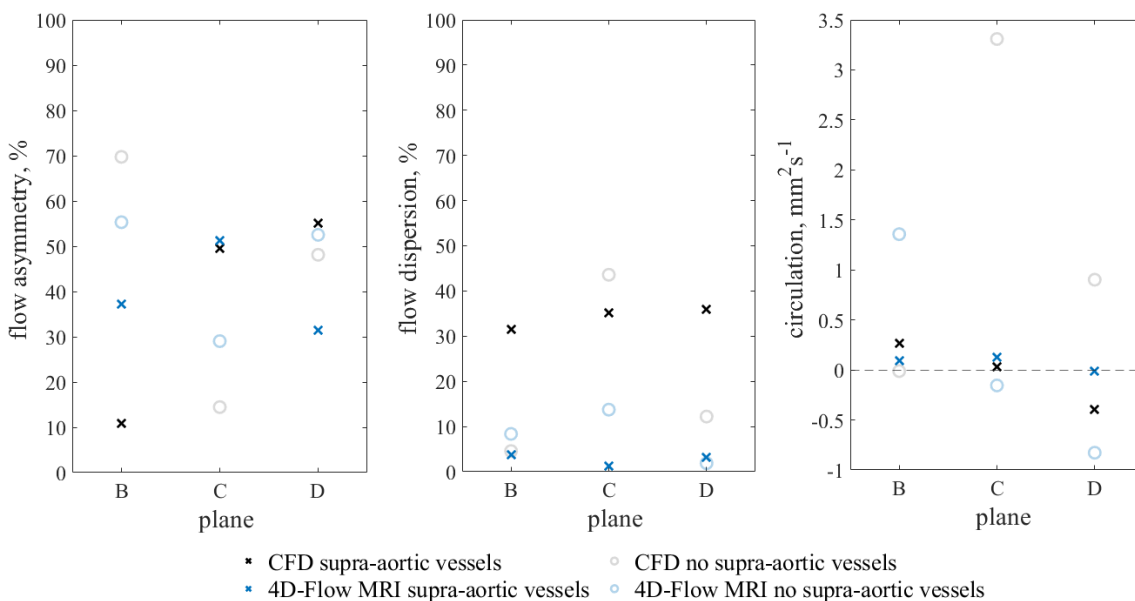


Figure 4.23. Flow asymmetry (%), flow dispersion (%), and through plane circulation (mm^2s^{-1}) at diastole for neonatal patient CoRaL071 at three planes of interest with the supra-aortic vessels included, compared to the corresponding values when the supra-aortic vessels are neglected. (*B*=mid-ascending aorta, *C*=aortic arch, *D*=mid-descending aorta).

It has been demonstrated that when constructing spatio-temporal patient-specific inlet conditions over the entire cardiac cycle, determining a function that is an accurate reproduction of the 4D-Flow MRI data at all stages of the cardiac cycle is challenging due to the significant differences in the velocities over the systolic and diastolic period, which are frequently orders of magnitude different. A higher order equation for the surface fit applied to the 4D-Flow MRI data should be used if more accuracy is desired over the diastolic period, or the 4D-Flow MRI data at the inlet must be mapped directly from the 4D-Flow MRI mesh to the CFD mesh. However, this requires significant amounts of data at each time-step, and only allows for discrete temporal variation, and not continuous. The direct mapping of the velocities methods is appropriate if only one time-step in the cycle is of interest, as the pulsatility of the cardiac cycle will not be modelled. By modelling one stage of the cardiac cycle, the use of a function to map the flow profile at the inlet would become more accurate also.

From the results presented here, it has been shown that by modelling the pulsatility of the cardiac cycle through applying one equation for all stages of the cardiac cycle, the accuracy of the simulations is reduced at one or both stages of the cardiac cycle. For the purposes of this research, the systolic period is of more interest as it is during that stage that the impacts of BAV or an AVR will

be present. During diastole the valve will not be open and as such the effects of BAV or an AVR will not be as pronounced. Therefore it is of greater importance that the pulsatility of the cardiac cycle is captured rather than the accuracy of the diastolic phase be increased. If the diastolic period of the cardiac cycle is of greater importance than the systolic, it is recommended to utilise a higher order equation when applying a surface fit to the 4D-Flow MRI data, or to model only the stage of interest and directly map the 4D-Flow MRI data onto the CFD mesh.

4.6 Supra-Aortic Vessels Within the Adult Cohort

To quantify the impacts of neglecting the supra-aortic vessels in adult patients, and to ensure the workflow with full complexity was suitable for patients of all ages and health conditions, the supra-aortic vessels were located in two additional patients with varying BAV phenotypes and helical flow directions. Spatio-temporal patient-specific inlet boundary conditions were applied, created using the methodology discussed in Section 3.5.3.2, alongside outflow percentages prescribed to the four outlets present in the domain. The different geometries and the location of the supra-aortic vessels for the two adult patients can be seen in Figure 4.24. Figure 4.24 demonstrates the inter-patient variability that is present in the thoracic aortic geometry that the workflow must be able to work with.

Using the *pimpleFoam* solver with OpenFOAM, the cardiac cycle was run and the results from systole and diastole compared to 4D-Flow MRI data. Blood was assumed to be incompressible, Newtonian, and homogeneous, using the properties detailed in Section 3.6. The $k - \omega$ SST turbulence model was incorporated into the numerical simulations as the cardiac cycle for both adult patients varies between the turbulent, transitional, and laminar regimes. The meshes applied to both geometries followed the same meshing strategy outlined in Section 3.4.4. Simulations were run using the same set-up as those within Sections 4.4 and 4.5.

4.6.1 OXBAV012

The flow asymmetry, flow dispersion, circulation, and velocity magnitude were evaluated at the three planes of interest in the mid-ascending aorta, aortic arch, and mid-descending aorta. As patient OXBAV012 was the patient participating in the preliminary simulations in Sections 4.2 and 4.3, the results from preliminary simulations are also compared to results from spatio-temporal patient-specific simulations with the supra-aortic vessels included, in addition being compared to 4D-Flow MRI data. The outflow conditions at the four outlets were calculated to be 69.15% of the flow exiting the domain through the descending aorta, 16.44% through the brachiocephalic artery, 4.959% through the left common carotid artery, and 9.454% through the left subclavian artery. The flow percentages calculated disagree with those suggested by both Middleman [59] and Caballero & Laín [57] in the descending aorta, brachiocephalic artery, and the left subclavian artery.

4.6.1.1 Systole

Contours of velocity magnitude from CFD simulations and 4D-Flow MRI data at the three planes of interest during systole can be seen in Figure 4.25. It is clear that the CFD data over-estimates the velocity magnitude within the mid-ascending aorta and aortic arch, but shows much better

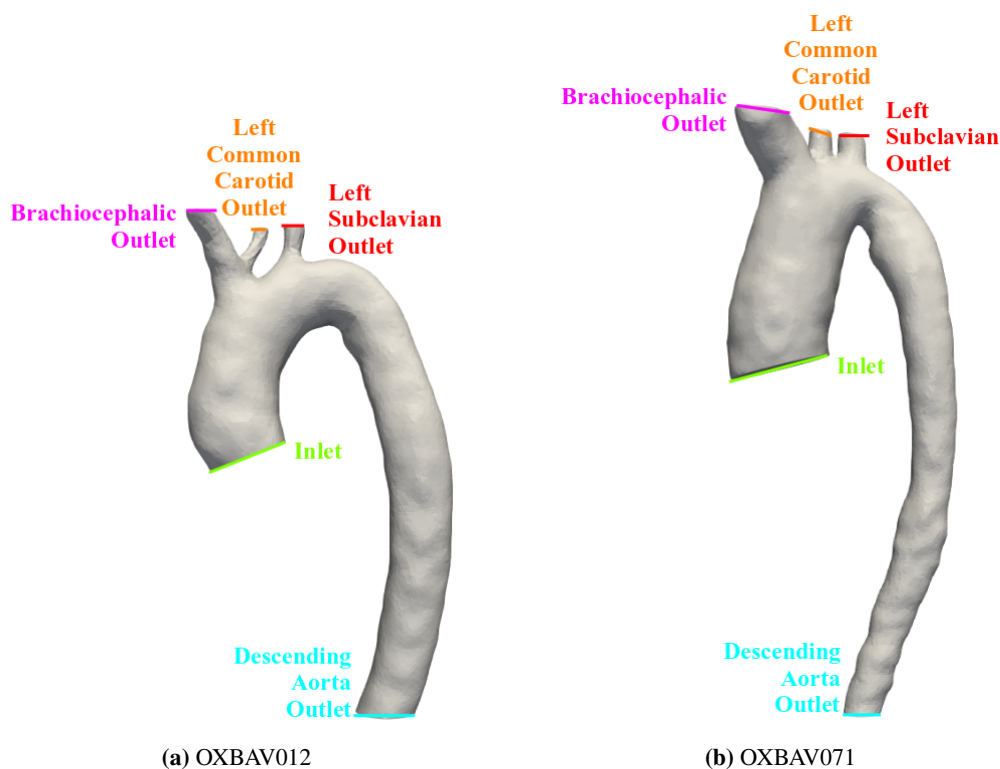


Figure 4.24. Geometry reconstruction of adult patients OXBAV012 and OXBAV071 showing the location of the additional three outlets of the supra-aortic vessels.

agreement within the descending aorta. The improved agreement in the descending aorta compared to the results within Sections 4.2 and 4.3 is expected. The maximum velocity magnitude predicted by CFD is within 8.265% of that predicted by 4D-Flow MRI data, reduced from 74.60% and 72.73% when steady-state plug profile and pulsatile plug profile CFD simulations are compared to 4D-Flow MRI data. The addition of the supra-aortic vessels as three additional outlets will cause a smaller volume of blood to be exiting the domain through the descending aorta, causing a reduction in flow velocity. This increased agreement is seen in the mid-ascending aorta and aortic arch also. In the ascending aorta, the maximum velocity magnitudes reported by CFD and 4D-Flow MRI are within 30.40% of each other, reduced from 69.31% and 63.40% for steady-state and pulsatile plug profile CFD simulations respectively. In the aortic arch the maximum velocity magnitude reported by CFD is within 31.26% of 4D-Flow MRI data, reduced from 93.59% and 68.94% for steady-state and pulsatile plug profile CFD simulations. Within the ascending aorta, despite the velocity magnitudes not being in agreement between the methods, it is clear that the flow patterns are similar, with both the 4D-Flow MRI and CFD data predicting a region of elevated velocity magnitude in the left, left-posterior, and posterior regions, and reduced velocity magnitude in the anterior and right-anterior regions. The flow profile within the descending aorta is also in good agreement, with both CFD and 4D-Flow MRI data suggesting a broad flow profile centred on the mid-line of the vessel. This is shown also within Figure 4.26, where it can be seen the flow asymmetry in the descending aorta is in excellent agreement.

Table 4.1 shows the quantitative agreement between CFD and 4D-Flow MRI velocity data in terms of the maximum and mean velocity over the three planes of interest. It can be seen that the mean velocity in the mid-ascending aorta and aortic arch is in good agreement, with a slight reduction in the mid-descending aorta. The maximum velocity is in poor agreement in the mid-ascending

aorta and aortic arch and reasonable agreement in the mid-descending aorta, as indicated in Figure 4.25.

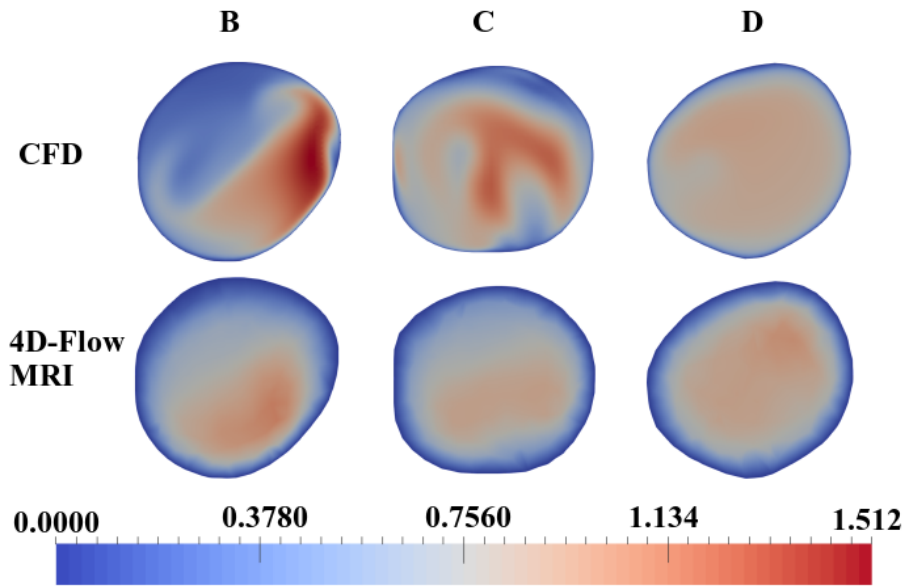


Figure 4.25. Contours of velocity magnitude (ms^{-1}) calculated through spatio-temporal patient-specific CFD simulations with the supra-aortic vessels included and 4D-Flow MRI data at systole at three planes of interest for the adult patient OXBAV012. (*B=mid-ascending aorta, C=aortic arch, D=mid-descending aorta*).

Plane	4D-Flow MRI		CFD		Difference Between Methods	
	$U_{mag_{max}}$ (ms^{-1})	U_{mean} (ms^{-1})	$U_{mag_{max}}$ (ms^{-1})	U_{mean} (ms^{-1})	$U_{mag_{max}}$ %	U_{mean} % difference
B	1.113	0.5660	1.512	0.5496	30.40	2.929
C	0.9201	0.5686	1.261	0.6044	31.26	6.103
D	1.013	0.6412	0.9326	0.7632	8.265	17.38

Table 4.1. Maximum and mean velocity magnitude (ms^{-1}) data at the three planes of interest during systole calculated using 4D-Flow MRI data and CFD data, including a comparison between the two methods at each location. (*B=mid-ascending aorta, C=aortic arch, D=mid-descending aorta*).

The flow asymmetry shown in Figure 4.26 demonstrates excellent agreement between 4D-Flow MRI data and CFD results within the aortic arch and descending aorta, improving on the results from both steady state simulations (55.67% and 52.07%) and pulsatile simulations (60.00% and 13.98%) with a plug profile applied to the inlet with differences between CFD and 4D-Flow MRI data of 0.8319% and 0.7323% in the aortic arch and mid-descending aorta respectively. However, the flow asymmetry in the ascending aorta indicates reduced agreement between the CFD and 4D-Flow MRI compared to preliminary simulations, with 29.90% difference between CFD and 4D-Flow MRI data compared to 15.90% and 18.97% for steady-state and pulsatile plug profile CFD simulations respectively. Flow dispersion shows there is good agreement between the CFD data and 4D-Flow MRI data in both the ascending aorta (2.359%) and aortic arch (9.849%). The flow dispersion in the descending aorta shows improved agreement to 4D-Flow MRI data compared to pulsatile CFD simulations with a plug profile.

The circulation indicates that there is good agreement in terms of magnitude and direction in the ascending aorta when comparing the spatio-temporal patient-specific inlet condition to the 4D-

Flow MRI data, and there is improved agreement compared to preliminary simulations. Across the aortic arch and descending aorta there is increased agreement between the spatio-temporal patient-specific CFD and 4D-Flow MRI data compared to the pulsatile plug flow from Section 4.3. It can also be seen that CFD and 4D-Flow MRI data agree that the helical flow is within normal limits in both the ascending aorta and descending aorta.

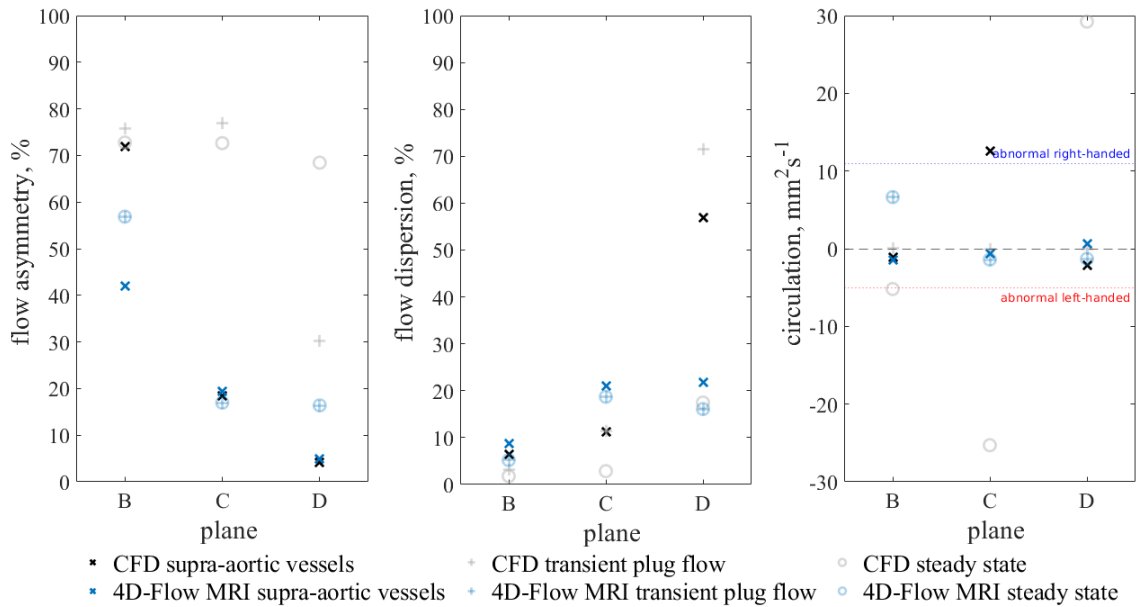


Figure 4.26. Flow asymmetry (%), flow dispersion (%), and through plane circulation (mm^2s^{-1}) at systole for patient OXBAV012 at three planes of interest. Results from steady state and transient simulations with a plug profile, and spatio-temporal patient-specific simulations with the supra-aortic vessels are compared alongside the corresponding 4D-Flow MRI data. (*B*=mid-ascending aorta, *C*=aortic arch, *D*=mid-descending aorta).

A cause of the discrepancies seen between the CFD data and 4D-Flow MRI data is likely all fluid-structure interaction in the thoracic aorta being neglected. The aorta is known to move radially and vertically throughout the cardiac cycle, and is in constant contact with the surrounding tissues, as well as being tethered through the intercostal, bronchial, and oesophageal arteries and is influenced by these movements and tethers. The compliance of the vessel as well as the impacts of the circulatory system outside of the domain of interest have also been neglected and will also be influencing the blood flow within the thoracic aorta. Additionally, the location of the outlets at the distal end of the supra-aortic vessels will be affecting the flow in the aortic arch as the boundary condition, that is known to be non-physical, is within five diameters downstream of the plane of interest in the aortic arch. A further limitation that will be contributing to the discrepancies seen between the CFD and 4D-Flow MRI data is the inlet condition that is applied. Although the inlet condition is both spatially and temporally patient-specific, it does not map the 4D-Flow MRI data directly, and as such there are interpolation errors present in the surface fit. This can be seen in the inlet conditions at systole for the patient OXBAV012, see Figure 4.27. Careful examination of Figure 4.27a indicates there are two main peaks within the 4D-Flow MRI velocity data; central and in the left-anterior region. The calculated CFD inlet condition replicates only the larger of the two peaks, in the left anterior region. A more accurate surface fit would be required to replicate the 4D-Flow MRI data exactly, which can be achieved through mapping the 4D-Flow MRI data onto the CFD mesh, as discussed in Section 3.5.3.1. However, this requires significant amounts of data and produces only a discrete temporal variation. As clinicians are interested in the large

changes in the flow patterns in the ascending aorta produced from surgical intervention, it must be considered whether the increased accuracy that would be gained from mapping the inlet condition directly is a feasible solution considering there is currently good agreement seen in terms of flow dispersion, circulation, and flow patterns between the CFD data and 4D-Flow MRI data in the mid-ascending aorta during systole.

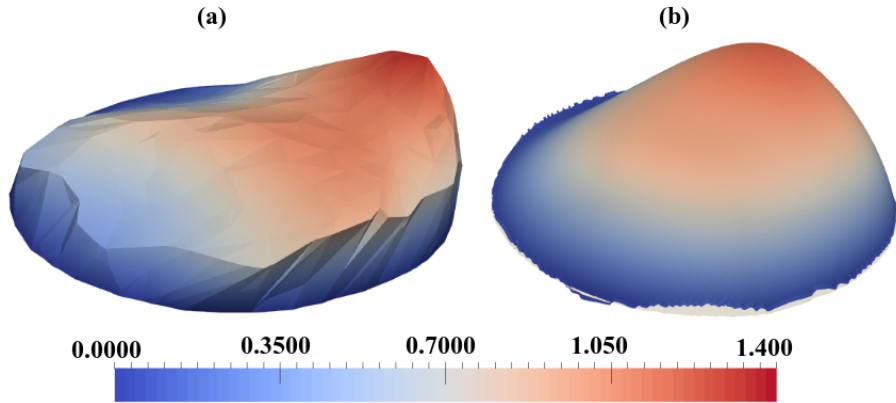


Figure 4.27. Velocity magnitude ($m s^{-1}$) data from the inlet plane at systole from 4D-Flow MRI data (a) and the calculated CFD inlet condition (b).

4.6.1.2 Diastole

Velocity magnitude contours in the mid-ascending aorta, aortic arch, and mid-descending aorta at diastole can be seen in Figure 4.28. There is reduced agreement in terms of the velocity magnitude and flow patterns in all three planes of interest compared to the velocity contours at systole (see Table 4.2). In the mid-ascending aorta and aortic arch, 4D-Flow MRI data predicts higher peak velocities and a sharper flow profile. The flow dispersion data supports this and shows CFD predicts a higher flow dispersion percentage and therefore a broader profile in all three planes. Table 4.2 gives a quantitative comparison of the velocity data at the three planes of interest during diastole. It can be seen that in terms of the maximum velocity, there is a larger difference between the two methods at each plane than there is during systole. The mean velocity shows better agreement between the two methods than the maximum velocity, with excellent agreement found in the mid-ascending aorta.

Plane	4D-Flow MRI		CFD		Difference Between Methods	
	$U_{mag_{max}}$ ($m s^{-1}$)	U_{mean} ($m s^{-1}$)	$U_{mag_{max}}$ ($m s^{-1}$)	U_{mean} ($m s^{-1}$)	$U_{mag_{max}}$ % difference	U_{mean} % difference
B	0.07827	0.02722	0.1080	0.02743	31.92	0.7574
C	0.09773	0.04458	0.1462	0.03893	39.74	14.93
D	0.08896	0.03972	0.1063	0.04938	17.76	21.70

Table 4.2. Maximum and mean velocity magnitude ($m s^{-1}$) data at the three planes of interest during diastole calculated using 4D-Flow MRI data and CFD data, including a comparison between the two methods at each location. (B=mid-ascending aorta, C=aortic arch, D=mid-descending aorta).

Figure 4.29 shows the flow asymmetry, flow dispersion, and circulation across the three planes of interest at diastole. It can be seen that in the aortic arch and mid-descending aorta there is excellent agreement between CFD and 4D-Flow MRI data in terms of flow asymmetry, with differences of

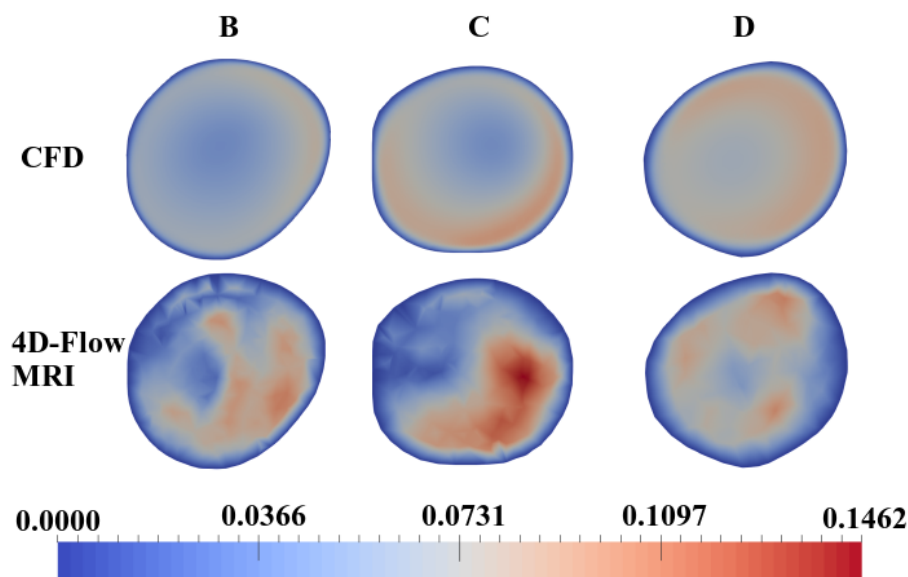


Figure 4.28. Contours of velocity magnitude ($m s^{-1}$) calculated through spatio-temporal patient-specific CFD simulations with the supra-aortic vessels included and 4D-Flow MRI data at diastole at three planes of interest for the adult patient OXBAV012. (*B*=mid-ascending aorta, *C*=aortic arch, *D*=mid-descending aorta).

only 2.732% and 0.8204% respectively. There is also improved agreement between the CFD and 4D-Flow MRI data when compared to preliminary pulsatile (35.61% and 31.25%) and steady-state plug profile CFD simulations (9.880% and 1.360%), shown in Sections 4.2 and 4.3. Additionally, there is improved agreement in the mid-ascending aorta compared to steady-state CFD simulations with a plug profile. The spatio-temporal patient-specific CFD simulations over-estimates the flow dispersion in all three planes compared to the 4D-Flow MRI data, indicating a much broader profile is present, with the largest difference in the descending aorta (30.46%). The low values determined from the 4D-Flow MRI data are likely a result of the smaller fluctuations that are found combined with the coarser spatial resolution and irregular cells created when viewing the 4D-Flow MRI results (as shown in Figure 4.20), meaning the top 15% of velocities have a small area. As the CFD data does not predict these smaller fluctuations as a result of the inlet conditions and has a much higher resolution, the area of the top 15% of velocities is much larger, therefore predicting a broader profile than is present in the 4D-Flow MRI data.

The circulation direction determined by CFD and 4D-Flow MRI in the aortic arch and mid-descending aorta agrees, and shows improved agreement from preliminary simulations in the mid-descending aorta. However, in the aortic arch and mid-ascending aorta there is reduced agreement compared to preliminary simulations. In addition to this, the helicity classifications from CFD and 4D-Flow MRI data are in agreement in all three planes with both methods showing normal levels of helicity.

The discrepancies found at diastole are likely a result of insufficient inlet conditions. Figure 4.30 shows the inlet conditions from 4D-Flow MRI and CFD at late diastole, and clearly shows that the CFD inlet condition is a simplification of the flow profile found in 4D-Flow MRI data. 4D-Flow MRI data indicates there are three velocity peaks across the plane, whereas the calculated CFD inlet condition only accurately replicates one of these velocity peaks. This clearly indicates that although the inlet condition is sufficient at diastole, there are still insufficiency's present at diastole

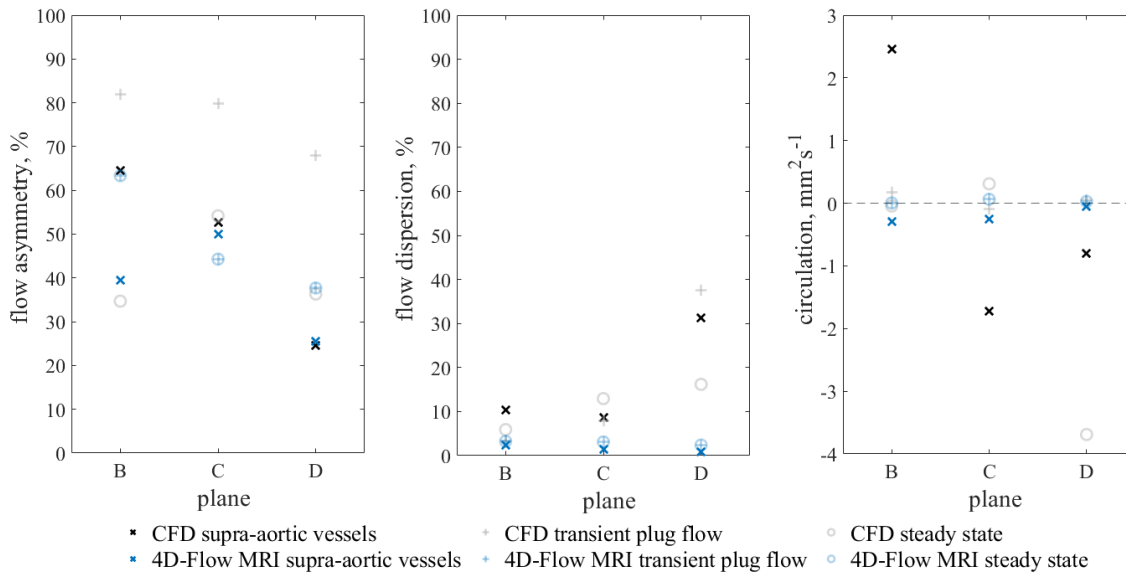


Figure 4.29. Flow asymmetry (%), flow dispersion (%), and through plane circulation ($mm^2 s^{-1}$) at diastole for patient OXBV012 at three planes of interest. Results from steady state and transient simulations with a plug profile, and spatio-temporal patient-specific simulations with the supra-aortic vessels are compared alongside the corresponding 4D-Flow MRI data. ($B=mid\text{-ascending aorta}$, $C=aortic arch$, $D=mid\text{-descending aorta}$).

that are leading to inaccuracies in the flow predicted by CFD throughout the thoracic aorta. In order to accurately model the flow during diastole, the inlet condition must be improved upon, either by mapping the data directly from 4D-Flow MRI onto the CFD mesh or through increasing the order of the surface fit applied. Modelling diastole separately to systole may also provide the best solution due to the large differences seen in the velocity magnitude between the two phases of the cardiac cycle. Additionally, FSI is neglected, which will influence the flow during diastole as the vessel walls act as a reservoir during systole. The elastic properties of the wall allow a more constant flow during diastole. As this is not modelled by the CFD workflow, it will be contributing to errors within the flow patterns and thus the haemodynamic indices. By neglecting the FSI, the movement of the aortic valve leaflets is not included in the numerical model. However, this movement is influencing the 4D-Flow MRI data and will contribute to discrepancies between the CFD and 4D-Flow MRI data.

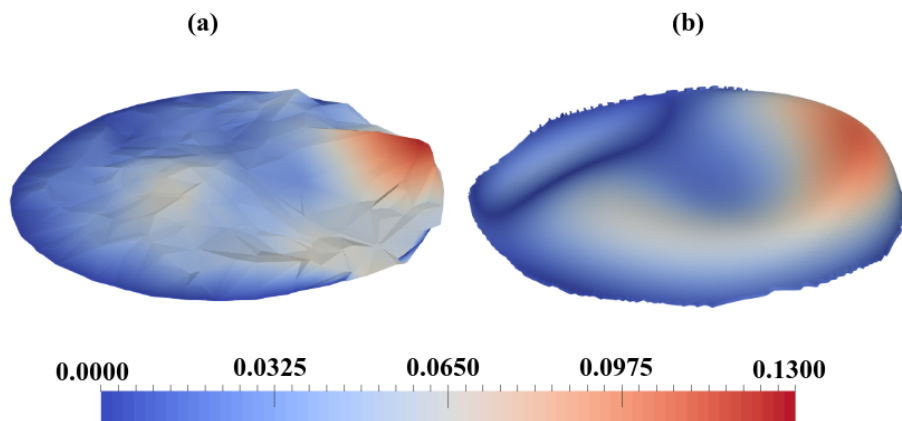


Figure 4.30. Velocity magnitude (ms^{-1}) data from the inlet plane at diastole from 4D-Flow MRI data (a) and the calculated CFD inlet condition (b).

4.6.2 OXBAV071

The flow asymmetry, flow dispersion, circulation, and velocity magnitude were evaluated at three planes of interest in the mid-ascending aorta, aortic arch, and mid-descending aorta for the adult patient OXBAV071, the BAV phenotype and patient details can be seen in Table 3.1 in Chapter 3. The 4D-Flow MRI data is compared to CFD data from simulations with a spatio-temporal patient-specific inlet condition and outflow boundary conditions at the four outlets. The outflow conditions were determined based on the cross sectional areas of the outlets and were found to be 22.91% of flow exiting the domain through the descending aorta, 54.33% through the brachiocephalic artery, 9.52% through the left common carotid artery, and 13.24% through the left subclavian artery.

The inlet conditions from 4D-Flow MRI and calculated for CFD simulations can be seen in Figure 4.31. Figure 4.31a shows that 4D-Flow MRI data suggests patient OXBAV071 experiences a highly complex flow profile across the inlet plane with a highly asymmetric and sharp flow profile, resulting from a severe BAV. Although the calculated inlet condition applied in the patient-specific CFD simulation (Figure 4.31b) replicates the velocity peak in the correct location and of the correct magnitude during systole ($t = 3-5$), the profile of the peak is clearly dissimilar to that seen in the 4D-Flow MRI data. The flow profile calculated has been smoothed significantly as a result of the interpolation required to create the inlet condition, and produces a profile much more akin to a parabolic velocity profile than that found in the 4D-Flow MRI. These inaccuracies found in the calculated inlet condition will contribute to differences in the haemodynamics between the 4D-Flow MRI and those predicted by the CFD methodology. During the systolic phase of the cardiac cycle, it appears that the calculated CFD inlet condition replicates the 4D-Flow MRI data better, however the smaller fluctuations found in the 4D-Flow MRI data are not replicated in the calculated CFD inlet condition, as is also seen for Patient OXBAV012 in Figure 4.30. This results in an inlet condition that is not fully replicating the aortic valve haemodynamics at all stages of the cardiac cycle.

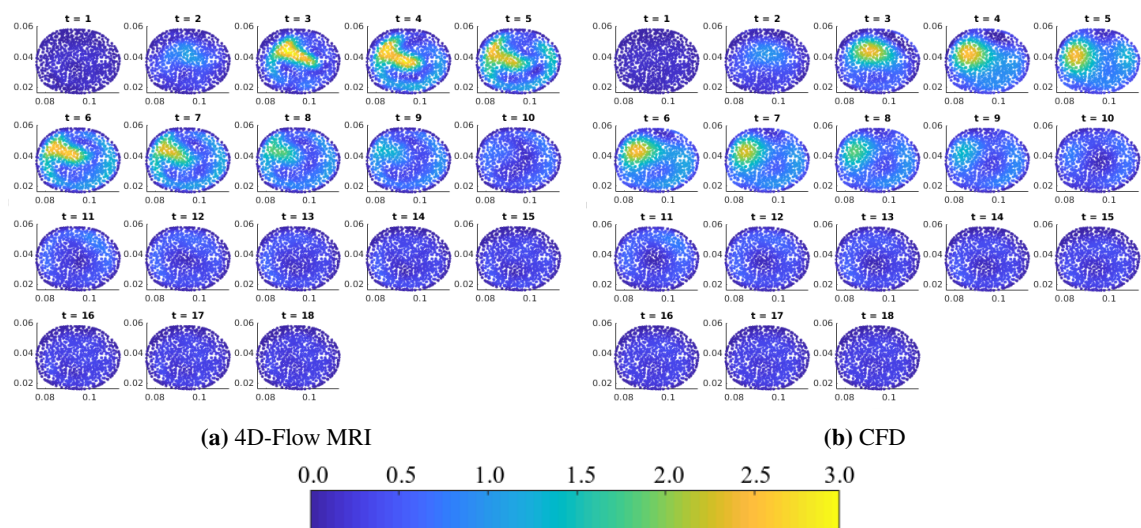


Figure 4.31. Velocity magnitude data (ms^{-1}) over the inlet plane found from 4D-Flow MRI data at each time-step over the course of the cardiac cycle (a), and the calculated CFD inlet condition at the corresponding times (b) for patient OXBAV071.

4.6.2.1 Systole

Contours of velocity magnitude calculated from CFD and 4D-Flow MRI data at systole can be seen in Figure 4.32 for the three planes of interest (the mid-ascending aorta, aortic arch, and mid-descending aorta). The flow patterns found in all three planes show good qualitative agreement between the methods with both CFD and 4D-Flow MRI results indicating there is a region of elevated velocity in the right-anterior region of the mid-ascending aorta. However, CFD data predicts higher velocity magnitudes will be present, with a difference of 24.61% between the maximum velocity magnitude reported by 4D-Flow MRI and CFD data. Velocity magnitudes are in good agreement within the aorta arch, with the maximum velocity found differing only by 6.548% when comparing the CFD data to 4D-Flow MRI data and the mean velocity differing by 14.44%. Velocity contours in the descending aorta indicate that CFD over-estimates the velocity magnitude compared to the 4D-Flow MRI, however both appear to suggest a broad and central flow profile.

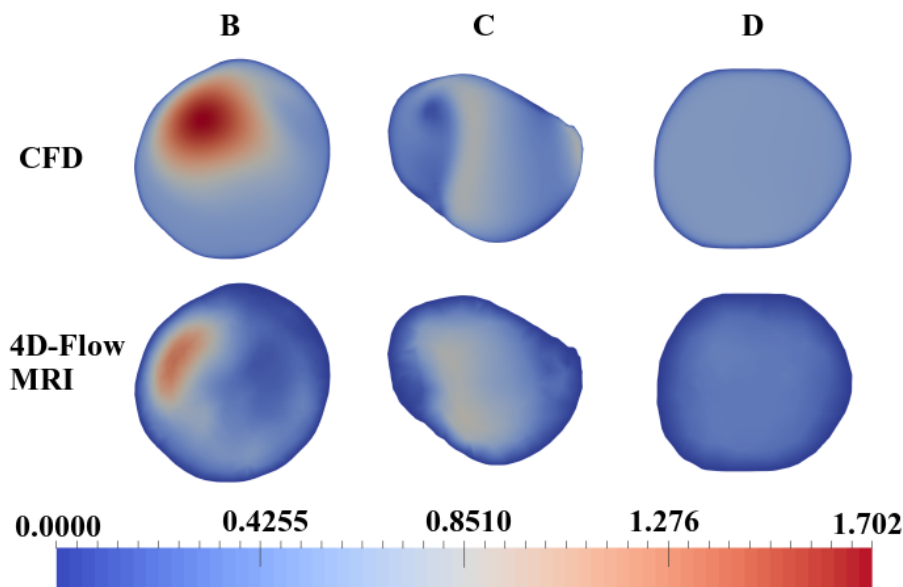


Figure 4.32. Contours of velocity magnitude (ms^{-1}) calculated through the CFD methodology and 4D-Flow MRI at three planes of interest for patient OXBAV071 at systole. (*B=mid-ascending aorta, C=aortic arch, D=mid-descending aorta*).

Despite the good qualitative agreement seen in the velocity contours, with both CFD and 4D-Flow MRI predicting the same flow patterns, it is clear that quantitatively there are large errors present. Table 4.3 details the mean and maximum velocities experienced in all three planes calculated using both CFD and 4D-Flow MRI data. Despite the large differences seen in Table 4.3, if clinicians are looking for large changes in the flow patterns as a result of surgical intervention, it is probable that the accuracy that is seen in the CFD data in terms of the flow patterns calculated at systole is sufficient to observe any changes as a result of an AVR.

The flow asymmetry, flow dispersion, and circulation were calculated from CFD and 4D-Flow MRI data at the three planes of interest and the results from systole are shown in Figure 4.33. It can be seen that there is reasonable agreement between the 4D-Flow MRI and CFD data in terms of flow asymmetry in all three planes of interest, reducing from a 20.67% difference in the mid-ascending aorta to 3.294% in the mid-descending aorta. The higher difference found in the mid-ascending aorta can be attributed to the fact that the flow in the ascending aorta is governed

Plane	4D-Flow MRI		CFD		Difference Between Methods	
	$U_{mag_{max}}$ ($m.s^{-1}$)	U_{mean} ($m.s^{-1}$)	$U_{mag_{max}}$ ($m.s^{-1}$)	U_{mean} ($m.s^{-1}$)	$U_{mag_{max}}$ %	U_{mean} % difference
B	1.329	0.3122	1.702	0.7413	24.61	81.47
C	0.8738	0.3853	0.8184	0.3334	6.548	14.44
D	0.3720	0.2152	0.5424	0.4893	37.27	77.80

Table 4.3. Maximum and mean velocity magnitude ($m.s^{-1}$) data for patient OXBAV071 at the three planes of interest during systole calculated using 4D-Flow MRI data and CFD data, including a comparison between the two methods at each location. (*B=mid-ascending aorta, C=aortic arch, D=mid-descending aorta*).

by the inlet condition, which has been shown to have several inaccuracies (see Figure 4.31), whilst flow in the mid-ascending aorta is primarily governed by the curvature and geometry of the aorta [120]. The inaccuracies in the CFD inlet condition are also causing the CFD data to underestimate the flow asymmetry in the mid-ascending aorta, as opposed to the over-estimations seen in the aortic arch and mid-descending aorta. As the interpolation applied smooths out the 4D-Flow MRI data, the sharper more eccentric profile that can be seen in Figure 4.31a is smoothed out and becomes closer to a parabolic profile, causing the centroid of the top 15% of velocities to move away from the periphery of the vessel and closer to the centre-line.

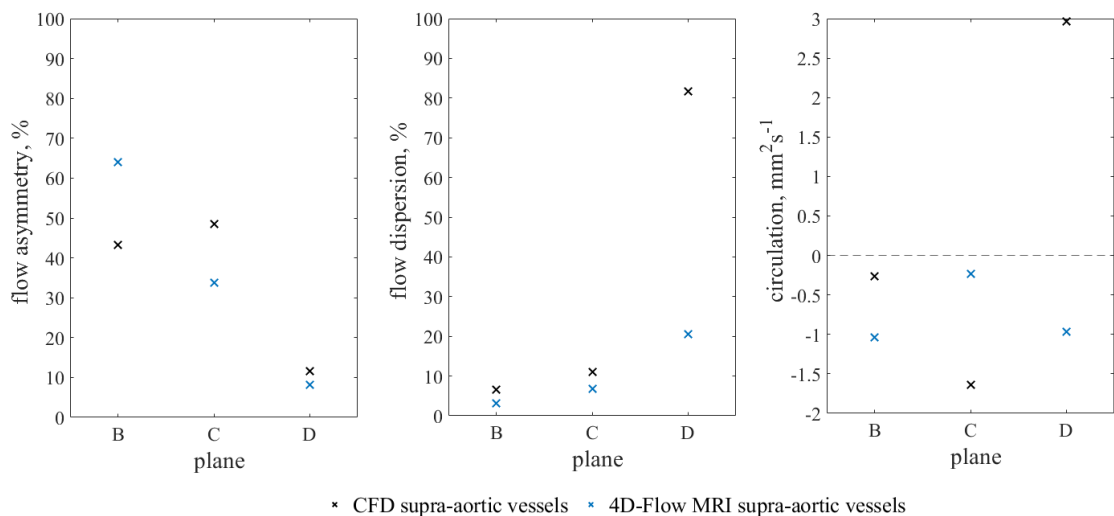


Figure 4.33. Flow asymmetry (%), flow dispersion (%), and through plane circulation ($mm^2.s^{-1}$) at systole for patient OXBAV071 at three planes of interest. (*B=mid-ascending aorta, C=aortic arch, D=mid-descending aorta*).

There is good agreement in the mid-ascending aorta and aortic arch in terms of flow dispersion with differences between the 4D-Flow MRI and CFD data of 3.541% and 4.122% respectively, with higher values being predicted by CFD data in both planes. However, there is a significant discrepancy between 4D-Flow MRI and CFD data within the descending aorta, with a difference of 61.15%. It is likely that this is due to 4D-Flow MRI data showing a number of small fluctuations in the flow, whilst CFD data does not predict the smaller fluctuations. Due to the method used to determine the flow dispersion, the smaller fluctuations result in the area of the top 15% of velocities being significantly smaller.

There are notable differences between CFD and 4D-Flow MRI data in terms of circulation in all

three planes ($> 100\%$), despite both methods agreeing on the circulation direction in the mid-ascending aorta and aortic arch. The large differences in circulation are likely a consequence of the circulation magnitude being highly sensitive to the inlet condition, combined with neglecting the fluid structure interaction and compliance of the vessel. The helicity levels predicted by both CFD and 4D-Flow MRI are within the normal range for all three planes of interest.

4.6.2.2 Diastole

Velocity contours from CFD simulations and 4D-Flow MRI across the three planes of interest can be seen in Figure 4.34. In the mid-ascending aorta, it is clear that the flow patterns seen in 4D-Flow MRI are also predicted by the patient-specific CFD simulation with both methods indicating a ring of higher velocity flow around the periphery of the vessel and a region of low flow towards the centre-line. However, the velocity magnitude is under-estimated by the patient-specific CFD simulation, with a difference in the maximum velocity magnitude of 21.00% reported between the two methods. As the flow progresses through the thoracic aorta and moves away from the inlet, the qualitative agreement between the CFD and 4D-Flow MRI data in terms of the flow patterns decreases, with CFD predicting discordant flow patterns and higher velocity magnitudes. The agreement between the CFD and 4D-Flow MRI data in terms of maximum and mean velocity experienced across the planes of interest is poor, as shown in Table 4.4. The variations seen between the CFD and 4D-Flow MRI data are likely a consequence of the inlet conditions being applied; the small fluctuations found in 4D-Flow MRI data at the inlet are not replicated in the calculated inlet condition creating dissimilar flow patterns and velocities.

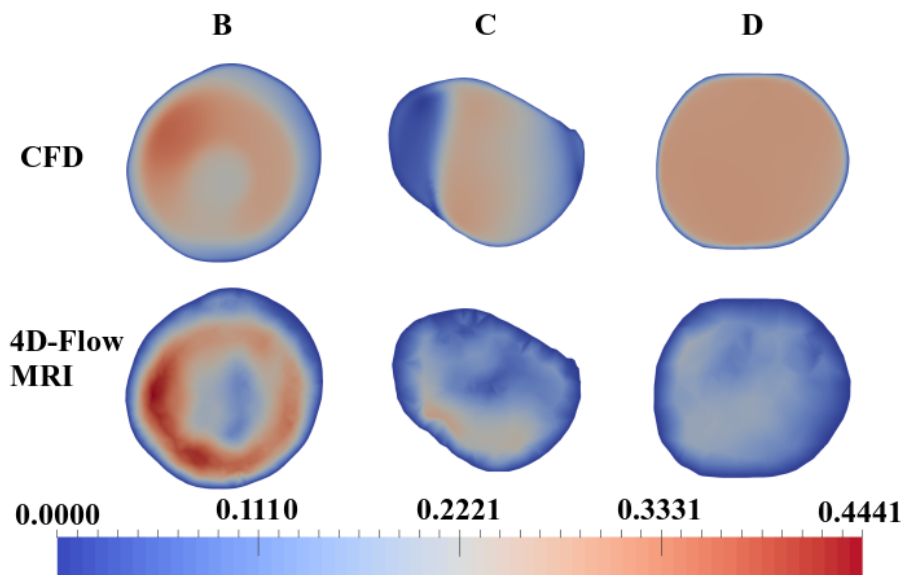


Figure 4.34. Contours of velocity magnitude (ms^{-1}) calculated through the CFD methodology and 4D-Flow MRI at three planes of interest for patient OXBV071 at diastole. (*B*=mid-ascending aorta, *C*=aortic arch, *D*=mid-descending aorta).

In the mid-ascending aorta, there is reasonable agreement between the 4D-Flow MRI and CFD data in terms of flow asymmetry, dispersion, and circulation magnitude, differing by 16.75%, 8.507%, and 6.310% respectively. The agreement seen in the haemodynamics indices confirms the qualitative agreement that can be seen in the flow patterns in Figure 4.34. Flow asymmetry in the aortic arch and mid-descending aorta show significantly reduced agreement compared to the mid-ascending aorta and to all three planes at systole.

Plane	4D-Flow MRI		CFD		Difference Between Methods	
	$U_{mag_{max}}$ (ms^{-1})	U_{mean} (ms^{-1})	$U_{mag_{max}}$ (ms^{-1})	U_{mean} (ms^{-1})	$U_{mag_{max}}$ %	U_{mean} % difference
B	0.4441	0.04414	0.3597	0.2298	21.00	135.6
C	0.2760	0.06443	0.2836	0.1562	2.716	83.16
D	0.1953	0.03131	0.2938	0.2676	40.28	158.1

Table 4.4. Maximum and mean velocity magnitude (ms^{-1}) data for patient OXBV071 at the three planes of interest during diastole calculated using 4D-Flow MRI data and CFD data, including a comparison between the two methods at each location. ($B=mid\text{-ascending aorta}$, $C=aortic arch$, $D=mid\text{-descending aorta}$).

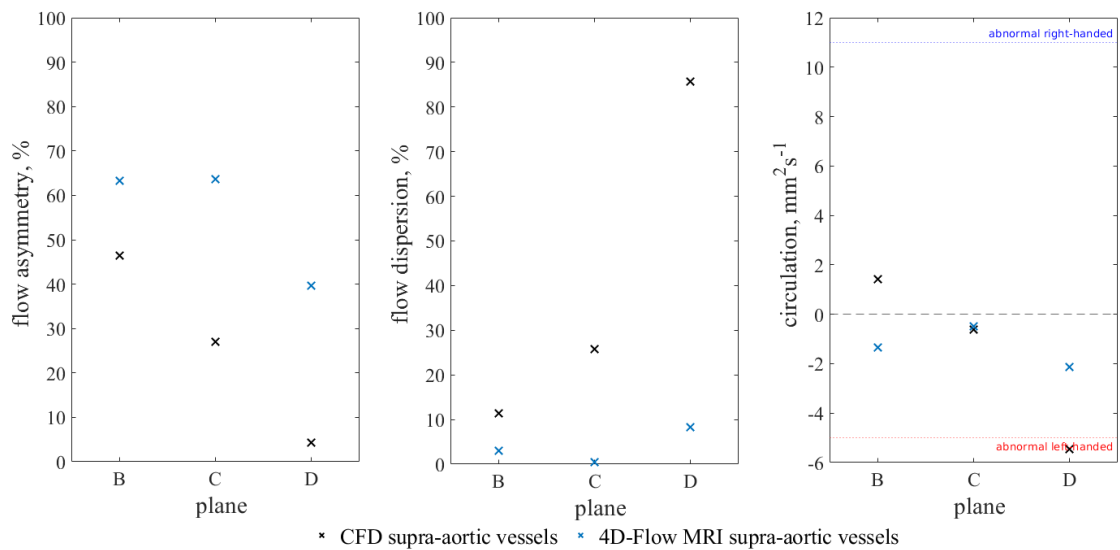


Figure 4.35. Flow asymmetry (%), flow dispersion (%), and through plane circulation (mm^2s^{-1}) at diastole for patient OXBV071 at three planes of interest. ($B=mid\text{-ascending aorta}$, $C=aortic arch$, $D=mid\text{-descending aorta}$).

There is poor agreement in the aortic arch and mid-descending aorta in terms of flow dispersion with the differences between the CFD and 4D-Flow MRI data increasing to 25.40% and 77.38%, with CFD data consistently predicting a higher flow dispersion and therefore a broader flow profile. This is to be expected as the smaller fluctuations that are found within the 4D-Flow MRI data are not predicted with the CFD methodology, therefore 4D-Flow MRI will suggest a sharper profile is present. Circulation magnitude shows poor agreement between the CFD and 4D-Flow MRI data in the aortic arch and mid-ascending aorta, with differences of 27.28% and 86.95%. However, despite the large differences found in the circulation magnitude, the direction agrees in two of the three planes, confirming the left handed helical flow that the patient is known to experience. In addition to confirming the left handed-helical flow, the helicity classification agrees in both the mid-ascending aorta and aortic arch. The choice in outlet condition at the distal end of the descending aorta will contribute to the haemodynamics found from 4D-Flow MRI data in the descending aorta not being replicated with the CFD methodology and to the larger differences seen in asymmetry, dispersion, and circulation in mid-descending aorta compared to the aortic arch and mid-ascending aorta. The simplistic outflow condition selected neglects to account for the compliance of the vessel and the circulatory system beyond the domain, which will influence the haemodynamics at all stages of the cardiac cycle. The simplistic outlet conditions applied to

the supra-aortic vessels will affect the haemodynamics within the aortic arch as the outlet planes are within five diameters downstream of the plane of interest.

4.7 Limitations

Despite the spatio-temporal inlet conditions applied in Sections 4.4, 4.5, and 4.6 producing good qualitative agreement in terms of flow patterns in the mid-ascending aorta between 4D-Flow MRI and CFD data during systole, it is clear that there are discrepancies present during diastole. The way in which the spatio-temporal inlet conditions are calculated causes the smaller fluctuations found during the diastolic phase to be smoothed out by the surface fit. This occurs as their magnitude is orders of magnitude smaller than the larger fluctuation seen during peak systole. Therefore applying the same surface fit to both stages of the cardiac cycle causes the smaller variations to be neglected. The surface fit selected must provide a reasonable estimation of the 4D-Flow MRI across all time-steps, however it was decided that the haemodynamics during systole were of higher importance than those at diastole, when the aortic valve is closed. Therefore ensuring the inlet condition accurately modelled the systolic flow profile was paramount. However, this has resulted in the CFD methodology predicting flow patterns that are inconsistent with those seen in 4D-Flow MRI data at diastole. The inlet conditions become a limitation to the methodology when the patient in question is exhibiting a highly complex flow profile at the aortic valve, as patient OXBAV071 does. As shown in Figures 4.31, the calculated inlet condition used for patient-specific CFD simulations does not fully replicate a complex flow profile. Using a surface fit of a higher order may reduce the differences, however directly mapping the 4D-Flow MRI data onto the pre-determined CFD mesh would produce the most physiologically accurate inlet condition.

As discussed in Section 3.8, the spatial and temporal variation the 4D-Flow MRI data is acquired at is a well known limitation, however the impact an insufficient resolution has on patient-specific CFD simulations has yet to be quantified. The spatial resolution must be considered carefully when the patient in question is neonatal, as the size of the voxels must be small enough such that the vessel is described by more than 6 voxels [169]. At the spatial resolutions used within this research, a singular voxel occupied 11.63% of the average neonatal ascending aortic diameter, whereas this was reduced to 4.377%–5.767% for adult patients. It can be seen therefore that although the resolution used for neonatal patients is refined compared to adult patients, the quality of imaging is reduced. The errors that result from insufficient spatial resolutions are addressed within research by Cherry *et al.* [185] and Chapter 6.

A clear limitation of the preliminary simulations (Sections 4.2 and 4.3) is the absence of the supra-aortic vessels. Neglecting the additional three outlets causes large differences in the haemodynamics in the aortic arch and descending aorta, artificially increasing the velocity magnitude. These differences can be seen clearly for the neonatal patient CoRaL072 in Figure 4.10 (without supra-aortic vessels) and Figure 4.19 (with supra-aortic vessels). This limitation was addressed in later patient-specific simulations by including the supra-aortic vessels when possible.

The outlet boundary conditions applied to both the preliminary simulations (0-pressure) and to simulations with four outlets (outflow conditions) are not physiologically accurate. The chosen boundary conditions neglect to account for the compliance of the vessel and the influence of the systemic circulatory system beyond the outlets. The choice in outlet condition impacts the flow

up to five diameters upstream of the outlets [79]. In the descending aorta, this will not impact the planes of interest as the descending aortic outlet plane is sufficiently distanced from the regions of interest for most patients participating in this research. However, due to the difficulties in segmenting and reconstructing the supra-aortic vessels in both adult and neonatal patients, the length of the supra-aortic vessels that was able to be successfully reconstructed is less than 5 diameters in length, meaning the flow in the aortic arch is very likely being influenced by insufficient outlet boundary conditions. As the ascending aorta is more than five diameters upstream of an outlet, it will not be affected by the choice in outlet boundary condition. To remove the errors produced from the outlet boundary condition choice in the aortic arch, the length of the supra-aortic vessels included in the reconstructed geometries should be a minimum of five diameters, provided the vessel is described by a minimum of 6 voxels.

The errors that are seen when comparing CFD to 4D-Flow MRI data during the diastolic period are also a likely consequence of neglecting the FSI between the aortic valve leaflets and the blood flow. As the aortic valve closes, secondary flow features will be created. The CFD workflow neglects to include the aortic valve leaflets, and as such the any flow features resulting from the deformation of the valve leaflets will not be predicted by the CFD data. It is likely that the magnitude of these additional flow features will be larger than the flow at the aortic valve during diastole, therefore they will influence the haemodynamics of the thoracic aorta. During systole, the velocity magnitude of any additional flow features will likely be smaller than the jet of blood being ejected. Therefore the motion of the aortic valve leaflets will influence flow during the diastolic flow more than the systolic flow.

It is challenging to differentiate the errors resulting from the choice in outlet conditions from those caused by neglecting FSI or through the assumptions made about the working fluid, meaning the accuracy of the choice of outlet conditions cannot be assessed from the results presented within Chapter 4. This limitation must be addressed by either implementing more complex boundary conditions such as the three-element Windkessel model, or by applying the workflow in a controlled environment where the circulatory system beyond the domain of interest can be removed and the vessel does not move radially or vertically. Additionally, removing the uncertainties of the Newtonian and homogeneous assumptions from consideration would help to clarify the largest source of error between FSI and outlet conditions.

4.8 Conclusions

The results presented within this Chapter from each iteration of the workflow show that the incremental changes to the numerical model have produced improvements in the CFD model. The workflow can successfully replicate the ascending aortic flow patterns and velocity magnitudes seen in 4D-Flow MRI and agrees with 4D-Flow MRI data on haemodynamic indices of interest. The final workflow presented accurately replicates systolic haemodynamics, however there is room for improvement when attempting to predict the diastolic haemodynamics. As the systolic phase of the cardiac cycle will be of more interest to clinicians as that is when the full impact of a BAV or AVR will be apparent, the workflow created could provide a useful aid in treatment planning. It has been shown that the workflow developed can be used on patients over wide range of ages and pathologies, and can be used for a minimal cost as a conscious effort was made to use open-source software where possible. As the workflow has been tested on a range of patients,

there is a high level of confidence that the results presented are accurate and the workflow will perform as intended if the inlet flow profile is altered to replicate that of an AVR.

Although there is good agreement between the CFD methodology and the 4D-Flow MRI data in the ascending aorta at systole, there are several limitations to the methodology that must be addressed if clinicians are expected to make decisions regarding surgical intervention and treatment planning based on the results of the numerical simulations. Primarily, the spatial resolution that the 4D-Flow MRI data is acquired at will be affecting not only the 4D-Flow MRI results that are being used to validate the CFD methodology, but also the CFD data itself as the numerical model is constructed using the 4D-Flow MRI data. Increasing the spatial resolution the 4D-Flow MRI data is acquired at would likely increase the agreement between the 4D-Flow MRI and CFD data. In order to further improve the agreement found between the 4D-Flow MRI and CFD data, the fluid-structure interactions between the vessel wall, aortic valve, surrounding tissues, and the working fluid must be incorporated into the numerical models. It was decided that this was outside the scope of this research however, as it would prohibitively increase the computational resources required for each simulation. Increasing the complexity of the outlet conditions to a three-element Windkessel model at each outlet would also increase the accuracy of the CFD simulations as this would take into account the circulatory system beyond the domain as well as the compliance of the vessel wall.

In order to improve the agreement between the CFD and 4D-Flow MRI data during diastole, based on the results presented, it is recommended to increase the order of the surface fit used to create the inlet conditions, or to map the 4D-Flow MRI data directly to the CFD mesh at the inlet, as discussed in Section 3.5.3. Incorporating an inlet condition that only replicates the diastolic phase of the cardiac cycle would also reduce the likelihood of the smaller fluctuations being neglected in the calculated inlet conditions, as the orders of magnitude difference between the phases of the cardiac cycle will not be present. Additionally, incorporating the FSI between the valve leaflets and blood would improve the physiological accuracy of the inlet conditions in the numerical model. It is likely that incorporating these further improvements would cause the haemodynamics predicted by CFD to agree to a higher degree with the 4D-Flow MRI data.

The work within this Chapter highlights the main issues that arise when attempting to predict the haemodynamics in the thoracic aorta of neonatal patients. It is clear from the results presented that the inclusion of the supra-aortic vessels is key, however this is a difficulty in neonatal patients due to the low flow velocities and the coarse spatial resolution available for the 4D-Flow MRI scan. A method to eliminate this limitation would be to artificially create additional patches at the top of the aortic arch and prescribe flow rates to them. However, this technique would also come with difficulties; primarily that if the vessels cannot be segmented then the outflow percentages cannot be determined as they are dependent on the cross-sectional area of the vessel. Ideally, a refined spatial resolution would allow the supra-aortic vessels to be identifiable in the 4D-Flow MRI data, and therefore able to be segmented. However, this is currently limited by the processing power of the 4D-Flow MRI scanners. Currently, the data processing power available does not allow the spatial resolution to be increased.

The assumption of Newtonian flow may also be contributing to the errors seen when comparing the CFD data to 4D-Flow MRI. As discussed in Section 2.4.3.1, Johnston *et al.* [52] and Caballero & Laín [57] both stated that at high velocities, the viscosity model selected appeared to make no

difference to the haemodynamics. However, research from both studies suggested that at low flow velocities, such as those experienced during the diastolic phase of the cardiac cycle, a Newtonian model affects the haemodynamics. It is possible therefore that the choice to use a Newtonian assumption was incorrect. However, as stated by both Caballero & Laín [57] and Karimi *et al.* [60], a non-Newtonian viscosity model may be inappropriate as the model's parameters are determined from steady-state experiments.

Chapter 5.

Validation of the Methodology Using a Flow Phantom

Contents

5.1 Introduction	120
5.2 Methodology	121
5.2.1 Experimental Set-up	121
5.2.2 Geometry Reconstruction	122
5.2.3 Boundary Conditions	123
5.2.3.1 Inlet	124
5.2.3.2 Outlets	127
5.2.4 Numerical simulations	128
5.3 Results	128
5.3.1 Systole	128
5.3.2 Diastole	130
5.4 Limitations	132
5.5 Conclusions	133

5.1 Introduction

In an effort to validate the workflow delineated in Chapters 3 and 4 that integrates 4D-Flow MRI data and CFD simulations, an experimental set-up was utilised. In collaboration with Kings College London, a flow phantom of the thoracic aorta and proximal supra-aortic vessels was used to model the blood flow *ex-vivo*. Flow phantoms allow the blood flow within sections of the cardiovascular system to be mimicked in a way that allows experiments to be undertaken that would not be possible in an *in-vivo* set-up. The benefits of using a flow phantom to model the blood flow through the thoracic aorta are the high levels of control over experimental conditions such as flow rates at the inlet and the geometry, choice in the working fluid, and the reproducibility of the experiments [186]. A flow phantom reduces the risk associated with working with biological materials, and removes the need for licensing and ethical approval. Flow phantoms also allow for easy flow visualisation due to their optical transparency. This enables a range of imaging systems with higher spatial and temporal resolutions than 4D-Flow MRI to be used, such as PIV and

Laser Doppler Anemometry (LDA). As the vessel geometry and flow rates of the phantom are in a controlled environment, and the systemic circulatory system and compliance of the vessel wall have been removed, some of the uncertainties that were previously introduced into patient-specific CFD simulations by collecting the 4D-Flow MRI data *in-vivo* have been removed. Through this, the accuracy of the methodology created can be ascertained.

The flow phantom was placed in a 4D-Flow MRI scanner, a cardiac cycle modelled and the 4D-Flow MRI data extracted. The experimental set-up used is detailed in Section 5.2.1. Once 4D-Flow MRI data of the flow phantom was collected, phantom-specific CFD simulations were conducted following the workflow outlined in Chapter 3. The geometry was reconstructed, flow phantom specific boundary conditions were created, and CFD simulations with the spatio-temporal inlet boundary conditions and outflow conditions at the supra-aortic and descending aortic outlets were run. The results from the CFD simulations are compared to those from the 4D-Flow MRI data before any limitations of the validation are discussed.

5.2 Methodology

The experimental set-up that was used and the construction of the phantom-specific CFD simulations are detailed within this Section. The set-up of the patient-specific CFD simulations is identical to that used within Sections 4.6 and 4.5, within Chapter 4.

5.2.1 Experimental Set-up

The flow phantom selected for use was the commercially available, anatomically correct, aortic flow phantom constructed of a transparent, soft silicon (T-S-N 005, Elastrat, Geneva, Switzerland) [187]. The anatomical phantom reproduced the vasculature of the thoracic aorta, supra-aortic branches and the left and right coronary arteries, and is shown in Figure 5.1. The phantom was placed into a 4mm thick acrylic box filled with a 1% agar solution, ensuring the phantom was surrounded by an ultrasound-conductive medium for ultrasound imaging and static tissue comparison for phase contrast imaging.

The anatomical flow phantom shown in Figure 5.1 was attached to a MRI-conditional pulsatile flow pump (CardioFlow 5000MR, Shelley Medical Imaging Technologies, London, Canada) [188] which allows physiological pulsatile inlet flows to be reproduced. The working fluid left the pulsatile flow pump and passed through a non-return valve before entering the flow phantom, where the coronary arteries were clamped shut to keep the majority of the fluid travelling through the ascending aorta. The three supra-aortic outlets and the descending aortic outlet directed the working fluid to a shut-off valve that was placed after the phantom, before the fluid flowed into a reservoir and returned to the pump, as shown in Figure 5.2. A model of a bicuspid aortic valve was mounted on a length of High Density Polyethylene (HDPE) piping which was inserted into the flow phantom; this allowed the valve to be placed at the approximate location of the aortic annulus. MRI images of the anatomical flow phantom and the aortic valve were taken in a 1.5T Achieva (Philips, The Netherlands). The location and geometry of the opened, and closed, BAV can be seen within the flow phantom in the 4D-Flow MRI images within Figure 5.3.

The working fluid that was run through the flow phantom circuit replicated the material properties of blood to ensure results were physiologically accurate and was Newtonian and homogeneous. A

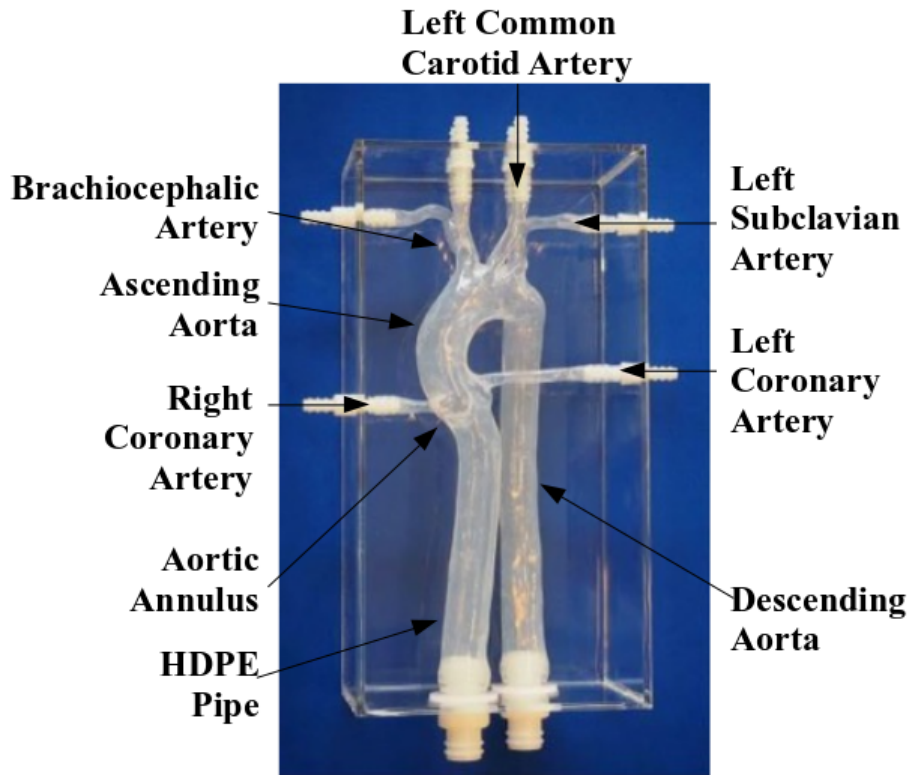


Figure 5.1. Anatomical flow phantom used in the experimental set-up to validate CFD methodology. The silicone flow phantom is shown in the 4mm acrylic box. Image taken from Elastrat [187].

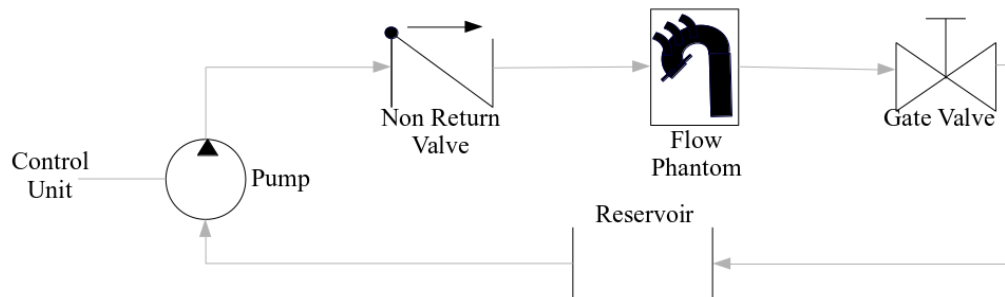


Figure 5.2. Flow circuit connected to the anatomical flow phantom.

solution of 60% distilled water and 40% glycerol was used as it is appropriate for MRI imaging [189, 190], and has the following physical properties:

- Dynamic viscosity: $\mu = 4.83 \times 10^{-3} Pa.s$
- Density: $\rho = 1119 kg^{-1}m^3$

Giving a kinematic viscosity of $\nu = 4.316 \times 10^{-6} \frac{m^2}{s}$; a reasonable approximation of the properties of blood at 37° , the average temperature of the human body.

5.2.2 Geometry Reconstruction

In order to run phantom-specific CFD simulations, an *in-silico* model of the flow phantom must be created. Using the methods described in detail in Section 3.3, the flow phantom geometry was reconstructed, including the supra-aortic vessels and neglecting the clipped off coronary arteries as they are not discernible in the 4D-Flow MRI data due to the low flow velocities that were created by clipping the vessels. Figure 5.4a shows the 4D-Flow MRI data of the flow phantom

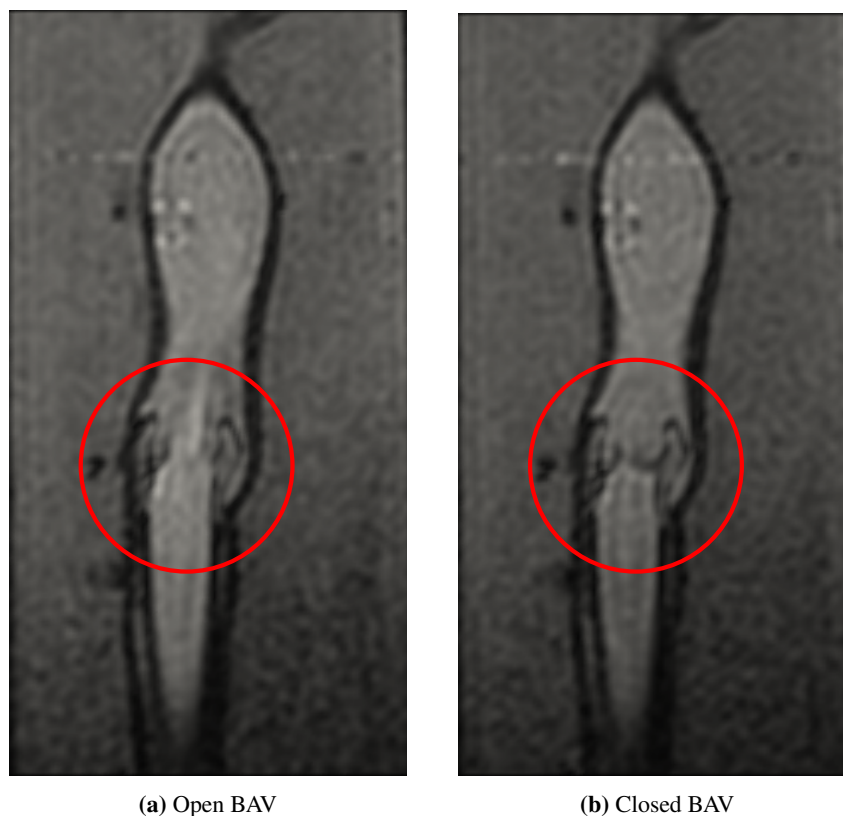


Figure 5.3. 4D-Flow MRI magnitude images taken in the coronal plane of the silicon flow phantom submerged in agar solution with BAV inserted. (a) demonstrates the open BAV, whilst (b) shows the aortic valve closed; one of the valve leaflets has restricted motion resulting in a reduced opening and an eccentric jet of blood being ejected.

where the impacts of BAV can be seen clearly through the eccentric and asymmetrical jet of blood that is being ejected from the aortic valve. It can be seen that the jet of blood is impinging on the vessel wall at the outer curvature of the aortic arch. Figure 5.4b clearly indicates the region where the HDPE pipe is joined to the anatomical flow phantom at the aortic annulus, and shows what appears to be a sudden expansion in the pipe diameter (highlighted in red) at the valve location. A notable artefact in the scan data can also be seen (highlighted in green), which further increased the complexity of the geometry reconstruction process. There is also a high level of noise throughout the scan, increasing the complexity of the contrast adjustment and thresholding processes. The final reconstructed *in-silico* geometry can be seen in Figure 5.4c compared to the 4D-Flow MRI data it is constructed from. The 4D-Flow MRI velocity data extracted once the geometry is reconstructed can be seen in Figure 5.5 over the course of the cardiac cycle, across a slice in the z plane.

5.2.3 Boundary Conditions

A spatio-temporal patient-specific inlet condition was applied to the inlet at the inferior ascending aorta, outflow conditions were applied to the four outlets at the distal end of the brachiocephalic artery, left common carotid artery, left subclavian artery, and the descending aorta. The walls were assumed to be rigid and the working fluid was assumed to have the same properties as described in Section 5.2.1, and was taken to be a Newtonian, incompressible, and homogeneous fluid.

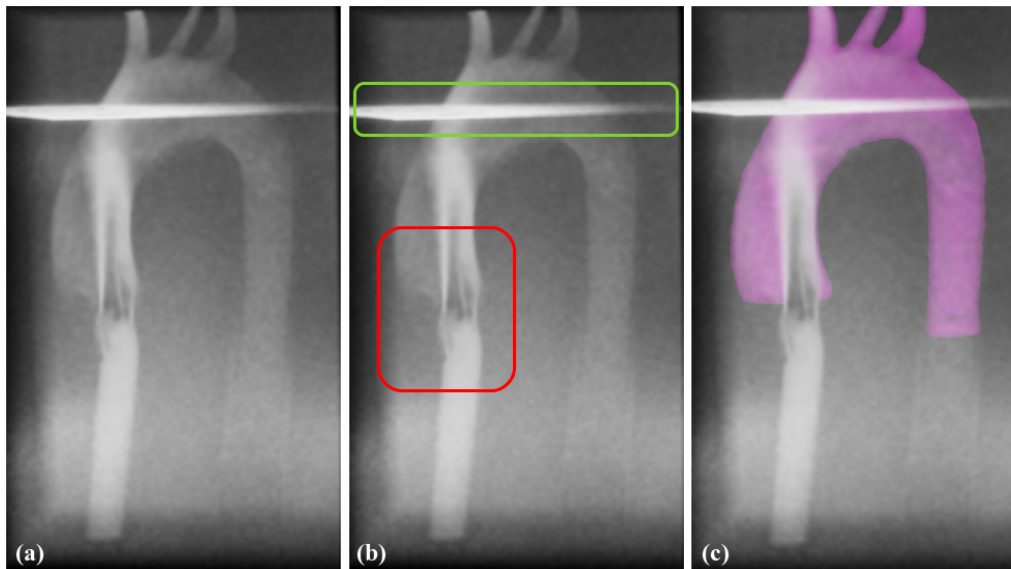


Figure 5.4. 4D-Flow MRI scan data of the flow phantom. (a) shows the 4D-Flow MRI data, (b) identifies the region where the two pipes with different diameters are joined (highlighted in red), as well as a region with a significant artefact in the data (highlighted in green), and (c) shows the reconstructed *in-silico* geometry using the method outlined in Section 3.3.

5.2.3.1 Inlet

A patient-specific spatio-temporal boundary condition was applied to the inlet slice following the methodology set out in Section 3.5.3. From the images in Figures 5.3 and 5.4 it is clear that there will be a highly asymmetric and eccentric flow profile being ejected into the ascending aorta in the positive y direction, from a plane that is parallel to the x axis. There is a region to the left of the ejected blood jet where there appears to be little to no flow being ejected into the aorta. The highly eccentric and asymmetric flow profile that the 4D-Flow MRI scan data alludes to can be seen clearly when the 4D-Flow MRI velocity magnitude data is plotted across the inlet plane over the course of the cardiac cycle, as shown in Figure 5.6. Figure 5.6 indicates that the calculated inlet conditions used in the CFD simulations are a reasonable approximation of the 4D-Flow MRI data in terms of the flow patterns found across the inlet, however the profile of the jet of ejected blood is simplified and smoothed out. This simplification is also seen within Patient OXBAV071, where the 4D-Flow MRI data also indicated a more complex flow profile at the aortic valve which was also smoothed and simplified by the calculated inlet condition.

The simplification of the flow profile can be seen most prominently at systole ($t = 6$), Figure 5.7 shows a more detailed view of the systolic inlet conditions. It highlights that the flow in the right, posterior, and anterior regions of the inlet plane is moving in the $-y$ direction whilst the jet of blood ejected is moving in the $+y$ direction, indicating that the flow movement in the region where there is no jet of blood it is a recirculation region and no flow is exiting through the valve in that location due to the fusion of the cusps.

Comparing the 4D-Flow MRI data to the calculated CFD inlet condition (Figure 5.7b) shows that although location and magnitude of the velocity peak are in reasonable agreement, the velocity vectors in the right, posterior, and anterior regions of the inlet plane are moving in the $+y$ direction. This will cause differences in the ascending aortic haemodynamics when compared to the 4D-Flow MRI. The full cardiac cycle was simulated using these inaccurate inlet boundary conditions and

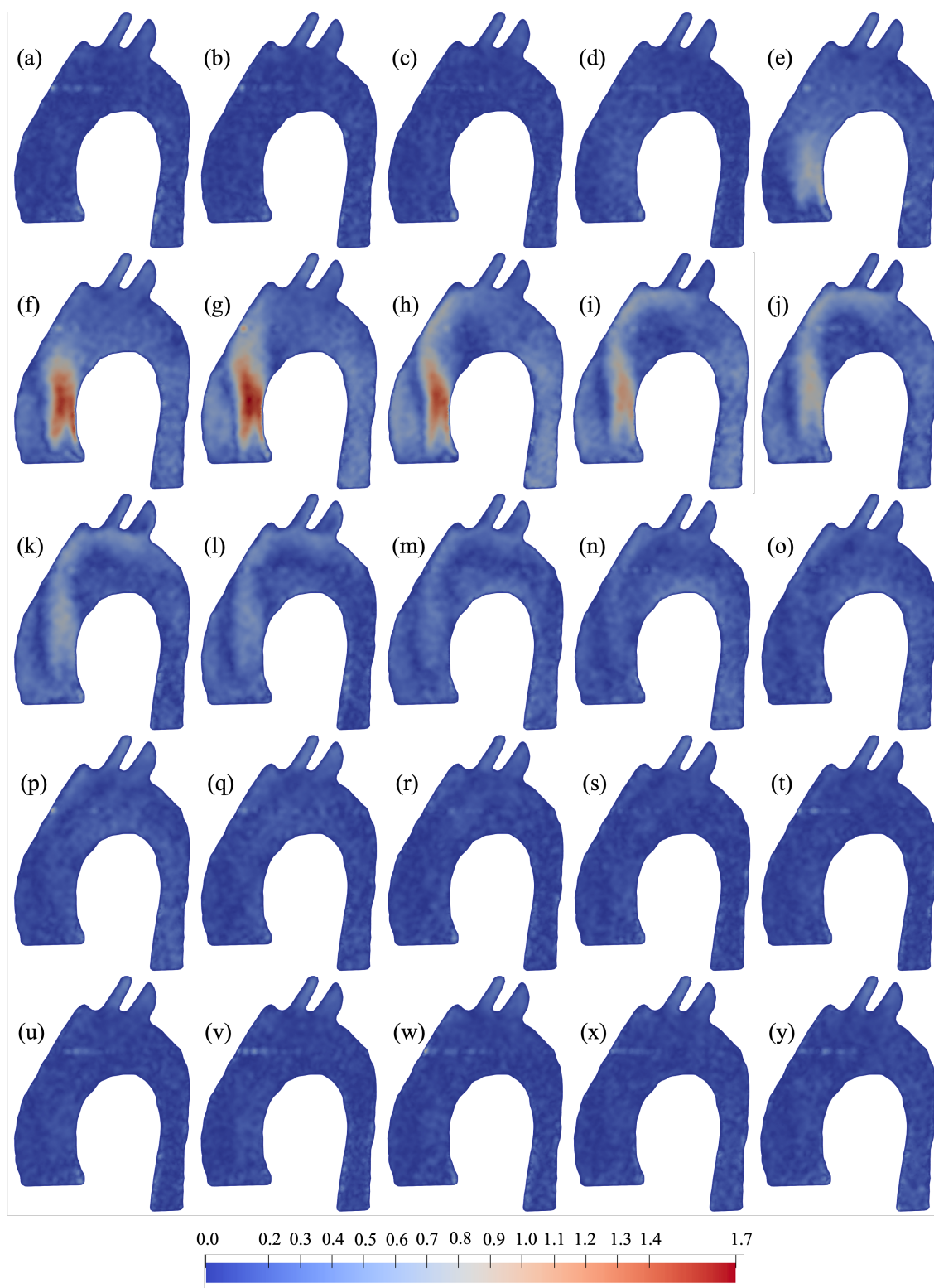
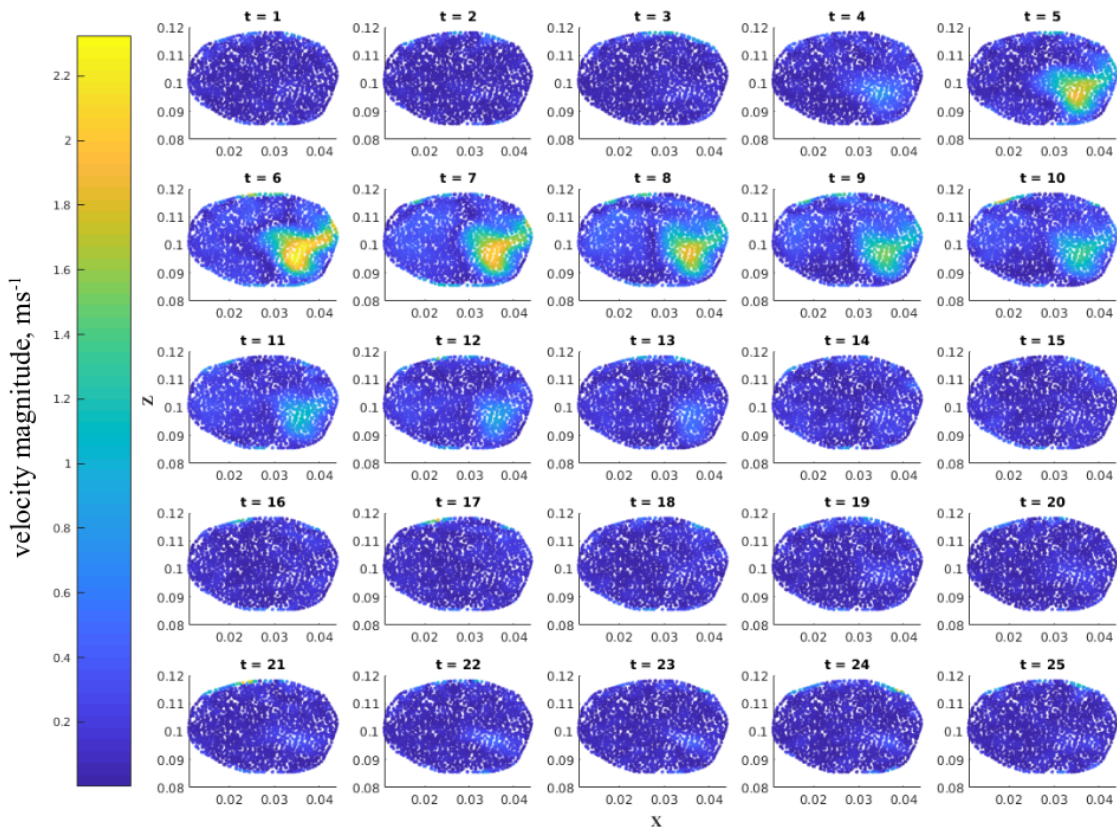
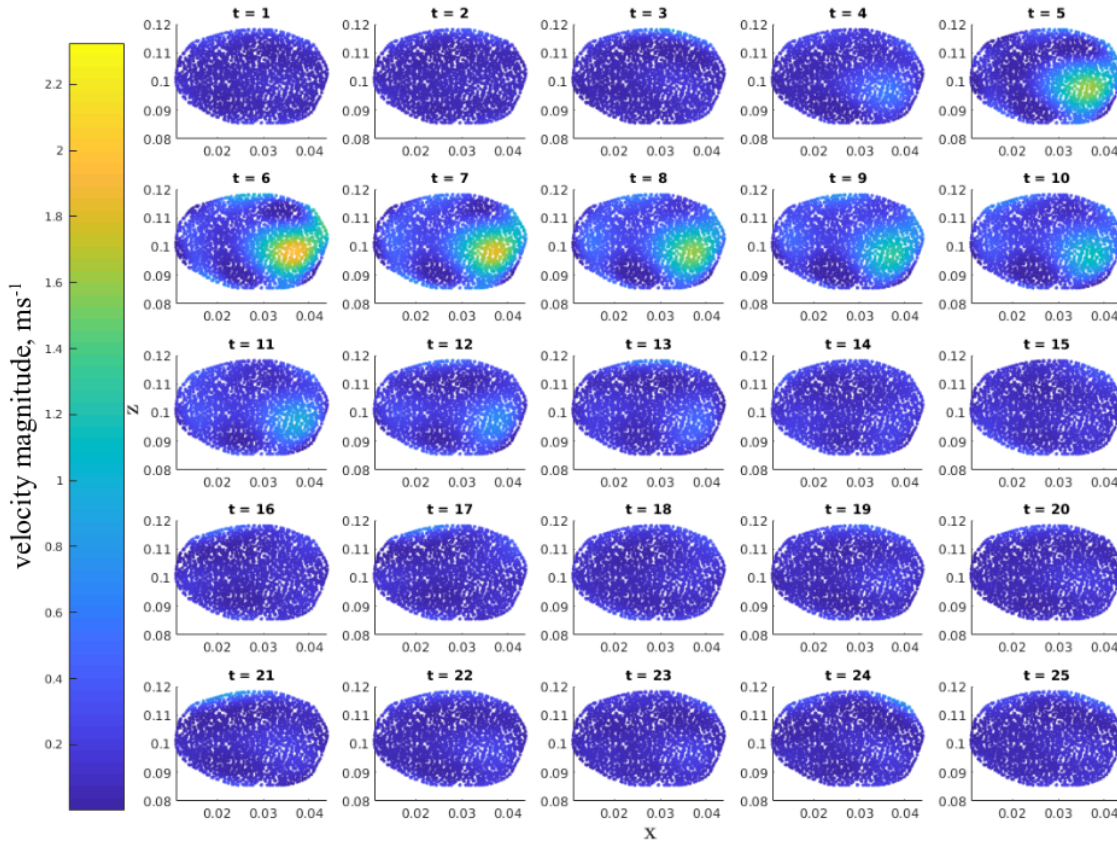


Figure 5.5. Velocity magnitude ($m s^{-1}$) contours across a slice in the z plane over the course of the cardiac cycle within the flow phantom. (a)=0s, (y)=0.7992s, with each timestep being 0.0333s in length.

compared to the 4D-Flow MRI data to demonstrate the differences an inaccurate inlet condition would cause. Figure 5.8a shows a large recirculation region in the left inferior region of the ascending aorta in the 4D-Flow MRI data that corresponds to the region on the inlet plane where there is flow in the $-y$ direction. Streamlines plotted from CFD simulations with the incorrect spatio-temporal patient-specific inlet condition shown in Figure 5.7b show no recirculation region present in the ascending aorta. The inconsistency in the vector direction across the right, posterior,



(a) 4D-Flow MRI



(b) CFD

Figure 5.6. Data points coloured by velocity magnitude (ms^{-1}) across the inlet plane over the cardiac cycle of the flow phantom, plotted using 4D-Flow MRI data (a), and the calculated inlet conditions applied in the CFD simulations (b).

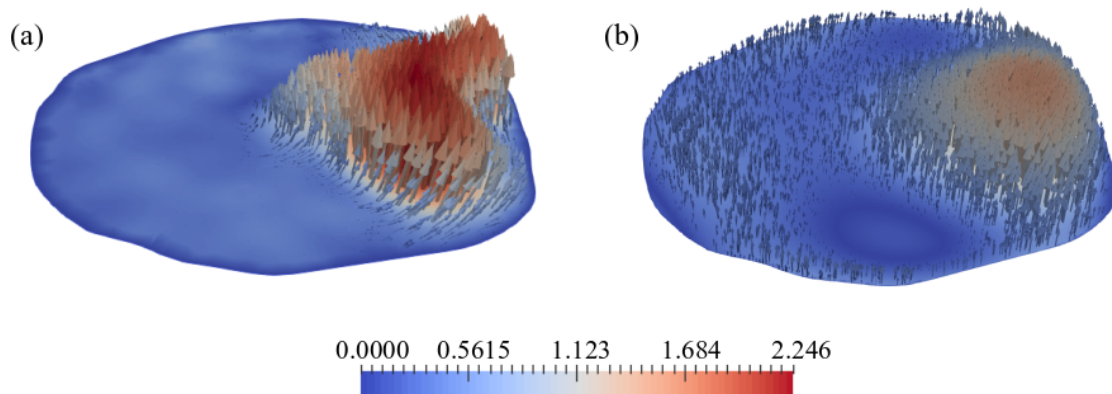


Figure 5.7. Velocity magnitude vectors across the inlet plane of the flow phantom calculated through 4D-Flow MRI (a) and initial CFD simulations (b) at systole.

and anterior regions in the inlet plane is the cause of the differences seen in the ascending aorta and brachiocephalic artery, and must be addressed to ensure the CFD tool is predicting the correct haemodynamics.

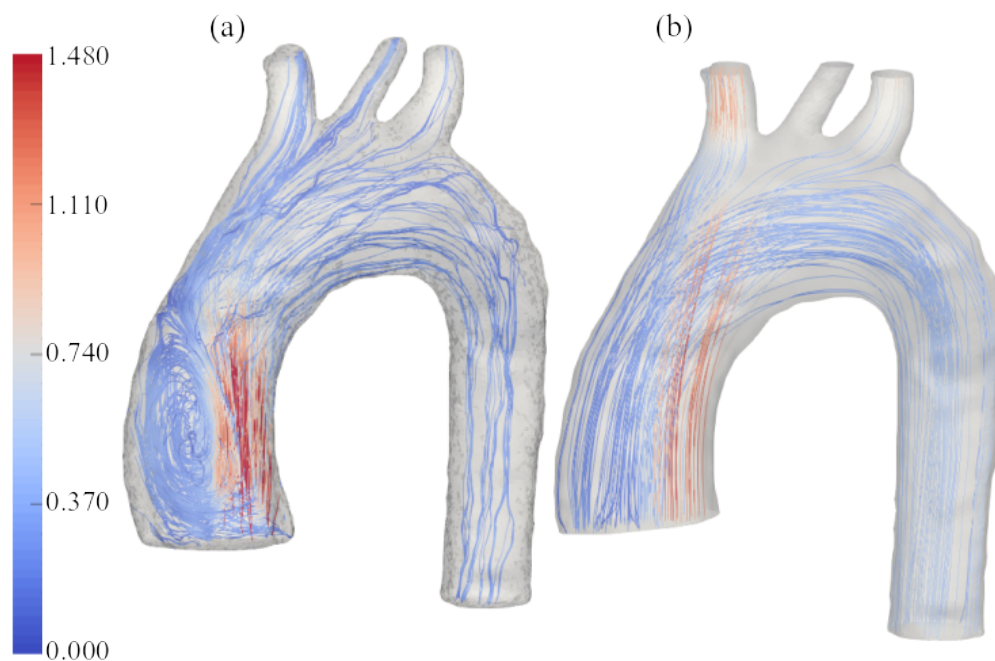


Figure 5.8. Streamlines coloured by velocity magnitude (ms^{-1}) within the flow phantom calculated through 4D-Flow MRI data (a) and initial CFD simulations (b) at systole.

The inlet condition was therefore adjusted to ensure the velocity direction appropriately replicated the complete fusion of the cusps which caused the zero flow across a section of the inlet plane. Figure 5.9 shows that the updated inlet conditions now accurately replicate the experimental data, and reproduce the recirculation region that is found in the left inferior region of the ascending aorta.

5.2.3.2 Outlets

Outflow percentages were prescribed at each of the four outlets based on the cross-sectional areas. It was calculated that 20.40% of the flow volume leaves through the brachiocephalic artery, 6.20% through the left common carotid artery, 10.72% through the left subclavian, and the remaining

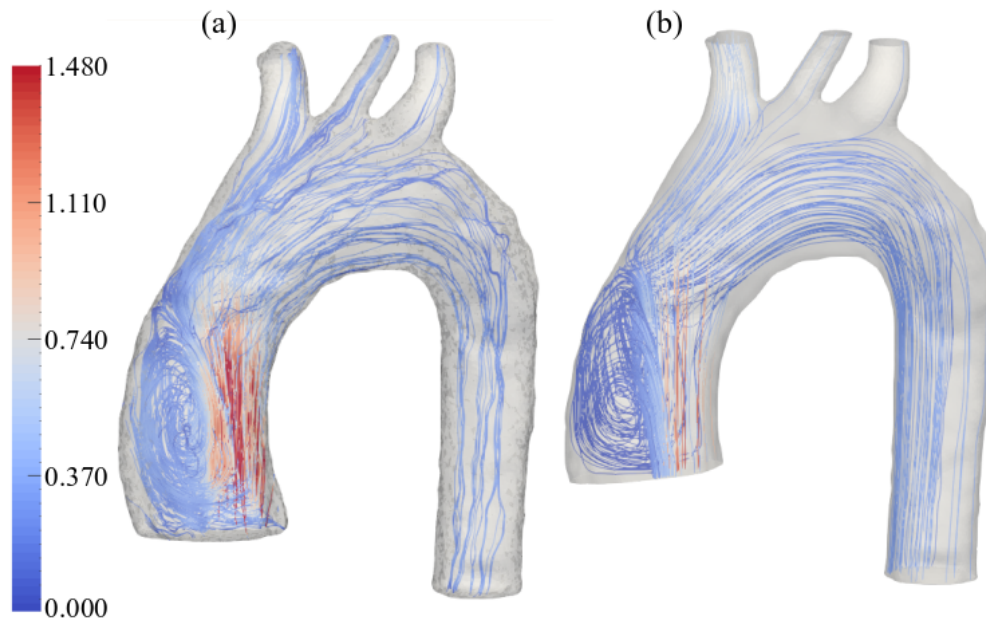


Figure 5.9. Streamlines coloured by velocity magnitude ($m s^{-1}$) within the flow phantom calculated through 4D-Flow MRI data (a) and CFD simulations with the updated inlet boundary condition (b) at systole.

62.68% through the descending aorta.

5.2.4 Numerical simulations

CFD simulations were performed using the transient, incompressible solver for Newtonian fluids, *pimpleFoam*, within OpenFOAM [6]. The working fluid was taken to be Newtonian, incompressible, and homogeneous with a dynamic viscosity and density as stated in Section 5.2.1. The $k-\omega$ SST turbulence model was incorporated into the numerical model as the blood flow was calculated to vary between the laminar, transitional, and turbulent regimes as the cardiac cycle progressed through systole and diastole. As the working fluid in the experimental set-up did not model a suspension of red blood cells, white blood cells, and platelets, the homogeneous assumption is correct and the Stokes number does not need to be determined throughout the cardiac cycle.

The meshing strategy outlined in Section 3.4.4.3 was applied to the reconstructed geometry of the flow phantom to ensure results were not affected by the grid density used. The mesh used consisted of 5,625,108 elements.

5.3 Results

5.3.1 Systole

Contours of velocity magnitude determined from 4D-Flow MRI and CFD data were plotted at three planes of interest in the mid-ascending aorta, aortic arch, and mid-descending aorta at systole, and results can be seen in Figure 5.10. In the mid-ascending aorta, it can be seen that there is excellent agreement between the 4D-Flow MRI data and the CFD data. Both 4D-Flow MRI and CFD data indicate a region of elevated velocity magnitude in the left and left-posterior region of the mid-ascending aorta. Alongside the flow patterns matching, the difference between the 4D-Flow MRI and CFD data in terms of maximum velocity magnitude is 3.950%, demonstrating the

excellent agreement. There is reduced qualitative agreement when observing the flow patterns and magnitude in the aortic arch and mid-descending aorta. It can be seen that the CFD methodology predicts a more uniform velocity flow field than that shown by the 4D-Flow MRI. The maximum velocity magnitude differs considerably between the two methods due to the smaller variations that are seen in the 4D-Flow MRI data. The mean velocities across the planes of interest in the aortic arch and mid-descending aorta show improved agreement compared to the maximum velocity magnitude, with agreement reducing as the flow progresses through the aorta, moving away from the patient-specific inlet conditions. Table 5.1 provides a summary of the maximum and mean velocities across the three planes of interest at systole.

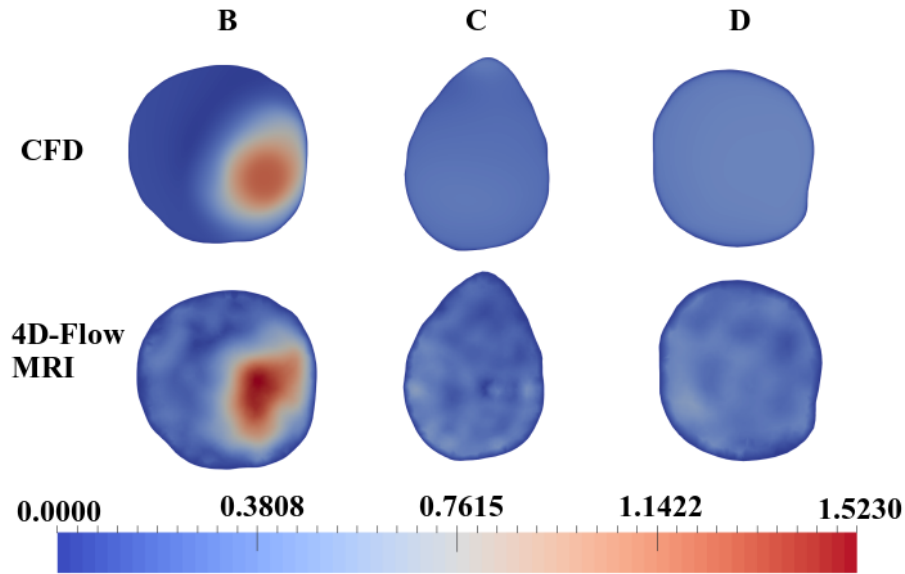


Figure 5.10. Contours of velocity magnitude ($m s^{-1}$) calculated through spatio-temporal patient-specific CFD simulations with the supra-aortic vessels included and 4D-Flow MRI data at systole at three planes of interest for the flow phantom. (B =mid-ascending aorta, C =aortic arch, D =mid-descending aorta).

Plane	4D-Flow MRI		CFD		Difference Between Methods	
	$U_{mag_{max}}$ ($m s^{-1}$)	U_{mean} ($m s^{-1}$)	$U_{mag_{max}}$ ($m s^{-1}$)	U_{mean} ($m s^{-1}$)	$U_{mag_{max}}$ % difference	U_{mean} % difference
B	1.523	0.3273	1.464	0.2936	3.950	10.86
C	0.5380	0.2043	0.3006	0.2405	56.62	16.30
D	0.5091	0.2398	0.3616	0.3205	33.88	28.81

Table 5.1. Maximum and mean velocity magnitude ($m s^{-1}$) data for the flow phantom at the three planes of interest during systole calculated from 4D-Flow MRI data and CFD data, including a comparison between the two methods at each location. (B =mid-ascending aorta, C =aortic arch, D =mid-descending aorta).

The flow asymmetry, flow dispersion, and circulation were also determined at the three planes of interest during systole. Figure 5.11 indicates that the ascending aorta provides the highest levels of agreement between the 4D-Flow MRI data and the CFD data in terms of flow asymmetry and flow dispersion, with differences of 49.23% and 41.47% respectively. Both the flow asymmetry and flow dispersion show poor agreement in the aortic arch and mid-descending aorta. The differences in flow asymmetry rise to 124.1% and 73.52% in the aortic arch and mid-descending aorta respectively, whilst the differences in flow dispersion rise to 197.9% and 192.2% respectively. This suggests that the inlet boundary conditions applied are appropriate and correctly predict the

haemodynamics within the ascending aorta during systole, and the flow asymmetry and flow dispersion are heavily impacted by the CFD data predicting a more uniform velocity field than that shown in 4D-Flow MRI data.

The circulation determined through CFD and 4D-Flow MRI data in all three planes is within the limits of normal flow, however disagrees on direction in all three planes. The large difference seen in the ascending aorta is likely a result of the large recirculation region that is found within the ascending aorta. Within the aortic arch and mid-descending aorta, there is significantly improved agreement between 4D-Flow MRI and CFD data, reducing from 190.9% in the mid-ascending aorta to 40.45% and 54.79% in the aortic arch and mid-descending aorta respectively.

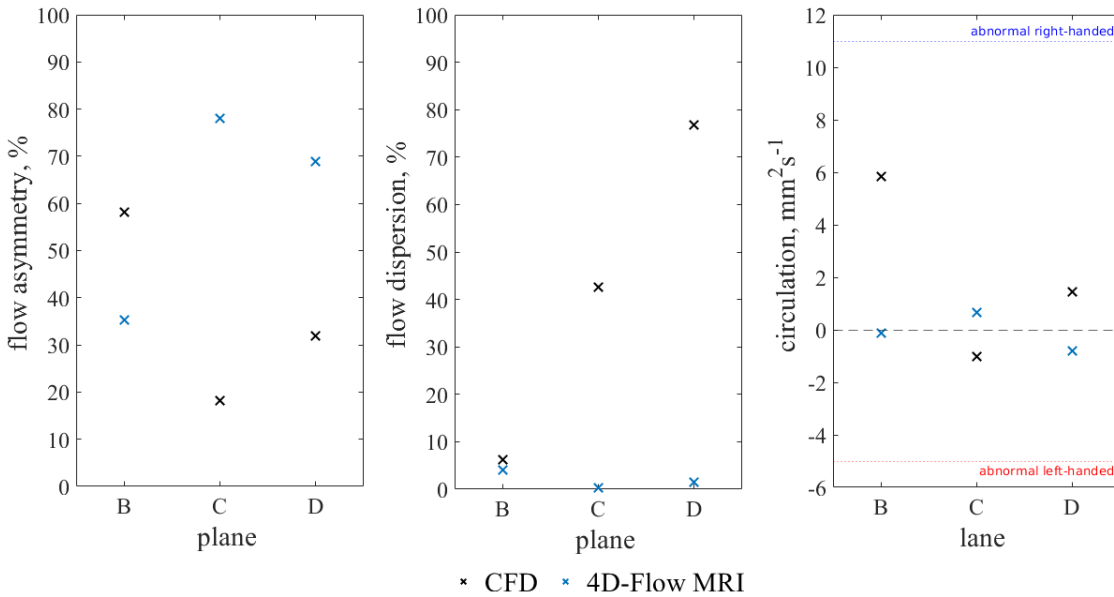


Figure 5.11. Flow asymmetry (%), flow dispersion (%), and through plane circulation (mm^2s^{-1}) at systole for the flow phantom at three planes of interest. (B=mid-ascending aorta, C=aortic arch, D=mid-descending aorta).

5.3.2 Diastole

Contours of velocity magnitude were determined from CFD and 4D-Flow MRI data for the three planes of interest at diastole, and can be seen in Figure 5.12. It can be seen from Figure 5.12 and 5.2 that there is poor agreement in terms of maximum velocity magnitude across all three locations between 4D-Flow MRI and CFD. This poor agreement is a result of the choice in inlet conditions poorly modelling the smaller fluctuations present at the aortic valve during diastole as discussed in detail in Chapter 4. It is also likely that the poor agreement between the 4D-Flow MRI and CFD data is a consequence of neglecting the aortic valve leaflets in the numerical simulations, whilst they are present in the flow phantom. Additionally, as the maximum velocity magnitude experienced within the flow phantom at systole is much higher than that within the patients participating in this research, it follows that the disagreement at diastole would be greater as there is a larger difference in the magnitudes of the velocities experienced between systole and diastole than for the patients participating within the research in Chapter 4. However, there is more reasonable agreement when observing the mean velocities across the three planes of interest, and is summarised in Table 5.2.

The flow asymmetry, flow dispersion, and circulation were calculated from 4D-Flow MRI and

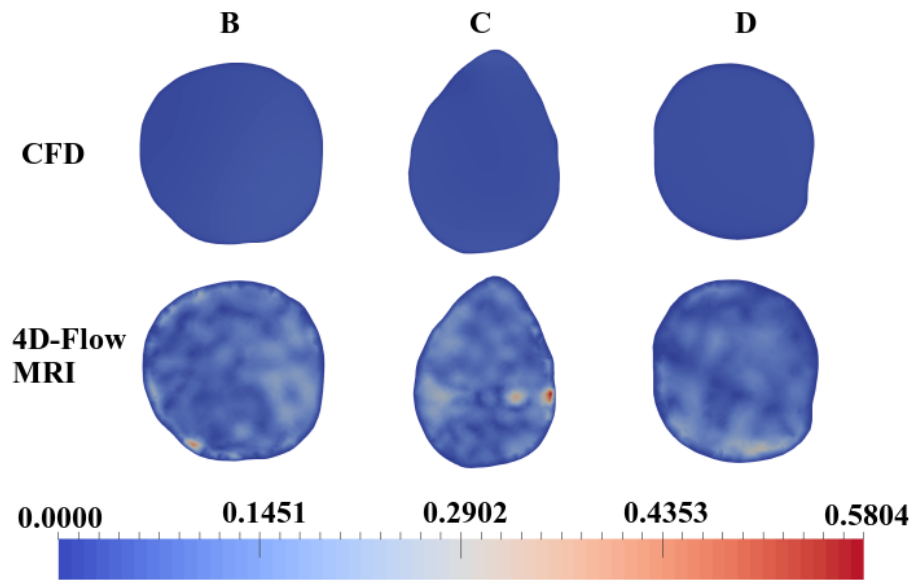


Figure 5.12. Contours of velocity magnitude (ms^{-1}) at three planes of interest for the flow phantom at diastole. Velocity contours calculated through the CFD methodology are given in (a), (c), and (e). Velocity contours calculated by 4D-Flow MRI are given in (b), (d), and (f).

Plane	4D-Flow MRI		CFD		Difference Between Methods	
	$U_{mag_{max}}$ (ms^{-1})	U_{mean} (ms^{-1})	$U_{mag_{max}}$ (ms^{-1})	U_{mean} (ms^{-1})	$U_{mag_{max}}$ %	U_{mean} % difference
B	0.3790	0.05143	0.05278	0.03794	151.1	30.20
C	0.5804	0.04296	0.04767	0.03012	169.6	35.13
D	0.2965	0.04068	0.03923	0.03445	153.3	16.58

Table 5.2. Maximum and mean velocity magnitude (ms^{-1}) data for the flow phantom at the three planes of interest during diastole calculated from 4D-Flow MRI data and CFD data, including a comparison between the two methods at each location. (B=mid-ascending aorta, C=aortic arch, D=mid-descending aorta).

CFD data for across all three planes of interest, and results can be seen in Figure 5.13. As found during systole, the flow asymmetry in the mid-ascending aorta offers the highest level of agreement between the CFD and 4D-Flow MRI data compared to the aortic arch and mid-descending aorta. The flow dispersion shows poor agreement in both the mid-ascending aorta and the mid-descending aorta, with CFD significantly overestimating the values. This is likely a result of the small fluctuations not being replicated by the CFD model. These fluctuations in the 4D-Flow MRI data may be a result of the aortic valve leaflets being incorporated into the flow phantom and neglected in the CFD model. The motion of the valve leaflets will cause secondary flow features within the aorta, however during systole these will not be of the same order of magnitude as the jet of blood being ejected, therefore neglecting these secondary flows at systole does not largely impact the haemodynamics of the thoracic aorta. However, during diastole, there is no jet of blood being ejected into the aorta, meaning the secondary flow features caused by the valve leaflets closing will be of the same order of magnitude or larger than the flow within the aorta. As the CFD model neglects the movement of the valve leaflets, the haemodynamics being predicted will be inaccurate and will be dissimilar to the haemodynamics shown in 4D-Flow MRI data. It is possible that this is the cause of the large differences seen between CFD and 4D-Flow MRI data during diastole.

There is reasonable agreement between the CFD and 4D-Flow MRI data in terms of circulation direction: agreeing in two of the three locations, alongside all three planes indicating the levels of helical flow are within normal flow limits. Good agreement can be seen in terms of circulation magnitude in the aortic and mid-descending aorta.

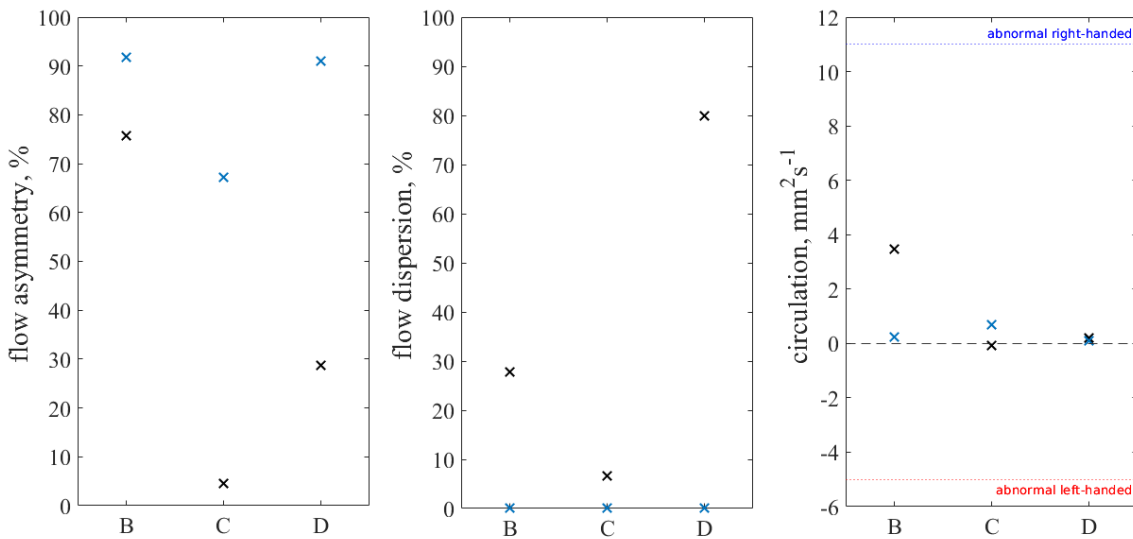


Figure 5.13. Flow asymmetry (%), flow dispersion (%), and through plane circulation (mm^2s^{-1}) values calculated using CFD and 4D-Flow MRI data at diastole for the flow phantom at three planes of interest.

5.4 Limitations

Although it is clear from the results presented that the CFD methodology replicates the 4D-Flow MRI scan data of the flow phantom in the mid-ascending aorta during systole, there are limitations to the flow phantom set up that was used and the CFD methodology implemented. Primarily, the flow phantom includes a bicuspid aortic valve attached to an HDPE pipe that is attached to the flow phantom at the aortic annulus, and as such includes the valve leaflets in the experimental set up. The valve leaflets can be seen to move in Figure 5.3. The CFD workflow used to predict the haemodynamics in the thoracic aorta does not incorporate the FSI of the aortic valves. It is likely that neglecting the aortic valve leaflets causes the secondary flow features to be eliminated in the CFD simulations, causing the haemodynamics to be incorrectly predicted during the diastolic phase of the cardiac cycle. To correctly model the haemodynamics in the thoracic aorta during the entire cardiac cycle, the aortic valve leaflets and any interaction between them and the blood flow must therefore be included in the CFD methodology.

An additional limitation is within the inlet conditions applied. Alongside neglecting the impacts of the aortic valve leaflets, the inlet conditions do not replicate the flow patterns during diastole accurately. It is likely this is a result of the smaller fluctuations that are present being neglected as they are orders of magnitude smaller than the jet of blood ejected during systole, causing the surface fit to not accurately replicate them. The inlet conditions slightly under predict the maximum velocity magnitude at the inlet. As demonstrated in Figure 5.6, the inlet condition reasonably estimates the location of the jet of ejected blood, but fails to accurately model the flow profile, simplifying it and smoothing out the 4D-Flow MRI data.

The spatial and temporal resolutions of the 4D-Flow MRI scan used to acquire data also present

a limitation to this investigation. Currently it is not known how much an insufficient spatial resolution will influence the 4D-Flow MRI data and therefore the subsequent patient-specific CFD simulations that are run. The extent to which the spatial resolution the 4D-Flow MRI data is acquired at influences the CFD results is discussed in more detail and quantified within Chapter 6.

The choice in outlet conditions do not present as a limitation when investigating the haemodynamics within the flow phantom as they do when predicting *in-vivo* haemodynamics as the compliance of the vessel and the resistance from the systemic circulatory distal to the outlets are not included in the experimental set-up. However, ideally the experimental set up would allow the supra-aortic vessels to be extended to more than 5 diameters upstream of the aortic arch, to ensure the haemodynamics of the thoracic aorta are not affected by the choice in outlet conditions. However, this is not possible with the flow phantom as the experimental set up does not include the full length of the supra-aortic vessels.

5.5 Conclusions

The results from the research within this Chapter indicate that the CFD workflow created within Chapter 3 can successfully replicate the haemodynamics within the ascending aorta at systole, replicating the maximum velocity to within 3.950% and the mean velocity to within 10.86% of the 4D-Flow MRI data. This suggests that if the systolic phase of the cardiac cycle is of interest to clinicians, the workflow presented within Chapter 3 will accurately replicate the haemodynamics to a good degree, allowing for any large changes as a result of altered flow profile at the aortic valve from an AVR to be detected. However, the results also indicate that the workflow created has significant limitations when the diastolic phase of the cardiac cycle is modelled. The inefficiencies have likely been magnified in the flow phantom as the peak velocities experienced during systole are larger than those experienced in the patients participating within the research in Chapter 4. From this, it can be assumed that the smaller the range in velocities between systole and diastole, the better the surface fit applied as the inlet conditions will perform.

Results within Section 5.3.2 clearly show that the CFD methodology struggles to accurately predict the haemodynamics of diastole, and as discussed this is likely a consequence of insufficient inlet conditions not replicating the smaller fluctuations that can be seen within the 4D-Flow MRI data combined with the decision to neglect the FSI between the blood and the aortic valve leaflets. The aortic valve leaflets will introduce secondary flow features that are not found within the CFD simulations as the FSI is neglected. These flow features will be more prominent during the diastolic phase of the cardiac cycle than the systolic phase due to the magnitude of the jet of blood that is ejected at systole.

The results within this Chapter indicate that when the radial and vertical movement of the thoracic aorta is removed from the 4D-Flow MRI data, in this case as the flow phantom is encased in a 1% agar solution and does not move during the 4D-Flow MRI acquisition, there is improved agreement between the CFD and 4D-Flow MRI data. This suggests that the FSI between the vessel walls, surrounding tissues, intercostal, oesophageal, and bronchial arteries, and the blood is vital and should not be neglected.

Chapter 6.

The Impacts of 4D-Flow MRI spatial resolution on patient-specific CFD simulations

Contents

6.1	Introduction	134
6.2	Methodology	136
6.2.1	Data Acquisition	136
6.2.2	Geometry Reconstruction	137
6.2.3	Meshing	140
6.2.4	Boundary Conditions	140
6.2.5	Numerical Simulations	144
6.3	Results	144
6.3.1	Velocity	144
6.3.2	Wall Shear Stress	149
6.3.3	Flow Asymmetry	152
6.3.4	Flow Dispersion	152
6.3.5	Circulation	154
6.4	Limitations	154
6.5	Conclusions	156

6.1 Introduction

As discussed in Chapter 2, MRI is frequently regarded as the 'gold standard' of medical imaging. 4D-Flow MRI builds on standard MRI, and as such is also regarded highly as a form of medical imaging. However, as the spatial resolution that is currently available is often of the same order of magnitude as the diameter of the vessel of interest, the accuracy of using 4D-Flow MRI to run patient-specific CFD simulations must be assessed as there may be too few voxels (≤ 6 across the diameter [169]) to accurately describe the flow [44]. When the spatial and temporal resolution used are too coarse, the parameters of the 4D-Flow MRI will be inadequate to capture the turbulence within the flow, and the peak velocities experienced within the vessels are likely to be

underestimated. The inferior image quality associated with coarser spatial resolutions will also lead to uncertainties in the geometry and vessel wall location, which is known to lead to uncertainties in parameters of interest such as WSS [35, 46]. It can be assumed that any subsequent patient-specific CFD simulations based on 4D-Flow MRI data will be affected by the spatial resolution the 4D-Flow MRI data is acquired at. It has been recommended by Dyverfeldt *et al.* [44] that a spatial resolution of $x \times y \times z \leq 2.5\text{mm} \times 2.5\text{mm} \times 2.5\text{mm}$ be used if imaging the aorta and pulmonary arteries, and a spatial resolution of $x \times y \times z \leq 3\text{mm} \times 3\text{mm} \times 3\text{mm}$ be used if imaging the whole heart and great vessels. It was also suggested to use isotropic voxels so results are not direction dependent. The spatial and temporal resolutions used in a selection of studies (2010 – 2019) can be seen in Table 6.1. It can be seen that using an isotropic spatial resolution is not common practice, with the spatial resolutions in the z direction being coarser than the x and y directions, in many cases coarser than recommended by Dyverfeldt *et al.* [44], meaning results will be direction dependent.

Study	Vessel Of Interest	Temporal Resolution (ms)	Spatial Resolution (mm^3)
Barker <i>et al.</i> [35]	Ascending Aorta	38.4-52.5	$1.8 - 2.1 \times 1.8 - 2.1 \times 2.0 - 2.8$
Barker <i>et al.</i> [35]	Ascending Aorta	40.8	$2.1 \times 2.1 \times 2.4$
Barker <i>et al.</i> [45]	Ascending Aorta	10-30	$0.82 - 1.56 \times 0.82 - 1.56 \times 5.0$
Hope <i>et al.</i> [46]	Ascending Aorta	74-77	$1.17 \times 1.56 \times 2.6$
Rose <i>et al.</i> [47]	Ascending Aorta	37.6-44	$1.23 - 3.46 \times 1.13 - 2.5 \times 1.2 - 3.0$
de Beaufort <i>et al.</i> [48]	Ascending Aorta	38-47	$2.0 - 3.0 \times 2.3 - 3.8 \times 3.4 - 5.0$
Biglino <i>et al.</i> [126]	Ascending Aorta	33.4	$2.2 \times 2.2 \times 2.2$
Hellmeier <i>et al.</i> [18]	Ascending Aorta	$\frac{1}{25}^{th}$ of a heartbeat	$1.83 - 2.25 \times 1.83 - 2.25 \times 2.0 - 2.8$
Kimura <i>et al.</i> [82]	Ascending Aorta	33	n/a
Kimura <i>et al.</i> [82]	Ascending Aorta	43	n/a
Miyazaki <i>et al.</i> [120]	Aortic Arch	49.2	$1.25 \times 1.25 \times 2.0$
Miyazaki <i>et al.</i> [120]	Aortic Arch	41.7	$0.885 \times 0.885 \times 1.0$
Soudah <i>et al.</i> [84]	Thoracic Aorta	45-49	$1.78 \times 1.78 \times 2.0$

Table 6.1. Spatial ($x \times y \times z\text{mm}^3$) and temporal (ms) resolutions of 4D-Flow MRI scans used in recent studies (2010-2019) that have utilised 4D-Flow MRI to acquire haemodynamic data.

As seen in Chapter 4, results from patient-specific CFD simulations are failing to adequately agree with those from 4D-Flow MRI even when spatio-temporal inlet conditions and the supra-aortic vessels are incorporated. It is likely that a large proportion of the errors reported between 4D-Flow MRI data and the corresponding CFD data can be attributed to insufficient 4D-Flow MRI spatial resolution. In order to correctly assess the accuracy of the CFD methodology created, the impact of 4D-Flow MRI spatial resolution on the subsequent patient-specific CFD simulations must be investigated. The repercussions of an insufficient spatial resolution on the reconstructed geometry and the inlet condition calculated from the 4D-Flow MRI data must be assessed. Although it has been long established that the spatial resolution of 4D-Flow MRI influences the accuracy of the scan, the errors that are introduced to the subsequent CFD simulations have yet to be quantified. It must be determined therefore what 4D-Flow MRI spatial resolution is appropriate

to successfully model haemodynamics within the thoracic aorta when using 4D-Flow MRI based CFD simulations. The work within this Chapter has been summarised in the research presented by Cherry *et al.* [185].

6.2 Methodology

6.2.1 Data Acquisition

As discussed in Sections 2.3 and 6.1, the spatial resolution of 4D-Flow MRI is a key limitation in its accuracy as an imaging technique. All adult patients participating in the research within this thesis underwent a 4D-Flow MRI with a spatial resolution of $2mm \times 1.67mm \times 2.2mm$ and a temporal resolution of $40ms$, as stated in Section 3.2, whilst all neonatal patients underwent a 4D-Flow MRI scan with a spatial resolution of $1mm \times 1mm \times 1mm$ and a temporal resolution of $33.6ms - 40ms$. It is highly likely that the resolutions that were used in 4D-Flow MRI acquisitions were inadequate to fully capture the turbulence within the flow, and may lead to high flow velocities experienced at peak systole to be underestimated.

In order to quantify the impact the 4D-Flow MRI resolution has on CFD simulations, an additional patient to those detailed in Section 3.2 has undergone four 4D-Flow MRI scans with varying spatial resolutions. The additional patient participating is identified as CoRaL080, and is a healthy adult with no known history of heart disease. The four spatial resolutions the 4D-Flow MRI data was acquired at were $1.5mm \times 1.5mm \times 1.5mm$, $2mm \times 2mm \times 2mm$, $3mm \times 3mm \times 3mm$, and $4mm \times 4mm \times 4mm$. Scans were acquired of the thoracic aorta and the proximal supra-aortic vessels on a 3T Magnitude Resonance system (Siemens 3.0 T PRISMA, Siemens Healthcare, Erlangen, Germany), with velocity encoding set to $150cm/s$ in all directions and flip angle was set to 7° . A temporal resolution of $\sim 35ms$ was used for the three coarsest spatial resolutions, whilst a coarser temporal resolution of $\sim 42ms$ was required for the finest spatial resolution. This was a result of the processing power available; a temporal resolution of $\sim 35ms$ was not achievable with the $1.5mm \times 1.5mm \times 1.5mm$ as the data-set generated was too large for the 4D-Flow MRI scanner to process. The acquisition times of the four scans were as follows; $4mm \times 4mm \times 4mm = 4$ minutes for a scan of the whole heart, $3mm \times 3mm \times 3mm = 8$ minutes for a scan of the whole heart, $2mm \times 2mm \times 2mm = 15$ minutes for a scan of the whole heart, and $1.5mm \times 1.5mm \times 1.5mm = 15$ minutes for a scan of the thoracic aorta only.

The difference in the image quality between the 4D-Flow MRI spatial resolutions is notable, and can be seen clearly in Figure 6.1. For the $4mm \times 4mm \times 4mm$ scan, the width of the individual voxel is of the same magnitude of the diameter of the thoracic aorta. The differences in the image quality is compared quantitatively in Table 6.2, where the number of voxels in the x and z directions are stated for an axial plane in the mid-ascending aorta (see Figure 6.2 for the cross-section and location of the plane in the mid-ascending aorta). This gives an indication as to the geometric accuracy of the spatial resolutions. Based on the number of voxels in the x and z directions across the ascending aorta reported within Table 6.2, it is apparent that the coarser resolutions will not have sufficient voxels, as recommended by Hofman *et al.* [169], to describe any vessels with a diameter smaller than the thoracic aorta, such as the supra-aortic vessels. Therefore, to ensure fair comparison between the spatial resolution was possible, the supra-aortic vessels were neglected for all spatial resolutions.

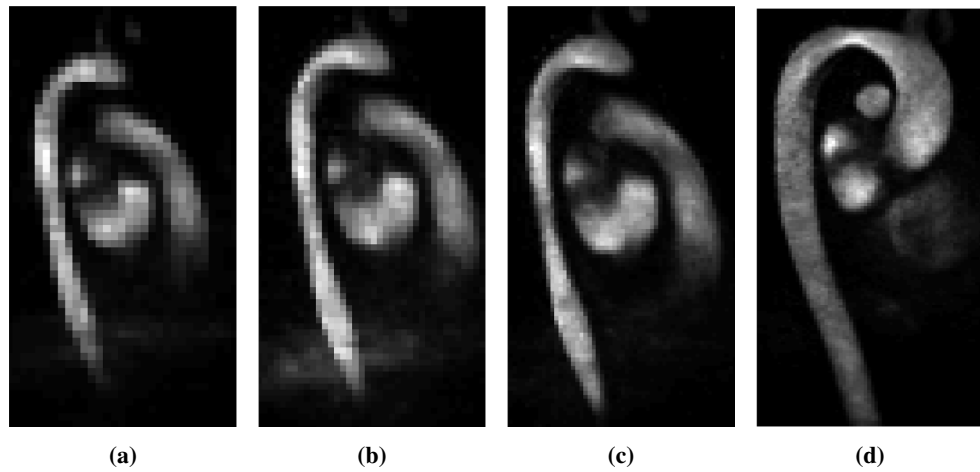


Figure 6.1. 4D-Flow MRI images in the same location in the sagittal plane of the thoracic aorta, taken at the four varying spatial resolutions for the patient CoRaL080. (a) = $4mm \times 4mm \times 4mm$, (b) = $3mm \times 3mm \times 3mm$, (c) = $2mm \times 2mm \times 2mm$, (d) = $1.5mm \times 1.5mm \times 1.5mm$.

Scan Resolution ($xmm \times ymm \times zmm$)	Number of Voxels in x direction	Number of Voxels in z direction
$4 \times 4 \times 4$	7	6
$3 \times 3 \times 3$	10	8
$2 \times 2 \times 2$	15	12
$1.5 \times 1.5 \times 1.5$	20	16

Table 6.2. The number of voxels in the x and z directions for the four scan resolutions in a slice in the axial plane in the mid-ascending aorta

Patient-specific CFD simulations were then run using the data from each resolution to reconstruct the geometry and calculate the inlet conditions, and results between 4D-Flow MRI and CFD from all spatial resolutions were compared to assess the errors stemming from the 4D-Flow MRI spatial resolution.

As each spatial resolution used required a separate 4D-Flow MRI acquisition, it is likely that there will be small natural variations present between the four acquisitions. A healthy cardiovascular system is known to have complex and non-linear variability patterns that can be described by mathematical chaos. Based on the acquisition times of the 4D-Flow MRI scans, the 24 hour and short-term (~ 5 minutes) Heart Rate Variability (HRV) of the patient must be noted [191]. The circadian rhythm, alongside core body temperature, metabolism and the sleep cycle are known to influence the 24 hour variability in blood pressure and heart rate of the patient [191, 192], whilst the respiration rate is also known to influence the heart rate and values obtained during normal breathing and paced breathing can vary significantly [193]. This suggests that small variations may be present between the four acquisitions.

6.2.2 Geometry Reconstruction

Using the methods outlined in Section 3.3, a patient-specific geometry was reconstructed from each of the four 4D-Flow MRI scans to create four distinct *in-silico* geometries that are suitable for use in the subsequent CFD simulations. The resulting *in-silico* models can be seen in Figure 6.3. It is clear that increasing the resolution of the 4D-Flow MRI scan significantly improves the quality of the reconstructed geometry that is created for CFD simulations. Utilising a coarse

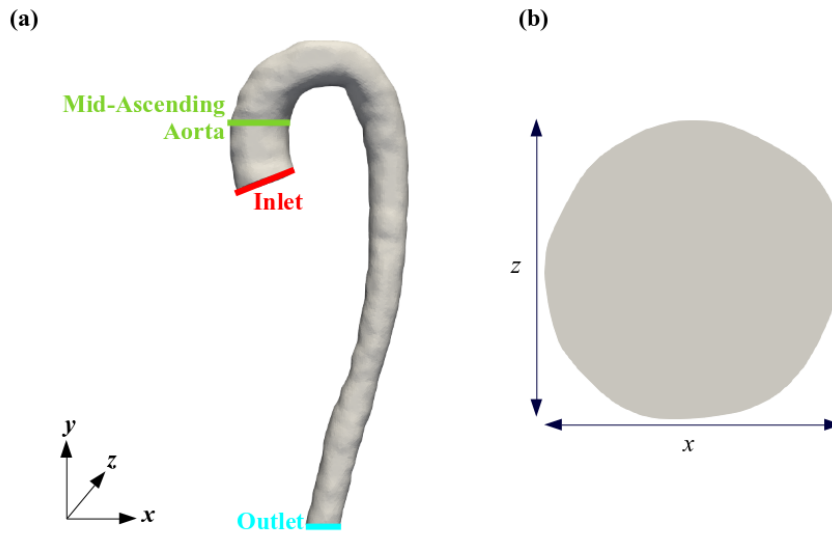


Figure 6.2. Location of inlet, outlet, and the plane of interest in the mid-ascending aorta for patient CoRaL080 (a), and the cross-section of the plane of interest in the mid-ascending aorta (b).

spatial resolution during the 4D-Flow MRI results in an *in-silico* model that is not smooth and has an irregular surface, which will have consequences when running patient-specific CFD simulations. The four *in-silico* geometries reconstructed were all based on the maximum reported dimensions during peak systole. This allows the movement of the aorta during the cardiac cycle to be neglected in all four cases, and ensures that the plane of interest in the mid-ascending aorta can be in the same local y location for each *in-silico* model. In all four cases the inlet plane was placed in the physiologically accurate location. This ensured comparison between the four spatial resolutions at the inlet and mid-ascending aortic planes would be appropriate and not affected by any misalignment of the planes between the resolutions.

To compare the impact the spatial resolution has on the reconstructed geometry of the thoracic aorta, the diameter of the inlet plane was calculated from the 4D-Flow MRI inlet data after segmentation had occurred and was compared to the inlet diameter calculated after meshing had occurred for all four spatial resolutions. Results can be seen in Table 6.3. There is excellent agreement between CFD and 4D-Flow MRI data in terms of diameter, with the agreement being $\leq 1\%$ for all four spatial resolutions. There are slight variations within the diameters between the resolutions in both the 4D-Flow MRI ($2.551\text{cm} \pm 0.08186$) and CFD data ($2.544\text{cm} \pm 0.08346$). The variation in diameters shows a clear trend in both CFD and 4D-Flow MRI data that implies that as the spatial resolution of the 4D-Flow MRI data is refined the diameter of the inlet plane reduces, resulting in the finest spatial resolution having the smallest inlet area.

Scan Resolution ($x\text{mm} \times y\text{mm} \times z\text{mm}$)	4D-Flow MRI Inlet Diameter (cm)	CFD Inlet Diameter (cm)
$4 \times 4 \times 4$	2.659	2.658
$3 \times 3 \times 3$	2.569	2.555
$2 \times 2 \times 2$	2.499	2.491
$1.5 \times 1.5 \times 1.5$	2.478	2.474

Table 6.3. Inlet plane diameters (cm) for all 4D-Flow MRI scans calculated from 4D-Flow MRI data and CFD data.

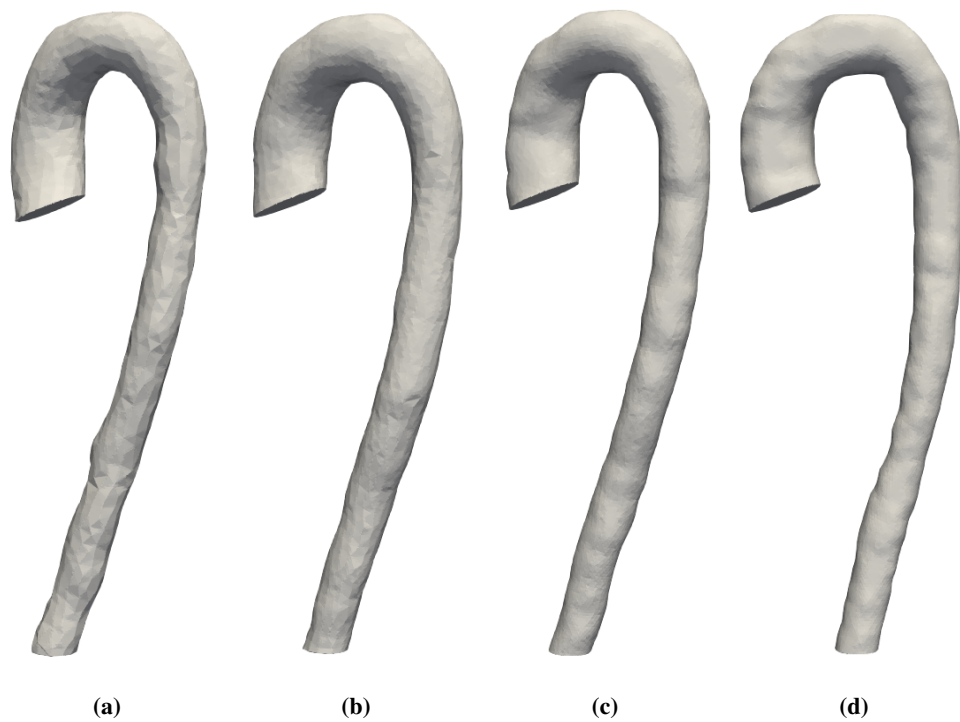


Figure 6.3. *in-silico* patient-specific geometries created from 4D-Flow MRI images from the four varying spatial resolutions for the patient identified as CoRaL080. (a) = $4mm \times 4mm \times 4mm$, (b) = $3mm \times 3mm \times 3mm$, (c) = $2mm \times 2mm \times 2mm$, and (d) = $1.5mm \times 1.5mm \times 1.5mm$.

This trend shows there is a clear relationship between the spatial resolution the 4D-Flow MRI data is acquired at and the vessel diameter and that the size of the reconstructed vessel is sensitive to the spatial resolution. It can be assumed that the overestimation that is present at the inlet plane when a coarse spatial resolution is used will be occurring throughout the domain, therefore a coarse 4D-Flow MRI spatial resolution will cause an overestimation of the vessel volume. It must also be noted that it is possible the segmentation and thresholding process described in Section 3.3 are contributing to the overestimation in vessel volume. As there is no method of determining the true size of the vessel *in-vivo*, the size of the potential error due to the geometry reconstruction process cannot be found. However, as the methods used for each spatial resolution are identical, any error due to the segmentation and thresholding processes will be similar and it can be assumed that the differences found between the four 4D-Flow MRI spatial resolutions can be attributed solely to the varying spatial resolutions.

Despite the clear differences in image quality and the reconstructed geometries, it is not common practice to run 4D-Flow MRI scans at a high spatial resolution for a wide range of reasons. Primarily this is due to higher resolution scans requiring a longer period of time to conduct; the $1.5mm \times 1.5mm \times 1.5mm$ acquisition takes approximately four times the length of the $4mm \times 4mm \times 4mm$ acquisition and scans a smaller area of the patient. The increasing times required are known to be difficult for the patient as they can become impatient, discomfort levels will rise, and often claustrophobia will be experienced. This discomfort means the patient is likely to move whilst undergoing the scan, introducing artefacts into the data-set. This may lead to insufficient information being collected during the scans. With neonatal patients, common practice is to conduct the scans whilst the patient is sleeping to reduce the artefacts that would otherwise be introduced through movement as it is more challenging to get a neonatal patient to lie still. This

allows a higher spatial resolution to be used; a necessary adjustment due to the smaller diameter of the blood vessels within neonatal patients.

Alongside patient comfort, the volume of data produced from high resolution scans is impractical and limits the resolution that can be used. Although recent advances in technology and image sequencing have allowed the processing power and spatial resolution of 4D-Flow MRI scanners to increase, within this research a spatial resolution higher than $1.5\text{mm} \times 1.5\text{mm} \times 1.5\text{mm}$ causes a system failure due to the volume of data produced. Increasing the temporal resolution of the 4D-Flow MRI data can also be problematic for these reasons.

6.2.3 Meshing

The meshing strategy outlined in Section 3.4 was applied to all four reconstructed geometries to ensure the results found were independent of the mesh density used. The mesh used comprised of ~ 2.3 million elements with element sizes in the range of $4.751 \times 10^{-5}\text{m} < \delta x < 8.370 \times 10^{-4}\text{m}$.

6.2.4 Boundary Conditions

Spatio-temporal patient-specific inlet boundary conditions were created from the velocity data extracted from the 4D-Flow MRI scans at each spatial resolution using the methods discussed in Section 3.5.3.2. The vessel walls were assumed to be rigid and a zero-pressure condition was applied to the outlet, this was deemed appropriate as it has been stated by Madhavan & Kemmerling [79] that 5 diameters upstream of the outlet there is little difference in the haemodynamics present between a 0-pressure and three-element Windkessel model.

The average volumetric flow rate across the inlet plane calculated from 4D-Flow MRI data from all four spatial resolutions can be seen in Figure 6.4. It is clear that as the spatial resolution is refined, the volumetric flow rate during the systolic period increases, suggesting that utilising an insufficient spatial resolution will result in an underestimation of the volumetric flow rate through the aortic valve. At systole there is a 37.86% difference in volumetric flow rate between the $4\text{mm} \times 4\text{mm} \times 4\text{mm}$ and $1.5\text{mm} \times 1.5\text{mm} \times 1.5\text{mm}$, reducing marginally to 33.03% over diastole. This indicates the magnitude of the differences that are being introduced to the subsequent patient-specific CFD simulations through the inlet conditions alone.

The variation that is present in the 4D-Flow MRI data across the inlet plane can be seen in Figure 6.5 where contours of velocity magnitude are shown over the systolic and diastolic phases. Across the inlet plane, the peak velocity magnitude over the systolic period appears to be consistent between the $3\text{mm} \times 3\text{mm} \times 3\text{mm}$, $2\text{mm} \times 2\text{mm} \times 2\text{mm}$, and $1.5\text{mm} \times 1.5\text{mm} \times 1.5\text{mm}$ spatial resolutions. However, the spatial variation over the inlet plane is considerable between the resolutions, with the largest difference in flow patterns between the $4\text{mm} \times 4\text{mm} \times 4\text{mm}$ and the finer resolutions. The $4\text{mm} \times 4\text{mm} \times 4\text{mm}$ resolution suggests a sharper profile, whilst the finer resolutions indicate a more broad profile is present. The large spatial variations between the resolutions combined with the variation in inlet area will be contributing to the significant variations found in the volumetric flow rate across the inlet plane.

The quantitative agreement between the 4D-Flow MRI data and the calculated CFD inlet conditions is shown in Tables 6.4 and 6.5 for the systolic and diastolic phases respectively. It can be seen that over the systolic period, as the spatial resolution is refined, the agreement between the

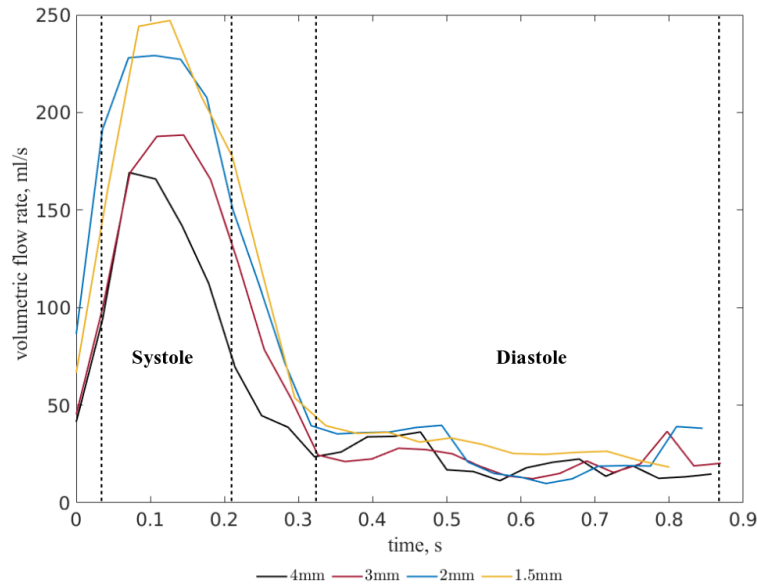


Figure 6.4. Volumetric flow rates (ml/s) at the inlet determined using 4D-Flow MRI data for all four spatial resolutions. The systolic and diastolic phases are shown enclosed by the dashed lines.

maximum velocity magnitude determined from 4D-Flow MRI data and CFD inlet conditions remains constant, and is $< 2\%$ for all spatial resolutions. This suggests that the methods used to calculate the spatio-temporal patient-specific inlet conditions are accurately replicating the 4D-Flow MRI data. As the spatial resolution is refined, the agreement between the two methods in terms of mean velocity across the inlet can be seen to improve, reducing from a 23.37% difference for the $4mm \times 4mm \times 4mm$ spatial resolution to 8.192% for the $1.5mm \times 1.5mm \times 1.5mm$ resolution. Table 6.4 indicates that the trends seen in 4D-Flow MRI data are also found in the CFD data; the maximum velocity magnitude decreases and the mean velocity increases as the resolution is refined. The data in Table 6.4 suggests that both the 4D-Flow MRI and calculated CFD inlet conditions are beginning to converge on an appropriate resolution, this is clearly demonstrated in Figure 6.6a. When observing the mean velocity over the inlet plane of the calculated CFD inlet conditions, there is a 22.77% difference between the $4mm \times 4mm \times 4mm$ and the $3mm \times 3mm \times 3mm$, reducing to a 16.70% difference between the $3mm \times 3mm \times 3mm$ and the $2mm \times 2mm \times 2mm$, and a 1.607% difference between the $2mm \times 2mm \times 2mm$ and $1.5mm \times 1.5mm \times 1.5mm$ respectively.

The variation seen in terms of the maximum velocity magnitude in the 4D-Flow MRI data ($0.8554 \pm 0.1085 m.s^{-1}$) is seen replicated within the calculated CFD data ($0.8574 \pm 0.09462 m.s^{-1}$). It must be acknowledged however that a small proportion of the differences between the four spatial resolutions must be attributed to the natural variations within the patient's heartbeat as discussed in Section 6.2.1.

During the diastolic phase of the cardiac cycle, the flow patterns across the inlet plane from 4D-Flow MRI data are in general agreement between the $3mm \times 3mm \times 3mm$, $2mm \times 2mm \times 2mm$, and $1.5mm \times 1.5mm \times 1.5mm$, see Figure 6.5. However, it is clear that as the spatial resolution is refined, maximum velocity magnitude experienced across the inlet increases. This trend can also be seen replicated within the calculated CFD inlet conditions in Table 6.5. Table 6.5 also indicates that as the resolution is refined, the agreement between the 4D-Flow MRI and CFD inlet condition

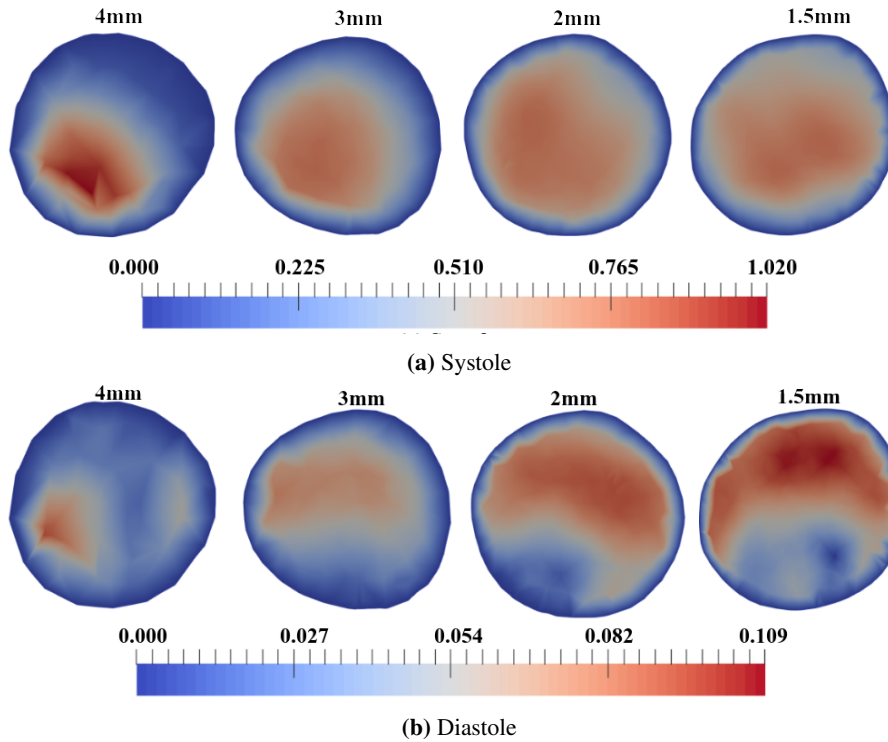


Figure 6.5. Velocity magnitude (ms^{-1}) contours over the inlet plane determined from 4D-Flow MRI data from the four 4D-Flow MRI spatial resolutions over the systolic (a) and diastolic (b) phases.

Spatial Resolution (mm^3)	4D-Flow MRI		CFD		Difference Between Methods	
	$U_{mag_{max}}$ (ms^{-1})	U_{mean} (ms^{-1})	$U_{mag_{max}}$ (ms^{-1})	U_{mean} (ms^{-1})	$U_{mag_{max}}$ % difference	U_{mean} % difference
4	1.018	0.2838	0.9988	0.3589	1.904	23.37
3	0.8052	0.3745	0.8209	0.4511	1.931	18.56
2	0.7986	0.4683	0.8010	0.5333	0.3001	12.98
1.5	0.7997	0.4835	0.8089	0.5248	1.144	8.192

Table 6.4. Maximum and mean velocity magnitude (ms^{-1}) data at the inlet plane during systole calculated using 4D-Flow MRI data and CFD data, including a comparison between the two methods for each spatial resolution.

in terms of the mean velocity over the inlet plane improves from 22.70% to 6.285%. The agreement between the two methods in terms of maximum velocity magnitude increases from the values being within 14.91% of each other to 3.613%. There is reduced agreement between the CFD and the 4D-Flow MRI data at diastole compared to systole which may be a result of insufficient velocity encoding during the 4D-Flow MRI acquisition. Figure 6.6b suggests the results at diastole are also beginning to converge on an appropriate resolution. The difference in mean velocity across the CFD inlet conditions between the $4mm \times 4mm \times 4mm$ and $3mm \times 3mm \times 3mm$ is 16.17%, reducing to 13.92% and 1.575% between the $3mm \times 3mm \times 3mm$ and $2mm \times 2mm \times 2mm$, and the $2mm \times 2mm \times 2mm$ and $1.5mm \times 1.5mm \times 1.5mm$ respectively. During the diastolic phase, the variation of the maximum velocity between the resolutions for 4D-Flow MRI data ($0.1009 \pm 0.006474ms^{-1}$) is seen echoed in the CFD data ($0.09988 \pm 0.009979ms^{-1}$).

It is clear that the $4mm \times 4mm \times 4mm$ resolution data disagrees with the data from all other

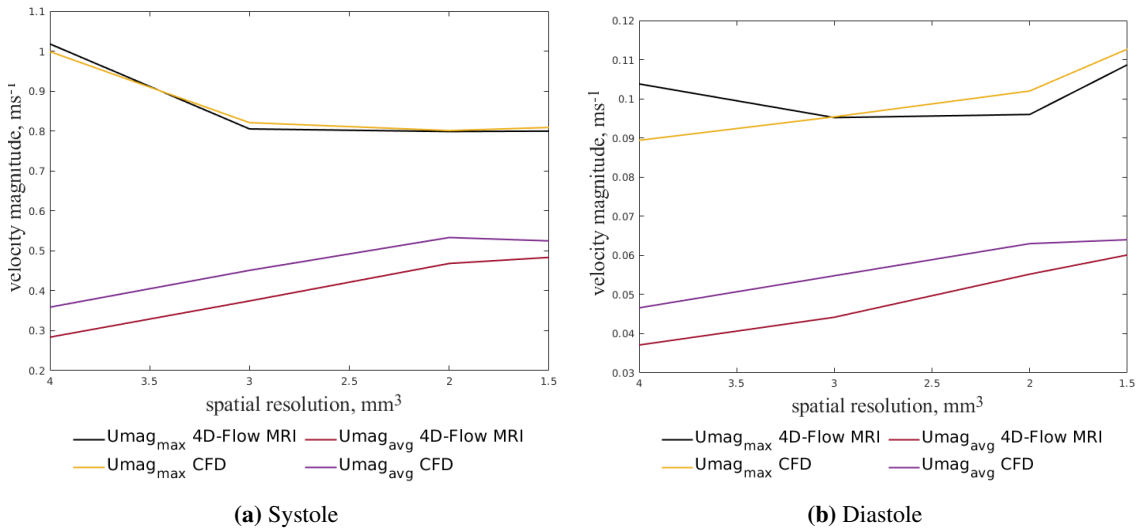


Figure 6.6. Maximum and mean velocity magnitude (ms^{-1}) data across the inlet plane calculated using 4D-Flow MRI data and CFD data at systole (a) and diastole (b).

spatial resolutions at both systole and diastole in terms of flow patterns and the velocity magnitude. Although the data at both systole and diastole appears to have begun to converge on an appropriate resolution, the velocity data has not yet fully converged.

Spatial Resolution (mm^3)	4D-Flow MRI		CFD		Difference Between Methods	
	$U_{mag_{max}}$ (ms^{-1})	U_{mean} (ms^{-1})	$U_{mag_{max}}$ (ms^{-1})	U_{mean} (ms^{-1})	$U_{mag_{max}}$ % difference	U_{mean} % difference
4	0.1038	0.03710	0.08940	0.04660	14.91	22.70
3	0.09520	0.04420	0.09540	0.05480	0.2099	21.41
2	0.09600	0.05520	0.1020	0.06300	6.061	13.20
1.5	0.1087	0.06010	0.1127	0.06400	3.613	6.285

Table 6.5. Maximum and mean velocity magnitude (ms^{-1}) data at the inlet plane during diastole calculated using 4D-Flow MRI data and CFD data, including a comparison between the two methods for each spatial resolution.

The trend seen over both systole and diastole where a refinement in resolution produces increased agreement between the 4D-Flow MRI data and the calculated inlet conditions is to be expected due to the method used to calculate the inlet conditions, described in Section 3.5.3.2. A coarser 4D-Flow MRI spatial resolution has fewer data points from which the velocity data can be extracted from, which the surface fit is created from. This will cause a lesser quality of fit as higher levels of interpolation will be required between the data points for the coarse spatial resolutions than the finer spatial resolutions. As the spatial resolution is increased, so too is the number of data points available to extract velocity data from, therefore the quality of the surface fit is improved, leading to improved agreement between the 4D-Flow MRI data and the calculated CFD data.

The inlet boundary condition results from the $1.5mm \times 1.5mm \times 1.5mm$ spatial resolution must be taken cautiously and no clinical conclusions can be drawn from the subsequent CFD simulations as it is likely that the results are still affected by insufficient 4D-Flow MRI resolution, as the inlet conditions have yet to converge on a solution. It has also been shown that any potential error in the 4D-Flow MRI data at the inlet that is a result of insufficient resolution will be present in the

inlet boundary condition of patient-specific CFD simulations. It must be concluded therefore that agreement between 4D-Flow MRI data and the subsequent patient-specific CFD results does not imply accurate results.

6.2.5 Numerical Simulations

Once a patient-specific geometry and patient-specific spatio-temporal boundary conditions were created for each spatial resolution, simulations were run. Three cardiac cycles were run to ensure periodicity was reached using *pimpleFoam*, the transient solver for incompressible, turbulent, Newtonian fluids, which uses the merged PISO-SIMPLE algorithm. This solver was selected as it allowed for a large time-step to be used, and the *adjustTimeStep* function to be used. A patient-specific Δt was calculated based on each spatial resolution using the Courant Number, (see Equation 4.1). All results were taken from the last cardiac cycle simulated.

The physical properties of blood used are outlined in Section 3.6.1 and it was taken to be Newtonian, incompressible, and homogeneous. The $k-\omega$ SST turbulence model was incorporated into the models, as discussed in Section 3.6.2, as the flow was calculated to vary between the laminar, transitional, and turbulent regimes throughout the cardiac cycle. Patient-specific values of k and ω were determined for each spatial resolution. The meshing strategy that was outlined in Section 3.4.4.3 was applied to all reconstructed geometries from all four spatial resolutions such that the results were not affected by the grid density.

All simulations were undertaken on ARC3, part of the high performance computing facilities at the University of Leeds.

6.3 Results

6.3.1 Velocity

The flow patterns present across a plane in the mid-ascending aorta can be seen in the contours of velocity magnitude shown in Figure 6.7 for the systolic and diastolic phases of the cardiac cycle. The flow patterns predicted from patient-specific CFD simulations have been compared to the 4D-Flow MRI data. At systole (Figure 6.7a), as the 4D-Flow MRI spatial resolution is refined, the maximum velocity magnitude increases. This is seen in both 4D-Flow MRI data and the subsequent CFD results, with the notable exception of the CFD simulation based on the $4mm \times 4mm \times 4mm$ 4D-Flow MRI acquisition. This trend is also seen in velocity contours over the diastolic period (Figure 6.7b) with coarser spatial resolutions predicting lower maximum values of velocity magnitude. Again, the CFD simulation based on the $4mm \times 4mm \times 4mm$ 4D-Flow MRI acquisition is an exception.

At systole, there are notable discrepancies between the 4D-Flow MRI data and the CFD data for a spatial resolution of $4mm \times 4mm \times 4mm$. Higher velocity magnitudes and differing flow patterns are predicted in the patient-specific CFD simulations, with the maximum velocity magnitude showing poor agreement between the CFD data and the 4D-Flow MRI data with a difference of 39.49%, and the mean velocity differing by 24.85% between the two methods. The more refined spatial resolutions of $3mm \times 3mm \times 3mm$, $2mm \times 2mm \times 2mm$, and $1.5mm \times 1.5mm \times 1.5mm$ show an improved agreement between the CFD results and 4D-Flow MRI data in terms of veloc-

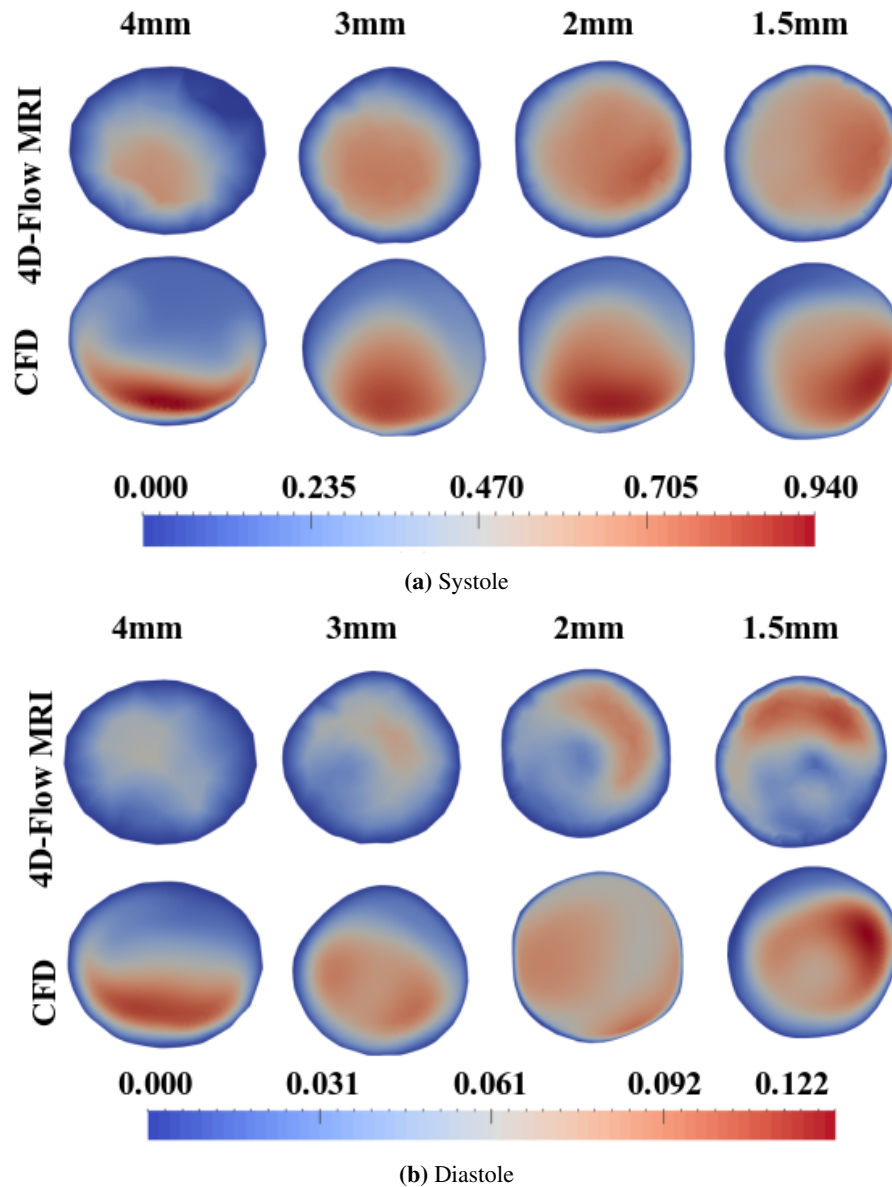


Figure 6.7. Velocity magnitude (ms^{-1}) contours from the systolic (a) and diastolic (b) phases over a plane in the mid-ascending aorta, comparing 4D-Flow MRI and CFD for all spatial resolutions.

ity magnitude and flow patterns present compared to the $4mm \times 4mm \times 4mm$ spatial resolution. The difference between the methods in terms of maximum velocity magnitude reduces to 19.44%, 14.19%, and 16.31% for the $3mm \times 3mm \times 3mm$, $2mm \times 2mm \times 2mm$, and $1.5mm \times 1.5mm \times 1.5mm$ respectively. At all four spatial resolutions, the velocity magnitudes predicted by CFD simulations are higher than those shown by the 4D-Flow MRI data. It is likely that this overestimation is a consequence of the supra-aortic vessels being neglected. When monitoring the agreement of the mean velocities between the CFD and 4D-Flow MRI data, the differences reduce from 24.85% for $4mm \times 4mm \times 4mm$, to 1.476% for the $3mm \times 3mm \times 3mm$ and $2mm \times 2mm \times 2mm$. Although the $1.5mm \times 1.5mm \times 1.5mm$ produces improved agreement compared to the $4mm \times 4mm \times 4mm$, the agreement is reduced compared to the $3mm \times 3mm \times 3mm$ and $2mm \times 2mm \times 2mm$, with a difference of 13.49% between the 4D-Flow MRI and CFD data. This data is summarised within Table 6.6. The reduced improvement seen in the $1.5mm \times 1.5mm \times 1.5mm$ resolution compared to the $2mm \times 2mm \times 2mm$ and $3mm \times 3mm \times 3mm$ resolution in terms of maximum and mean velocity is likely to be a direct

result of the coarser temporal resolution that was required to collect 4D-Flow MRI data at the finest spatial resolution.

Spatial Resolution (mm^3)	4D-Flow MRI		CFD		Difference Between Methods	
	$U_{mag_{max}}$ (ms^{-1})	U_{mean} (ms^{-1})	$U_{mag_{max}}$ (ms^{-1})	U_{mean} (ms^{-1})	$U_{mag_{max}}$ % difference	U_{mean} % difference
4	0.6272	0.2646	0.9358	0.3396	39.49	24.85
3	0.6941	0.3958	0.8436	0.4016	19.44	1.476
2	0.7891	0.4707	0.9096	0.4777	14.19	1.476
1.5	0.7659	0.4910	0.9019	0.4289	16.31	13.49

Table 6.6. Maximum and mean velocity magnitude (ms^{-1}) data at the mid-ascending aortic plane during systole calculated using 4D-Flow MRI data and CFD data, including a comparison between the two methods for each spatial resolution.

The increasing difference found in the mean velocity and maximum velocity for the $1.5mm \times 1.5mm \times 1.5mm$ compared to the $3mm \times 3mm \times 3mm$ and $2mm \times 2mm \times 2mm$ can be seen in Figure 6.8a, where the velocity magnitude profile calculated from CFD results along the x -axis of the plane of interest in the mid-ascending aorta during the systolic period of the cardiac cycle is plotted. The CFD simulations based on the $3mm \times 3mm \times 3mm$ and $2mm \times 2mm \times 2mm$ spatial resolutions demonstrate similar profiles with peak values close in range whilst the $1.5mm \times 1.5mm \times 1.5mm$ displays an alternate flow profile with a higher peak value. The $4mm \times 4mm \times 4mm$ also predicts a different profile to the remaining three spatial resolutions. The velocity profile along the z -axis can also be seen in Figure 6.8c. At systole, the $4mm \times 4mm \times 4mm$ again produces an alternate profile to the remaining spatial resolutions, which all display similar velocity profiles with small variations in magnitude. It can be seen that the $1.5mm \times 1.5mm \times 1.5mm$ demonstrates a lower velocity magnitude than the $2mm \times 2mm \times 2mm$ and $3mm \times 3mm \times 3mm$. This is likely a result of the flow patterns between the resolutions altering; Figure 6.7 indicates the location of the peak velocity shifts from the left region towards the left-posterior region at the most refined spatial resolution.

As with the results at systole, during the diastolic period the CFD simulation based on the $4mm \times 4mm \times 4mm$ 4D-Flow MRI scan predicts higher velocity magnitudes and contrasting flow patterns when compared to the 4D-Flow MRI data of the same spatial resolution. There is a significant difference between the 4D-Flow MRI data and CFD data in terms of the maximum velocity, with a difference of 56.76% rising to 60.59% when observing the mean velocity across the plane between the CFD and 4D-Flow MRI data. The agreement between 4D-Flow MRI data and the subsequent patient-specific CFD simulations improves as the spatial resolution of the 4D-Flow MRI is refined. The $3mm \times 3mm \times 3mm$ reports a difference in maximum velocity of 23.53% between the 4D-Flow MRI and CFD data, $2mm \times 2mm \times 2mm$ suggests a 4.471% difference, which is further reduced to 3.670% for a spatial resolution of $1.5mm \times 1.5mm \times 1.5mm$. This data is summarised within Table 6.7.

Figure 6.7 indicates that during the diastolic phase of the cardiac cycle there are differences in the flow patterns present across the plane of interest in the mid-ascending aorta when comparing 4D-Flow MRI results to the corresponding CFD data of the same spatial resolution, and when comparing the various spatial resolutions to each other for both 4D-Flow MRI data and CFD data.

Spatial Resolution (mm^3)	4D-Flow MRI		CFD		Difference Between Methods	
	$U_{mag_{max}}$ (ms^{-1})	U_{mean} (ms^{-1})	$U_{mag_{max}}$ (ms^{-1})	U_{mean} (ms^{-1})	$U_{mag_{max}}$ % difference	U_{mean} % difference
4	0.06131	0.02599	0.1099	0.04859	56.76	60.59
3	0.07451	0.02902	0.09438	0.05193	23.53	56.61
2	0.09052	0.03700	0.09466	0.05067	4.471	31.18
1.5	0.1177	0.04063	0.1221	0.06024	3.670	38.88

Table 6.7. Maximum and mean velocity magnitude (ms^{-1}) data at the mid-ascending aortic plane during diastole calculated using 4D-Flow MRI data and CFD data, including a comparison between the two methods for each spatial resolution.

The differences present in the flow patterns have resulted in the CFD simulations over-predicting the mean velocity across the plane of interest considerably for all spatial resolutions. This is further demonstrated by Figure 6.8, where the flow profiles along the x -axis over the diastolic phase of the cardiac cycle determined from CFD data are shown. There is a different flow profile present for each spatial resolution, with the $1.5mm \times 1.5mm \times 1.5mm$ spatial resolution displaying a higher peak value than the remaining coarser spatial resolutions. It is probable that this is a consequence of the coarser temporal resolution that was utilised when acquiring the data. It is also possible that the inter-scan variability of the patients heart rate is contributing to the differences found between the 4D-Flow MRI scans, and therefore the CFD simulations based on the 4D-Flow MRI data. The velocity magnitude plotted along the z -axis also demonstrates all four resolutions give a range in flow profiles, similarly to results at systole, the $4mm \times 4mm \times 4mm$ demonstrates the highest peak velocity magnitude.

Figure 6.8 shows the velocity magnitude calculated through OpenFOAM simulations along the x -axis of a plane in the mid-ascending aorta during systole and diastole. At both systole and diastole, CFD results based on the $1.5mm \times 1.5mm \times 1.5mm$ spatial resolution present a different flow profile. During systole the CFD data based on the $1.5mm \times 1.5mm \times 1.5mm$ predicts a higher peak velocity magnitude than the CFD simulations based on the coarser 4D-Flow MRI spatial resolutions. This increase can be attributed to the coarser temporal resolution that was required for the $1.5mm \times 1.5mm \times 1.5mm$ 4D-Flow MRI. It can also be seen from Figure 6.8 that the velocities from all spatial resolutions in both the x - and z -axis' are not yet converging on a velocity magnitude or flow pattern at either stage of the cardiac cycle. As it is clear that there is no true 4D-Flow MRI 'gold-standard' to compare the 4D-Flow MRI based CFD results to it must be assumed that results based on the $1.5mm \times 1.5mm \times 1.5mm$ spatial resolution are still being impacted by the spatial and temporal resolution used to acquire the 4D-Flow MRI data. As the temporal resolution for this scan is different to the other scans it is not possible to decipher whether the improved spatial resolution or the decreased temporal resolution has the biggest influence over the results.

The variability of the 4D-Flow MRI based CFD results must be compared between the spatial resolutions. There is significant variation present in the results at both systole and diastole. During the systolic phase of the cardiac cycle, over all spatial resolutions investigated, the mean and standard deviation for the 4D-Flow MRI based CFD velocity data is calculated to be $0.4120 \pm 0.05758ms^{-1}$, whilst the corresponding value for 4D-Flow MRI data is calculated to be $0.4055 \pm$

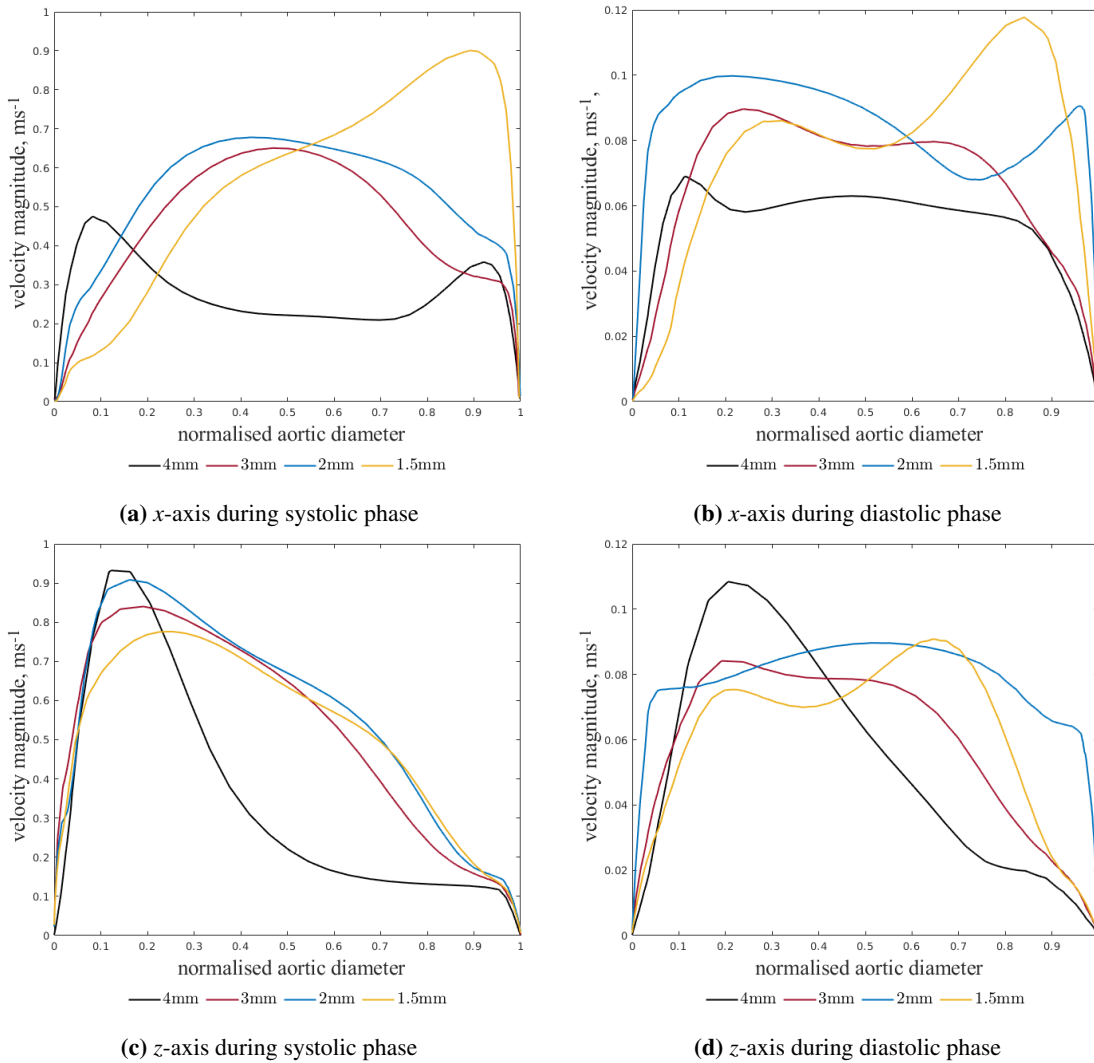


Figure 6.8. Velocity magnitude (ms^{-1}) along the *x*- and *z*-axis' across a plane at the mid-ascending aorta over the systolic and diastolic phases for the four CFD simulations based on the varying spatial resolutions.

$0.1025ms^{-1}$. This suggests that the variability that is present in the 4D-Flow MRI data due to insufficient spatial resolution will be found within the CFD data. Over all four spatial resolutions during the diastolic phase, the mean and standard deviation of the velocity data over the plane of interest was calculated to be $0.05286 \pm 0.005113ms^{-1}$ for the CFD data, whilst the corresponding value for 4D-Flow MRI data is $0.03316 \pm 0.006809ms^{-1}$. This shows that there is a slight increase in variability in the 4D-Flow MRI data than there is in the CFD data during both the systolic and diastolic phases of the cardiac cycle.

Qualitatively, the velocity magnitude contours present in the ascending aorta show better agreement at systole between the 4D-Flow MRI data and CFD results than at diastole. It is likely that this is a consequence of the inlet conditions being applied. During systole, the aortic valve opens causing a distinct and sharp flow profile, close to a parabolic profile, to be present at the inlet location. During the diastolic phase of the cardiac cycle, the aortic valve closes: there is no longer a distinct flow profile at the inlet. The fluctuations in the flow profile that are present at the inlet location during diastole are smaller in magnitude and more numerous than during systole, so are harder to capture accurately through the fit that is calculated from the 4D-Flow MRI data. This results in an inlet condition that may inaccurately model the small fluctuations during diastole,

causing incorrect flow patterns to be modelled within the ascending aorta. It is also possible that insufficient velocity encoding during the 4D-Flow MRI scan is contributing to the disagreement seen at diastole. Additionally, the choice to neglect the motion of the aortic valve leaflets in the 4D-Flow MRI based CFD simulations will impact the haemodynamics predicted.

Although the general trend seen in the velocity results suggests that as the spatial resolution is refined, the agreement between the 4D-Flow MRI data and the CFD results improves, the $1.5\text{mm} \times 1.5\text{mm} \times 1.5\text{mm}$ spatial resolution is an exception. The differences between the 4D-Flow MRI and CFD results increase slightly from the $2\text{mm} \times 2\text{mm} \times 2\text{mm}$ spatial resolution, whilst still remaining an improvement from the $3\text{mm} \times 3\text{mm} \times 3\text{mm}$ spatial resolution. This is likely a result of the temporal resolution used for the $1.5\text{mm} \times 1.5\text{mm} \times 1.5\text{mm}$ case being coarser than that used for the remaining spatial resolutions. The impacts of the coarser temporal resolution can be seen clearly when comparing the mean velocities calculated from CFD data across the axial plane in the mid-ascending aorta at diastole. There is a 6.639% difference between the values reported for the $4\text{mm} \times 4\text{mm} \times 4\text{mm}$ and the $3\text{mm} \times 3\text{mm} \times 3\text{mm}$ scan, reducing to only 2.456% between the $3\text{mm} \times 3\text{mm} \times 3\text{mm}$ and $2\text{mm} \times 2\text{mm} \times 2\text{mm}$, which then increases to 17.26% between the $2\text{mm} \times 2\text{mm} \times 2\text{mm}$ and $1.5\text{mm} \times 1.5\text{mm} \times 1.5\text{mm}$.

6.3.2 Wall Shear Stress

It is known that WSS is dependent on the spatial and temporal resolution of the 4D-Flow MRI scan [35, 46, 84, 120, 194, 195], and many studies have concluded that a coarse spatial resolution underestimates the WSS [84, 120, 194, 195]. The degree to which any subsequent patient-specific CFD simulations based on the 4D-Flow MRI data vary is unknown and must be quantified. The WSS was calculated from patient-specific CFD data and 4D-Flow MRI data at eight locations on the vessel wall at the plane of interest in the mid-ascending aorta during the systolic and diastolic phases allowing the variation in the WSS measurements due to the spatial resolution of the 4D-Flow MRI scan to be quantified. Plots of WSS magnitude are shown in Figure 6.9 for systole and diastole from both CFD data and 4D-Flow MRI data. The WSS magnitudes calculated directly from 4D-Flow MRI data show that a refinement in the spatial resolution of the 4D-Flow MRI scan causes an increase in the WSS magnitude at systole and diastole. The $1.5\text{mm} \times 1.5\text{mm} \times 1.5\text{mm}$ spatial resolution produces the highest WSS magnitude at both systole and diastole when compared to the other, more coarse, spatial resolutions. The WSS results determined from patient-specific CFD simulations do not follow the same trend, and all four sets of results based on the four different spatial resolutions predict WSS values of similar magnitudes.

During systole, results from all four CFD simulations agree and indicate there is a region of elevated WSS in the posterior and left-posterior region (Figure 6.9a). This elevated region of WSS is also suggested by results from the $1.5\text{mm} \times 1.5\text{mm} \times 1.5\text{mm}$ 4D-Flow MRI scan, but is not present in the $4\text{mm} \times 4\text{mm} \times 4\text{mm}$, $3\text{mm} \times 3\text{mm} \times 3\text{mm}$, or $2\text{mm} \times 2\text{mm} \times 2\text{mm}$ 4D-Flow MRI data (Figure 6.9b). However, when comparing the magnitudes of the WSS values within the posterior and left-posterior region, it is evident that the patient-specific CFD over-predicts the magnitude at all four spatial resolutions compared to the 4D-Flow MRI data. In all other regions (*L*, *LA*, *A*, *RA*, *R*, *RP*), the magnitude of the WSS predicted through the patient-specific CFD simulations matches the magnitude of the results from 4D-Flow MRI to a much better degree. Statistical comparison (Wilcoxon signed rank test, $\alpha = 0.05$) between the CFD data and 4D-Flow MRI data

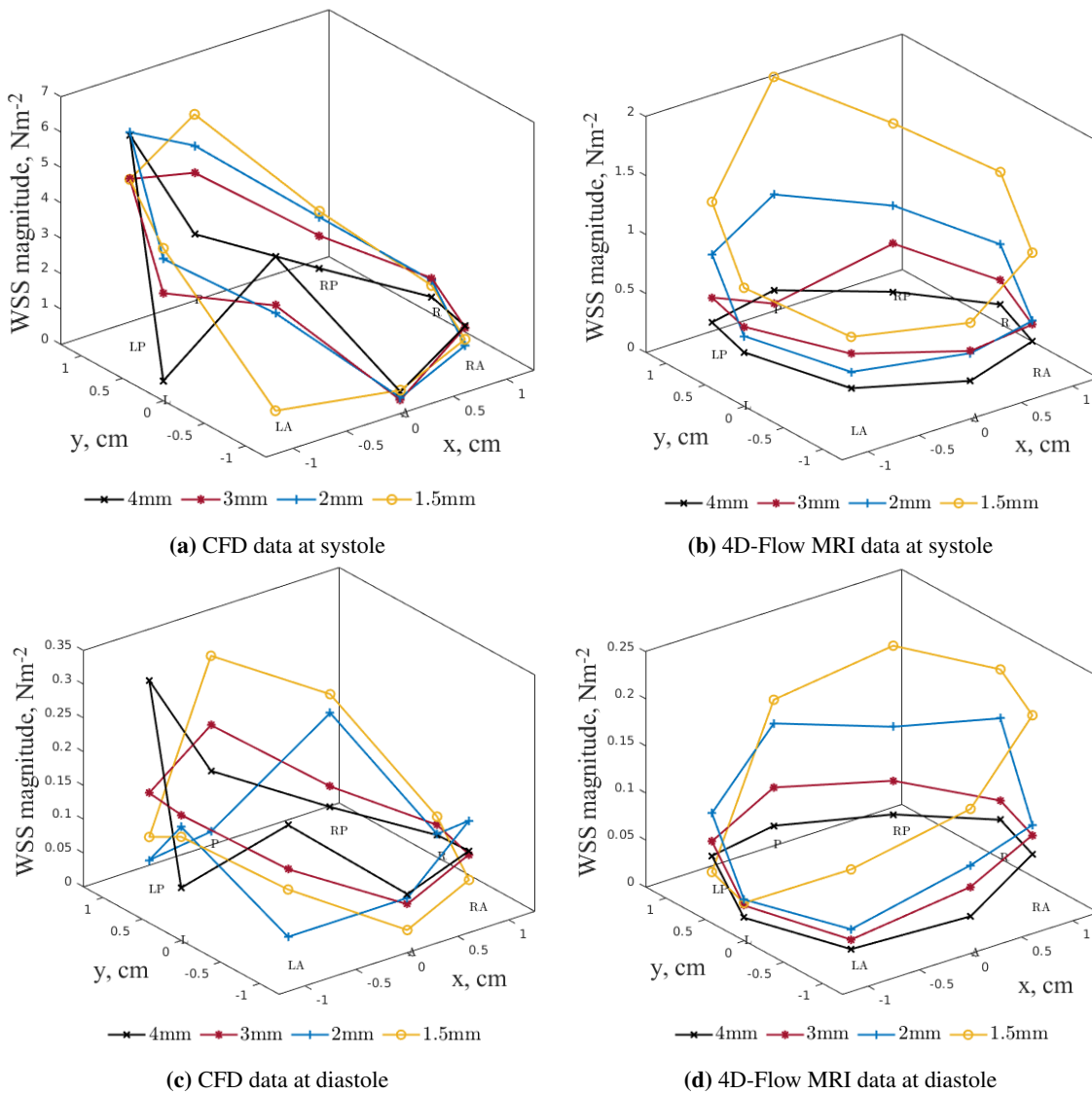


Figure 6.9. Wall shear stress magnitude (Nm^{-2}) at eight locations on the mid-ascending aortic wall determined from 4D-Flow MRI data and CFD data during the systolic and diastolic phases of the cardiac cycle. R=right, RP=right-posterior, P=posterior, LP=left-posterior, L=Left, LA=left-anterior, A=anterior, RA=right-anterior.

at systole determined the differences found for the $4mm \times 4mm \times 4mm$, $3mm \times 3mm \times 3mm$, and $2mm \times 2mm \times 2mm$ spatial resolutions are all statistically significant ($p < 0.05$), whilst comparison between the CFD data and 4D-Flow MRI data for the $1.5mm \times 1.5mm \times 1.5mm$ spatial resolution concluded the differences in WSS magnitude were insignificant. This suggests a coarse spatial resolution has significant impacts on the accuracy of WSS measurements at systole in any subsequent patient-specific CFD simulations that are performed, and a spatial resolution of $1.5mm \times 1.5mm \times 1.5mm$ provides reasonable agreement between 4D-Flow MRI data and results from patient-specific CFD simulations. However, the WSS results have not yet converged on an appropriate spatial resolution so it cannot be said if agreement between the CFD data and 4D-Flow MRI data implies physiologically accurate results.

During diastole, the CFD data does not follow the trend seen in the 4D-Flow MRI data over diastole of a refined spatial resolution producing higher levels of WSS. Figure 6.9c suggests that CFD simulations predict WSS values of similar magnitude regardless of the spatial resolution of

the 4D-Flow MRI data the simulations are based on. 4D-Flow MRI data at diastole indicates again that a coarser spatial resolution produces under-estimations in the WSS magnitudes (Figure 6.9d). Due to the increasing 4D-Flow MRI WSS magnitudes seen with finer spatial resolutions, the agreement between the CFD data and the 4D-Flow MRI data improves as the spatial resolution is refined. Statistical comparison (Wilcoxon signed rank test, $\alpha = 0.05$) has shown that the differences between the CFD and 4D-Flow MRI data for the $4\text{mm} \times 4\text{mm} \times 4\text{mm}$ spatial resolution are statistically significant ($p < 0.05$) whilst the differences between results for all other spatial resolutions are found to be insignificant.

The increased agreement as resolution is refined is demonstrated clearly in Figure 6.10. Figure 6.10 shows the average WSS magnitude values on the vessel wall for the plane of interest in the mid-ascending aorta. During both the systolic and diastolic phases, it is evident that as the spatial resolution is refined, the 4D-Flow MRI data shows a clear trend of increasing WSS magnitudes. This increase in 4D-Flow MRI WSS values results in improved levels of agreement between the 4D-Flow MRI data and CFD simulation data as the spatial resolution is refined. When comparing the agreement levels between the CFD data and the 4D-Flow MRI data for the $4\text{mm} \times 4\text{mm} \times 4\text{mm}$ at systole, there is a 151.9% difference, which reduces to 58.09% as the spatial resolution is increased to $1.5\text{mm} \times 1.5\text{mm} \times 1.5\text{mm}$. This is mirrored at diastole, with the difference between methods being 106.7% for the $4\text{mm} \times 4\text{mm} \times 4\text{mm}$ spatial resolution reducing to a difference of 21.67% for the $1.5\text{mm} \times 1.5\text{mm} \times 1.5\text{mm}$ spatial resolution. The mean and standard deviation of the WSS results show that there is much greater variability across all spatial resolutions in the WSS measurements taken from 4D-Flow MRI data at both systole ($0.6509 \pm 0.4184\text{Nm}^{-2}$) and diastole ($0.08250 \pm 0.04795\text{Nm}^{-2}$), than in the WSS measurements taken from CFD results at systole ($2.1960 \pm 0.2767\text{Nm}^{-2}$) and diastole ($0.1030 \pm 0.01469\text{Nm}^{-2}$).

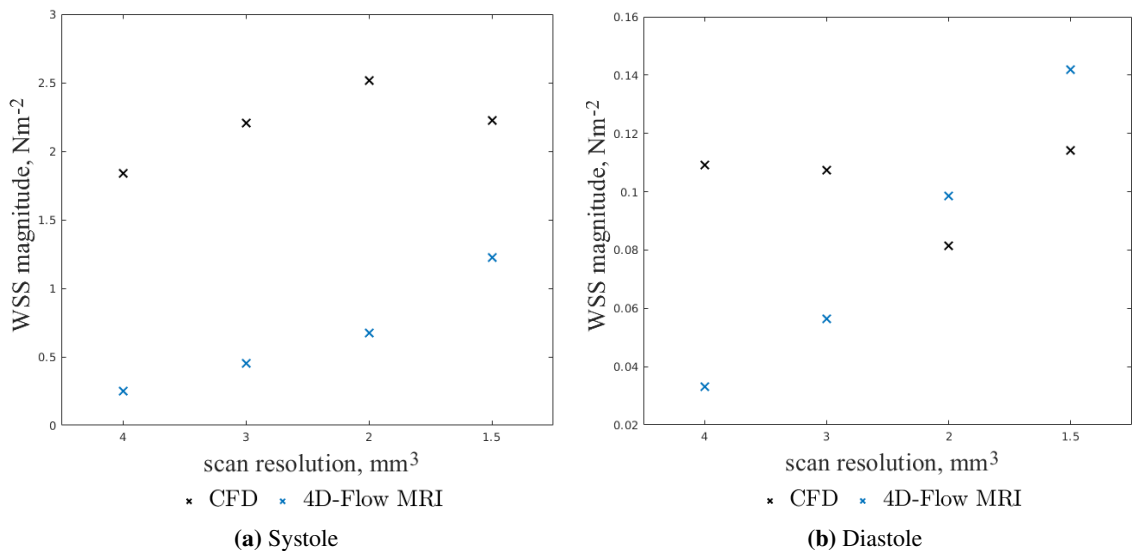


Figure 6.10. Average wall shear stress magnitude (Nm^{-2}) over the eight locations of the plane in the mid-ascending aorta, calculated with 4D-Flow MRI data and CFD data for all four spatial resolutions during the systolic and diastolic phases.

As it is known that coarse spatial resolutions result in an under-estimation of WSS magnitude, the results for the 4D-Flow MRI data at both systole and diastole appear to support the conclusions drawn from studies into the impacts of 4D-Flow MRI spatial resolution on WSS. This implies therefore that the disagreement seen between the patient-specific CFD results and 4D-Flow MRI

data for the $4mm \times 4mm \times 4mm$, $3mm \times 3mm \times 3mm$, and $2mm \times 2mm \times 2mm$ spatial resolutions is due to the 4D-Flow MRI data underestimating the WSS magnitude, rather than the corresponding CFD results overestimating the WSS magnitude. This underestimation of WSS is likely causing the 4D-Flow MRI data from the coarser spatial resolutions to not predict the region of elevated WSS in the posterior and left-posterior regions at systole that the 4D-Flow MRI data from the $1.5mm \times 1.5mm \times 1.5mm$ spatial resolution and all CFD results have all indicated is present. As it is known that WSS is systematically underestimated by 4D-Flow MRI data, there is no available 'gold-standard' 4D-Flow MRI data to compare the 4D-Flow MRI based CFD data to. It is not possible therefore to say if the larger values of WSS calculated by CFD simulations are erroneous, or the true values. 4D-Flow MRI scans must be acquired at higher spatial resolutions until the WSS values converge on a magnitude, and the WSS results from the corresponding CFD data must then be compared to it.

6.3.3 Flow Asymmetry

The flow asymmetry was calculated at the plane in the mid-ascending aorta for each spatial resolution using the Equation 3.9. Figure 6.11 shows the calculated flow asymmetry values for CFD and 4D-Flow MRI data during the systolic and diastolic phases of the cardiac cycle. It can be seen that during systole, the CFD results for the $4mm \times 4mm \times 4mm$, $3mm \times 3mm \times 3mm$, and $2mm \times 2mm \times 2mm$ spatial resolutions are beginning to converge on a value of $\sim 62\%$. However, the $1.5mm \times 1.5mm \times 1.5mm$ shows a more eccentric flow profile and does not agree with the value arrived at by the coarser spatial resolutions. This is likely a result of the reduced temporal resolution. As the 4D-Flow MRI data is beginning to converge on a lower value of $\sim 48\%$, the agreement between CFD and 4D-Flow MRI data increases for a spatial resolution of $1.5mm \times 1.5mm \times 1.5mm$ compared to the $2mm \times 2mm \times 2mm$. The $2mm \times 2mm \times 2mm$ demonstrates the best agreement between the CFD and 4D-Flow MRI data, with a difference of 13.80% increasing to 25.53% for a spatial resolution of $1.5mm \times 1.5mm \times 1.5mm$. At all spatial resolutions, the CFD data over-predicts the degree of flow asymmetry, producing a more eccentric flow profile than 4D-Flow MRI data suggests. This can also be seen visually in the velocity contours within Figure 6.7a.

During the diastolic phase of the cardiac cycle, it can be seen that the 4D-Flow MRI data and CFD data are in significantly better agreement than at systole. The agreement between the CFD and 4D-Flow MRI data increases as the spatial resolution is refined, improving from a 14.60% difference at the $4mm \times 4mm \times 4mm$ spatial resolution to only 5.695% for a spatial resolution of $1.5mm \times 1.5mm \times 1.5mm$. Despite the improved agreement seen and the agreement between CFD and 4D-Flow MRI appearing to converge on a difference of $\sim 5\%$, the value of flow asymmetry at diastole has not yet begun to converge. As the data at diastole has not yet begun to converge it is not possible to confirm if the flow asymmetry value reported is correct, or is still being influenced by the spatial or temporal resolution of the 4D-Flow MRI acquisition.

6.3.4 Flow Dispersion

Flow dispersion was calculated in the plane in the mid-ascending aorta for all four spatial resolutions, and results for the systolic and diastolic phases calculated from CFD and 4D-Flow MRI data can be seen in Figure 6.12. It can be seen that at systole, both CFD and 4D-Flow MRI data

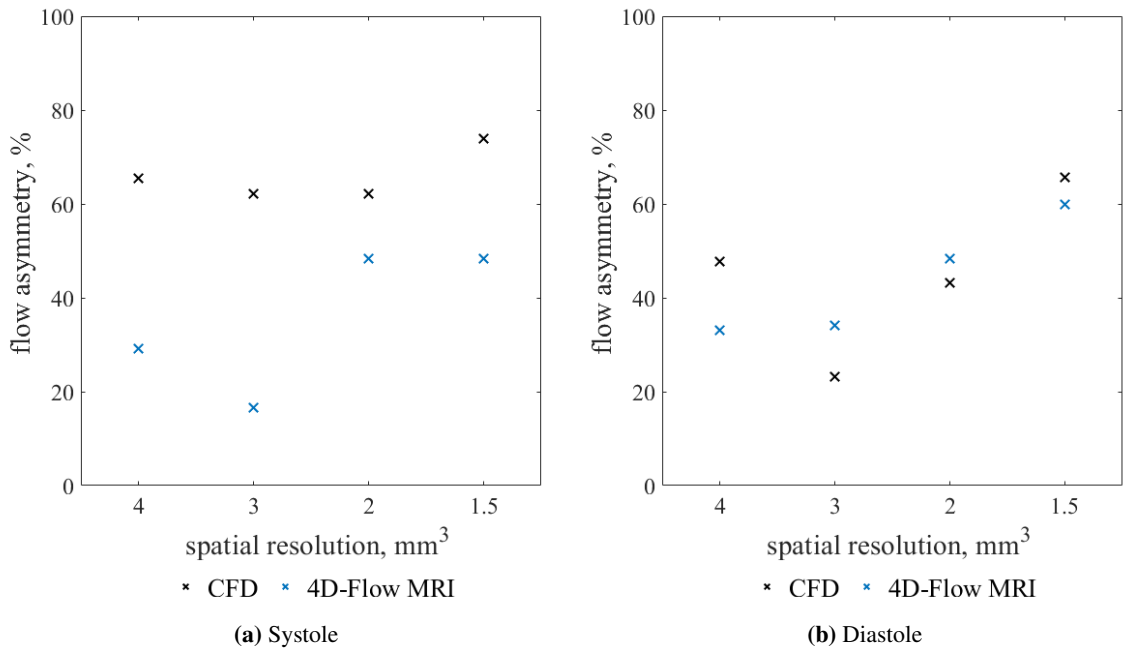


Figure 6.11. Flow asymmetry (%) calculated at the plane in the mid-ascending aorta from CFD and 4D-Flow MRI data at systole (a) and diastole (b) for all spatial resolutions.

follow the same trend, and show good agreement at all four spatial resolutions, with the difference between the two methods remaining $< 8\%$ for all spatial resolutions. This is echoed throughout the diastolic phase of the cardiac cycle, with the difference between the values reducing to $< 1\%$ for a spatial resolution of $1.5\text{mm} \times 1.5\text{mm} \times 1.5\text{mm}$. At all four spatial resolutions, the CFD data predicts a marginally broader profile than the 4D-Flow MRI suggests.

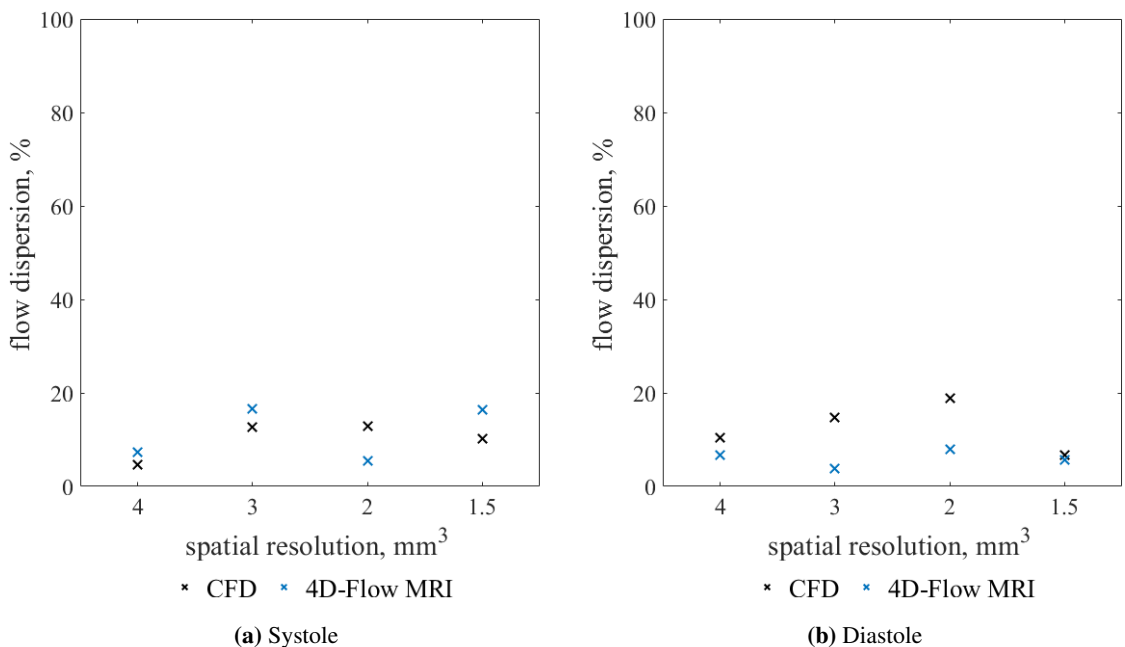


Figure 6.12. Flow dispersion (%) calculated at the plane in the mid-ascending aorta from CFD and 4D-Flow MRI data at systole (a) and diastole (b) for all spatial resolutions.

Despite both CFD and 4D-Flow MRI data at the four spatial resolutions predicting flow dispersion values within a close range, the spatial resolutions have not yet begun to converge on a value. However, as the CFD simulation based on the $1.5\text{mm} \times 1.5\text{mm} \times 1.5\text{mm}$ spatial resolution

produces excellent agreement with 4D-Flow MRI at the systolic and diastolic phases that is an improvement on that seen with the $2\text{mm} \times 2\text{mm} \times 2\text{mm}$ spatial resolution, a spatial resolution coarser than $1.5\text{mm} \times 1.5\text{mm} \times 1.5\text{mm}$ cannot be recommended.

6.3.5 Circulation

Figure 6.13 shows the through plane circulation determined across the plane of interest in the mid-ascending aorta for all four spatial resolutions, calculated from CFD and 4D-Flow MRI data. It can be seen that during both the systolic and diastolic phases, the circulation values calculated from 4D-Flow MRI data remain somewhat constant regardless of the spatial resolution, and all suggest a positive direction, excepting the $2\text{mm} \times 2\text{mm} \times 2\text{mm}$ during systole.

The through plane circulation values predicted through the CFD methodology over-estimate the magnitude, notably the CFD simulation based on the $1.5\text{mm} \times 1.5\text{mm} \times 1.5\text{mm}$ at systole and the CFD simulation based on the $2\text{mm} \times 2\text{mm} \times 2\text{mm}$ at diastole. As discussed in Sections 4.5 and 4.6, the inclusion of the supra-aortic vessels has a significant impact on the circulation values within the mid-ascending aorta and improves the agreement between 4D-Flow MRI and CFD data. It is likely that the decision to neglect the supra-aortic vessels, for the purpose of consistency between resolutions, contributes to the significant differences seen in the through plane circulation values in the mid-ascending aorta.

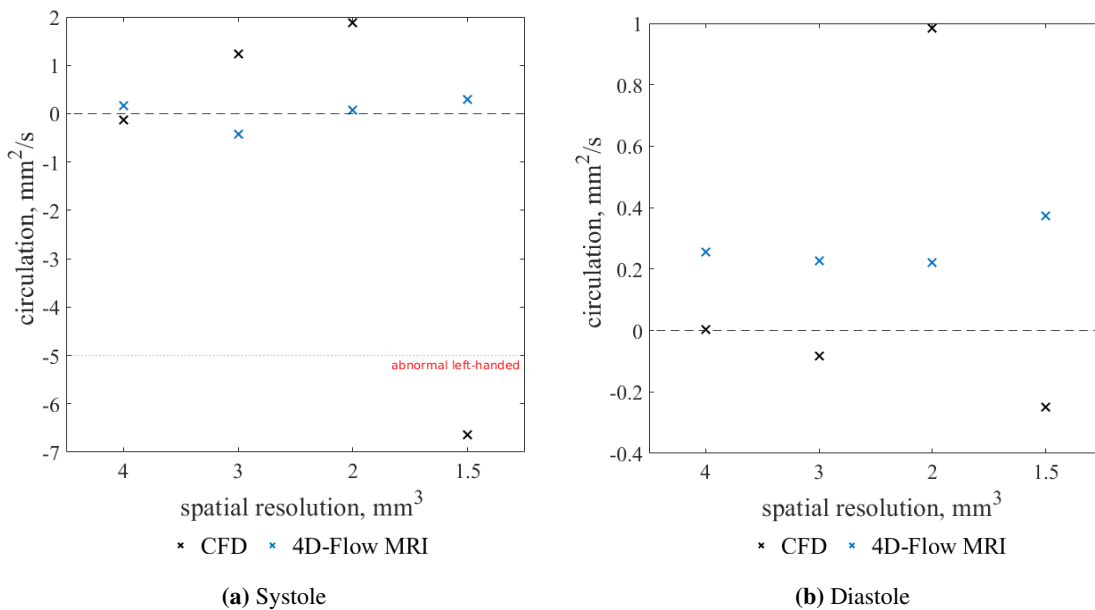


Figure 6.13. Through plane circulation (mm^2s^{-1}) calculated at the plane in the mid-ascending aorta from CFD and 4D-Flow MRI data at systole (a) and diastole (b) for all spatial resolutions.

6.4 Limitations

Although the impacts of varying the spatial resolution have been investigated in this Chapter, the impacts of varying the temporal resolution has not been looked into. It is probable that the temporal resolution of 4D-Flow MRI scans will have a significant impact on subsequent CFD simulations as the spatial resolution does. In order to fully evaluate the accuracy of 4D-Flow MRI based CFD simulations, the temporal resolution of the 4D-Flow MRI scans must be investigated independently from varying the spatial resolution. Despite the temporal resolution not being of

interest within this Chapter, the temporal resolution used to acquire the 4D-Flow MRI data in this study was not consistent across the four acquisitions. As discussed in Section 6.2.1, this was a result of the available processing power of the 4D-Flow MRI scanner used. This has influenced the results of the $1.5\text{mm} \times 1.5\text{mm} \times 1.5\text{mm}$ spatial resolution scan, therefore any differences between the $4\text{mm} \times 4\text{mm} \times 4\text{mm}$, $3\text{mm} \times 3\text{mm} \times 3\text{mm}$, $2\text{mm} \times 2\text{mm} \times 2\text{mm}$ and the $1.5\text{mm} \times 1.5\text{mm} \times 1.5\text{mm}$ cannot be attributed solely to the spatial resolution. The coarser temporal resolution used will produce results that were less accurate than had the finer temporal resolution been used.

The patient participating in the research within this Chapter was not part of the cohort discussed in Section 3.2 and was instead a healthy adult without a diagnosis of BAV or any known heart defect or heart disease. A consequence of this is that any recommendations as to the appropriate scan resolution needed for conducting patient-specific CFD simulations applies solely to healthy adult patients. It is not yet known explicitly how the spatial resolution will impact neonatal simulations, or patients with existing heart conditions such as BAV, where the vessel will be significantly smaller in diameter or the blood flow experienced will be abnormal. It is highly likely the recommendations for spatial resolution would be significantly finer for a neonatal patient due to the decrease in the size of the vessel of interest to ensure the appropriate ratio between vessel diameter and voxel size is kept. Before a recommendation can be made for situations where the vessel is smaller or the flow more complex, research into the impacts of the spatial resolution must be completed on patients that are neonatal or experience abnormal flow.

The investigation into the spatial resolution of 4D-Flow MRI scans was conducted on one patient only. In order to confirm the conclusions are robust, ideally multiple patients with a range of heart defects and vessel sizes should be investigated to ensure the trends seen are not anomalous. In the CFD simulations conducted, blood was assumed to be a Newtonian, homogeneous and incompressible fluid. In order to improve the accuracy of the simulations these assumptions should be removed. The supra-aortic vessels were neglected in this study, as the coarse resolution scans had too few voxels to describe the flow and geometry adequately enough for analysis [44, 169]. For consistency, they were therefore removed from all four spatial resolutions. The outlet boundary condition, a zero-pressure condition applied to the inferior end of the descending thoracic aorta, provides another limitation to the CFD simulations, as discussed in Section 2.5.2. A more physiologically accurate boundary condition, such as a three-element Windkessel model, would improve the haemodynamics within the descending aorta. As the plane of interest was more than five diameters upstream of the outlet, a zero-pressure boundary condition was considered a suitable assumption [79]. More detail regarding the choice of outlet boundary condition can be found in Section 2.5.2.

The vessel walls were assumed to be rigid despite the thoracic aorta being known to move radially and vertically throughout the cardiac cycle. To account for the impacts this movement has, FSI must be included in the CFD simulations. The effects of the vessel wall being impacted by the blood flow and in turn impacting the blood flow itself, the surrounding tissue and the tethering of the aorta through the intercostal, bronchial, and oesophageal arteries all play a part in the blood flow experienced through the thoracic aorta. The aortic valve leaflets and their interaction with the blood flow was also neglected. However, a decision to neglect all movement of the thoracic aorta and aortic valve was made in an attempt to reduce the computational cost of the simulations.

6.5 Conclusions

It has been demonstrated within this Chapter that the spatial resolution of the 4D-Flow MRI scan used to construct patient specific geometry and inlet conditions has major consequences on any subsequent patient-specific CFD simulations that are undertaken in terms of the volumetric flow rate, vessel diameter, velocity, WSS, and the flow asymmetry, dispersion, and circulation.

The differences that arise between the CFD simulations based on the four resolutions have been established and discussed. Refining the spatial resolution of the 4D-Flow MRI scan from $4\text{mm} \times 4\text{mm} \times 4\text{mm}$ to $1.5\text{mm} \times 1.5\text{mm} \times 1.5\text{mm}$ produces a difference in the mean velocity magnitude over a plane in the mid-ascending aorta of 23.23% during systole, and 21.42% during diastole respectively. It has been shown that there is a considerable lack of consistency in the velocity results when comparing the spatial resolutions during the systolic and diastolic phases of the cardiac cycle, in both the 4D-Flow MRI data and the subsequent patient-specific CFD data. However, as the spatial resolution is refined, the agreement between the 4D-Flow MRI and CFD data improves markedly. Results from 4D-Flow MRI velocity magnitude contours indicate that a coarse spatial resolution will underestimate the velocity magnitude of the flow, whilst a finer spatial resolution will show a higher velocity magnitude in the thoracic aorta. This trend is also present in CFD data, excluding the $4\text{mm} \times 4\text{mm} \times 4\text{mm}$ spatial resolution which appears to erroneously predict higher velocity magnitudes alongside dissimilar flow patterns. It can also be seen that CFD results appear to overestimate the velocity when compared to the 4D-Flow MRI results.

When observing WSS results, it can be seen that despite the 4D-Flow MRI data and CFD results not following the same trend, the agreement between the two methods improves as the spatial resolution increases to the extent that the differences between the 4D-Flow MRI data and CFD results during the systolic and diastolic phases of the cardiac cycle can be said to be insignificant ($p > 0.05$) for the finest spatial resolution (Wilcoxon signed rank test, $\alpha = 0.05$). This can be compared to all other spatial resolutions producing significant differences between the 4D-Flow MRI and CFD data at one or both stages of the cardiac cycle.

Flow asymmetry results demonstrate the best agreement between the 4D-Flow MRI and CFD data with the $2\text{mm} \times 2\text{mm} \times 2\text{mm}$ spatial resolution at systole, and with the $1.5\text{mm} \times 1.5\text{mm} \times 1.5\text{mm}$ during diastole. However, at both stages of the cardiac cycle it is clear that results have not yet begun to converge and are likely being influenced by the increased temporal resolution of the $1.5\text{mm} \times 1.5\text{mm} \times 1.5\text{mm}$ scan. Flow dispersion is in good agreement between the 4D-Flow MRI and CFD data (differences $< 10\%$) at all four spatial resolutions during systole. This agreement is also seen during the diastolic phase, with the differences reducing to $< 1\%$ with a spatial resolution of $1.5\text{mm} \times 1.5\text{mm} \times 1.5\text{mm}$. Circulation results show little agreement between the 4D-Flow MRI and CFD data, and do not appear to show any trends in relation to the spatial resolution of the 4D-Flow MRI data; circulation magnitudes reported using 4D-Flow MRI data remain relatively close across all four spatial resolutions. It is possible that the decision to neglect the supra-aortic vessels in impacting the circulation values more than the insufficient spatial resolutions. To confirm this, a study varying the spatial resolution whilst including the supra-aortic vessels should be conducted. However, as previously discussed the coarse spatial resolutions used in this research do not allow for this to be undertaken.

The results presented within this investigation show that 4D-Flow MRI spatial resolutions of

$4mm \times 4mm \times 4mm$, $3mm \times 3mm \times 3mm$, and $2mm \times 2mm \times 2mm$ are wholly unsuitable for use in patient-specific CFD simulations as it has been shown that an insufficient spatial resolution produces poor agreement between 4D-Flow MRI data and CFD results of the same spatial resolution, in addition to poor agreement with results from a more refined spatial resolution. However, a $1.5mm \times 1.5mm \times 1.5mm$ spatial resolution cannot be recommended for use without caution. As there is no known 'gold-standard' and results have not yet converged on a solution, the error that may be present in patient-specific CFD simulations based on 4D-Flow MRI data acquired with a spatial resolution of $1.5mm \times 1.5mm \times 1.5mm$ is still unknown. Caution must also be advised with the results from the $1.5mm \times 1.5mm \times 1.5mm$ spatial resolution due to the coarser temporal resolution that was used to acquire the 4D-Flow MRI data. Despite this, it is recommended based on the results within this Chapter that when 4D-Flow MRI data is used to construct and run patient-specific CFD simulations on healthy adult patients, a minimum spatial resolution of $1.5mm \times 1.5mm \times 1.5mm$ should be used to avoid inaccurate data being used in any subsequent CFD simulations, resulting in geometry and inlet conditions that are not physiologically accurate. A spatial resolution coarser than $1.5mm \times 1.5mm \times 1.5mm$ will generate results with substantial errors that greatly underestimate the magnitude of the velocity within the thoracic aorta, as well as produce differences in terms of the geometry, the volumetric flow rate, and the WSS.

As the patient participating in this research is a healthy individual with no heart disease, the research presented does not investigate the impacts of 4D-Flow MRI resolution on patient-specific CFD studies of diseased aortas. Therefore recommendations cannot be made regarding a spatial resolution that would be appropriate for diseased aortas. However, as the presence of disease or heart defects results in more complex flow features, it is likely that a spatial resolution of $1.5mm \times 1.5mm \times 1.5mm$ must be the minimum used, and if possible a finer resolution must be utilised to avoid any complex flow features being neglected. Neonatal or paediatric patients must also require a finer spatial resolution than suggested within this research due to the size of the vessels present in patients smaller than an adult. As discussed in Section 4.7, when using a spatial resolution of $1mm \times 1mm \times 1mm$ for a neonatal patient, a singular voxel occupied 11.63% of the average neonatal ascending aortic diameter; this is equivalent to the $3mm \times 3mm \times 3mm$ spatial resolution investigated within this Chapter, as a voxel at that resolution occupies 11.68% of the ascending aortic diameter. It can therefore be taken that the results presented within Chapter 4 are heavily impacted by the spatial resolution used to acquire the 4D-Flow MRI data.

As discussed in Section 2.5.5, CFD is quickly becoming an invaluable tool in the medical field and there is a drive towards using it to aid in treatment planning, diagnostics, monitoring disease progression and risk stratification. When this is the case, great caution is advised if using an inappropriate spatial resolutions as any miscalculation as a result of resolution may lead to misleading or inaccurate results being passed onto clinicians, which may have serious consequences for the patient in question.

Chapter 7.

Summary

Contents

7.1	Conclusions	158
7.1.1	Chapter 4: Patient-Specific Results from Methodology Development	158
7.1.2	Chapter 5: Validation of Methodology Using a Flow Phantom	159
7.1.3	Chapter 6: The Impacts of 4D-Flow MRI Spatial Resolution on Patient-Specific CFD Simulations	160
7.2	Implications of the Results	161
7.3	Further Work	161

7.1 Conclusions

The purpose of this research was to create a workflow that would combine CFD and 4D-Flow MRI, that has the potential to allow post-surgical haemodynamics to be modelled prior to surgical intervention being undertaken, enabling clinicians to conduct patient-specific treatments with the best possible outcome for the individual patient. This research has successfully created a methodology that would be capable of modelling a range of inlet profiles, such as those that would arise from a range of AVR's. Alongside this, the research focused on highlighting and investigating the main challenges, such as the spatial resolution of the 4D-Flow MRI data and the human error introduced through geometry reconstruction, that are associated with patient-specific cardiac modelling. The main outcomes of the research (Chapters 4-6) are summarised below and are related back to the initial project aims and objectives that were outlined in Section 1.4:

7.1.1 Chapter 4: Patient-Specific Results from Methodology Development

- A workflow has been created that combines CFD and 4D-Flow MRI and successfully recreates patient-specific geometries that are suitable for use in CFD simulations. [**Aim 1, Objective 2**].
- Preliminary patient-specific steady-state simulations were conducted at systole and diastole in addition to preliminary transient simulations of the full cardiac cycle, which provided direction for the research to move in. This allowed the largest sources of error that are present in patient-specific modelling of the thoracic aorta using 4D-Flow MRI data to be

identified. Both adult and neonatal patients participated in the research, demonstrating the workflow is suitable for a wide age range. [**Aim 1, Objective 3**].

- A range of inlet conditions were tested during the development of the workflow. Temporally patient-specific and spatio-temporally patient-specific inlet conditions were compared, alongside steady-state and transient plug profiles. This preliminary work enabled the development of the spatio-temporal patient-specific inlet boundary conditions that were later integrated into the model that successfully replicated the ascending aortic haemodynamics. [**Aim 2, Objective 2**].
- The spatio-temporal patient-specific boundary conditions that were developed accurately replicate the flow patterns in the ascending aorta that are seen in the 4D-Flow MRI data. The methods used to create the spatio-temporal patient-specific inlet conditions would allow all AVR types to be modelled, as long as the expected flow profile resulting from the AVR's is already known, as it can be coded into the inlet boundary conditions. Results have demonstrated that there is full confidence in the inlet conditions accurately predicting the ascending aortic haemodynamics accurately, and would allow the large changes that clinicians are looking for to be observed in-silico prior to surgical intervention to ensure the best possible outcome is achieved on a patient-specific basis. [**Aim 1, Objective 4**].
- The results show that including the supra-aortic vessels is key to predicting the flow in the aortic arch and descending aorta as it introduces an additional three outlets. Results also suggest that the haemodynamics are being affected by insufficient outlet boundary conditions, particularly the supra-aortic vessel outlets as they are within 5 diameters downstream of the flow being analysed. [**Aim 2, Objective 3**].
- The workflow created appears to predict the haemodynamics better at systole when a clear and distinct flow profile is present at the aortic valve. Modelling systole and diastole through the same inlet condition causes diastolic results to be less accurate than if they were modelled separately or the inlet conditions were mapped directly from 4D-Flow MRI data. Incorporating the motion of the aortic valve leaflets would improve the inlet conditions at diastole.
- The choice in viscosity model may be impacting the haemodynamics throughout the cardiac cycle, notably during the diastolic period. It is known that when velocities are low, a Newtonian assumption will underestimate the WSS and other haemodynamic indices of interest.

7.1.2 Chapter 5: Validation of Methodology Using a Flow Phantom

- Using a flow phantom enabled the circulatory system distal to the outlets, and the fluid-structure interactions between the vessel wall and blood to be removed from consideration. This allowed the methodology to be validated as some of the main challenges of replicating in-vivo haemodynamics were removed. [**Aim 1, Objective 5**].
- The ascending aortic haemodynamics demonstrate excellent agreement in terms of flow patterns, with the maximum velocity showing only a 3.950% difference between CFD and 4D-Flow MRI data at systole once the main in-vivo aspects of patient-specific CFD mod-

elling are removed from consideration. The flow patterns also show excellent agreement with both CFD and 4D-Flow MRI data indicating a region of elevated velocity in the posterior and left-posterior region.

- The spatio-temporal patient-specific inlet conditions accurately capture the recirculation region that can be seen in the ascending aorta in the 4D-Flow MRI data. However, they fail to capture the secondary flow features that are caused by the motion of the aortic valve leaflets as the valve leaflets are neglected by the CFD simulations.
- The good agreement found between 4D-Flow MRI and CFD data in the ascending aorta at systole suggests that the errors found within Chapter 4 in the ascending aorta's can be attributed to the systemic circulatory system distal to the outlets, the vessel wall compliance and movement during the cardiac cycle, and therefore the choice in outlet boundary conditions. The errors during diastole can also be attributed to the decision to neglect the aortic valve leaflet movement, and insufficient inlet boundary conditions. Removing the uncertainty surrounding the Newtonian and homogeneous assumptions may also be contributing to the good agreement seen.

7.1.3 Chapter 6: The Impacts of 4D-Flow MRI Spatial Resolution on Patient-Specific CFD Simulations

- This research has quantified the magnitude of the errors that are found in patient-specific CFD simulations that are caused by acquiring 4D-Flow MRI data at an insufficient spatial resolution. It has helped to shed light on the key areas that impact the accuracy and reliability of patient-specific CFD simulations. It offers recommendations as to an appropriate spatial resolution to use if clinical conclusions are to be drawn from the CFD data; spatial resolutions coarser than $1.5\text{mm} \times 1.5\text{mm} \times 1.5\text{mm}$ have been shown to be completely unsuitable for use in patient-specific CFD simulations and will cause errors within patient-specific simulations, resulting in reduced agreement with the 4D-Flow MRI data and incorrect haemodynamics to be predicted. However, even the finest spatial resolution cannot yet be recommended for use when attempting to draw clinical conclusions from the CFD data as the data has not yet converged on a spatial resolution. The coarser temporal resolution that was used will also impact the results to an unknown degree. [**Aim 2, Objective 4**].
- It has been demonstrated that a coarse spatial resolution will produce significant differences in terms of volumetric flow rate, velocity, vessel diameter, WSS, flow asymmetry, flow dispersion, and circulation. This suggests that all spatio-temporal patient-specific results within Chapter 4 will be affected by the spatial resolution of the 4D-Flow MRI data, particularly the neonatal patients that were participating in the research, as hypothesised in Chapter 4.
- As the spatial resolution of the 4D-Flow MRI data is refined, the agreement that is found between the 4D-Flow MRI data and CFD data is increased in terms of velocity and WSS. A coarse spatial resolution underestimates the velocity magnitude, this trend is seen in both CFD and 4D-Flow MRI data. Across a plane in the mid-ascending aorta, the difference in terms of the maximum velocity magnitude at systole between the 4D-Flow MRI data and the CFD data reduces from 39.49% to 16.31% and from 56.76% to 3.670% at diastole as

the spatial resolution is refined from $4mm \times 4mm \times 4mm$ to $1.5mm \times 1.5mm \times 1.5mm$.

- In terms of the WSS, it has been shown that the agreement between CFD and 4D-Flow MRI increases as the spatial resolution is refined, such that a spatial resolution of $1.5mm \times 1.5mm \times 1.5mm$ produces differences between CFD and 4D-Flow MRI data that are insignificant at both systole and diastole (Wilcoxon signed rank test, $\alpha = 0.05$). For all other spatial resolutions the differences are significant at one or both stages of the cardiac cycle. At systole, the differences between CFD and 4D-Flow MRI data in terms of average WSS magnitude reduces from 151.9% to 58.09%, and from 106.7% to 21.67% at diastole.

7.2 Implications of the Results

This thesis has constructed a methodology that combines 4D-Flow MRI data and CFD techniques, enabling spatio-temporal patient-specific simulations to be conducted. In addition to creating a workflow, the limitations of patient-specific modelling have been discussed in detail, and an insight has been given into the impacts that the spatial resolution of 4D-Flow MRI data has on the subsequent patient-specific in-silico geometry and simulations. From this research, a recommendation has been made regarding the minimum spatial resolution that must be used when using 4D-Flow MRI data to create patient-specific CFD simulations.

The research within this thesis has demonstrated the necessity of including spatially and temporally varying patient-specific inlet conditions that can replicate a range of BAV phenotypes, as well as a healthy flow profile. The magnitude of the errors that can be attributed to human error within the geometry reconstruction process have been quantified and discussed, as have the errors that can be attributed to neglecting to include the brachiocephalic, left common carotid, and left subclavian arteries in the geometry.

Validating the workflow created using a flow phantom has shown that the methods used can qualitatively replicate the flow patterns and accurately predict the velocity magnitude within the ascending aorta at systole. The results therefore suggest that the methodology works as intended.

7.3 Further Work

Patient-specific CFD modelling of the thoracic aorta has significant improvements and advances to take before it becomes common practice in diagnosis, risk stratification, treatment planning and surgical procedures. Some of the key areas that require development before any clinical conclusions can be drawn from patient-specific CFD simulations are summarised below:

1. 4D-Flow MRI Resolution:

- (a) 4D-Flow MRI scans of higher spatial resolutions from the same patient are required to fully establish the spatial resolution required to ensure any results are not affected the CFD simulations. The spatial resolutions must be varied independently of the temporal resolution.
- (b) The spatial resolution must be investigated for a range of patients, as it has been hypothesised within this research that neonatal patients and patients with complex flow patterns resulting from a range of pathologies may require a finer resolution than that

required for a healthy adult patient with normal aortic haemodynamics.

- (c) The temporal resolution must be investigated as it is likely that it has a similar impact on the 4D-Flow MRI data as the spatial resolution does, and thus on the subsequent CFD data. The temporal resolution must be varied independently of the spatial resolution and patients with a wide range in age and pathologies and valve phenotypes must participate in the research.

2. Fluid-Structure Interaction:

- (a) The interactions between the blood and the vessel walls and aortic valve leaflets must be modelled and incorporated into the simulation as they will influence the haemodynamics.
- (b) The interactions between the vessel walls and the surrounding tissues and the tethering through the intercostal, bronchial, and oesophageal arteries must also be taken into account as it is known that this will also affect the blood flow within the thoracic aorta. Patient specific parameters should be used when modelling the vessel wall, as the presence of any pathologies and abnormal flow will affect the vessel wall itself, and are known to alter its properties. Therefore using generalised parameters or values collected from *ex-vivo* porcine samples will be inaccurate. It is also likely the properties will vary with the age of the patient, as adults are more likely to have stenosis or calcified valves and vessel walls than neonatal patients.

3. Outlet boundary conditions

- (a) The outlet boundary conditions used should be updated to be more physiologically accurate. The two- and three- element windkessel models are more physiologically appropriate, and would improve the accuracy of the workflow. This would alter the haemodynamics within the aortic arch and descending aorta within 5 diameters upstream of the outlets.

4. Inlet conditions at diastole

- (a) The inlet conditions at diastole require improvement. The method that was used to create spatio-temporal patient-specific inlet conditions shows deficiencies during the diastolic period as the fluctuations are much smaller than those during systole, therefore they are neglected by the surface fit. This means the agreement between CFD and 4D-Flow MRI is notably reduced at diastole when compared to systole.
- (b) Applying a higher accuracy surface fit, or directly mapping the 4D-Flow MRI data onto the CFD mesh would improve the accuracy of the inlet conditions, however both techniques come with associated difficulties that need addressing before the new inlet conditions would be appropriate. It is likely that the addition of FSI of the valve leaflets would be the most physiologically accurate approach to recreate the inlet conditions during diastole.

5. Experimental Work

- (a) Additional experimental work and the corresponding CFD scenarios would allow for more detailed and thorough validation of the methodology created to combine CFD

and 4-Flow MRI data.

- (b) Ensuring any additional experimental work utilised an alternate method of quantifying and measuring the haemodynamic indices of interest other than 4D-Flow MRI would enable the quantification of the errors that can be attributed to the acquisition of the 4D-Flow MRI data rather than the CFD methodology.
- (c) Experimental work and the corresponding CFD scenarios investigating the effects of altering the inlet conditions to reproduce the flow found from a range of BAV phenotypes and AVR options would allow the scope of the CFD methodology to be tested.

6. Methodology

- (a) Creating a new tool or metric to monitor the flow asymmetry will be key to avoid any errors introduced to the 4D-Flow MRI data from irregular data points.

References

1. Stephanie, L., Joy, L. & Vidu, G. Genetics of valvular heart disease. *Current cardiology reports* **16**, 487–503 (2014).
2. Ha, H., Kim, G. B., Kweon, J., Lee, S. J., Kim, Y. H., Kim, N. & Yang, D. H. The influence of the aortic valve angle on the hemodynamic features of the thoracic aorta. *Scientific Reports* **6**. ISSN: 20452322 (2016).
3. Edlin, J., Youssefi, P., Bilkhu, R., Figueroa, C. A., Morgan, R., Nowell, J. & Jahangiri, M. Haemodynamic assessment of bicuspid aortic valve aortopathy: a systematic review of the current literature. *European Journal of Cardio-Thoracic Surgery* **55**, 610–617 (2019).
4. Michelena, H. I., Khanna, A. D., Mahoney, D., Margaryan, E., Topilsky, Y., Suri, R. M., Eidem, B., Edwards, W. D., Sundt, T. M. & Enriquez-Sarano, M. Incidence of aortic complications in patients with bicuspid aortic valves. *Journal of the American Medical Association* **306**, 1104–1112. ISSN: 00987484 (2011).
5. Michelena, H. I., Prakash, S. K., Della Corte, A., Bissell, M. M., Anavekar, N., Mathieu, P., Bossé, Y., Limongelli, G., Bossone, E., Benson, D. W., *et al.* Bicuspid aortic valve: identifying knowledge gaps and rising to the challenge from the International Bicuspid Aortic Valve Consortium (BAVCon). *Circulation* **129**, 2691–2704 (2014).
6. OpenCFD Ltd. *OpenFOAM* version 6. July 10, 2018. <https://openfoam.org/download/>.
7. Quarteroni, A., Manzoni, A., Vergara, C., *et al.* *Mathematical Modelling of the Human Cardiovascular System: Data, Numerical Approximation, Clinical Applications* (Cambridge University Press, 2019).
8. Itu, L. M., Sharma, P. & Suci, C. *Patient-specific hemodynamic computations: Application to personalized diagnosis of cardiovascular pathologies* 1–227. ISBN: 9783319568539 (Springer International Publishing, 2017).
9. Augoustides, J. G. & Cheung, A. T. *Aneurysms and Dissections* 191–217 (Elsevier, 2014).
10. Nishimura, R. A., Otto, C. M., Bonow, R. O., Carabello, B. A., Erwin, J. P., Guyton, R. A., O’Gara, P. T., Ruiz, C. E., Skubas, N. J., Sorajja, P., Sundt, T. M. & Thomas, J. D. 2014 AHA/ACC guideline for the management of patients with valvular heart disease: A report of the American college of cardiology/American heart association task force on practice guidelines. *Journal of the American College of Cardiology* **63**. ISSN: 15583597 (2014).
11. Piatti, F., Pirola, S., Bissell, M., Nesteruk, I., Sturla, F., Della Corte, A., Redaelli, A. & Votta, E. Towards the improved quantification of in vivo abnormal wall shear stresses in

- BAV-affected patients from 4D-flow imaging: Benchmarking and application to real data. *Journal of Biomechanics* **50**, 93–101. ISSN: 0021-9290 (2017).
12. Ward, C. Clinical significance of the bicuspid aortic valve. *Heart* **83**, 81–85. ISSN: 13556037 (2000).
 13. Bissell, M. M., Loudon, M., Hess, A. T., Stoll, V., Orchard, E., Neubauer, S. & Myerson, S. G. Differential flow improvements after valve replacements in bicuspid aortic valve disease: A cardiovascular magnetic resonance assessment. *Journal of Cardiovascular Magnetic Resonance* **20**, 1–10. ISSN: 1532429X (2018).
 14. Youssefi, P., Gomez, A., He, T., Anderson, L., Bunce, N., Sharma, R., Figueroa, C. A. & Jahangiri, M. Patient-specific computational fluid dynamics—assessment of aortic hemodynamics in a spectrum of aortic valve pathologies. *The Journal of Thoracic and Cardiovascular Surgery* **153**, 8–20.e3. ISSN: 00225223 (2017).
 15. Yoganathan, A. P., He, Z. & Casey Jones, S. Fluid Mechanics of Heart Valves. *Annual Review of Biomedical Engineering* **6**, 331–362. ISSN: 1523-9829 (2004).
 16. Pibarot, P. & Dumesnil, J. G. Prosthetic heart valves: Selection of the optimal prosthesis and long-term management. *Circulation* **119**, 1034–1048 (2009).
 17. Dasi, L. P., Simon, H. A., Sucusky, P. & Yoganathan, A. P. Fluid mechanics of artificial heart valves. *Clinical and Experimental Pharmacology and Physiology* **36**, 225–237. ISSN: 03051870 (2009).
 18. Hellmeier, F., Nordmeyer, S., Yevtushenko, P., Bruening, J., Berger, F., Kuehne, T., Goubergrits, L. & Kelm, M. Hemodynamic Evaluation of a Biological and Mechanical Aortic Valve Prosthesis Using Patient-Specific MRI-Based CFD. *Artificial Organs* **42**, 49–57. ISSN: 15251594 (2018).
 19. Hoerstrup, S. P. & Weber, B. Biological heart valves. *European Heart Journal* **36**, 325–326 (2015).
 20. Vesely, I. The evolution of bioprosthetic heart valve design and its impact on durability. *Cardiovascular Pathology* **12**, 277–286 (2003).
 21. Zakerzadeh, R., Hsu, M.-C. & Sacks, M. S. Computational methods for the aortic heart valve and its replacements. *Expert review of medical devices* **14**, 849–866 (2017).
 22. De Gaetano, F., Bagnoli, P., Zaffora, A., Pandolfi, A., Serrani, M., Brubert, J., Stasiak, J., Moggridge, G. D. & Costantino, M. L. A newly developed tri-leaflet polymeric heart valve prosthesis. *Journal of mechanics in medicine and biology* **15**, 1540009 (2015).
 23. Yoganathan, A. P., Chandran, K. & Sotiropoulos, F. Flow in prosthetic heart valves: state-of-the-art and future directions. *Annals of biomedical engineering* **33**, 1689–1694 (2005).
 24. Xu, F., Morganti, S., Zakerzadeh, R., Kamensky, D., Auricchio, F., Reali, A., Hughes, T. J., Sacks, M. S. & Hsu, M.-C. ICES REPORT 17-11 (2017).
 25. Pedley, T. J. *The fluid mechanics of large blood vessels* (Cambridge University Press, 1980).
 26. Krstic, M. Mixing Control for Jet Flow. *Combustion Processes in Propulsion: Control, Noise, and Pulse Detonation*, 87–96 (2006).
 27. Whitmore, R. *Rheology of the Circulation* (Elsevier Science & Technology, 1968).

28. Lehoux, S. & Tedgui, A. Cellular mechanics and gene expression in blood vessels. *Journal of biomechanics* **36**, 631–643 (2003).
29. Tronc, F., Wassef, M., Esposito, B., Henrion, D., Glagov, S. & Tedgui, A. Role of NO in flow-induced remodeling of the rabbit common carotid artery. *Arteriosclerosis, thrombosis, and vascular biology* **16**, 1256–1262 (1996).
30. Guzzardi, D. G., Barker, A. J., Van Ooij, P., Malaisrie, S. C., Puthumana, J. J., Belke, D. D., Mewhort, H. E., Svystonyuk, D. A., Kang, S., Verma, S., *et al.* Valve-related hemodynamics mediate human bicuspid aortopathy: insights from wall shear stress mapping. *Journal of the American College of Cardiology* **66**, 892–900 (2015).
31. Sigovan, M., Hope, M. D., Dyverfeldt, P. & Saloner, D. Comparison of four-dimensional flow parameters for quantification of flow eccentricity in the ascending aorta. *Journal of Magnetic Resonance Imaging* **34**, 1226–1230 (2011).
32. Burris, N. S. & Hope, M. D. Bicuspid valve-related aortic disease: flow assessment with conventional phase-contrast MRI. *Academic radiology* **22**, 690–696 (2015).
33. Della Corte, A., Bancone, C., Conti, C. A., Votta, E., Redaelli, A., Del Viscovo, L. & Cotrufo, M. Restricted cusp motion in right-left type of bicuspid aortic valves: a new risk marker for aortopathy. *The Journal of thoracic and cardiovascular surgery* **144**, 360–369 (2012).
34. Verma, S. & Siu, S. C. Aortic dilatation in patients with bicuspid aortic valve. *New England Journal of Medicine* **370**, 1920–1929 (2014).
35. Barker, A. J., Markl, M., Bürk, J., Lorenz, R., Bock, J., Bauer, S., Schulz-Menger, J. & Von Knobelsdorff-Brenkenhoff, F. Bicuspid aortic valve is associated with altered wall shear stress in the ascending aorta. *Circulation: Cardiovascular Imaging*. ISSN: 19419651 (2012).
36. De Nisco, G., Hoogendoorn, A., Chiastra, C., Gallo, D., Kok, A. M., Morbiducci, U. & Wentzel, J. J. The impact of helical flow on coronary atherosclerotic plaque development. *Atherosclerosis* **300**, 39–46 (2020).
37. Morbiducci, U., Ponzini, R., Rizzo, G., Cadioli, M., Esposito, A., Montevecchi, F. M. & Redaelli, A. Mechanistic insight into the physiological relevance of helical blood flow in the human aorta: an in vivo study. *Biomechanics and modeling in mechanobiology* **10**, 339–355 (2011).
38. Liu, X., Pu, F., Fan, Y., Deng, X., Li, D. & Li, S. A numerical study on the flow of blood and the transport of LDL in the human aorta: the physiological significance of the helical flow in the aortic arch. *American Journal of Physiology-Heart and Circulatory Physiology* **297**, H163–H170 (2009).
39. Morbiducci, U., Ponzini, R., Rizzo, G., Cadioli, M., Esposito, A., De Cobelli, F., Del Maschio, A., Montevecchi, F. M. & Redaelli, A. In vivo quantification of helical blood flow in human aorta by time-resolved three-dimensional cine phase contrast magnetic resonance imaging. *Annals of biomedical engineering* **37**, 516 (2009).
40. Morbiducci, U., Ponzini, R., Gallo, D., Bignardi, C. & Rizzo, G. Inflow boundary conditions for image-based computational hemodynamics: impact of idealized versus measured velocity profiles in the human aorta. *Journal of biomechanics* **46**, 102–109 (2013).

41. Morbiducci, U., Kok, A. M., Kwak, B. R., Stone, P. H., Steinman, D. A., Wentzel, J. J., *et al.* Atherosclerosis at arterial bifurcations: evidence for the role of haemodynamics and geometry. *Thromb Haemost* **115**, 484–492 (2016).
42. Bissell, M. M., Hess, A. T., Biasioli, L., Glaze, S. J., Loudon, M., Pitcher, A., Davis, A., Prendergast, B., Markl, M., Barker, A. J., *et al.* Aortic dilation in bicuspid aortic valve disease: flow pattern is a major contributor and differs with valve fusion type. *Circulation: Cardiovascular Imaging* **6**, 499–507 (2013).
43. Lawley, C. M., Broadhouse, K. M., Callaghan, F. M., Winlaw, D. S., Figtree, G. A. & Grieve, S. M. 4D flow magnetic resonance imaging: role in pediatric congenital heart disease. *Asian Cardiovascular and Thoracic Annals* **26**, 28–37 (2018).
44. Dyverfeldt, P., Bissell, M., Barker, A. J., Bolger, A. F., Carlhäll, C.-J., Ebbers, T., Francios, C. J., Frydrychowicz, A., Geiger, J., Giese, D., Hope, M. D., Kilner, P. J., Kozerke, S., Myerson, S., Neubauer, S., Wieben, O. & Markl, M. 4D flow cardiovascular magnetic resonance consensus statement. *Journal of Cardiovascular Magnetic Resonance* **17**, 72. ISSN: 1532-429X (2015).
45. Barker, A. J., Lanning, C. & Shandas, R. Quantification of hemodynamic wall shear stress in patients with bicuspid aortic valve using phase-contrast MRI. *Annals of biomedical engineering* **38**, 788–800 (2010).
46. Hope, M. D., Hope, T. A., Crook, S. E., Ordovas, K. G., Urbania, T. H., Alley, M. T. & Higgins, C. B. 4D flow CMR in assessment of valve-related ascending aortic disease. *JACC: Cardiovascular Imaging* **4**, 781–787 (2011).
47. Rose, M. J., Jarvis, K. B., Barker, A. J., Schnell, S., Allen, B. D., Robinson, J. D., Markl, M. & Rigsby, C. K. Evaluating the disease progression of pediatric bicuspid aortic valve patients using 4D flow MRI data. *Journal of Cardiovascular Magnetic Resonance* **18**, P170. ISSN: 1532-429X (2016).
48. De Beaufort, H. W., Shah, D. J., Patel, A. P., Jackson, M. S., Spinelli, D., Yang, E. Y., Ghosn, M. G., Autry, K., Igo, S. R., Lumsden, A. B., Little, S. H., Trimarchi, S. & Bismuth, J. Four-dimensional flow cardiovascular magnetic resonance in aortic dissection: Assessment in an ex vivo model and preliminary clinical experience. *The Journal of Thoracic and Cardiovascular Surgery* **157**, 467–476.e1. ISSN: 0022-5223 (2019).
49. Van der Palen, R. L., Roest, A. A., van den Boogaard, P. J., de Roos, A., Blom, N. A. & Westenberg, J. J. Scan–rescan reproducibility of segmental aortic wall shear stress as assessed by phase-specific segmentation with 4D flow MRI in healthy volunteers. *Magnetic Resonance Materials in Physics, Biology and Medicine* **31**, 653–663 (2018).
50. Squires, K. D. in *Direct and large-eddy simulation V* 465–480 (Springer, 2004).
51. Spalart, P. R. *Comments on the feasibility of LES for wings, and on a hybrid RANS/LES approach in Proceedings of first AFOSR international conference on DNS/LES* (1997).
52. Johnston, B. M., Johnston, P. R., Corney, S. & Kilpatrick, D. Non-Newtonian blood flow in human right coronary arteries: steady state simulations. *Journal of Biomechanics* **37**, 709–720. ISSN: 0021-9290 (2004).
53. Ballyk, P., Steinmann, D. & Ethier, C. Simulation of non-Newtonian blood flow in an end-to-side anastomosis. *Biorheology* **31**, 565–586 (1994).

54. Walburn, F. & Schneck, D. A Constitutive Equation for Whole Human Blood. *Biorheology* **13**, 201–210 (1976).
55. Cho, Y. & Kensey, K. Effects of the non-Newtonian viscosity of blood on flows in a diseased arterial vessel. Part 1: Steady flows. *Biorheology* **28**, 241–62 (1991).
56. Fung, Y.-C. *et al. Mechanical properties of living tissues* (Springer).
57. Caballero, A. & Laín, S. Numerical simulation of non-Newtonian blood flow dynamics in human thoracic aorta. *Computer Methods in Biomechanics and Biomedical Engineering* **18**, 1200–1216. ISSN: 1025-5842 (2015).
58. Herschel, W. & Bulkley, R. *Measurement of consistency as applied to rubber-benzene solutions* in *Am. Soc. Test Proc* **26** (1926), 621–633.
59. Middleman, S. *Transport phenomena in the cardiovascular system* (John Wiley & Sons, 1972).
60. Karimi, S., Dabagh, M., Vasava, P., Dadvar, M., Dabir, B. & Jalali, P. Effect of rheological models on the hemodynamics within human aorta: CFD study on CT image-based geometry. *Journal of Non-Newtonian Fluid Mechanics* **207**, 42–52 (2014).
61. Shibeshi, S. S. & Collins, W. E. The rheology of blood flow in a branched arterial system. *Applied Rheology* **15**, 398–405 (2005).
62. Buchanan, J., Kleinstreuer, C., Hyun, S. & Truskey, G. Hemodynamics simulation and identification of susceptible sites of atherosclerotic lesion formation in a model abdominal aorta. *Journal of biomechanics* **36**, 1185–1196 (2003).
63. Boyd, J., Buick, J. M. & Green, S. Analysis of the Casson and Carreau-Yasuda non-Newtonian blood models in steady and oscillatory flows using the lattice Boltzmann method. *Physics of Fluids* **19**, 093103 (2007).
64. Morbiducci, U., Gallo, D., Massai, D., Ponzini, R., Deriu, M. A., Antiga, L., Redaelli, A. & Montecchi, F. M. On the importance of blood rheology for bulk flow in hemodynamic models of the carotid bifurcation. *Journal of biomechanics* **44**, 2427–2438 (2011).
65. O’Callaghan, S., Walsh, M. & McGloughlin, T. Numerical modelling of Newtonian and non-Newtonian representation of blood in a distal end-to-side vascular bypass graft anastomosis. *Medical engineering & physics* **28**, 70–74 (2006).
66. Johnston, B. M., Johnston, P. R., Corney, S. & Kilpatrick, D. Non-Newtonian blood flow in human right coronary arteries: transient simulations. *Journal of biomechanics* **39**, 1116–1128 (2006).
67. Qiao, Y., Zeng, Y., Ding, Y., Fan, J., Luo, K. & Zhu, T. Numerical simulation of two-phase non-Newtonian blood flow with fluid-structure interaction in aortic dissection. *Computer Methods in Biomechanics and Biomedical Engineering* **22**, 620–630. ISSN: 14768259 (2019).
68. Soulis, J. V., Giannoglou, G. D., Chatzizisis, Y. S., Seralidou, K. V., Parcharidis, G. E. & Louridas, G. E. Non-Newtonian models for molecular viscosity and wall shear stress in a 3D reconstructed human left coronary artery. *Medical Engineering and Physics*. ISSN: 13504533 (2008).
69. Jin, S., Yang, Y., Oshinski, J., Tannenbaum, A., Gruden, J. & Giddens, D. *Flow patterns and wall shear stress distributions at atherosclerotic-prone sites in a human left coronary*

- artery—an exploration using combined methods of CT and computational fluid dynamics in *The 26th Annual International Conference of the IEEE Engineering in Medicine and Biology Society* **2** (2004), 3789–3791.
70. Morris, P. D., Narracott, A., Von Tengg-Kobligk, H., Soto, D. A. S., Hsiao, S., Lungu, A., Evans, P., Bressloff, N. W., Lawford, P. V., Rodney Hose, D. & Gunn, J. P. Computational fluid dynamics modelling in cardiovascular medicine. *Heart* **102**, 18–28. ISSN: 1468201X (2016).
 71. Morlacchi, S., Colleoni, S. G., Cárdenes, R., Chiastra, C., Diez, J. L., Larrabide, I. & Migliavacca, F. Patient-specific simulations of stenting procedures in coronary bifurcations: two clinical cases. *Medical engineering & physics* **35**, 1272–1281 (2013).
 72. De Jaegere, P., De Santis, G., Rodriguez-Olivares, R., Bosmans, J., Bruining, N., Dezutter, T., Rahhab, Z., El Faquir, N., Collas, V., Bosmans, B., Verheghe, B., Ren, C., Geleinse, M., Schultz, C., Van Mieghem, N., De Beule, M. & Mortier, P. Patient-Specific Computer Modeling to Predict Aortic Regurgitation after Transcatheter Aortic Valve Replacement. *JACC: Cardiovascular Interventions* **9**, 508–512. ISSN: 18767605 (2016).
 73. Zhu, Y., Chen, R., Juan, Y.-H., Li, H., Wang, J., Yu, Z. & Liu, H. Clinical validation and assessment of aortic hemodynamics using computational fluid dynamics simulations from computed tomography angiography. *Biomedical Engineering Online* **17**, 1–12. ISSN: 1475-925X (2018).
 74. Youssefi, P., Gomez, A., Arthurs, C., Sharma, R., Jahangiri, M. & Figueroa, C. A. Impact of patient-specific inflow velocity profile on hemodynamics of the thoracic aorta. *Journal of Biomechanical Engineering* **140**, 1–14. ISSN: 15288951 (2018).
 75. Bonfanti, M., Franzetti, G., Maritati, G., Homer-Vanniasinkam, S., Balabani, S. & Díaz-Zuccarini, V. Patient-specific haemodynamic simulations of complex aortic dissections informed by commonly available clinical datasets. *Medical Engineering and Physics*. ISSN: 18734030 (2019).
 76. Gijssen, F., Allanic, E., Van de Vosse, F. & Janssen, J. The influence of the non-Newtonian properties of blood on the flow in large arteries: unsteady flow in a 90 curved tube. *Journal of biomechanics* **32**, 705–713 (1999).
 77. Bordones, A. D., Leroux, M., Kheyfets, V. O., Wu, Y.-A., Chen, C.-Y. & Finol, E. A. Computational Fluid Dynamics Modeling of the Human Pulmonary Arteries with Experimental Validation. *Annals of Biomedical Engineering* **46**, 1309–1324. ISSN: 0090-6964 (2018).
 78. Otani, T., Al-Issa, A., Pourmorteza, A., McVeigh, E. R., Wada, S. & Ashikaga, H. A Computational Framework for Personalized Blood Flow Analysis in the Human Left Atrium. *Annals of Biomedical Engineering* **44**, 3284–3294. ISSN: 0090-6964 (2016).
 79. Madhavan, S. & Kemmerling, E. M. C. The effect of inlet and outlet boundary conditions in image-based CFD modeling of aortic flow. *Biomedical engineering online* **17**, 1–20 (2018).
 80. Fuster, V., Harrington, R. A. & Walsh, R. A. *Hurst's The Heart* (New York: Health Professions Division, McGraw-Hill, 2011).
 81. Pirola, S., Jarral, O., O'Regan, D., Asimakopoulos, G., Anderson, J., Pepper, J., Athanasiou, T. & Xu, X. Computational study of aortic hemodynamics for patients with an abnormal

- aortic valve: The importance of secondary flow at the ascending aorta inlet. *APL bioengineering* **2**, 026101 (2018).
82. Kimura, N., Nakamura, M., Komiya, K., Nishi, S., Yamaguchi, A., Tanaka, O., Misawa, Y., Adachi, H. & Kawahito, K. Patient-specific assessment of hemodynamics by computational fluid dynamics in patients with bicuspid aortopathy. *The Journal of Thoracic and Cardiovascular Surgery* **153**, S52–S62.e3. ISSN: 0022-5223 (2017).
 83. Callaghan, F. M. & Grieve, S. M. Spatial resolution and velocity field improvement of 4D-flow MRI. *Magnetic Resonance in Medicine* **78**, 1959–1968. ISSN: 07403194 (2017).
 84. Soudah, E., Casacuberta, J., Gamez-Montero, P. J., Pérez, J. S., Rodríguez-Cancio, M., Raush, G., Li, C. H., Carreras, F. & Castilla, R. Estimation of Wall Shear Stress Using 4D Flow Cardiovascular Mri and Computational Fluid Dynamics. *Journal of Mechanics in Medicine and Biology* **17**, 1750046. ISSN: 0219-5194 (2016).
 85. Pirola, S., Cheng, Z., Jarral, O., O'Regan, D., Pepper, J., Athanasiou, T. & Xu, X. On the choice of outlet boundary conditions for patient-specific analysis of aortic flow using computational fluid dynamics. *Journal of biomechanics* **60**, 15–21 (2017).
 86. Skiadopoulos, A., Neofytou, P. & Housiadas, C. Comparison of blood rheological models in patient specific cardiovascular system simulations. *Journal of Hydrodynamics, Ser. B* **29**, 293–304. ISSN: 1001-6058 (2017).
 87. Vignon-Clementel, I. E., Figueroa, C. A., Jansen, K. E. & Taylor, C. A. Outflow boundary conditions for three-dimensional finite element modeling of blood flow and pressure in arteries. *Computer methods in applied mechanics and engineering* **195**, 3776–3796 (2006).
 88. Hayes, S. *Statical essays: containing haemastaticks* (W. Innys and R. Manby, London, 1733).
 89. Safar, M. E. & Levy, B. I. Resistance Vessels in Hypertension. *Comprehensive Hypertension E-Book*, 145 (2007).
 90. Westerhof, N., Lankhaar, J.-W. & Westerhof, B. E. The arterial windkessel. *Medical & biological engineering & computing* **47**, 131–141 (2009).
 91. Benetos, A., Safar, M., Rudnichi, A., Smulyan, H., Richard, J.-L., Ducimetière, P. & Guize, L. Pulse pressure: a predictor of long-term cardiovascular mortality in a French male population. *Hypertension* **30**, 1410–1415 (1997).
 92. Mitchell, G. F., Moyé, L. A., Braunwald, E., Rouleau, J.-L., Bernstein, V., Geltman, E. M., Flaker, G. C., Pfeffer, M. A. & Investigators, f. t. S. Sphygmomanometrically determined pulse pressure is a powerful independent predictor of recurrent events after myocardial infarction in patients with impaired left ventricular function. *Circulation* **96**, 4254–4260 (1997).
 93. Frank, O. *Die grundform des arteriellen pulses: Mathematische Analyse. Erste Abhandlung* (1899).
 94. Wetterer, E. *Quantitative relationships between current strength and pressure in the natural circulation with time-variable elasticity of the arterial chamber* (JF Lehmanns Verlag, 1940).
 95. Wetterer, E. Flow and pressure in the arterial system, their hemodynamic relationship, and the principles of their measurement. *Minnesota medicine* **37**, 77 (1954).

96. Wetterer, E. *The effect of cardiac activity on the dynamics of the arterial system* in *Clinical Weekly* **34** (1956), 609–609.
97. Wetterer, E. & Kenner, T. *Fundamentals of arterial pulse dynamics* (Springer Berlin-Heidelberg-New York, 1968).
98. Stergiopoulos, N., Westerhof, B. E. & Westerhof, N. Total arterial inertance as the fourth element of the windkessel model. *American Journal of Physiology-Heart and Circulatory Physiology* **276**, H81–H88 (1999).
99. LaDisa, J. F., Alberto Figueroa, C., Vignon-Clementel, I. E., Jin Kim, H., Xiao, N., Ellwein, L. M., Chan, F. P., Feinstein, J. A. & Taylor, C. A. Computational simulations for aortic coarctation: representative results from a sampling of patients. *Journal of Biomechanical Engineering* **133**, 091008 (2011).
100. Laskey, W. K., Parker, H. G., Ferrari, V. A., Kussmaul, W. G. & Noordergraaf, A. Estimation of total systemic arterial compliance in humans. *Journal of Applied Physiology* **69**, 112–119. ISSN: 01617567 (1990).
101. Randall, O. S., Esler, M. D., Calfee, R. V., Bulloch, G. F., Maisel, A. S. & Culp, B. Arterial compliance in hypertension (1976).
102. Rosen, I. & White, H. The relation of pulse pressure to Stroke volume. *American Journal of Physiology-Legacy Content* **78**, 168–184 (1926).
103. Segers, P., Brimiouille, S., Stergiopoulos, N., Westerhof, N., Naeije, R., Maggiorini, M. & Verdonck, P. Pulmonary arterial compliance in dogs and pigs: the three-element windkessel model revisited. *American Journal of Physiology-Heart and Circulatory Physiology* **277**, H725–H731 (1999).
104. Segers, P., Verdonck, P., Deryck, Y., Brimiouille, S., Naeije, R., Carlier, S. & Stergiopoulos, N. Pulse pressure method and the area method for the estimation of total arterial compliance in dogs: sensitivity to wave reflection intensity. *Annals of biomedical engineering* **27**, 480–485 (1999).
105. Liu, Z., Brin, K. P. & Yin, F. Estimation of total arterial compliance: an improved method and evaluation of current methods. *American Journal of Physiology-Heart and Circulatory Physiology* **251**, H588–H600 (1986).
106. Romarowski, R. M., Lefieux, A., Morganti, S., Veneziani, A. & Auricchio, F. Patient-specific CFD modelling in the thoracic aorta with PC-MRI-based boundary conditions: A least-square three-element Windkessel approach. *International Journal for Numerical Methods in Biomedical Engineering* **34**, 1–21. ISSN: 20407947 (2018).
107. Menut, M., Bousset, L., Escriva, X., Bou-Said, B., Walter-Le Berre, H., Marchesse, Y., Milon, A., Della Schiava, N., Lermusiaux, P. & Tichy, J. Comparison between a generalized Newtonian model and a network-type multiscale model for hemodynamic behavior in the aortic arch: validation with 4D MRI data for a case study. *Journal of biomechanics* **73**, 119–126 (2018).
108. Bäumlner, K., Vedula, V., Sailer, A. M., Seo, J., Chiu, P., Mistelbauer, G., Chan, F. P., Fischbein, M. P., Marsden, A. L. & Fleischmann, D. Fluid–structure interaction simulations of patient-specific aortic dissection. *Biomechanics and Modeling in Mechanobiology*. ISSN: 16177940 (2020).

109. Morbiducci, U., Gallo, D., Massai, D., Consolo, F., Ponzini, R., Antiga, L., Bignardi, C., Deriu, M. A. & Redaelli, A. Outflow conditions for image-based hemodynamic models of the carotid bifurcation: implications for indicators of abnormal flow. *Journal of biomechanical engineering* **132** (2010).
110. Klabunde, R. *Cardiovascular physiology concepts* (Lippincott Williams & Wilkins, 2011).
111. Saikrishnan, N., Mirabella, L. & Yoganathan, A. P. Bicuspid aortic valves are associated with increased wall and turbulence shear stress levels compared to trileaflet aortic valves. *Biomechanics and Modeling in Mechanobiology* **14**, 577–588. ISSN: 16177940 (2015).
112. Nerem, R. & Seed, W. An in vivo study of aortic flow disturbances. *Cardiovascular research* **6**, 1–14 (1972).
113. Nerem, R., Seed, W. & Wood, N. An experimental study of the velocity distribution and transition to turbulence in the aorta. *Journal of Fluid Mechanics* **52**, 137–160 (1972).
114. Peacock, J., Jones, T., Tock, C. & Lutz, R. The onset of turbulence in physiological pulsatile flow in a straight tube. *Experiments in fluids* **24**, 1–9 (1998).
115. Falsetti, H. L., Carroll, R. J., Swope, R. D. & Chen, C. Turbulent blood flow in the ascending aorta of dogs. *Cardiovascular research* **17**, 427–436 (1983).
116. Stettler, J. & Hussain, A. F. On transition of the pulsatile pipe flow. *Journal of Fluid Mechanics* **170**, 169–197 (1986).
117. Sarpkaya, T. Experimental determination of the critical Reynolds number for pulsating Poiseuille flow. *Journal of Basic Engineering* **88**, 589–598 (1966).
118. Xu, D., Warnecke, S., Song, B., Ma, X. & Hof, B. Transition to turbulence in pulsating pipe flow. *Journal of Fluid Mechanics* **831**, 418–432 (2017).
119. Fung, Y.-C. Biomechanics: circulation. *Shock* **9**, 155 (1998).
120. Miyazaki, S., Itatani, K., Furusawa, T., Nishino, T., Sugiyama, M., Takehara, Y. & Yasukochi, S. Validation of numerical simulation methods in aortic arch using 4D Flow MRI. *Heart and Vessels* **32**, 1032–1044. ISSN: 16152573 (2017).
121. Ziegler, M., Lantz, J., Ebbers, T. & Dyverfeldt, P. Assessment of turbulent flow effects on the vessel wall using four-dimensional flow MRI. *Magnetic Resonance in Medicine* **77**, 2310–2319. ISSN: 15222594 (2017).
122. Smagorinsky, J. General Circulation Experiments with the Primitive Equations. I. The Basic Experiment. *Monthly Weather Review* **91**, 99–164 (1963).
123. Nicoud, F. & Ducros, F. Subgrid-scale stress modelling based on the square of the velocity gradient tensor. *Flow, turbulence and Combustion* **62**, 183–200 (1999).
124. Menter, F. R. Two-equation eddy-viscosity turbulence models for engineering applications. *AIAA journal* **32**, 1598–1605 (1994).
125. Nordmeyer, S., Hellmeier, F., Yevtushenko, P., Kelm, M., Lee, C.-B., Lehmann, D., Kropf, S., Berger, F., Falk, V., Knosalla, C., Kuehne, T. & Goubergrits, L. Abnormal aortic flow profiles persist after aortic valve replacement in the majority of patients with aortic valve disease: how model-based personalized therapy planning could improve results. A pilot study approach. *European Journal of Cardio-Thoracic Surgery*. ISSN: 1010-7940 (2019).

126. Biglino, G., Cosentino, D., Steeden, J. A., De Nova, L., Castelli, M., Ntsinjana, H., Pennati, G., Taylor, A. M. & Schievano, S. Using 4D Cardiovascular Magnetic Resonance Imaging to Validate Computational Fluid Dynamics: A Case Study. *Frontiers in Pediatrics* **3**. ISSN: 2296-2360 (2015).
127. Perinajova, R., Juffermans, J. F., Westenberg, J. J., van der Palen, R. L., van den Boogaard, P. J., Lamb, H. J. & Kenjereš, S. Geometrically induced wall shear stress variability in CFD-MRI coupled simulations of blood flow in the thoracic aortas. *Computers in Biology and Medicine* **133**, 104385 (2021).
128. Jayendiran, R., Campisi, S., Viallon, M., Croisille, P. & Avril, S. Hemodynamics alteration in patient-specific dilated ascending thoracic aortas with tricuspid and bicuspid aortic valves. *Journal of Biomechanics* **110**, 109954 (2020).
129. Bakhshinejad, A., Baghaie, A., Vali, A., Saloner, D., Rayz, V. L. & D'Souza, R. M. Merging computational fluid dynamics and 4D Flow MRI using proper orthogonal decomposition and ridge regression. *Journal of biomechanics* **58**, 162–173 (2017).
130. Baretta, A., Corsini, C., Yang, W., Vignon-Clementel, I. E., Marsden, A. L., Feinstein, J. A., Hsia, T.-Y., Dubini, G., Migliavacca, F., Pennati, G., *et al.* Virtual surgeries in patients with congenital heart disease: a multi-scale modelling test case. *Philosophical Transactions of the Royal Society A: Mathematical, Physical and Engineering Sciences* **369**, 4316–4330 (2011).
131. Pennati, G., Migliavacca, F., Dubini, G., Pietrabissa, R., Fumero, R. & de Leval, M. R. Use of mathematical model to predict hemodynamics in cavopulmonary anastomosis with persistent forward flow. *Journal of Surgical Research* **89**, 43–52 (2000).
132. Pennati, G., Migliavacca, F., Dubini, G., Pietrabissa, R. & de Leval, M. R. A mathematical model of circulation in the presence of the bidirectional cavopulmonary anastomosis in children with a univentricular heart. *Medical engineering & physics* **19**, 223–234 (1997).
133. Kung, E., Baretta, A., Baker, C., Arbia, G., Biglino, G., Corsini, C., Schievano, S., Vignon-Clementel, I. E., Dubini, G., Pennati, G., *et al.* Predictive modeling of the virtual Hemi-Fontan operation for second stage single ventricle palliation: two patient-specific cases. *Journal of biomechanics* **46**, 423–429 (2013).
134. Esmailie, F., Razavi, A., Yeats, B., Sivakumar, S. K., Chen, H., Samaee, M., Shah, I. A., Veneziani, A., Yadav, P., Thourani, V. H., *et al.* Biomechanics of Transcatheter Aortic Valve Replacement Complications and Computational Predictive Modeling. *Structural Heart* **6**, 100032 (2022).
135. Dowling, C., Gooley, R., McCormick, L., Firoozi, S. & Brecker, S. J. Patient-specific computer simulation to predict long-term outcomes after transcatheter aortic valve replacement. *Journal of Cardiovascular Computed Tomography* **16**, 254–261 (2022).
136. Quarteroni, A. & Formaggia, L. Mathematical Modelling and Numerical Simulation of the Cardiovascular system. *Handbook and Numerical Analysis* **12**, 3–127 (2004).
137. Hirschhorn, M., Tchantchaleishvili, V., Stevens, R., Rossano, J. & Throckmorton, A. Fluid Structure interaction modeling in cardiovascular medicine – A systematic review 2017–2019. *Medical Engineering & Physics*, 1–13. ISSN: 13504533 (2020).

138. Peskin, C. S. Flow patterns around heart valves: A numerical method. *Journal of Computational Physics* **10**, 252–271. ISSN: 10902716 (1972).
139. Sodhani, D., Reese, S., Aksenov, A., Soğancı, S., Jockenhövel, S., Mela, P. & Stapleton, S. E. Fluid-structure interaction simulation of artificial textile reinforced aortic heart valve: Validation with an in-vitro test. *Journal of Biomechanics* **78**, 52–69. ISSN: 18732380 (2018).
140. Benra, F. K., Dohmen, H. J., Pei, J., Schuster, S. & Wan, B. A comparison of one-way and two-way coupling methods for numerical analysis of fluid-structure interactions. *Journal of Applied Mathematics* **2011**. ISSN: 1110757X (2011).
141. Capellini, K., Gasparotti, E., Cella, U., Costa, E., Fanni, B. M., Groth, C., Porziani, S., Biancolini, M. E. & Celi, S. A novel formulation for the study of the ascending aortic fluid dynamics with in vivo data. *Medical Engineering & Physics* **91**, 68–78 (2021).
142. Crosetto, P., Reymond, P., Deparis, S., Kontaxakis, D., Stergiopoulos, N. & Quarteroni, A. Fluid-structure interaction simulation of aortic blood flow. *Computers and Fluids* **43**, 46–57. ISSN: 00457930 (2011).
143. Langewouters, G. J. *Visco-elasticity of the human aorta in vitro in relation to pressure and age* PhD thesis (Krips Repro, 1982).
144. Liu, J., Shar, J. A. & Sucosky, P. Wall shear stress directional abnormalities in BAV aortas: Toward a new hemodynamic predictor of aortopathy? *Frontiers in Physiology* **9**, 1–9. ISSN: 1664042X (2018).
145. Nowak, M., Melka, B., Rojczyk, M., Gracka, M., Nowak, A. J., Golda, A., Adamczyk, W. P., Isaac, B., Białycki, R. A. & Ostrowski, Z. The protocol for using elastic wall model in modeling blood flow within human artery. *European Journal of Mechanics, B/Fluids* **77**, 273–280. ISSN: 09977546 (2019).
146. Bazilevs, Y., Takizawa, K. & Tezduyar, T. in *Computational Fluid–Structure Interaction: Methods and Applications* 191–258 (John Wiley & Sons, Ltd, 2012). ISBN: 9781118483565.
147. Alishahi, M., Alishahi, M. M. & Emdad, H. Numerical simulation of blood flow in a flexible stenosed abdominal real aorta. *Scientia Iranica* **18**, 1297–1305. ISSN: 10263098 (2011).
148. Lantz, J., Renner, J. & Karlsson, M. Wall shear stress in a subject specific human aorta - Influence of fluid-structure interaction. *International Journal of Applied Mechanics* **3**, 759–778. ISSN: 17588251 (2011).
149. Reymond, P., Crosetto, P., Deparis, S., Quarteroni, A. & Stergiopoulos, N. Physiological simulation of blood flow in the aorta: Comparison of hemodynamic indices as predicted by 3-D FSI, 3-D rigid wall and 1-D models. *Medical Engineering and Physics* **35**, 784–791. ISSN: 18734030 (2013).
150. Bathe, M. & Kamm, R. A fluid-structure interaction finite element analysis of pulsatile blood flow through a compliant stenotic artery. *Journal of Biomechanical Engineering* **121**, 360–369 (1999).
151. Li, Z. & Kleinstreuer, C. Fluid-structure interaction effects on sac-blood pressure and wall stress in a stented aneurysm. *Journal of Biomechanical Engineering* **127**, 662–671 (2005).

152. Quarteroni, A., Tuveri, M. & Veneziani, A. Computational vascular fluid dynamics: Problems, models and methods. *Computing and Visualization in Science* **2**, 163–197. ISSN: 14330369 (2000).
153. Mendez, V., Di Giuseppe, M. & Pasta, S. Comparison of hemodynamic and structural indices of ascending thoracic aortic aneurysm as predicted by 2-way FSI, CFD rigid wall simulation and patient-specific displacement-based FEA. *Computers in Biology and Medicine* **100**, 221–229. ISSN: 18790534 (2018).
154. Hasan, A., Kolahdouz, E. M., Enquobahrie, A., Caranasos, T. G., Vavalle, J. P. & Griffith, B. E. Image-based immersed boundary model of the aortic root. *Medical Engineering and Physics* **47**, 72–84. ISSN: 18734030 (2017).
155. Pasta, S., Rinaudo, A., Luca, A., Pilato, M., Scardulla, C., Gleason, T. G. & Vorp, D. A. Difference in hemodynamic and wall stress of ascending thoracic aortic aneurysms with bicuspid and tricuspid aortic valve. *Journal of Biomechanics* **46**, 1729–1738. ISSN: 00219290 (2013).
156. Pasta, S., Gentile, G., Raffa, G. M., Bellavia, D., Chiarello, G., Liotta, R., Luca, A., Scardulla, C. & Pilato, M. In Silico Shear and Intramural Stresses are Linked to Aortic Valve Morphology in Dilated Ascending Aorta. *European Journal of Vascular and Endovascular Surgery* **54**, 254–263. ISSN: 15322165 (2017).
157. Tango, A. M., Salmons-Smith, J., Ducci, A. & Burriesci, G. Validation and Extension of a Fluid–Structure Interaction Model of the Healthy Aortic Valve. *Cardiovascular Engineering and Technology* **9**, 739–751. ISSN: 18694098 (2018).
158. Updegrove, A., Wilson, N. M., Merkow, J., Lan, H., Marsden, A. L. & Shadden, S. C. SimVascular: an open source pipeline for cardiovascular simulation. *Annals of biomedical engineering* **45**, 525–541 (2017).
159. Grande Gutierrez, N., Mathew, M., McCrindle, B. W., Tran, J. S., Kahn, A. M., Burns, J. C. & Marsden, A. L. Hemodynamic variables in aneurysms are associated with thrombotic risk in children with Kawasaki disease. *International Journal of Cardiology* **281**, 15–21. ISSN: 18741754 (2019).
160. Ward, E. P., Shiavazzi, D., Sood, D., Marsden, A., Lane, J., Owens, E. & Barleben, A. Computed tomography fractional flow reserve can identify culprit lesions in aortoiliac occlusive disease using minimally invasive techniques. *Annals of vascular surgery* **38**, 151–157 (2017).
161. Kasinpila, P., Kong, S., Fong, R., Shad, R., Kaiser, A. D., Marsden, A. L., Woo, Y. J. & Hiesinger, W. Use of patient-specific computational models for optimization of aortic insufficiency after implantation of left ventricular assist device. *Journal of Thoracic and Cardiovascular Surgery* **94304**. ISSN: 1097685X (2020).
162. Razavi, A., Sachdeva, S., Frommelt, P. C. & Jr, J. F. L. *Patient-Specific Numerical Analysis of Coronary Flow in Children with Intramural Anomalous Aortic Origin of Coronary Arteries* ISBN: 4144395715 (Elsevier Inc., 2020).
163. Autodesk, Inc. *meshMixer* version 2019.05. Dec. 9, 2019. <https://www.meshmixer.com>.

164. HeartFlow Inc. *Transforming the diagnosis and management of coronary artery disease worldwide* www.heartflow.com. (accessed: 23.09.2020).
165. Arthurs, C. J., Khlebnikov, R., Melville, A., Marčan, M., Gomez, A., Dillon-Murphy, D., Cuomo, F., Silva Vieira, M., Schollenberger, J., Lynch, S. R., *et al.* CRIMSON: An open-source software framework for cardiovascular integrated modelling and simulation. *PLOS Computational Biology* **17**, e1008881 (2021).
166. Theriault-Lauzier, P., Messika-Zeitoun, D. & Piazza, N. Patient-Specific Computer Simulation in TAVR: Will the Technology Gain Widespread Adoption? *Cardiovascular Interventions* **13**, 1813–1815 (2020).
167. El Faquir, N., De Backer, O., Bosmans, J., Rudolph, T., Buzzatti, N., Bieliauskas, G., Collias, V., Wienemann, H., Schiavi, D., Cummins, P., *et al.* Patient-specific computer simulation in TAVR with the self-expanding Evolut R valve. *Cardiovascular Interventions* **13**, 1803–1812 (2020).
168. The MathWorks Inc. *MatLAB* version (R2019a). 2019.
169. Hofman, M. B., Visser, F. C., Van Rossum, A. C., Vink, G. Q., Sprenger, M. & Westerhof, N. In vivo validation of magnetic resonance blood volume flow measurements with limited spatial resolution in small vessels. *Magnetic resonance in medicine* **33**, 778–784 (1995).
170. Geiger, J., Callaghan, F. M., Burkhardt, B. E., Valsangiacomo Buechel, E. R. & Kellenberger, C. J. Additional value and new insights by four-dimensional flow magnetic resonance imaging in congenital heart disease: application in neonates and young children. *Pediatric Radiology* **51**, 1503–1517 (2021).
171. Ramirez-Suarez, K. I., Tierradentro-Garcia, L. O., Otero, H. J., Rapp, J. B., White, A. M., Partington, S. L., Harris, M. A., Vatsky, S. A., Whitehead, K. K., Fogel, M. A., *et al.* Optimizing neonatal cardiac imaging (magnetic resonance/computed tomography). *Pediatric Radiology*, 1–15 (2021).
172. Abalo, K. D., Rage, E., Leuraud, K., Richardson, D. B., Le Pointe, H. D., Laurier, D. & Bernier, M.-O. Early life ionizing radiation exposure and cancer risks: systematic review and meta-analysis. *Pediatric radiology* **51**, 45–56 (2021).
173. Schooler, G. R., Cravero, J. P. & Callahan, M. J. Assessing and conveying risks and benefits of imaging in neonates using ionizing radiation and sedation/anesthesia. *Pediatric radiology*, 1–6 (2021).
174. Cohen, S., Liu, A., Gurvitz, M., Guo, L., Therrien, J., Laprise, C., Kaufman, J. S., Abrahamowicz, M. & Marelli, A. J. Exposure to low-dose ionizing radiation from cardiac procedures and malignancy risk in adults with congenital heart disease. *Circulation* **137**, 1334–1345 (2018).
175. Nolte, D., Urbina, J., Sotelo, J., Sok, L., Montalba, C., Valverde, I., Osses, A., Uribe, S. & Bertoglio, C. Validation of 4D Flow based relative pressure maps in aortic flows. *Medical image analysis* **74**, 102195 (2021).
176. Sotelo, J., Urbina, J., Valverde, I., Tejos, C., Irarrazaval, P., Andia, M. E., Uribe, S. & Hurtado, D. E. 3D quantification of wall shear stress and oscillatory shear index using a finite-element method in 3D CINE PC-MRI data of the thoracic aorta. *IEEE transactions on medical imaging* **35**, 1475–1487 (2016).

177. Sotelo, J., Urbina, J., Valverde, I., Mura, J., Tejos, C., Irrarrazaval, P., Andia, M. E., Hurtado, D. E. & Uribe, S. Three-dimensional quantification of vorticity and helicity from 3D cine PC-MRI using finite-element interpolations. *Magnetic resonance in medicine* **79**, 541–553 (2018).
178. Bock, J., Frydrychowicz, A., Stalder, A. F., Bley, T. A., Burkhardt, H., Hennig, J. & Markl, M. 4D phase contrast MRI at 3 T: Effect of standard and blood-pool contrast agents on SNR, PC-MRA, and blood flow visualization. *Magnetic Resonance in Medicine: An Official Journal of the International Society for Magnetic Resonance in Medicine* **63**, 330–338 (2010).
179. Kintel, M. *OpenSCAD* version 2019.05. Dec. 9, 2019.
180. Netgen. *Netgen* version 8.6.10. Dec. 9, 2019.
181. Creative Fields Ltd. *cfMesh* version 1.1.2. Dec. 9, 2019.
182. Jung, J., Lyczkowski, R. W., Panchal, C. B. & Hassanein, A. Multiphase hemodynamic simulation of pulsatile flow in a coronary artery. *Journal of biomechanics* **39**, 2064–2073 (2006).
183. Dill, D. B. & Costill, D. L. Calculation of percentage changes in volumes of blood, plasma, and red cells in dehydration. *Journal of applied physiology* **37**, 247–248 (1974).
184. Hess, A. T., Bissell, M. M., Glaze, S. J., Pitcher, A., Myerson, S., Neubauer, S. & Robson, M. D. Evaluation of Circulation, Γ , as a quantifying metric in 4D flow MRI. *Journal of Cardiovascular Magnetic Resonance* **15**, 1–2 (2013).
185. Cherry, M., Khatir, Z., Khan, A. & Bissell, M. The Impact of 4D-Flow MRI Spatial Resolution on Patient-Specific CFD Simulations of the Thoracic Aorta. *Scientific Reports* **12**, 15128 (2022).
186. Hoskins, P. R., Hoskins, P. R., Lawford, P. V., Lawford, P. V., Doyle, B. J. & Doyle, B. J. *Cardiovascular biomechanics* (Springer, 2017).
187. Elastrat. *Elastrat: Anatomical Vascular Models* <https://elastrat.com/product-thorax-heart-flexible-240-t-s-n-005.php>. (accessed: 06.09.2022).
188. Simutec. *Shelley Medical Imaging Technologies* <http://www.simutec.com/>. (accessed: 14.09.2022).
189. Smith, R. F., Rutt, B. K. & Holdsworth, D. W. Anthropomorphic carotid bifurcation phantom for MRI applications. *Journal of Magnetic Resonance Imaging* **10**, 533–544 (1999).
190. Summers, P. E., Holdsworth, D. W., Nikolov, H. N., Rutt, B. K. & Drangova, M. Multisite trial of MR flow measurement: phantom and protocol design. *Journal of Magnetic Resonance Imaging: An Official Journal of the International Society for Magnetic Resonance in Medicine* **21**, 620–631 (2005).
191. Shaffer, F. & Ginsberg, J. P. An overview of heart rate variability metrics and norms. *Frontiers in public health*, 258 (2017).
192. Hower, I. M., Harper, S. A. & Buford, T. W. Circadian rhythms, exercise, and cardiovascular health. *Journal of circadian rhythms* **16** (2018).

193. Nunan, D., Sandercock, G. R. & Brodie, D. A. A quantitative systematic review of normal values for short-term heart rate variability in healthy adults. *Pacing and clinical electrophysiology* **33**, 1407–1417 (2010).
194. Stalder, A. F., Russe, M., Frydrychowicz, A., Bock, J., Hennig, J. & Markl, M. Quantitative 2D and 3D phase contrast MRI: optimized analysis of blood flow and vessel wall parameters. *Magnetic Resonance in Medicine: An Official Journal of the International Society for Magnetic Resonance in Medicine* **60**, 1218–1231 (2008).
195. Petersson, S., Dyverfeldt, P. & Ebbers, T. Assessment of the accuracy of MRI wall shear stress estimation using numerical simulations. *Journal of Magnetic Resonance Imaging* **36**, 128–138 (2012).